

Development of Novel Coatings for Full Field Strain Measurements

Thesis submitted for the degree of Doctor of Philosophy

William FRASER

The University of Sheffield

Faculty of Engineering

Department of Mechanical Engineering

Submission Date

July 2023

Acknowledgements

I would like to thank my industrial sponsors, Arkema UK Wetherby, Airbus and NPL for their assistance throughout my research. Airbus; Paul Richardson and Ian Jones, thank you for your invaluable insight into the industrial applications of reflection photoelasticity providing enthusiasm for the research that provided substantial confidence in the developed technology. NPL; Michael Gower and Mark Gee, thank you for your expertise providing helpful guidance, and knowledge that assisted the understanding of the developed technology. Without Arkema UK's involvement; Dr Richard Plenderleith, Dr Sen Liu and Hannah Young, the research would have not been possible. Through offering support, guidance and expertise to substantial time spent in their facilities, mentoring and donating their UV curer to the University, you have been an incredible part of this research and I am grateful for all you have done. I would especially like to thank Dr Sen Liu for the considerable time you spent helping within this research. Your guidance with the first few years were crucial to the success of the research, thank you.

I would also like to thank Geoff Calvert who often went above and beyond. Thank you for letting me disturb your retirement with my questions, you are a big part of why I have enjoyed conducting this work. I hope you are rallying as much as you possibly can.

I am indebted to the technical staff within the University; Richard Kay and Christopher Todd, whose involvement and attitude made working within the University a pleasure.

I am incredibly thankful to my amazing family for their love and support throughout this research. To my parents; David and Julie Fraser, and grandparents; Peter Fraser, Graham and Katheleen Booth, thank you so much for all your love, encouragement and interest into all I have achieved. To my brother and his fiancée; Jacob Fraser and Masha Chadry, you have provided much humour that assisted me to bear through the difficult times of this research. I would also like to thank my partner's family; Duncan and Hilary Cheshire & Beth and Ant Rex, whose support has been enormous. You will all be forced to read my thesis to truly understand how you have helped me achieve everything in this research.

To my wonderful partner Becca Cheshire, thank you so much for everything. Without your endless love and support I would not have had the confidence to start and finish this journey. I promise I will stop forcing you to observe every bit of photoelasticity I stumble upon...every other bit on the other hand will be viewed in great detail.

I would like to finish by thanking my incredible Ph.D. supervisors Dr Rachel Tomlinson and Dr Andrew Parnell. Your openness, guidance and patience has been paramount to the success of this research. Whilst going through your own hardships you have still remained supportive and immensely helpful. You have provided me with an amazing opportunity and I have thoroughly enjoyed working with you both.

Abstract

Reflection Photoelastic Stress Analysis (RPSA) is an experimental technique used in industries to assist in a variety of design and manufacture processes. Users can benefit from immediate qualitative and quantitative information, for example, about maximum shear strains in complex geometries. One such user of RPSA, and the focus of this research, is Airbus that perform RPSA within the manufacturing process of their aircraft wing assemblies. Although insightful, RPSA procedures suffer from complicated application processes, a need for skilled engineers and large timescales for data collection. These issues all stem from one vital component — the photoelastic coating material. Common commercially available RPSA coatings are designed in such a way to compensate for failings in RPSA apparatus that were once insensitive to small changes in component surface strain. However, current commercially available automated photoelastic collection and analysis apparatus have given the potential for RPSA to be a truly effective method. This is due to high detection sensitivity of better than 0.1 nm that translates to a 20 $\mu\epsilon$ resolution. RPSA techniques could benefit and compensate for using easy to apply, thinner ($\sim$50 μm) but less sensitive coatings. As a result, this research aims to investigate and develop a novel, time-efficient and 'smart' coating material that updates current RPSA methods. Whilst applications at Airbus are the focus of this research the wider applicability of this coating is extensive. Within this thesis, the key criteria for the new coating are outlined and explained by reviewing relevant theory, literature and all conducted experimental research. Coating development is divided into two main investigative topics: reflection photoelasticity (RPE) and mechanoluminescence (ML).

The RPE development topic utilised a range of UV curable resins that were rationally designed into an optimum formulation. The coating was designed and tested with the automated RPE imaging device — the Grey Field Polariscope (GFP). The choice of UV curable materials provides a new range of rapid application coatings boasting

a 20 s cure time whilst possessing similar RPE sensitivities of existing commercial products. Additionally, the coating was designed with thickness correction capabilities within post-processing to further promote the ease of use of the coating. By introducing a red tint to the formulation and imaging with the GFP, it was shown that thickness differences could be corrected in order to provide accurate RPSA data. At targetted thicknesses of $\sim$50 μm, correction by manipulation of different wavelengths of light has not been attempted before. Performing calibration experiments, the clear (WF31) and red tinted (WF-Red1) UV curable materials possessed strain-optic coefficients of $K =$ 0.0982 $\pm$ 0.0018 & 0.080 $\pm$ 0.003 respectively — medium-high sensitivity coatings.

The ML topic investigated the introduction of a mechanoluminescent phosphor to the developed UV curable formulation to produce a novel dual-technique strain imaging coating. ML materials generate light under the influence of strain with the intensity able to provide a map of the surface's strain field. The objective was to capture the production of ML light whilst performing RPE simultaneously in order to provide additional information that would support both techniques. The commonly researched ML material strontium aluminate $SrAl_2O_4$:Eu was utilised and was added at a 30 % weight percentage to the optimised UV curable formulation. It was demonstrated for the first time that concurrent measurement of both techniques was possible by filtering the green ML light against RPE performed monochromatically using red light. Qualitative comparisons demonstrated it utility, however challenges utilising ML within elastic conditions limits it use. Firstly, it was observed that the ML coating had a 'one-shot' application with the intensity of produced light diminishing with subsequent loads. This was a result of the ML phosphor debonding with the carrier resin. Additionally, the light production within elastic conditions was poor requiring high strain rates to produce observable conditions. As a result, eliminating all ambient light is a prerequisite for successful application. However, ML demonstrated relativity high light intensities when at areas of high strain, singularities, and when the component breached its elastic limit. Therefore, it has been shown that ML's potentially usefulness could be a validation technique to go alongside photoelasticity.

The research has successfully demonstrated the high performance of a new reflection

coating with the ability for application, data collection and processing, and coating removal to be performed in one single day — an order of magnitude better than existing techniques. Combination with ML materials for simultaneous RPE and ML capture has been demonstrated with the ability for RPE validation however not without difficulties. However, a novel technique/apparatus has been designed and implemented which allows for the first time PE and ML data to be measured simultaneously.

Contents

1 Introduction **1**
- 1.1 Research objectives . . . 1
- 1.2 Essential Coating Properties . . . 5
- 1.3 Thesis overview . . . 6
  - 1.3.1 Photoelastic coating development . . . 7
  - 1.3.2 Mechanoluminescent coating development . . . 8

2 Background theory and current state of the art **9**
- 2.1 Birefringence . . . 9
- 2.2 Molecular basis of birefringence . . . 13
- 2.3 Measuring birefringence . . . 15
  - 2.3.1 Polarisation and interference . . . 16
  - 2.3.2 The linear polariscope . . . 18
  - 2.3.3 Interference patterns . . . 20
  - 2.3.4 The circular polariscope . . . 22
  - 2.3.5 Fringe analysis - automated photoelasticity . . . 24
  - 2.3.6 Reflection photoelasticity . . . 26
  - 2.3.7 Simultaneous capture . . . 30
  - 2.3.8 The Poleidoscope . . . 31
  - 2.3.9 The GFP1600 . . . 32
    - 2.3.9.1 The subtraction facility . . . 41
- 2.4 Photoelastic coatings and applications . . . 41
  - 2.4.1 Current coating materials . . . 41
  - 2.4.2 Example applications . . . 44
  - 2.4.3 Airbus . . . 48
- 2.5 Mechanoluminescence . . . 49
  - 2.5.1 Materials . . . 50
  - 2.5.2 Mechanoluminescence in tridymite structures . . . 50
- 2.6 Visualising and interpreting stress distributions . . . 52
- 2.7 Conclusions . . . 56

3 Coating development **58**
- 3.1 UV curable resins and preliminary research . . . 58
  - 3.1.1 UV curable resins . . . 61
  - 3.1.2 Preliminary research . . . 64

3.2 Formulation screening . . . 66
3.2.1 Formulations . . . 67
3.2.2 Coating applications . . . 70
3.2.2.1 Methodology - UV curable materials . . . 70
3.2.2.2 Results and analysis - UV curable materials . . . 72
3.2.2.3 Methodology - PS-1E . . . 76
3.2.2.4 Results and analysis - PS-1E . . . 79
3.2.3 Photoelastic response of UV curable formulations . . . 80
3.2.3.1 Methodology . . . 80
3.2.3.2 Results and analysis . . . 84
3.2.4 Viscosity . . . 89
3.2.5 Solvent resistance . . . 90
3.2.6 Adhesion . . . 90
3.2.7 Flexibility . . . 91
3.2.8 Glass transition temperature . . . 91
3.2.9 Screening conclusions . . . 92
3.3 Coating optimisation . . . 94
3.3.1 Reviewing the curing process . . . 94
3.3.1.1 Methodology . . . 95
3.3.1.2 Results and analysis . . . 96
3.3.2 Optimising the formulation . . . 97
3.3.2.1 Design of experiments . . . 97
3.3.2.2 Methodology . . . 97
3.3.2.3 Results and analysis . . . 100
3.3.3 Coating calibration . . . 106
3.3.3.1 Methodology . . . 106
3.3.3.2 Results and analysis . . . 109
3.3.4 Discussion and conclusions . . . 110

4 The effects of curing time on photoelastic response 112
4.1 Repeat WF31 photoelastic measurements . . . 112
4.1.1 Methodology . . . 112
4.1.2 Results and analysis . . . 113
4.2 The effects of curing time on photoelastic response . . . 114
4.2.1 Methodology . . . 115
4.2.2 Results and analysis . . . 116
4.3 Maximising cure conversion . . . 118
4.3.0.1 ATR-FTIR . . . 118
4.3.1 Methodology . . . 120
4.3.2 Results and analysis . . . 122
4.4 Discussion and conclusions . . . 125

5 Light source placement and reflective backings 128
5.1 Light source placement - preliminary testing . . . 129
5.1.1 Methodology . . . 130
5.1.2 Results and analysis . . . 131

5.1.3 Discussion and conclusions . . . 133
5.2 The effects of surface finish . . . 135
5.2.1 Methodology . . . 135
5.2.2 Results and analysis . . . 140
5.2.3 Surface reflectivity . . . 146
5.2.3.1 Methodology . . . 146
5.2.3.2 Results and analysis . . . 148
5.2.4 Discussion and conclusions . . . 149

6 Tinted coatings for thickness measurements 151
6.1 Theory . . . 153
6.2 Methodology . . . 153
6.3 Results and analysis . . . 157
6.4 Discussions and conclusions . . . 163

7 Coating calibration 164
7.1 Methodology . . . 164
7.2 Results and analysis . . . 167
7.3 Discussions and conclusions . . . 169

8 Industrial focused applications 171
8.1 Research laboratory based investigations . . . 171
8.1.1 GLARE Sample . . . 172
8.1.1.1 Methodology . . . 172
8.1.1.2 Results and analysis . . . 172
8.1.2 Carbon fibre sample . . . 174
8.1.2.1 Methodology . . . 174
8.1.2.2 Results and analysis . . . 175
8.2 Applications in industrial setting . . . 178
8.2.1 Coating application and curing . . . 179
8.2.2 Aluminium dogbones . . . 180
8.2.2.1 Methodology . . . 180
8.2.2.2 Results and analysis . . . 180
8.2.3 Test wing structure . . . 185
8.2.3.1 Methodology . . . 185
8.2.3.2 Results and analysis . . . 187
8.3 Discussion and conclusions . . . 192

9 Mechanoluminescence 194
9.1 Capturing mechanoluminescence - initial observations . . . 195
9.1.1 Methodology . . . 195
9.1.2 Results and analysis . . . 199
9.2 Capturing mechanoluminescence - cyclic loading . . . 201
9.2.1 Methodology . . . 201
9.2.2 Results and analysis . . . 203
9.3 Capturing mechanoluminescence - repeatability . . . 206
9.3.1 Methodology . . . 207

9.3.2 Results and analysis . . . 209
9.3.2.1 Single rise with stress riser . . . 209
9.3.2.2 Single rise without stress riser . . . 212
9.3.2.3 Changes in load applied . . . 215
9.3.2.4 Changes in displacement rate . . . 216
9.4 Mechanoluminescence mechanisms . . . 218
9.4.1 Coating structures before and after load . . . 218
9.4.1.1 Methodology . . . 218
9.4.1.2 Results and analysis . . . 220
9.4.2 Thickness measurements . . . 223
9.4.2.1 Methodology . . . 223
9.4.2.2 Results and analysis . . . 224
9.5 Simultaneous photoelasticity and mechanoluminescence . . . 226
9.5.1 Methodology . . . 226
9.5.2 Results and analysis . . . 229
9.5.2.1 Simultaneous capture . . . 229
9.5.2.2 WF-SAOE photoelastic calibration . . . 233
9.6 Discussion and conclusions . . . 234

10 Discussion **238**
10.1 Summary . . . 238
10.2 Research aims . . . 239
10.3 Development of a UV curable photoelastic coating . . . 241
10.4 Using a UV curable coating for reflection photoelastic strain analysis . . . 244
10.4.1 Sample preparation . . . 245
10.4.2 UV coating application . . . 247
10.4.3 Performing photoelastic strain analysis . . . 248
10.4.4 Analysis . . . 250
10.5 Overall performance of the photoelastic material . . . 252
10.6 A dual photoelastic and mechanoluminescent coating . . . 253

11 Conclusions **255**
11.1 Photoelastic coatings . . . 255
11.2 Mechanoluminescence . . . 261

12 Future development **263**
12.1 Coating optimisation and application . . . 263
12.2 Reflective backings . . . 265
12.3 Quantifying environmental effects and setup . . . 265
12.4 Mechanoluminescence . . . 266

A Coating development **278**
A.1 Viscosity . . . 278
A.1.1 Methodology . . . 278
A.1.2 Results and analysis . . . 278
A.2 Solvent resistance . . . 280
A.2.1 Methodology . . . 280

A.2.2 Results and analysis . . . 282
A.3 Adhesion . . . 282
A.3.1 Methodology . . . 282
A.3.2 Results and analysis . . . 284
A.4 Flexibility . . . 285
A.4.1 Methodology . . . 285
A.4.2 Results and analysis . . . 285
A.5 Glass transition temperature . . . 287
A.5.1 Methodology . . . 287
A.5.2 Results and analysis . . . 289

B Maximising cure conversion 290
B.0.1 Theory . . . 290
B.0.1.1 Differential scanning calorimetry . . . 290
B.0.2 Methodology . . . 291
B.0.2.1 Differential scanning calorimetry . . . 291
B.0.2.2 ATR-FTIR . . . 292
B.0.3 Results and analysis . . . 294
B.0.3.1 Differential scanning calorimetry (DSC) . . . 294
B.0.3.2 ATR-FTIR . . . 297

C Primed samples 299
C.1 Methodology . . . 299
C.2 Results and analysis . . . 300

D t-test verdicts 304

E Time to achieve maximum cure conversion: WF-Red1 & WF-SAOE 309

F GFP1600 data: Incremental loading example 311

List of Figures

1.1 Diagram of linear polarised light being spilt into two components with a retardation (δ) induced between them. The resultant light is formed by the birefrigent material as the incident light passes through. 2
1.2 Image of an aircraft nose landing gear with the strain field made visible using reflection photoelasticity. Used with permission from Airbus. 4

2.1 An example of unpolarised light passing through a birefringent crystal such as calcite. The propagation direction of light is parallel to the optical axis of the crystal. The light passes through as if it was an isotropic material all at the same speed. 10
2.2 An example of incident polarised light passing through a birefringent crystal such as calcite. The light propagation direction is at an angle to the optical axis. The ordinary and extraordinary ray pass through the material at different velocities essentially separating from one another into different components. 11
2.3 An example of incident polarised light passing through a birefringent crystal such as calcite. The light propagation direction is perpendicular to the optical axis. The ordinary and extraordinary ray pass through the material in the same direction but different speeds. There is now a path difference between them as indicated. 12
2.4 The effect of uniaxial tension on the polymer chain. Orientation of the major axes of the ellipses contributes to orientation birefringence whilst the torsion effects are contributions of the glassy birefringence. 14
2.5 The chemical structure of polycarbonate featuring two benzene ring structures. . . 15
2.6 An example of two light waves travelling within the same plane and along the same axis. These wave possess equal amplitude and wavelength, but a phase difference is observed between them. This results in a wave that will have a net amplitude of the sum of each individual wave amplitude. 16
2.7 A schematic of a dark-field linear polariscope used to visualise the relative retardation between the light waves that emerge from a birefringent material. 18
2.8 An example of an isoclinic fringe, highlighted red, superimposed on a number of smaller isochromatic fringes. This interference pattern is of a disc in diametral compression captured using a linear dark-field polariscope. Data shared with permission by the University of Sheffield. 20
2.9 Diagram of a disc in diametral compression undergoing photoelastic analysis using a circular polariscope, see section 2.3.4. This results in removal of the isoclinic fringes observed in figure 2.8. Data shared with permission by the University of Sheffield. . 21

2.10 Diagram of a disc in diametral compression undergoing photoelastic analysis using a circular polariscope with a white light source. This results in coloured isochromatic fringes. Data shared with permission by the University of Sheffield. 22
2.11 Schematic of a circular polariscope. The setup is similar to that of a linear polariscope but with the addition of two quarter-wave plates. This setup is used to produce interference patterns without generating isoclinic fringes. 23
2.12 A linear polariscope used in a reflection photoelastic configuration. This arrangement allows for normal incidence 27
2.13 A circular polariscope used in a reflection photoelastic configuration. This arrangement is used in commercially available reflection polariscopes. 27
2.14 Schematic of the PSIOS system. Here light is reflected off a sample of interest with a photoelastic coating applied. Light enters the camera array and is split into four separate components with their intensities recorded by one of four CCD cameras. . . 30
2.15 Schematic of the a poleidoscope. Light that interacts with a photoelastic specimen is incident into the poleidoscope setup. Four separate images are formed and processed by a single CCD camera. 31
2.16 A diagram illustrating the two components of circularly polarised light that travel parallel to the fast axis, E_1, and slow axis, E_2. The fast axis is at an angle β to a reference direction. The peanut shaped ellipse is the resultant shape from squaring the amplitude of the ellipse. The orientation of the analyser is highlighted with respect to the major axis. 35
2.17 Mohr's circle for plane strain. It is a geometric representation of the 2D transformation of strains at a point in a specimen. It can be used for the determination of the relationship between normal, ϵ, and shear, γ, strains. The principal strains are denoted at ϵ_1, maximum strain and ϵ_2, minimum strain. 36
2.18 Light output image taken by a GFP1600 with corresponding intensity key demonstrating light intensity in arbitrary units. 37
2.19 Direction output image taken by a GFP1600 with corresponding key demonstrating first principal stress direction. **(a)** represents a beam coated with a thin UV curable resin with zero applied stress. **(b)** the same beam as image (a) however a load is applied at one end of the beam whilst the other is fixed. As observed, the first principal stress direction is orientated parallel to the long face of the beam. 38
2.20 The same Mohr's Circle as figure 2.17 however altered to demonstrate the Deltavision software outputs Shear0 (γ_0), Shear45 (γ_{45}), and ShearMax (γ_{max}). 38
2.21 Table highlighting the GFP output and what the corresponding sign translates to in terms of normal strain. 40
2.22 The crystal structure of the tridymite $SrAl_2O_4$ along (010). The black outline represents the unit cell and the direction of the tetrahedra are marked as U(up) and D(down). Red represents O^{2-} and green Sr^{2+}. 50
2.23 The elastico-mechanoluminescent (EML) process shown in an energy level diagram of $SrAl_2O_4$:Eu. The electrons within the Eu dopant ions are excited into the conduction band which are then trapped by the oxygen vacancies. The application of a mechanical load detraps the carriers back into the conduction band and into the excited state of the dopant. The de-excitation process then emits the observed ML light. 52

2.24 Comparisons of finite element analysis models of various stress distribution with experimentally recorded mechanoluminescent light distribution shown in a pseudo colour. 53
2.25 **(a)** The measured light distribution at a tensile load of 3.5kN. **(b)** The same light distribution image as (a) but transformed to illustrate stress according to the calibration curve. **(c)** FEM model of the same setup demonstrating that it is in agreement with image (b). 55

3.1 Chemical Structure of Lambson's UviCure S105, a cycloaliphatic epoxide resin. The cycloaliphatic epoxide can be seen at either end of the structure. 59
3.2 Chemical Structure of Lambson's UviCure S140, an oxetane resin. The four-membered ring structure of the oxetane is highlighted. An aromatic ring structure can be observed at the far right of the structure. 59
3.3 Chemical Structure of Lambson's SpeedCure 992, a sulfonium hexafluorophosphate cationic photoinitiator. The cation sulphur atom is surrounded by benzene ring structures with the hexafluorophosphate, PF_6^6, anion moiety. 60
3.4 Chemical Structure of the epoxide resin UviCure S105. 61
3.5 Chemical Structure of the epoxide resin UviCure S128. 61
3.6 Chemical Structure of the oxetane resin UviCure S160. 62
3.7 Chemical Structure of the oxetane resin UviCure S150. 62
3.8 Chemical Structure of the oxetane resin UviCure S140. 62
3.9 Chemical Structure of the oxetane resin UviCure S130. 63
3.10 Chemical Structure of the photoinitiator SpeedCure 976. 63
3.11 Chemical Structure of the photoinitiator SpeedCure 992. 64
3.12 Example of pitting within a test sample, WF19. Pitting of this sample appeared after curing. This was the worst case out of all 27 formulations. 73
3.13 WF3 applied to an aluminium beam. The appearance of shrinkage is severe within the thicker regions of the coating demonstrating a rippling within the coating. . . . 73
3.14 WF4 applied to an aluminium beam. Shrinkage is observed throughout the main bulk of the coated region. 74
3.15 WF11 applied to an aluminium beam. Severe shrinkage around the edges and ends of the coated region with shrinkage also observed in the main bulk. 74
3.16 WF22 applied to an aluminium beam. Clear coating however the effects of a failed thumb twist test presenting rippling at one end. 75
3.17 WF25 applied to an aluminium beam. Mainly clear coating however a strip of shrinkage is observed at one end of the beam. 76
3.18 WF27 applied to an aluminium beam. Clear coating however thicker regions at one end demonstrated artefacts in the coating appearance. 76
3.19 **(a)**: An aluminium beam being prepared for bonding a PS - 1E sheet to the open area. The cut-out of the sheet is observed on the left beam with a protective cover. The area surrounding is masked off. **(b)**: Two 0.032 in feeler gauges were used to ensure that the spread of the silver adhesive is uniform across the open area. 78
3.20 The finished sample. The masking tape was removed leaving a clean adhesive boundary around the sheet. The protective cover was also removed from the sheet and is now ready for testing. 79

3.21 PhotoStress PS - 1E bonded to a steel Q panel with a PC - 10 adhesive. The sheet is surrounded by an adhesive border which is angled to create a bevel. 80
3.22 Image of the Vishay photoelastic calibration rig with an aluminium beam mounted. The aluminium beam has a coating applied between the markings close to the securing end. A micrometer applies a load to the free end of the beam causing it to act like a cantilever. 81
3.23 The experimental setup for the initial measurements of photoelastic performance of the 27 formulations. A GFP1600 looks directly onto the coated region of an aluminium beam mounted in a calibration rig that inflicts cantilever loads onto the beam. A circularly polarised light source illuminates the coated region. 82
3.24 Shear 45 output images of the same aluminium beam coated with WF23. The green box highlights the area birefringence data were extracted from. The key relates the observed colour with a relative retardation in nm. **(a)** Zero deflection image. **(b)** Maximum deflection (20.32 mm) image. 82
3.25 The measured retardation of three PS-1E coated beams whilst analysing the shear 45 output within Deltavision. The response starts to curve due to limitations of the GFP1600. 84
3.26 Both graphs plot the shear 45 dataset. **Group a**: Individual resin component formulations. **Group b**: Combinations of S105 and S130 with WF4 (S105) as a comparison. 85
3.27 Both graphs plot the shear 45 dataset. **Group c**: Combinations of S105 and S140 with WF4 (S105) as a comparison. **Group d**: Combinations of S105 and S160 with WF1 (S160) and WF4 (S105) as a comparison. 85
3.28 Both graphs plot the shear 45 dataset. **Group e**: Combinations of S160 and S140 with WF1 (S160) as a comparison. **Group f**: Combinations of S160 with equal parts S140 and S130 with WF1 (S160) as a comparison. 86
3.29 Both graphs plot the shear 45 dataset. **Group g**: Combinations of S160 and S105 with fixed 10 % of S140. WF1 (S160) plotted as a comparison. **Group h**: Combinations of S160 and S105 with fixed 10 % of S130. WF1 (S160) plotted as a comparison. 86
3.30 Four UV curable formulations plotted alongside the commercially available PS-1E sheet for a comparison. The ShearMax output is plotted with the retardation normalised per 10 μm of thickness. 87
3.31 Shear45 image of the sample WF16a demonstrating multiple regions of differing thickness. 88
3.32 Light image of the sample WF17b demonstrating a non-uniform reflective backing. . 89
3.33 The comparison between non-heat treated and heat treated samples for the formulations WF17 and WF23. The retardation data were extracted from the Shear Max output of the GFP1600. 96
3.34 Normalised subtracted retardation of DOE3, the solid line represents the gradient with the value used as photoelastic magnitude. The line extends to the y-intercept that was used to determine the shape of the response. 99
3.35 Normalised retardation without the subtraction applied for DOE6. The highlighted datum point indicates where initial retardation measurements were taken from. . . 100

3.36 Photoelastic responses for all nine Design of Experiments (DOE) formulations. Unprocessed and subtracted ShearMax datasets are observed with the initial retardation, gradient intercepts and slopes. 101
3.37 The photoelastic response of OptDOE2, a formulation designed through a DOE statistical package. Both unprocessed and subtracted datasets are visible. 102
3.38 Comparisons of subtracted normalised retardation between DOE2, 3, 6 & 9 and OptDOE2. 103
3.39 Comparisons of unprocessed normalised retardation between DOE2, 3, 6 & 9 and OptDOE2. 104
3.40 Comparisons of unprocessed normalised retardation between DOE9 and PS-1E. . . . 105
3.41 Configurations of strain gauges used the measurement of the principal strain difference. Gauges labelled 1 and 2 were used. 107
3.42 Calculations of the strain optic coefficient for DOE9 and PS-1E using the cantilever beam test rig 109

4.1 The photoelastic responses of all eleven WF31 samples. The measurements demonstrate a variety of unexpected responses. 114
4.2 The photoelastic responses of five sample sets at various cure and wait times of either 1 — 4 hours **(a)** and 24 hours **(b)**. Subtraction post-processing has not been performed. 116
4.3 The photoelastic responses of five sample sets at various cure and wait times of either — 4 hours **(a)** and 24 hours **(b)**. The resdiual retardation has been subtracted from each data point. 117
4.5 Example infrared spectrum of the uncured UV curable formulation WF31. Various peaks are observed at different wavenumber ranges 119
4.4 A diagram of the attenuated total reflection (ATR) sampling technique used alongside infrared spectroscopy. An infrared beam internally reflects in a crystal and produces evanescent waves at the surface of the crystal. These evanescent waves penetrate into the sample at different amounts depending on the incident angle and wavelength of light. The information of the interacting wave is passed along the beam to a detector. 119
4.6 Real-time ATR-FTIR apparatus. The modified ATR accessory is positioned in the FTIR spectrometer. A fibre cable is directing the light from an external UV light source. 121
4.7 Graphs of epoxy and oxetane cure conversions using real-time ATR-FTIR spectroscopy. The UV light output was reduced with an iris aperture of 30 %. 122
4.8 Graphs of epoxy and oxetane cure conversions using real-time ATR-FTIR spectroscopy. The UV light output was reduced with an iris aperture of 100 %. 123
4.9 Graphs of epoxy and oxetane cure conversions using real-time ATR-FTIR spectroscopy. The formulation's photoinitator was changed to the more efficient SpeedCure 976. The UV light output was reduced with an iris aperture of 30 %. 124
4.10 Graphs of epoxy and oxetane cure conversions using real-time ATR-FTIR spectroscopy. The formulation's photoinitator was changed to the more efficient SpeedCure 976. The UV light output was reduced with an iris aperture of 100 %. 124

5.1 The experimental setup for light source placement investigations. The GFP was positioned so the beam was in a horizontal orientation. Two light sources can be seen, labelled 1 and 2. These numbers represent the two positions that were used. . 130

5.2 The unprocessed retardation data of samples WF31b **(a)**, WF31c **(b)** & WF31e **(c)** using various light source configurations during photoelastic investigations. 131
5.3 The subtracted unnormalised retardation data of the samples WF31b **(a)**, WF31c **(b)** & WF31e **(c)** using various light source configurations during photoelastic investigations. The subtraction post processing facility was performed to remove the initial retardation from each loaded image. 132
5.4 The retardation data of an aluminium beam coated with a photoelastic sheet, PS-1e. PS-1e is a polycarbonate sheet, 0.25 mm thick, that was bonded to the aluminium beam through the use of a two-part epoxy adhesive. The retardation data has had no post processing applied. 133
5.5 Two experimental setups investigating the effects on the signal-to-noise ratio of photoelastic response. The light sources were positioned above the sample and side-by-side within the same imaging plane of the GFP1600's imaging lens. 137
5.6 Superimposed image of two aluminium samples. The original position was an image at the sample at 0 kN whilst the shifted position was at an applied load of 31 kN. The image was capturing during the image translation facility in Deltavision. 138
5.7 GFP1600 image of a sandblasted sample in tension. The green area represents where photoelastic data was taken between samples. Here the retardation is dominated by one colour. 139
5.8 Light output images captured by the GFP1600. The light sources were positioned above the GFP1600 angled down onto the aluminium samples. 140
5.9 Light output images captured by the GFP1600. The light sources were positioned either side of the GFP1600 in the same horizontal plane as the imaging lens. 140
5.10 Normalised retardation against stress for aluminium samples coated with PS-1E, a commercially available photoelastic coating. The data points represent the average retardation values and the error bars represent the corresponding standard deviations. This data was extracted from an area drawn within the images taken by the GFP1600. Each sample was labelled with thickness measurements and is presented in the legend. 141
5.11 Normalised and subtracted retardation against stress for aluminium samples coated with the UV curable formulation. The aluminium samples were initially roughly polished with sandpaper. The data points represent the average retardation values and the error bars represent the corresponding standard deviations. These data was extracted from an area drawn within the images taken by the GFP1600. 142
5.12 Normalised and subtracted retardation against stress for aluminium samples coated with the UV curable formulation. The aluminium samples were initially sandblasted with 60 grit sand. The data points represent the average retardation values and the error bars represent the corresponding standard deviations. These data was extracted from an area drawn within the images taken by the GFP1600. 142
5.13 Normalised and subtracted retardation against stress for aluminium samples coated with the UV curable formulation. The aluminium samples were initially coated with a silver paint. The data points represent the average retardation values and the error bars represent the corresponding standard deviations. These data was extracted from an area drawn within the images taken by the GFP1600. 143
5.14 Comparisons of all four surface finishes when the light sources were in plane. A difference in response magnitude was observed. 144

5.15 Comparisons of measured retardation for painted and sandblasted samples with different surface finishes. The light configuration was in plane. This was to determine if surface finish affected the measured retardation. 145
5.16 The setup used to quantify surface reflectivity performance of the various surface finishes. An optical goniometer was used that direct lights down one rail and the reflected light is captured by a detector positioned along the other rail. 147
5.17 The intensity of the reflected light from various surface finishes at a fixed detector position. 148

6.1 An aluminium sample coated with WF31 that has been placed in tension. The grey field polariscope was used to analyse the image to measure the induced retardation. The orange areas represent an increase in retardation due to increased thickness only. 152
6.2 Comparison between clear WF31 and red tinted WF31 with a red transparent resin dye. **a** demonstrates the initial deep red colour. **b** demonstrates the colour after being spread to a wet film thickness of approximately 60 μm. 154
6.3 A schematic (not to scale) of the wedge sample used to calibrate the tinted WF31 formulation. Two glass slides with a glass cover slide spacer forms the wedge with a thickness range of (18 - 40) — (150 - 240) μm. One slide was painted silver to provide a reflective backing. The other slide has been omitted from the diagram for clarity. 155
6.4 The light intensity output of the GFP1600 imaging a wedge of WF-Red1 to calibrate the coating for thickness measurements. Along the blue line each red and blue light pixel value was recorded. The difference in light intensity was observed due to change in formulation thickness. 156
6.5 A wedge of tinted WF31 calibrated for thickness. The colours within this image represent different thicknesses. 158
6.6 Calculated thickness across the wedge against the ratio between blue and red light intensity. A 4^{th} polynomial has been fitted onto the curve. The calculated coefficients are then used within Deltavision to measure thickness using the tinted UV curable formulation. 158
6.7 The input of calibration coefficients into Deltavision. The five coefficients A - E were calculated through a 4^{th} polynomial equation that equates the ratio of blue and red light to thickness. 159
6.8 A slide to validate the calibration data of WF-Red1. The slide was applied with WF-Red1 using a K-bar and cured using UV light. The calculated thickness value was close to the measured value using a micrometre. 160
6.9 Seven 4^{th} degree polynomial fits using coefficients calculated from seven WF-Red1 wedge samples. The thickness ranges are both the entire wedge and a thickness range that the cured coating usual exists within after application. 161
6.10 Data binning performed on figure 6.6 which smooths the data preventing overfitting. 162

7.1 A primed aluminium sample adhered with a stacked rosette strain gauge. The instrumentation wires are soldered onto terminal pads which would also be connected to leadwires. The leadwires connect to a P3 strain indicator and recorder for testing. 165

7.2 Calculations of strain-optic coefficient for WF31. Retardation (δ) against double the coating thickness (d) multiplied by the principal strain difference (($\epsilon_1 - \epsilon_2$)). Each solid line represents the linear analysis formed on each sample. The value of each line's gradient is the corresponding strain-optic coefficient as highlighted in the legend. 167
7.3 Calculations of strain-optic coefficient for WF-Red1. Retardation (δ) against double the coating thickness (d) multiplied by the principal strain difference (($\epsilon_1 - \epsilon_2$)). Each solid line represents the linear analysis formed on each sample. The value of each line's gradient is the corresponding strain-optic coefficient as highlighted in the legend. 168
7.4 Comparisons of the light intensity output of WF31 and WF-Red1 samples. Both coatings were applied onto aluminium samples painted with the same silver paint. The high density of hot spot pixels within the WF-Red1 sample demonstrates a large reduction in the signal-to-noise ratio. 169

8.1 The GLARE sample prior to the application of a silver paint and WF-Red1. RPSA was performed on the sample using the GFP1600. The sample was placed in uniaxial tension with a stacked rosette strain gauge monitoring the strain away from the hole. 172
8.2 A GLARE sample with an applied load of 9 kN. A comparison between no correction and thickness correction is demonstrated. The effects of meniscus around the hole and on the edges of the sample have been removed and an expected strain map is observed more clearly in the corrected version. 173
8.3 The carbon fibre sample created with an added defect. The sample has an 8 ply quasi-isotropic layup with a piece of PTFE tape placed between the second and third layer. The defect was undetectable both visibly and physically on the surface of layer one. 174
8.4 Carbon fibre samples applied with a silver paint and the UV curable photoelastic coating WF-Red1. Defects were purposely included between the second and third layers. RPSA was performed using the GFP1600. 175
8.5 RPSA Data of a carbon fibre composite sample that was made with an added defect. The sample was loaded at 2 kN and the defect is highlighted in the green box. The red UV curable formulation was used to correct for thickness differences across the samples. 176
8.6 Comparisons of principal strain difference of the carbon fibre sample calculated using RPSA and measured directly using strain gauges. RPSA data was calculated using a strain-optic coefficient of 0.083. 177
8.7 Comparisons between RPE and DIC strain analysis on a carbon fibre manufactured with a defect between the layers. The defect is mostly easily demonstrated in the RPSA data, **(a)**, compared to DIC, **(b) & (c)** 178
8.8 GFP1600 images, analysed by the software Deltavision, of an aluminium dogbone in uniaxial tension at a load of 225 kN. The images demonstrate both thickness measures and strain analysis with the scales indicating the values of the colours shown in the images. A strain-optic coefficient of 0.08 was inputted into the software for strain analysis. 181

8.9 Strain-optic coefficient calculation from an aluminium dogbone applied in uniaxial tension at Airbus' AIRTeC site. The linear response produced a value for K of WF-Red1 of 0.0690 $\pm$ 0.0004. The calculated value is lower than the previously calculated value of 0.08 $\pm$ 0.03. 182
8.10 The comparison of measured retardation values with the strain gauge values of an aluminium dogbone in uniaxial tension. The non-linear response was unexpected and indicated a problem with experimental setup. 183
8.11 Three light images taken from the GFP1600 of the aluminium dogbone with three different loads. The light conditions change between the loads that relate to the unusual differences in retardation values demonstrated in figure 8.10. 184
8.12 A schematic demonstrating an approximate layout of the underside of the test wing structure. Rows of bolt heads ran along the length of the wing with perpendicular rows of bolts at various locations along the wing. The two red section illustrate the locations where RPSA took place. 186
8.13 The application of WF-Red1 on a test wing structure at two different locations. WF-Red1 was brushed on and cured using a handheld curer. Curing was performed in sections due to the size of location being bigger than the output window of the curer. 186
8.14 Reflection photoelastic strain analysis (RPSA) performed on a test wing structure using WF-Red1 at location 1. The location for RPSA was towards the support of the wing on the bottom of the wing at the edge. At this location the surface was in compression. The location of the support was at the right of each image. 188
8.15 Reflection photoelastic strain analysis (RPSA) performed on a test wing structure using WF-Red1. The location for RPSA was approximately at a quarter of the wing's length closest to the support. At this location the surface was in compression. The location of the support was at the right of each image. 189
8.16 Reflection photoelastic strain analysis (RPSA) performed on a test wing structure using WF-Red1. This location focused on the problem hot spot illustrated in figure 8.15. The effects of brush strokes are drastically increasing the presence of noise. . . 190
8.17 Thickness measurements on both locations performed by Deltavision. The appearance of brush marks looks similar between the locations however the photoelastic response at location 2, **(b)**, is negatively impacted by their presence. Location 1, **(a)**, is not affected to the same degree. 191

9.1 The micrometer adjustable blade applicator was used to spread the ML coating across a sample. Two micrometers adjust the position of a blade with respect to the sample. Once a sufficient thickness was setup the blade pushes the coating across the sample. The applicator was placed on a smooth glass plate to increase the uniformity of the coating's thickness. 196
9.2 Example of cured WF-SAOE on an aluminium coupon with a circular stress riser. The coating was spread onto the sample with the hole using a micrometer adjustable blade and cured for 20 s using UVC light. 197
9.3 Mechanoluminescence observed in WF-SAOE applied to an aluminium coupon with a circular stress riser drilled in the middle of the sample. Across three applied loads a change in ML was observed. ML only appeared when approaching and breaching the plastic limit of the coupon. 199

9.4 The change in grey value when the applied load increased at 2.5 mm min^{-1}. The grey value was recorded 1 mm away from the hole. Minimal detection of ML was observed until around 12 kN, the ML suddenly increased at loads greater than 19 kN. 200
9.5 Comparison of ML produced by WF-SAOE and WF-SAOED during the first rise to the upper load limit. WF-SAOED demonstrated much greater PL but almost no ML at the maximum load. WF-SAOE demonstrated visible ML at the upper load limit. . . 203
9.6 Captured ML light intensity of WF-SAOE during a cyclic loading scenario. The grey values were recorded 0.5 — 0.6 mm away from the hole. A reduction in peak ML light intensity was observed after each cycle. 204
9.7 Comparison between initial captured ML and captured ML of a repeat run. The sample and coating were the same and re-excitation was performed prior to the repeat. 205
9.8 A repeat application of cyclic loading on the same sample as figures 9.6 and 9.7 but with a new coating. The maximum peak intensity is still reduced from the initial loading sequence. 206
9.9 An aluminium coupon with a circular stress riser under uniaxial load. Maximum load is applied and the observed ML around the hole is observed. Several bright hot spots are shown which are thick markers of the highly photoluminescent SAOED combined with the UV curable formulation WF31 and cured. 207
9.10 The recorded ML of WF-SAOE on two samples undergoing a tensile load of up to 10 kN at a position rate of 1 mms^{-1}. Each sample had three repeats that results in a loss of ML intensity at each repeat. 210
9.11 Normalised grey value vs time. The applied force ranged from 0 - 10 kN at a position rate of 1mm/s. Comparing between figure 9.10 demonstrates that coating thickness affects the intensity of ML light. 211
9.12 The qualitative comparisons between recorded ML light intensities at different maximum loads, at a displacement rate of 1 mms^{-1}, applied to an aluminium coupon in uniaxial tension. The increase in light intensity is minimal until the sample goes into plasticity where the measured light output saturates the detector. 213
9.13 Normalised grey value against time for aluminium coupons without a stress riser. Each sample was applied with a 10 kN load at a displacement rate of 1 mms^{-1}. The peak intensities were observed however very low in signal when compared to previous applications. Exponential fits were applied to determine repeatability. . . . 214
9.14 Intensity of ML for aluminium coupons at different maximum loads. A limitation in the applied load can be observed with low peak ML from 5 kN samples. An overlap between 7.5 — 10 kN is also observed further demonstrating difficulties that lie with the technique. 216
9.15 Peak intensity of ML for aluminium coupons at different calculated applied stress for various displacement rates. Rates between 0.25 — 1 mms^{-1} demonstrated no change in the captured ML intensity which allows for flexibility on the displacement rate. However, higher displacement rates, 2 mms^{-1}, produced higher captured intensity but with it being harder to capture all information. 217
9.16 A 90 ^{o} SEM stub that has been prepared for SEM imaging. Two sections of coating (loaded and unloaded) have been placed onto a stub with the cross section orientated 90^{o} to enable imaging of that face. The coating cross sections have been coated with gold and a silver conductive paint ensures conductive contact between the stub and the coating material. 219

9.17 Electron backscattered diffraction spectrometry (EDS) conducted on a backscattered electron image of the coating after load. The software analysed the points in the marked regions at the bright spots thought to be the ML material and the grey surrounding medium thought to be the carrier formulation. EDS identifies these claims to be correct. 221
9.18 SEM images of two coatings **(a)** before and **(b)** after the application of load at x1900 — x2000 magnification. A high density of ML material is contained within the carrier formulation. The structure of the formulation degrades from after applications of load that suggests the transfer of strain from the formulation to the ML material is disrupted. 222
9.19 SEM images of two coatings **(a)** before and **(b)** after the application of load at x10000 magnification. The images have focused on ML particles surrounded by the resin carrier formulation. Large voids are observed around the ML particles after load producing discontinuities that disrupt the transfer of strain. 222
9.20 The photoluminescence captured from a wedge of WF-SAOE immediately after excitation with a white light source. The thickest part of the wedge occurs where the light intensity is at its greatest. 224
9.21 Grey value (intensity) against the thickness of the wedge for three different samples. Each plot shows differences which indicates difficulties in capturing thickness. 225
9.22 The dual camera setup for simultaneous PE and ML investigations. Target filters are attached to the cameras to allow PE to be conducted monochromatically in the red wavelengths whilst not interfering with the excitation and ML production. 227
9.23 The region of interest manipulator within the GFP2500. Four images are shown that have passed through a kaleidoscopic lens. The adhesive grid of the lens has been highlighted and the region of interest are the white boxes focusing around the hole. The lens changes the field of view between the top and bottom images. 228
9.24 Images demonstrating the simultaneous capture of ML and PE on aluminium coupons **(a)** & **(b)** with a stress riser. The coupons were in uniaxial tension with a maximum load of 10 kN applied. The area highlighted in the PE images was an artefact of the camera captured in all images. 230
9.25 Images demonstrating the capture of ML and PE on aluminium coupons **(a)** & **(b)** with a stress riser. The coupons were in uniaxial tension with a maximum load of 10 kN applied. The images were taken with different lenses to provide different magnifications around the hole. **(a)** A lens of variable focal length between 15 - 70 mm was used. **(b))** A 28 mm macro lens was used to image closer to the hole. Photoelastic images were taken using the GFP1600. 231
9.26 Superimposed images of the ML response (magenta) and the PE response (cyan). The PE response image was transparent allowing for any differences in between the responses to be observed. 232
9.27 Strain-optic coefficient calculations for aluminium coupons (WF-SAOE_Al_x) and steel dogbones (WF-SAOE_SD_x) that show different values of K between the sample materials. 233

10.1 The viscosity of WF31 measured using cone and plate rheometry at a temperature range between 5 — 60 ^{o}C. Through heating the sample beyond room temperature the viscosity decreases allowing for potential spray coating operations. 240

10.2 Chemical Structure of the oxetane resin UviCure S160 241
10.3 Comparisons of normalised retardation between WF31 and PS-1E. The data has not been post-processed. Aluminium beams coated with either WF31 or PS-1E were subjected to cantilever loading and at various deflections photoelastic data was captured. 242
10.4 The outlined procedure a user should follow to use a UV curable formulation as a reflection photoelastic coating for strain analysis. Timescales are associated to each task. 244
10.5 Comparisons of all four surface finishes when the light sources were in plane. A difference in response magnitude was observed. 245
10.6 The intensity of the reflected light from various surface finishes at a fixed detector position. 246
10.7 Normalised retardation against stress for aluminium samples coated with the UV curable formulation. The aluminium samples were initially coated with a silver paint. The data points represent the average retardation values and the error bars represent the corresponding standard deviations. This data was extracted from an area drawn within the images taken by the GFP1600. 249
10.8 Comparisons of principal strain difference calculated using RPSA and measured directly using strain gauges. RPSA data was calculated using a strain-optic coefficient of 0.083. 252

11.1 Comparisons between the determination of strain-optic coefficient (K) of WF31, **(a)**, and WF-Red1, **(b)**, from experiments. The calculated values of K for each dataset are highlighted in the legend 256
11.2 The captured difference in photoelastic response as a result of differences in curing time. Measurements were taken on coated beams in cantilever deflections with post processing performed to remove the effects of residual birefringence and light source errors. 257
11.3 Normalised retardation against stress for aluminium beams coated with the UV curable formulation. The aluminium beams were initially coated with a silver paint. The data points represent the average retardation values and the error bars represent the corresponding standard deviations. This data was extracted from an area drawn within the images taken by the GFP1600. 258
11.4 The photoelastic response of three aluminium beams that were sandblasted (SB) and then subsequently painted with a silver paint. A measured rise in magnitude was observed when using the silver paint. 259
11.5 Images demonstrating the capture of ML and PE on an aluminium coupon with a stress riser. The coupons were in uniaxial tension with a maximum load of 10 kN applied. The images were taken with a series of lenses to provide different magnifications around the hole. 261

A.1 A bar chart demonstrating the viscosity changes between all groups. S160 is the most viscous individual resin with S105, S140 and S130 acting as diluents. 280
A.2 Example of the visible streak observed on sample WF4 during the solvent resistance test. At this point the number of cycles, back and forth motion, of solvent soaked cotton bud was recorded. 281

A.3 A bar chart demonstrating the solvent resistance of the 27 formulations. 13 formulations were shown to be chemically resistant. . . . 282
A.4 5 x 5 grid marked into a cured formulation coated onto a steel Q-panel. The spacing between the lines were 2 mm. . . . 283
A.5 A bar chart demonstrating the adhesion of the 27 formulations. A large proportion of the formulations either possess great or poor adhesion. . . . 284
A.6 Four-point and three-point bend test rigs used to measure the flexibility of the 27 formulations. The separation of the contact points is highlighted . . . 285
A.7 Differential scanning calorimetry of WF1 performed to measure the formulation's glass transition temperature. The DSC procedure used two cycles to reset the thermal history, both cycles are presented. Within cycle 1, the location of the T_g transition is unclear as a melting peak has superimposed over the transition event. 288
A.8 A bar chart demonstrating the glass transition temperature of the 27 formulations. . 289

B.1 FTIR spectrometer with a Golden Gate style ATR accessory attached. A section of cured WF31 is firmly pressed onto the ATR crystal ready for analysis. . . . 293
B.2 Differential scanning calorimetry analysis of WF31 that was subjected to a 5s cure with two different wait periods. . . . 294
B.3 Differential scanning calorimetry analysis of WF31 that was subjected to a 15s cure with two different wait periods. . . . 294
B.4 Differential scanning calorimetry analysis of WF31 that was subjected to a 30s cure with two different wait periods. . . . 295
B.5 Differential scanning calorimetry analysis of WF31 that was subjected to a 45s cure with two different wait periods. . . . 295
B.6 Differential scanning calorimetry analysis of uncured WF31. . . . 296
B.7 Graphs of cure conversion, calculated from ATR-FTIR data, against curing time for two separate wait periods. Data points represent the mean whilst errors bars represent the standard uncertainty for the five repeat measurements. . . . 297

C.1 One half of a friction shim coated with an aerospace primer. This image shows the matt finish of the green paint . . . 299
C.2 The light output image of a primed aluminium sample, sprayed aerospace epoxy paint, coated with a UV curable formulation. The image demonstrates uniform shade of grey across the central region of the sample. . . . 300
C.3 Shear Max images taken by the GFP1600 observing a primed and coated aluminium sample during zero load, **(a)**, and maximum load, **(b)**. . . . 301
C.4 The measured normalised retardation against the principal strain difference. The principal strain difference was calculated from a stacked rosette strain gauge adhered to the sample at the location of retardation extraction. Three primed samples were coated with silver paint and subjected to two loading cycles each. The coating was reapplied after each cycle. . . . 302
C.5 Measured retardation against cantilever deflection for an aluminium sample at the point where retardation data was extracted. 11 samples were tested providing responses that lacked precision. . . . 303

D.1 The main t-test results from the effects of UV light irradiation time (curing time) on the photoelastic response. The Photoelastic response was normalised to enable independent and paired t-tests. 308

E.1 Graphs of epoxy and oxetane cure conversions of WF-Red1 using real-time ATR-FTIR spectroscopy. The UV light output was reduced with an iris aperture of 100 %. The measured time to reach maximum cure conversion was the same as WF31. 309

E.2 Graphs of epoxy and oxetane cure conversions of WF-SAOE using real-time ATR-FTIR spectroscopy. The UV light output was reduced with an iris aperture of 100 %. The measured time to reach maximum cure conversion was the same as WF31. 310

F.1 GFP1600 data for each applied load of the Glass Laminate Aluminum Reinforced Epoxy (GLARE) specimen analysed in section 8.1.1. 312

Notation

List of Symbols

α	Phase difference
α	Relative phase difference
β	The angle the fast axis makes with a reference direction
Δn	Difference between the extraordinary refractive index and ordinary refractive index of a birefringent material
δ	Relative retardation
γ	Magnitude of shear strains calculated through the grey-field polariscope's video lock-in algorithm
γ_0	The grey-field polariscope's Shear0 output which highlights shear strains orientated in the 0/90 degrees reference frame
γ_{45}	The grey-field polariscope's Shear45 output which highlights shear strains orientated in the $\pm$45 degrees reference frame
γ_{max}	The grey-field polariscope's ShearMax output which highlights maximum in-plane shear strains, equivalent to the difference of the principal strains.
κ	Angle between a reference axis and analyser
λ	Wavelength
ν	Poisson's Ratio

ω	Angular frequency
ω	angular frequency
Φ	Angle between a reference axis and the slow axis of the output quarter wave plate
ϕ	Angle the fast axis of circularly polarised light makes with respect to a reference direction
σ_n	Principal stress where n = 1, 2 or 3
σ_s	Von Mises equivalent stress
θ_{n_i}	Angle of the analyser which triggers the image capture during the grey-field polariscope's capture process
A_1, A_2	Separate wave amplitudes
A_x	Absorbance where x indicates if it is the peak of interest, a reference or an uncured peak of interest
C	The stress-optic coefficient
Cp	Specific heat capacity
d	Sample thickness
E	Young's modulus
E_1, E_2	Separate electric wave vectors
$e_{distortion}$	distortion energy density
E_{maj}, E_{min}	Electric wave vectors of the major and minor axis of elliptically polarised light
e_{volume}	volume change energy density
g	gram
H_p	Enthalpy of a partially cured material
H_u	Enthalpy of an uncured material
I	Resultant intensity
i_{1-4}	Intensity observed in each quadrant of the kaleidoscope lens used in a poleidoscope
I_{1-6}	Light intensity observed at six different phase-steps using a transmission polariscope.
I_m	Intensity of stray light
I_o	Initial intensity
I_v	Intensity emerging when all axes of the polariscope and specimen are parallel
J_{n_i}	The sampled image intensity during the grey-field polariscope's capture process
K	Strain-optic coefficient
k	Wavenumber

K_{GFP}	Grey-field polariscope's calibration constant
N	Fringe order
n_{air}	Refractive index of air
n_e	Extraordinary refractive index
N_i	Number of images captured during the grey-field polariscope's capture process
n_i	The image number during the grey-field polariscope's capture process
n_o	Ordinary refractive index
Q	Heat
R	Resistance
T	Temperature
T	Transmittance
t	time in seconds
t	time
W	Watts
x	Wave position
X, Y	Separate images created through the grey-field polariscope's lock-in algorithm
c	Speed of light in a vacuum
E_ϕ	Resultant light electric wave vector captured by a grey-field polariscope
n	Refractive index of a material
v	Speed of light in a medium
ϵ	Normal strain
θ	Isoclinic angle, angle of fast axis of specimen to reference axis
θ_{oa}	The angle between light propagation and a crystal's optical axis

Abbreviations and Subscripts

T_g	Glass transition temperature
ATR	Attenuated total reflection
DML	Deformation mechanoluminescence
DOE	Design of experiments
DSC	Differential Scanning Calorimeter
EML	Elastico-mechanoluminescence
FEA	finite element analysis

fps	frames per second
FTIR	Fourier-transform infrared
GFP	Grey field polariscope
GFP	Grey-field polariscope
GLARE	Glass laminate aluminium reinforced epoxy
GU	Gloss units
K	Strain-optic coefficient
LPC	Luminescent photoelastic coatings
ML	Mechanoluminescence
PL	Photoluminescence
PML	Plastic-mechanoluminescence
RPE	Reflection photoelasticity
RPSA	Reflection photoelastic stress analysis
SAOE	Strontium aluminate doped with Europium, $SrAl_2O_4$:Eu
SAOED	Strontium aluminate doped with Europium and Dysprosium, $SrAl_2O_4$:Eu,Dy
TML	Tribomechanoluminescence
VOC	Volatile organic compounds
WF31	The best performing formulation as referred to as DOE9
WMG	Warwick manufacturing group

Chapter 1

Introduction

1.1 Research objectives

This research has a primary aim to update reflection photoelastic strain analysis (RPSA) techniques to provide an easier, faster and more insightful solution. The applications of the coating will be extensive but will have a focus on applications within Airbus for example RPSA investigations on airframe assembly strains. The end objective is to identify new coating materials that can be utilised as a rapid 'hot spot' detection that both locates and quantifies areas of damage.

Reflection Photoelastic Stress Analysis (RPSA) is a well-established experimental strain analysis technique where users benefit from immediate qualitative and quantitative information such as maximum shear strains in complex geometries [1, 2]. Reflection photoelasticity (RPE) enables photoelastic analysis on opaque structures [3] by utilising a thin temporarily birefringent material that is adhered to a prototype with a reflective backing to form a photoelastic coating. Birefringence describes a material having an anisotropic optical property where the refractive index is dependent on the orientation of light propagation and the light polarisation. Photoelasticity (PE) manipulates this property as the magnitude of birefringence will change dependent on the load applied to the material as highlighted in figure 1.1.

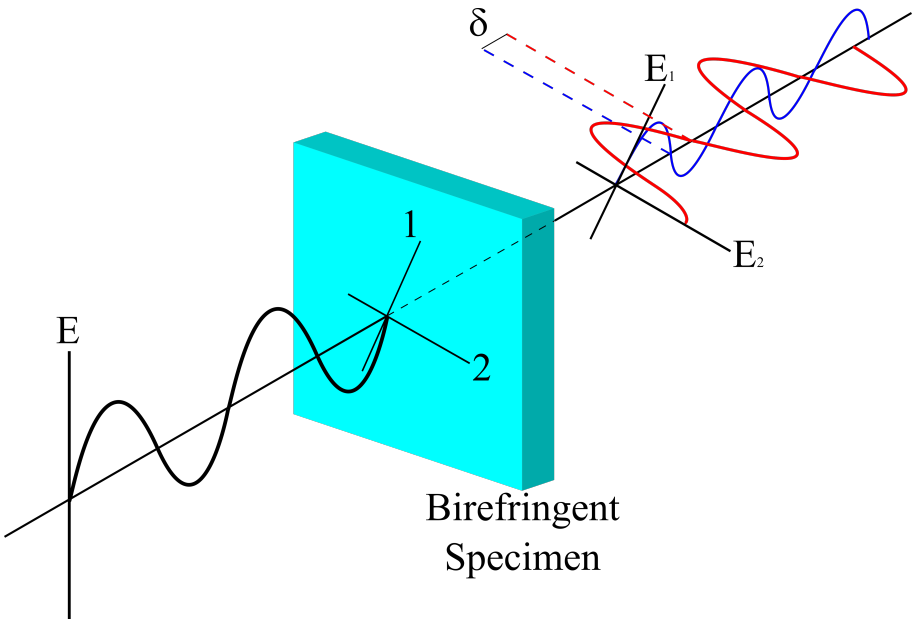


Figure 1.1: Diagram of linear polarised light being spilt into two components with a retardation (δ) induced between them. The resultant light is formed by the birefrigent material as the incident light passes through.

Figure 1.1 provides a simple diagram to demonstrate the effects of birefringence. The birefringent sample is orientated such that the incident linearly polarised light travelling in one plane, splits into two separate waves orientated along axes 1 and 2 of the material. These axes possess refractive indices of different values so the light travels through them at different speeds that induces a phase difference, or retardation (δ), between the emerging light. The magnitude of δ changes, dependent on the load applied to the material and it is this induced value of δ that photoelasticity captures and translates in valuable strain data. This information is then used by Airbus's engineers to assist in the management of the structural health of an aircraft. Furthermore, RPSA is used for refinement and validation of computational stress analysis models [4–6] which are used extensively in industry in the process of creating new components or for making design modifications to existing parts. RPSA benefits from being a physics-based technique resulting in direct observation of induced strain through optical setups. Model-based techniques, such as finite element analysis, rely on the information inputted, it is a mathematical interpretation of reality based on the user's assumptions of boundary conditions, such as assembly stresses and material properties. It is important to validate any modelling with an experimental technique. In this instance RPSA is able to provide quantitative data on material stress response and the boundary conditions. Together these are crucial to understanding the long-term structural integrity of an aircraft.

RPSA methods and analysis benefit from being relatively inexpensive, with photoelastic responses being easy to measure provided a suitable photoelastic coating and polarising elements are utilised in order record the desired data. However, complicated coating application processes, a need for skilled engineers and large timescales for data collection deter the use of existing RPSA methods. These issues all stem from one vital component — the photoelastic coating material. Commonly used photoelastic coatings include flat and rigid polycarbonate sheets [7], mouldable plastic sheets and spreadable two-part epoxy adhesives [8]. Currently, the thicknesses of common photoelastic coatings exists between a range of 0.25 — 3.2 mm [7–10], and these are selected by the user depending on their requirements. A thicker coating provides increased sensitivity, however it must be carefully selected to prevent any reinforcement effects the coating may have on the bonded component. Any reinforcement would distort the measured photoelastic response thus providing inaccurate strain information. A new ultra-thin coating, whilst maintaining sensitivity, could eliminate this risk of reinforcement. Methods for the application of photoelastic sheets onto components follow complicated instructions that require skill and patience [11, 12]. Contourable plastic sheets follow detailed mixing procedures with multiple polymerisation stages with the manufacturer's instructions stating "subjective" guidelines which become "apparent with practise." When shaping, issues such as overhanging the material can stretch the coating and unnoticed air pockets between the component and coating can obscure the true photoelastic response, resulting in inaccuracies in the strain measurement. Further issues may occur during the adhesion and machining processes. In the former, a two-part reflective adhesive is spread uniformly over the component surface. The coating is placed on top and pushed down into the adhesive. Improper application can create pockets of air between the coating and sample resulting in further misrepresentation of the photoelastic response. Machining processes of the coating can inadvertently introduce undesirable edge birefringence through the generation of heat build-up producing subsequent residual strains within the coating. Additionally, processes need to be treated with care to prevent any damage through cracking and chipping. Finally, once the coating has been applied, the complete curing time can take upwards of 24 hours before any analysis can take place.

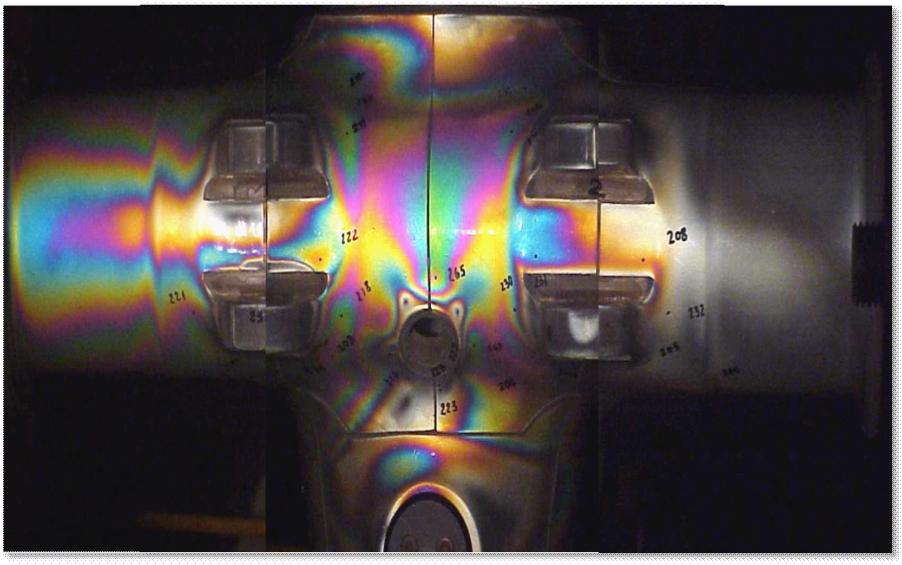


Figure 1.2: Image of an aircraft nose landing gear with the strain field made visible using reflection photoelasticity. Used with permission from Airbus.

As an example, the coating application in figure 1.2 would have taken several weeks to apply. If the coating application drawbacks are overcome, then recent developments and commercial availability in automated collection and analysis of photoelastic data will give potential for RPSA to be a truly effective and rapid method.

Furthermore, figure 1.2 illustrates an example of contouring a photoelastic sheet to a fairly intricate component. Applying these sheets is a multistep process that will be discussed in greater detail in chapter 3.2. This arguably gets more complicated when applying to an assembly of components. For example, consider an Airbus A320ceo that has a wingspan of 35.8 m [13]. Coating such an area whilst accounting for many details, such as large curved panels, motorised flaps and rivet holes, takes several weeks with a high level of skill needed to apply in an accurate and precise manner. The reason why these coatings are used, and have not changed in the previous 50 years, is a result of the capability of the acquisition and processing apparatus used to measure stresses and strains. But improvements in automated acquisition and software mean the photoelastic sheets could be replaced with a simpler and smarter solution. Digital polariscopes [14], optical arrangements that enable detection of photoelastic responses, allow for increased ease-of-use with a sub-fringe retardation resolution of greater than 0.1 nm which translates to a principal strain difference resolution of 20 micro-strain. These devices allow for new coatings to be developed that can focus on additional desirable properties that were once constrained by the necessity for sensitivity. The proposed new

coating comes in the form of a relatively thin UV curable coating, 50 — 100 μm, that could be sprayed onto the area of interest. This would be a huge improvement for a number of reasons:

- A sprayable coating would be quicker to apply, especially for large areas. This would then lead to reduced aircraft downtimes.
- A UV curable coating has capabilities of being cured in a matter of seconds rather than hours when using epoxy adhesives.
- An advancement in bespoke coating materials would allow for a selection of desirable properties for the coating to be used alongside current high sensitivity digital RPSA apparatus.

The aim is to produce a coating and method that not only improves time efficiency and economics of the RPSA process, but also delivers a more insightful way of investigating aircraft assemblies. To achieve this, the developed photoelastic coating will be combined with a mechanoluminescent material to produce a dual-technique strain imaging facility. Mechanoluminecent materials produce light when energised by strain that can be recorded to produce an additional strain map. In order to achieve these aims, the coating must meet a number of essential criteria.

1.2 Essential Coating Properties

The requirements for the new coating was determined through discussions with Airbus engineers and external photoelasticians. Resultant criteria was established and the coating must satisfy the following requirements:

1. Birefringent to enable photoelastic measurements, with a constant or at least a definable strain-optic coefficient, a parameter that quantifies a material's sensitivity.
2. Luminescent when energised by strain, mechanoluminescence, with definable strain characteristics.
3. Ideally sprayable, with a constant or known thickness, for ease of application.
4. As thin as practically possible whilst keeping reinforcing effects to a minimum.
5. Fast curing.
6. Meet current and known future health and safety requirements.

7. For use within confined spaces without need for specialist protective equipment.

8. Easy to remove, leaving no evidence on the final component or structure.

Requirements 3 — 8 describe how the coating material should be handled in an industrial setting. A sprayable coating, requirement 3, would be faster to apply whilst negating the need of skilled workers whilst a known thickness is necessary for strain measurements using the RPSA method. Requirement 4 describes that a thinner coating would result in less material used resulting in a faster application. It also mentions that there should be very little reinforcing effects which could interfere with the photoelastic measurements by altering the stresses and strains between or within components. The coating should be fast curing, requirement 5, to prevent any material running, especially on curved or vertical surfaces, and to reduce the coating preparation time. Requirements 6 & 7 are straightforward to understand but are highly important. Materials that satisfy these criteria can be applied in the current setup environment with minimal changes to existing equipment. Finally, requirement 8 describes after all the testing is complete the coating should be removed, unless the coatings can be deemed safe for flight.

However, the most important features of the coating are the properties that allow visualisation of the mechanical stresses and strains of a component of interest. Requirement 1 & 2 highlights that the coating should be dual purpose, photoelastic and mechanoluminescent. This ensures that quantifiable data can be taken away from conducting the relevant analysis technique. Discussing these phenomena is crucial for a full understanding of this project.

1.3 Thesis overview

The thesis features a number of investigative chapters that explore the optimisation of a new photoelastic coating material before establishing experimental procedures that will form a standard operating procedure. Combination with the second technique, mechanoluminescence, with an aim to produce increased insight than photoelasticity can provide alone will conclude this research. Analysis and discussion are made in each section with overall dicussion following the review of all experimental work. Recommendations on future research will be outlined before the concluding review of this research.

1.3.1 Photoelastic coating development

After introduction of the background theory and state-of-the-art, chapter 2, this research focused on the combination of various UV curable resins to create formulations that were analysed as a photoelastic coating. The physical, chemical and optical properties of these formulations were investigated in order to determine the best performing materials. In section 3.2, properties such as solvent resistance and adhesion allowed for determination of the coating's removability whilst photoelastic performance, flexibility and viscosity enabled conclusions in regard to its ultimate applicability. By exploring a large sample set's performance, a single formulation was optimised as a photoelastic coating in chapter 3.3. Finalising on one coating formulation enabled systematic testing on the photoelastic procedure.

The procedure of using the coating was explored with investigations focusing on different aspects in order to extract accurate data with high confidence. The curing mechanism of the coating was reviewed to ensure that any changes to the photoelastic response were being accounted for. The curing process for UV curable materials contain variations compared to two-part epoxies where the curing processes takes several hours to complete. The curing process of the materials in this research are triggered and progressed by the continued illumination of short wavelength UV light (UV-C). Since short timescales were needed to produce hard-to-the-touch coatings it was possible to produce partially cured coating that had an effect on photoelastic performance. Investigations were conducted and documented in chapter 4 to determine best curing practises to ensure high confidence of the accuracy of the photoelastic data. The effects of light source placement and surface reflectivity were reviewed in section 5 to provide further context into often overlooked procedures that had considerable impact on the extracted results. Light source placement analysed the effects of uncalibrated light sources with methods of accounting for them outlined within post-processing. In this context, uncalibrated light sources are not producing perfectly circular polarised light, distorting the true photoelastic response. Surface reflectivity investigations, section 5.2.3, quantified the negative impacts certain backings have on the measured photoelastic response. Dull and diffusive surfaces, whilst reflective were shown to have negative impacts on the photoelastic sensitivity, this investigation showed the importance of careful consideration of a reflective backing.

Upon completion of the analysis of important setup procedures the research investigated how to extract accurate strain data. In order to calculate strain, the coating's thickness must be known

as well as the strain-optic coefficient K. K is a factor that contains coating material properties that effectively provides a value of the coating's sensitivity. Coating thickness adopted established techniques to measure variations of coloured light through the coating by introducing coloured tints to the coatings as discussed in chapter 6. A red tint was introduced and relationships between blue and red light were mapped onto thickness and this relationship was used in order to perform automatic thickness corrections across an image. In chapter 7, the K values for coating were calculated by performing experiments with samples having a known strain field.

Finally in section 8.2, the established coating and procedure was applied within industry to explore its performance outside a research laboratory. The coating was applied onto a test wing structure at Airbus to assess its performance onto large structures with the coating applied to areas that presented various logistical challenges.

1.3.2 Mechanoluminescent coating development

Chapter 9 documents the final investigation was combining the UV curable formulation with a powdered ML material. Various investigations were performed to determine its applicability, individual mechanoluminescent (ML) performance and the combined ML and photoelastic performance.

The application of the coating was reviewed with a focus on the appearance of the cast coating with a formulation containing a large portion of a powdered substance. Application techniques were reviewed alongside the curing performance.

Preliminary ML performance investigations analysed methods of capture and analysis of the measured ML light. Methods to establish performance and repeatability were conducted to determine how the ML intensity could be translated into strain information. Challenges and limitations of this technique will be reviewed.

Finally, the dual technique coating underwent concept demonstration to determine the performance and establish its applicability.

Chapter 2

Background theory and current state of the art

This chapter reviews all relative theory, current photoelastic and mechanoluminescent materials, and developments in research. This research's intention is coating development however to aid its understanding the chapter will firstly present the theory of photoelasticity and how certain materials are able to allow users to visualise the states of stress within a material. Secondly, how optical setups and techniques are utilised for the measurements in photoelasticity and the translation of observations into stress and strain information will be reviewed. Developments of these techniques will be outlined with a detailed account of the selected technique, use of a grey-field polariscope, in this research analysed. This information will support a review of current photoelastic coatings and their developments. This chapter will finish by introducing mechanoluminesence and its mechanisms. The selection of suitable mechanoluminescent materials will be outlined with example experimental research reviewed.

2.1 Birefringence

Birefringence is a term used to describe the property of optically anisotropic materials, usually non-cubic structures, where a material's refractive index differs depending on the polarisation and propagation direction of light incident on it [15]. The refractive index of a material is a dimensionless number that represents the ratio of the speed of light in a vacuum and speed of light in a material of interest. The refractive index of a material is described through equation 2.1

$$n = \frac{c}{v} \tag{2.1}$$

where n is the refractive index of a material, c the speed of light in a vacuum and v the speed of light through the material [16]. Common naturally-occurring examples of optically anisotropic materials include crystalline calcite and quartz.

Consider unpolarised light incident on a crystal of calcite. Unpolarised light can be thought of as many light waves that are linearly polarised in a random collection of transverse directions. Orientation of the crystal with respect to the propagation direction of this light is important when trying to observe birefringence. If the crystal is orientated such that the propagation of light is parallel to the optical axis of the crystal, no birefringence is observed. The light will behave as if it is travelling through an optically isotropic material, such as annealed glass. In this case, the light will pass through the crystal which will have effectively one refractive index, described as the ordinary index n_o. The light will travel through at the same speed and due to orientation of the light, no refraction will occur. This is illustrated in figure 2.1 with the emergent light highlighted as two separate light components mutually perpendicular to one another. It is important to highlight the emergent light would still be unpolarised however for added clarity and comparisons with other arrangements only two emerging light components will be visualised.

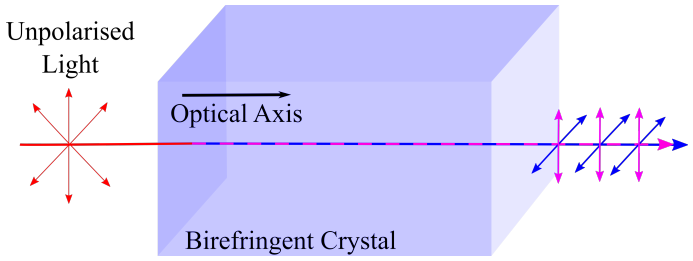


Figure 2.1: An example of unpolarised light passing through a birefringent crystal such as calcite. The propagation direction of light is parallel to the optical axis of the crystal. The light passes through as if it was an isotropic material all at the same speed.

However, orientate the crystal so that the light propagation is no longer parallel to this optical axis and the light is then refracted into two rays. By linearly polarising the incident light, better control over the refraction is achieved. The incident light is now linearly polarised with light components constrained to one transverse direction. The emergent light is split into two components with the

polarisation of these rays mutually perpendicular to each other and will travel through the material at different velocities as shown by figure 2.2.

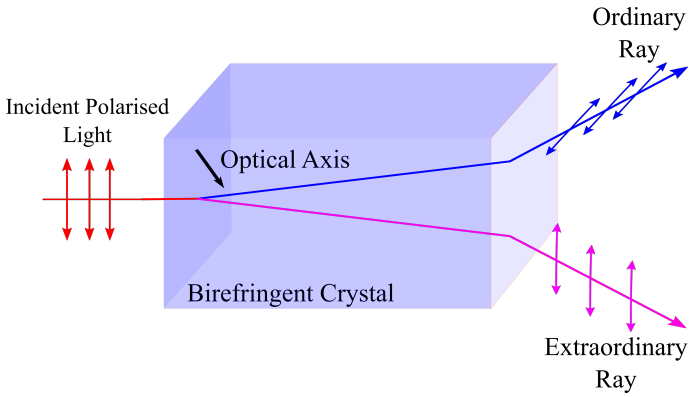


Figure 2.2: An example of incident polarised light passing through a birefringent crystal such as calcite. The light propagation direction is at an angle to the optical axis. The ordinary and extraordinary ray pass through the material at different velocities essentially separating from one another into different components.

One ray is defined as the ordinary ray and has a polarisation perpendicular to the optical axis and experiences the ordinary refractive index of calcite, 1.658. The orthogonal ray is labelled as the extraordinary ray and experiences a material refractive index that varies between the material's ordinary index and extraordinary index, n_e, of calcite, 1.486. This variation is dependent on the angle between the incident light propagation direction and the material's optical axis [16, 17]. The equation to calculate the refractive index the extraordinary ray exhibits in a material is defined by equation 2.2

$$n = \frac{1}{\sqrt{\frac{cos^2\theta_{oa}}{n_o^2} + \frac{sin^2\theta_{\ oa}}{n_e^2}}} \tag{2.2}$$

where θ_{oa} is the angle between the light propagation and the optical axis of the crystal [18, 19]. The magnitude of birefringence can be quantified by taking the difference between the calculated extraordinary and ordinary refractive index, equation 2.3 [20–22].

$$\Delta n = |n_e - n_o| \tag{2.3}$$

where Δn is the birefringence and n_e, in this case, is the calculated extraordinary index the

extraordinary ray experiences.

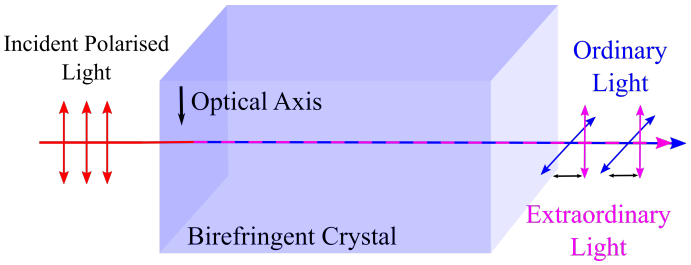


Figure 2.3: An example of incident polarised light passing through a birefringent crystal such as calcite. The light propagation direction is perpendicular to the optical axis. The ordinary and extraordinary ray pass through the material in the same direction but different speeds. There is now a path difference between them as indicated.

Figure 2.3 illustrates the case when the initial light propagation direction is perpendicular to the optical axis. In this situation, the ordinary and extraordinary rays are once again spilt into two components that travel at different speeds. However, their trajectories take the same path resulting in a path difference between the two rays. This can be also described as a relative phase difference or retardation. Relative retardation, δ can be calculated through equation 2.4

$$\delta = \left(\frac{|n_e - n_o|}{n_{air}}\right) d = \left(\frac{\Delta n}{n_{air}}\right) d \tag{2.4}$$

where d is the thickness of the sample and n_{air} the refractive index of the surrounding air in which the sample would be held in [23].

Birefringence plays a key part in RPSA techniques as the application of mechanical stress onto originally optically isotropic materials can cause them to become optically anisotropic. This induced anisotropy, temporary birefringence, is retained only during the application of a load and once removed, the material regains its optical isotropic nature [24]. RPSA then utilises important relationships which occur when induced stresses cause temporary birefringence in photoelastic materials. Firstly, the orientation of the principal axes of refractive index in fact coincide with the principal stress axes. Secondly, each refractive index is some linear function of the principal stress components. Principal stresses describe the maximum and minimum values of normal stress along mutually perpendicular principal axes where shear stress is zero [25,26]. Using these relationships the relative retardation can then be expressed through what is known as the stress-optic law, equation

2.5

$$\delta = Cd(\sigma_1 - \sigma_2) \tag{2.5}$$

where C is the stress-optic coefficient (material specific and wavelength dependent), d sample thickness and $\sigma_1 - \sigma_2$ the difference between principal stresses [27]. This can be compared to equation 2.4 and using $n_{air} = 1$ to give the following expression.

$$|n_e - n_o| = C(\sigma_1 - \sigma_2) \tag{2.6}$$

Light waves travel at velocities proportional to the magnitude of principal stresses.

2.2 Molecular basis of birefringence

It is more appropriate to describe the molecular basis of birefringence to best reflect how materials used in this research, chapter 3.1, impact birefringence. This research utilises polymer coatings as the birefringent media and understanding how changes to molecular structure impact birefringence is important. A polymer molecular chain is considered to be geometrically asymmetric with its impact on the polarisation of light varying dependent on the direction of a molecule [28]. In a non-orientated state (random arrangement of molecules), the overall impact on the anisotropic polarisability of the repeating units within the polymer ultimately balance one another resulting in no observable birefringence. However, if these chains were to orientate themselves along the same plane, then birefringence is exhibited. For example, polymers that are injection moulded to produce various components are easily orientated in the polymer's molten state by the flow and deformation of the manufacture process [28]. As these objects cool the orientation is maintained and the residual birefringence is observed. This 'orientation birefringence' is dominant within rubbery regions that enable changes of molecular chain orientation, for example during uniaxial loads. Additionally, birefringence is also contributed by when polymers are deformed below their glass transition temperature. Glass transition temperature (T_g) is the temperature region for amorphous materials, such as epoxies, where the polymer transitions from a glassy state to a soft and rubbery state. Below the glass transition temperature a material is elastic and a proportional relationship

between stress and 'glassy birefringence' is exhibited. Both orientation and glassy birefringence contributes to the overall birefringence of the material. To understand their differences the individual molecules in a polymer chain can be thought of as individual flat ellipses joined together. The major axes of the ellipses orientate in various directions and the faces of the ellipses are also positioned in various directions. Under the influence of uniaxial tension the chain orientate to face in the same direction, orientation birefringence, and the faces of the ellipse twist into the same plane, glassy birefringence. An exaggerated demonstration is illustrated in figure 2.4.

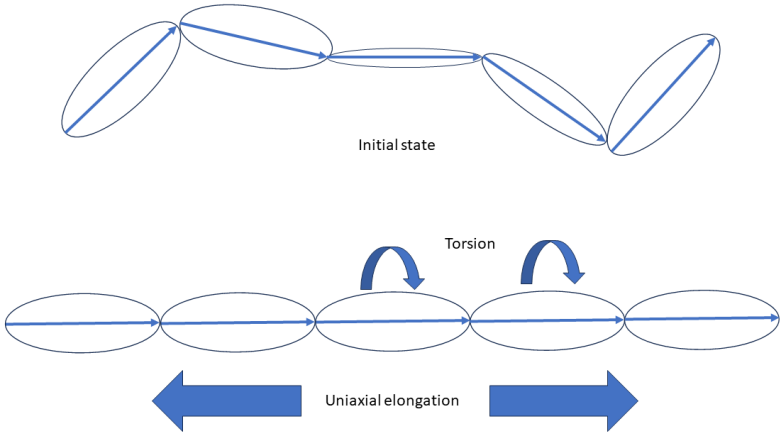


Figure 2.4: The effect of uniaxial tension on the polymer chain. Orientation of the major axes of the ellipses contributes to orientation birefringence whilst the torsion effects are contributions of the glassy birefringence.

A high performing photoelastic material should possess positive contributions of the two birefringent factors. Materials that possess high contributions to the glassy birefringence are those that possess benzene ring structures within their chemical composition, for example polycarbonate features two benzene ring structures figure 2.5.

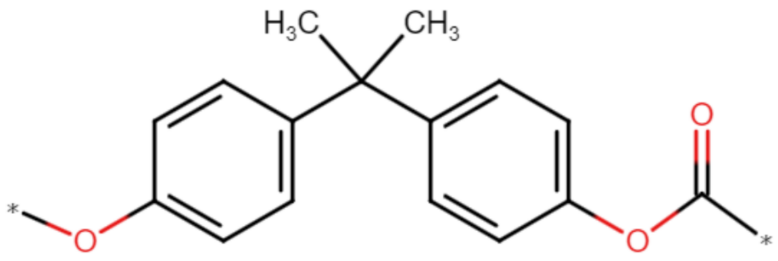


Figure 2.5: The chemical structure of polycarbonate featuring two benzene ring structures.

Under uniaxial tension the orientation of the benzene ring is suggested to be orientated in the elongation direction. Furthermore, The introduction of the benzene ring structures also increase the material's refractive index, due to a redshift in the wavelength absorption, which is linked to the creation of birefringent materials [28]. The effects of the orientation birefringence of polycarbonate are also relatively high with the polymer possessing significant asymmetric polarisability with chains pointed in similar orientations. Polycarbonate is a sensitive photoelastic material often used within RPSA investigations. It is important to note that by introducing optical symmetric additives, groups or monomers has a negative impact on the orientation birefringence however the glassy birefringence is independent of these additions.

2.3 Measuring birefringence

With the information outlined in sections 2.1 and 2.2, the next steps are to understand how to measure and translate the data to perform stress analysis on an object of interest.Within this section both transmission and reflection photoelasticity will be reviewed to introduce multiple photoelastic experimental techniques. The fundamentals of transmission light photoelasticity are reviewed first by introducing various arrangements of the polariscope and other methods to extract desired data. The analysis methods described will then be used to discuss reflection photoelasticity and introduce more complex techniques developed from systems used within transmission photoelasticity. Any limitations of these systems will be reviewed and solutions highlighted.

It is important to note that this research focuses on coating development not imaging techniques and/or apparatus improvements. Whilst decisions to use certain techniques are outlined, the choice of apparatus is insignificant and user should choose whichever technique is most appropriate for the task.

2.3.1 Polarisation and interference

As mentioned in section 2.1, birefringent materials cause a relative retardation, also represented as a phase difference, between two orthogonally linearly polarised rays of light that emerge from the material. Allowing this light to reach a light intensity sensor would yield nothing of significance. However, by rotating the polarisation of one ray to become parallel with the other would create an interference between the two that can be described through the principle of superposition. When two or more propagating waves are incident on the same point, the resultant amplitude at that point is equal to the vector sum of the amplitudes of the individual waves [29].

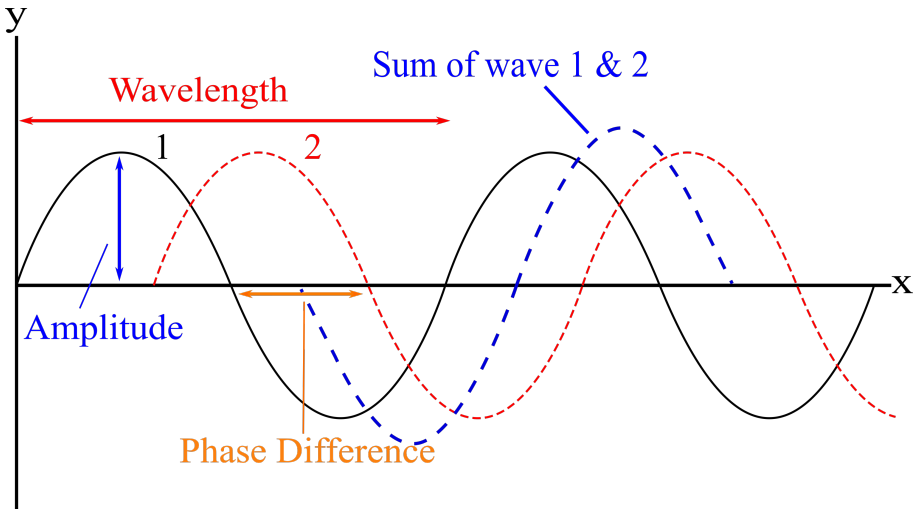


Figure 2.6: An example of two light waves travelling within the same plane and along the same axis. These wave possess equal amplitude and wavelength, but a phase difference is observed between them. This results in a wave that will have a net amplitude of the sum of each individual wave amplitude.

Figure 2.6 illustrates two light waves travelling in the same space with the same polarisation, amplitude and wavelength. An observable phase difference is labelled between the two waves. A resultant wave will be produced with a net amplitude as described by the principle of superposition. This then leads to interference patterns in the form of light and dark fringes, which can be described

mathematically.

$$\begin{aligned} \vec{E}_1 &= A_1 cos\,(kx - \omega t) \\ \vec{E}_2 &= A_2 cos\,(kx - \omega t + \alpha) \end{aligned} \tag{2.7}$$

Equation 2.7 describes the electric field vectors, $\vec{E}$, of the two waves where A_n is the amplitude of a wave, k the wavenumber, x the wave position, ω the angular frequency, t time in seconds and α the relative phase difference. The resultant wave that emerges from the interference of these two waves is simply the sum of $\vec{E}_1$ and $\vec{E}_2$.

$$\vec{E} = \vec{E}_1 + \vec{E}_2 = A\,[cos\,(kx - \omega t) + cos\,(kx - \omega t + \alpha)] \tag{2.8}$$

In equation 2.8 the amplitude $A = A_1 = A_2$. By using a suitable trigonometric identity, equation 2.8 is reduced to 2.9

$$\vec{E} = 2A cos\left(\frac{\alpha}{2}\right)\left[cos\left(kx - \omega t + \frac{\alpha}{2}\right)\right] \tag{2.9}$$

Interference between these two waves is a result of the amplitude component only (outside the square brackets). Intensity, I, of the resultant wave is the square of the amplitude

$$I = I_o cos^2\left(\frac{\alpha}{2}\right) \tag{2.10}$$

with I_o the intensity of the resultant light wave at $\alpha = 0$. Therefore by examining equation 2.9, we find that when the phase difference is an even multiple of π the amplitude is twice the individual waves and four times the intensity, constructive interference. However, if the phase difference is an odd multiple of π then the resultant amplitude and intensity will be zero, destructive interference [15, 19, 30].

2.3.2 The linear polariscope

In order to combine the light, that emerges from a birefringent material, a polariscope is used. A simple linear polariscope is constructed out of a light source incident on a birefringent material which is placed between two linear polarisers. The light which passes through this setup can interfere with one another and is captured and recorded by a sensor, such as a camera or photodiode connected to an oscilloscope.

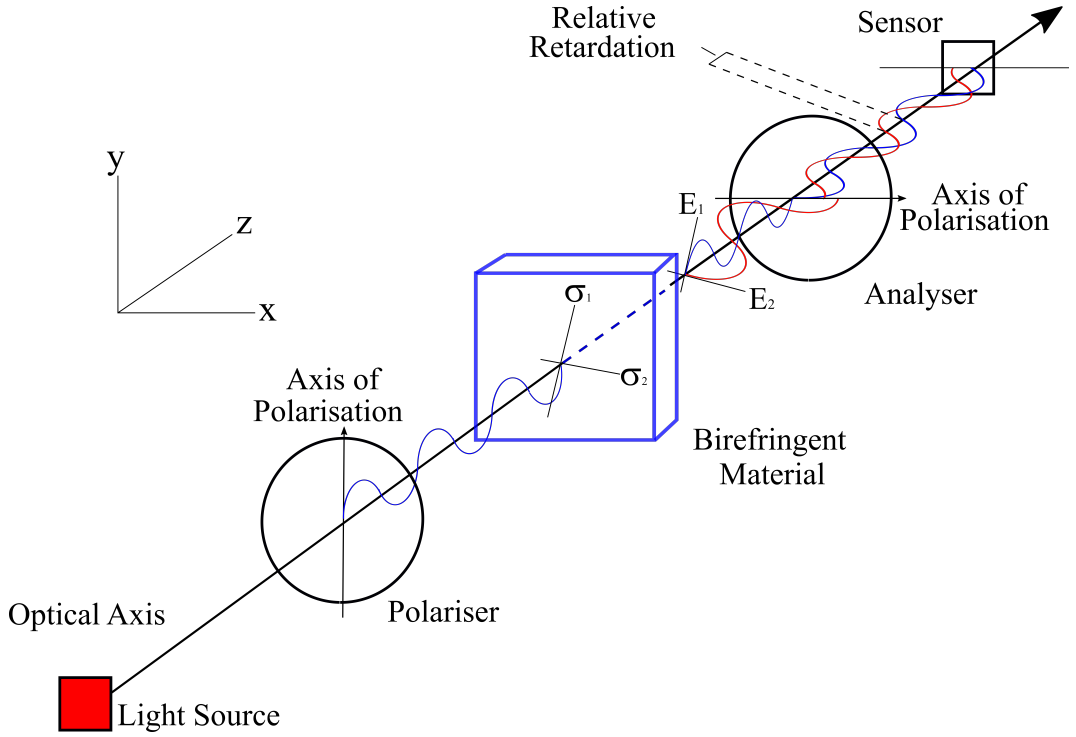


Figure 2.7: A schematic of a dark-field linear polariscope used to visualise the relative retardation between the light waves that emerge from a birefringent material.

Figure 2.7 illustrates the setup of a dark-field linear polariscope. The term dark-field, in this context, indicates that the polariser's axes of polarisation are mutually perpendicular to one another. Unpolarised light, usually monochromatic, travels along an optical axis and passes through the polariser. The light is then polarised parallel to the axis of polarisation of the polariser and has an electric vector equal to equation 2.7 without the relative phase difference. Polarised light is then incident on the birefringent material and, as described above, splits into separate components polarised parallel to the perpendicular principal axes of the material, σ_1 and σ_2. The waves that emerge from the material are now travelling along the optical axis in different orientations, with the same amplitude and with a phase difference between them. These waves are expressed as

$$\begin{aligned}\vec{E}_1 &= Acos\left(kx - \omega t\right) cos\theta \\ \vec{E}_2 &= Acos\left(kx - \omega t + \alpha\right) sin\theta\end{aligned} \tag{2.11}$$

where θ is the angle between the analyser polarisation axis and the axis of polarisation of $\vec{E}_2$. These orthogonally polarised waves then pass through an analyser, causing these waves to travel in both the xz plane. The individual wave components are now expressed as

$$\begin{aligned}\vec{E}_1 &= Acos\left(kx - \omega t\right) cos\theta sin\theta \\ \vec{E}_2 &= -Acos\left(kx - \omega t + \alpha\right) sin\theta cos\theta\end{aligned} \tag{2.12}$$

These waves are now able to interfere with one another and the resultant electric wave vector is the sum of the individual wave components. By using suitable trigonometric identities, the resultant wave vector is expressed as

$$\vec{E} = Asin\left(\frac{\alpha}{2}\right) sin2\theta \left[sin\left(kx - \omega t + \frac{\alpha}{2}\right)\right] \tag{2.13}$$

With the wavefunction component within the square brackets and the amplitude component outside. As mentioned, interference is a product of amplitude only and the wave intensity is the square of this component.

$$\begin{aligned}\vec{E} &= Asin\left(\frac{\alpha}{2}\right) sin2\theta \\ I &= I_o sin^2\left(\frac{\alpha}{2}\right) sin^2 2\theta\end{aligned} \tag{2.14}$$

Within equations 2.14, there possesses two conditions that would result in destructive interference. The simplest case to consider is when $\sin 2\theta = 0$ or $\frac{\pi}{2}$. This is describing the situation where the principal stress axes of the material align with the crossed axes of polarisation of the polariser and analyser. As a result, directions of the principal stress axes can be determined. The second condition to consider is when the phase difference $\alpha = 0, 2\pi, 4\pi, ...2N\pi$ where N is an integer number. This can also be expressed as $N\lambda$. With this condition no light is generated, at a particular point, when the retardation between the waves is an integer multiple of the wavelength of the incident light. This information can be used to calculate principal stress differences by reintroducing equation 2.5

and substituting the following condition.

$$\begin{aligned} N &= \frac{\delta}{2\pi} = \frac{d}{\lambda} C(\sigma_1 - \sigma_2) \\ \frac{N\lambda}{Cd} &= (\sigma_1 - \sigma_2) \end{aligned} \tag{2.15}$$

Knowing the stress-optic coefficient, material thickness, and fringe order, N, then the difference between the principal stresses can be calculated.

Since these two destructive conditions exist the resulting interference pattern can be a confusing mixture of bright and dark lines and patches. Learning how to decipher these patterns is crucial [31].

2.3.3 Interference patterns

An interference pattern is made up of a number of lines of uniform intensity known as fringes. In photoelastic analysis these fringes demonstrate loci of points that have either constant relative retardation, integer number of wavelength, or constant inclination of the principal axes and stress. This information allows for the calculation of the orientation of the principal stress axes or the difference between the principal stresses. The reason the retrievable data cannot be extracted from a single fringe is because a fringe is either labelled as an isoclinic or an isochromatic.

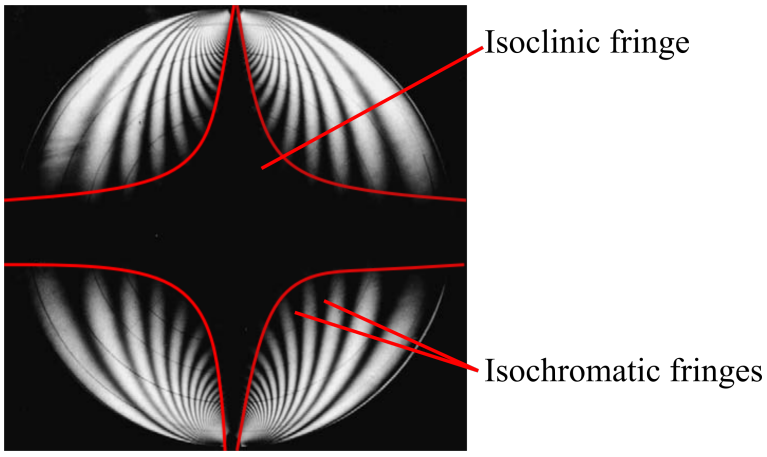


Figure 2.8: An example of an isoclinic fringe superimposed on a number of smaller isochromatic fringes. This interference pattern is of a disc in diametral compression captured using a linear dark-field polariscope. Data shared with permission by the University of Sheffield.

Figure 2.8 highlights an isoclinic fringe in a transperant disc subjected to diametral compression. The application of load are at opposite sides of the disc at the top and bottom of the disc. Isoclinic

fringes are areas where the principal axes of the material are parallel to the polariser and analyser's axes of polarisation. Within equation 2.14 isoclinics are generated from the $sin2\theta$ component. These fringes denote the principal stress directions over the extent of the model. Isoclinic fringes always appear black and don't move when the load on a material changes. They do appear to move if the crossed polarisation axes of the polariser and analyser rotate relative to the photoelastic medium, in fact a new isoclinic fringe is being generated. What is also observed in figure 2.8 are the thinner fringes that appear with the isoclinic fringe. These are known as isochromatic fringes and are dominated by isoclinic fringes whenever they appear together.



Figure 2.9: Diagram of a disc in diametral compression undergoing photoelastic analysis using a circular polariscope, see section 2.3.4. This results in removal of the isoclinic fringes observed in figure 2.8. Data shared with permission by the University of Sheffield.

Figure 2.9 demonstrates a collection of isochromatic fringes without an isoclinic fringe present. The isochromatic fringes in this image appear black as monochromatic light is being used. However, if a white light source is used these fringes would appear coloured, figure 2.10.

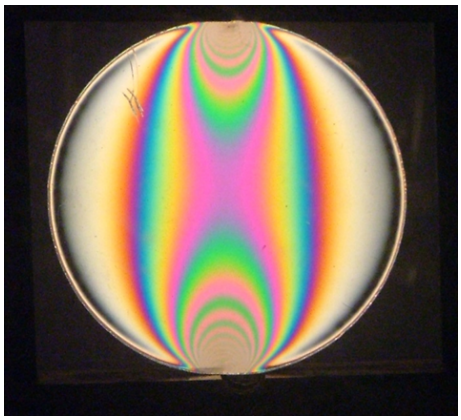


Figure 2.10: Diagram of a disc in diametral compression undergoing photoelastic analysis using a circular polariscope with a white light source. This results in coloured isochromatic fringes. Data shared with permission by the University of Sheffield.

Isochromatic fringes are loci of points having constant principal stress difference. Within equation 2.14 isochromatics are generated from the $sin\left(\frac{\alpha}{2}\right)$ component and destructive interference occurs when the relative retardation is an integer number of wavelengths. So for one wavelength amount of retardation an isochromatic fringe will be generated and assigned as a first-order fringe, two wavelengths amount of retardation will produce another isochromatic fringe and assigned as a second-order fringe and so on. This describes the fringe order number in equation 2.15. Knowing the exact fringe order number is crucial when gathering stress data using a polariscope. Difficulties in the proper labelling of fringe orders include areas of stress concentrations and the dominating isoclinic fringes that obscure the isochromatic fringes. These problems can be solved by utilising different techniques as outlined in sections 2.3.4 - 2.3.9.

2.3.4 The circular polariscope

The circular polariscope, figure 2.11, introduces two new optical elements to the linear polariscope setup. These are quarter-wave plates that sit between the two polarisers and surround the birefringent material being analysed. A quarter-wave plate is itself constructed out of a birefringent material causing light that passes through it to split into two orthogonally polarised waves. In a circular polariscope the light incident on the first input wave plate is already linearly polarised by the polariser. The emergent beam from this wave plate causes a phase difference of $\frac{\pi}{2}$, $\frac{\lambda}{4}$, to occur between the two components of light. If the principal axis of polarisation of the first wave plate is positioned 45^o from the axis of polarisation of the polariser, then circularly polarised light is generated. Circularly

polarised light, if approaching an observer, would appear to have an electric vector of equal magnitude but its direction rotating in either a clockwise or counter-clockwise motion.

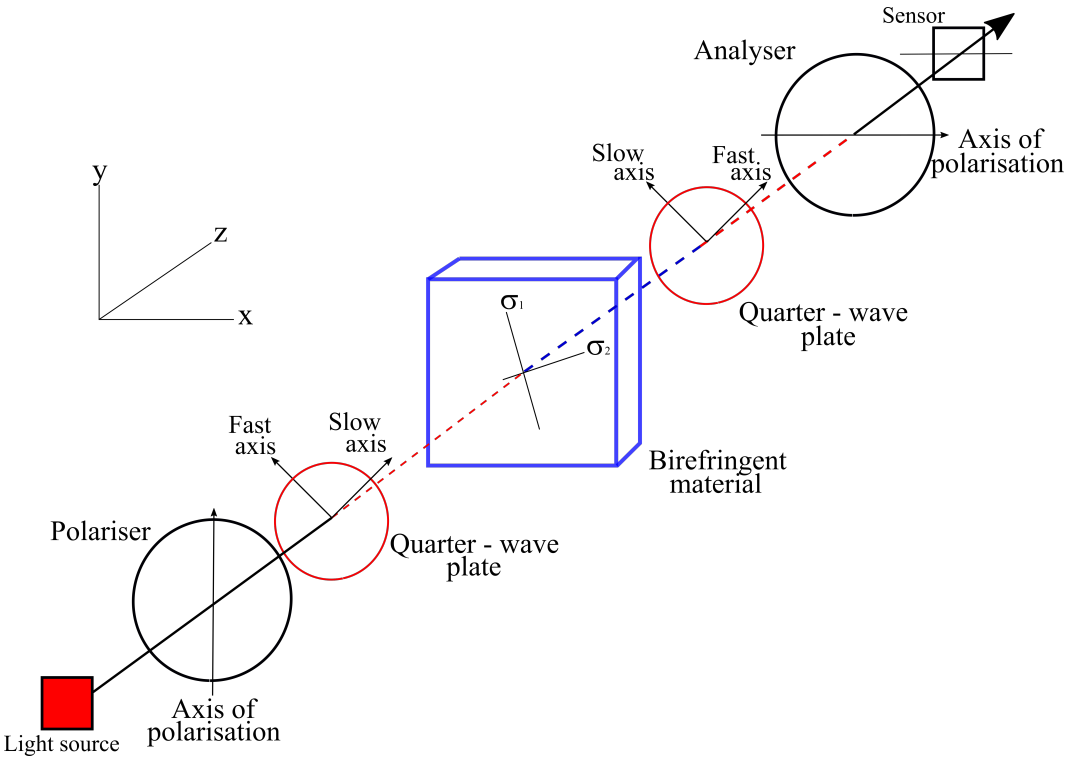


Figure 2.11: Schematic of a circular polariscope. The setup is similar to that of a linear polariscope but with the addition of two quarter-wave plates. This setup is used to produce interference patterns without generating isoclinic fringes.

Figure 2.11 illustrates the layout of a circular polariscope. The polariser and analyser have axes of polarisation parallel to the y and x axis respectively. The input quarter-wave plate has its fast axis (light polarised along this axis experiences a lower refractive index of light polarised along the slow axis) positioned $\frac{-\pi}{4}$ from the polariser's axis of polarisation. Passing circularly polarised light through the sample produces an interference pattern without the presence of isoclinic fringes. The output wave plate is flipped in respect to the input, the fast axis is positioned $\frac{\pi}{4}$ from axis of polarisation of the first polariser. Unpolarised light is first linearly polarised in the yz plane and incident on the input quarter-wave plate. The birefringent material within the quarter-wave plate splits it into two orthogonal waves with a $\frac{\lambda}{4}$ relative retardation between them causing circularly polarised light to be incident on a birefringent sample. The sample induces a further undefined retardation between the light waves causing the emerging light to become elliptically polarised. Like circular polarisation, elliptically polarised light's electric field vector rotates in a rotary motion but with varying magnitude

so that the vector draws out an ellipse shape if observing this elliptically polarised light directly. This unknown relative retardation is measured by passing the light through the output wave plate and analyser. The light is then linearly polarised along the xz plane and the interference at the point of the sensor is measured. As with the linear polariscope, the resultant amplitude component of the electric wave vector is responsible for the fringe pattern produced. The resultant amplitude component from the electric wave vector, for the dark field setup, is expressed as

$$\vec{E} = Asin\left(\frac{\alpha}{2}\right) \tag{2.16}$$

equation 2.16 demonstrates that destructive interference is produced when the phase difference $\alpha = 0, 2\pi, 4\pi, ..., 2N\pi$. This then generates an isochromatic only interference pattern [31].

2.3.5 Fringe analysis - automated photoelasticity

In order to gather the desired quantitative information from an interference pattern, effective and efficient fringe analysis must be performed. Assigning fringe orders to a set of isochromatic fringes is no trivial task. Fringe patterns taken from materials under load are often unevenly spaced, as observed in figure 2.9. Areas which include high densities of closely spaced fringes occur at stress concentrations and make manual fringe ordering a slow and inaccurate process. This is also unappealing for applications in industry which understandably benefit from fast, accurate and sensitive fringe analysis. Such techniques include spectral analysis, Fourier analysis and phase-stepping methods [32–34]. The latter is the approach of most interest for this research and is adopted in the apparatus used at Airbus in their photoelastic analysis.

Phase-stepping in photoelasticity was first introduced by Hecker and Morche in 1986 [35]. Phase-stepping requires multiple intensity captures of the interfering wave using different orientations of differing combinations of the polarising optics [36–38]. The following description describes the procedure utilised by work conducted by Patterson and Wang using a transmission polariscope [36]. Here, the input quarter wave plate is kept fixed with its fast axis $-\frac{\pi}{4}$ to the axis of polarisation of the polariser. The orientations of the output wave plate and analyser are then changed to produce full-field isoclinic and isochromatic maps in which relative retardation and principal stress directions can be measured. Patterson and Wang developed a procedure which required six phase-stepped images to be captured

in order to determine isoclinic and isochromatic parameters. The light intensity observed through a circular polariscope for any point in the specimen, after the analyser, can be expressed as

$$I = I_m + \frac{I_v}{2} + \frac{I_v}{2}\left[sin2(\kappa - \Phi)cos\alpha - sin2(\theta - \Phi)cos2(\kappa - \Phi)sin\alpha\right] \tag{2.17}$$

where κ is angular position of the analyser, Φ the angular position of the output quarter-wave plate, θ isoclinic angle, I_v the intensity emerging when all axes of the polariscope and specimen are parallel and I_m represents the stray light. Six images are taken at varying positions of κ and Φ to help improve the signal-to-noise ratio and to solve for the four unknowns shown in the following equations, table 2.1 [39].

Image Number	Φ	κ	Light Intensity
1	0	$\frac{\pi}{4}$	$I_1 = I_m + \frac{I_v}{2}(1 + cos\alpha)$
2	0	$\frac{-\pi}{4}$	$I_2 = I_m + \frac{I_v}{2}(1 - cos\alpha)$
3	0	0	$I_3 = I_m + \frac{I_v}{2}(1 - sin\alpha sin2\theta)$
4	$\frac{\pi}{4}$	$\frac{\pi}{4}$	$I_4 = I_m + \frac{I_v}{2}(1 + sin\alpha cos2\theta)$
5	$\frac{\pi}{2}$	$\frac{\pi}{2}$	$I_5 = I_m + \frac{I_v}{2}(1 + sin\alpha sin2\theta)$
6	$\frac{3\pi}{4}$	$\frac{3\pi}{4}$	$I_6 = I_m + \frac{I_v}{2}(1 - sin\alpha cos2\theta)$

Table 2.1: Six optical arrangements with the corresponding intensity equations used to determine principal stress direction and the relative retardation.

Using the various equations for light intensity from table 2.1, the periodic isoclinic angle and relative phase difference can be calculated through the following equations

$$\theta = \frac{1}{2}tan^{-1}\left(\frac{I_5 - I_3}{I_4 - I_6}\right) \tag{2.18}$$

$$\alpha = tan^{-1}\left[\frac{I_4 - I_6}{(I_1 - I_2)cos2\theta}\right] \tag{2.19}$$

However, a few drawbacks exist when utilising this method. The first being the fact that at phase differences of $0, \frac{\pi}{2}, \frac{3\pi}{2}, ...$ reduces equation 2.17 to

$$I = I_m + \frac{I_v}{2} + \frac{I_v}{2}\left[sin2(\kappa - \Phi)\right] \tag{2.20}$$

within equation 2.20 there is no isoclinic parameter, θ, leading to interpolation or replacement of data at these points [33]. To overcome this, phase stepping techniques have developed to a ten-step approach proposed by Ramji and Ramesh [32, 34, 40]. The technique combines a four-step approach [41] for isoclinic data evaluation with the six-step approach demonstrated in table 2.1.

The sequential nature of data capture using these methods is unfavourable when wanting to capture any dynamic changes to load of the sample. Changing the orientation of the optical elements takes time and can be prone to human error in potentially misplacing the desired orientation, causing errors in the final intensity recordings. These errors increase further if the chosen quarter-wave plates specified wavelength does not match the chosen wavelength of light used [39, 42]. Therefore, if dynamic testing is required an alternative method is required. Before a solution is discussed, another photoelastic technique must be discussed.

2.3.6 Reflection photoelasticity

Reflection photoelasticity (RPE), is a technique used to perform photoelastic analysis on opaque structures [3]. RPE relies on utilising a thin temporarily birefringent material that is adhered to a prototype with a reflective backing to form a photoelastic coating. Rather than the photoelastic specimens being directly loaded, as in figures 2.7 and 2.11, the surface strains developed on the prototype are transmitted through to the applied photoelastic coating. Examples of photoelastic coatings are presented in section 2.4. Disadvantages of transmission photoelasticity occur during the transferral of data collected from a photoelastic model to the actual prototype [43]. Difficulties during data transferral arise from the fact that the prototype will most likely be constructed out of a different material, carry different loads, or have differing dimensions. To combat these problems, a scaling law can be applied in all cases which do not need to consider material properties, a detailed discussion can be found in an article by Cloud [43]. RPE benefits by being cost effective, easier to apply than transmission photoelasticity, and able to yield accurate strain measurements over the entire surface of the structure being studied.

An important observation about transmission photoelasticity is that the photoelastic analysis of a specimen can only be related to stresses if normal incidence is used. This can easily be observed in figures 2.7 and 2.11 as the light source and sensor are fixed to the same reference axis. Within RPE,

normal incidence can be achieved if utilising a partial mirror in a plane polariscope arrangement, figure 2.12.

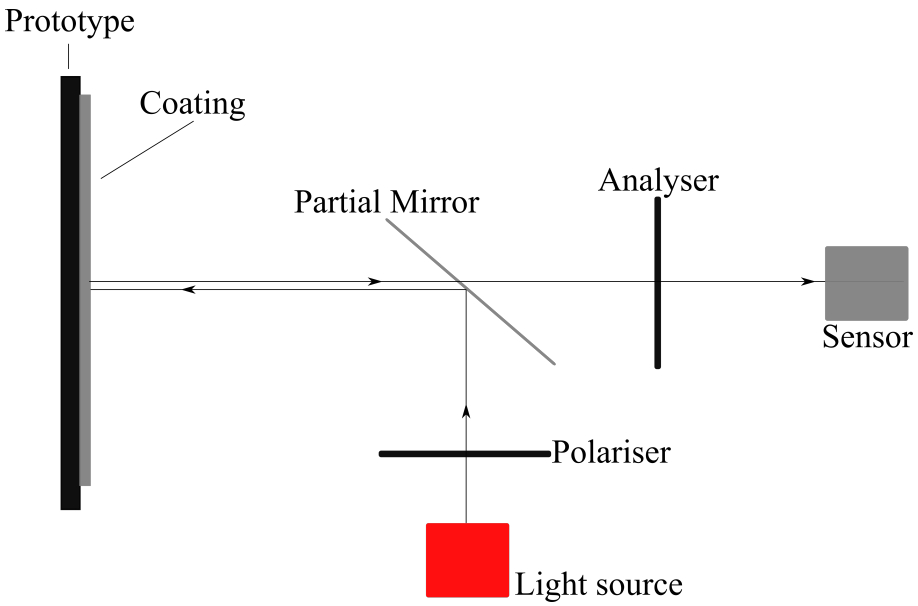


Figure 2.12: A linear polariscope used in a reflection photoelastic configuration. This arrangement allows for normal incidence

However, to convert figure 2.12 into a circular polariscope, compensation is required to counteract the change in the ellipticity of polarisation caused by the partial mirror. As a result, another more favourable arrangement is used which features in commercially available devices, for example the device featured in section 2.3.9.

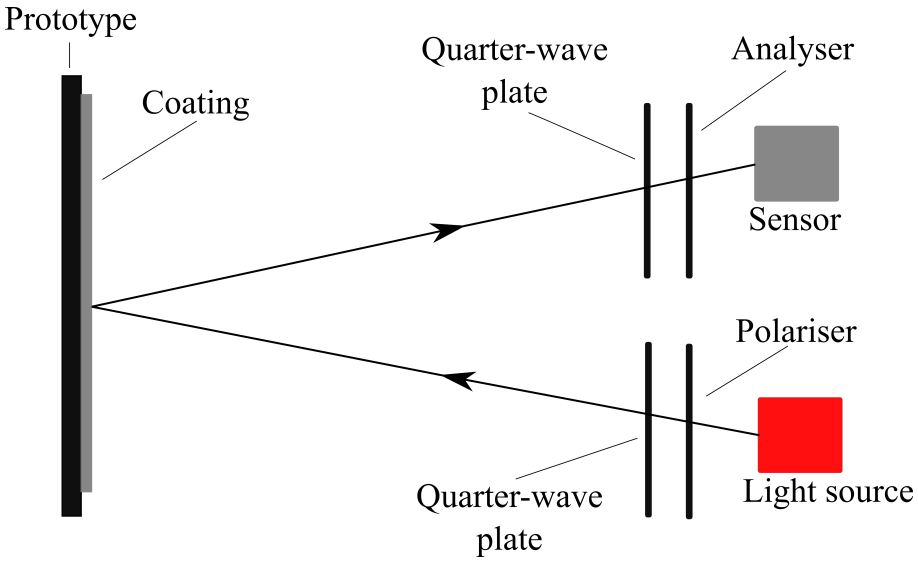


Figure 2.13: A circular polariscope used in a reflection photoelastic configuration. This arrangement is used in commercially available reflection polariscopes.

Figure 2.13 demonstrates the alternative arrangement, which adopts an angle of oblique rather than normal incidence. The oblique angle in these arrangements is usually of the order of 4 ^{o} which has a negligible influence on the optical pattern interpretation [3, 44]. This recommendation can be achieved through maximising the distance between the coated sample and the sensor.

When analysing the coating's interference pattern captured using RPE, there exists some key differences when comparing to transmission photoelasticity. Firstly, isoclinic fringes still represent the direction of the principal stresses and strains if the coating and material are within the limits of elasticity. The differences occur when considering the isochromatic data. Strains in the coating surface are assumed to be the same as the strains in the prototype surface, however the stresses in the prototype do not directly yield from the isochromatic data. Light reflecting off a photoelastic coating will travel through it twice resulting in the following isochromatic fringe expression

$$N = \frac{2Cd}{\lambda}(\sigma_1 - \sigma_2) \tag{2.21}$$

In order to relate stresses in the coating to those in the prototype, an equation which includes the coating's modulus of elasticity, E, and Poisson's Ratio, ν, is used

$$(\sigma_1 - \sigma_2)_c = \left[\frac{E_c}{1+\nu_c}\right](\epsilon_1 - \epsilon_2)_c \tag{2.22}$$

where the subscript 'c' is used to denote the coating. Equations 2.21 and 2.22 can be combined to obtain the isochromatic order in terms of coating strain

$$N = \left[\frac{2Cd}{\lambda}\right]\left[\frac{E_c}{1+\nu_c}\right](\epsilon_1 - \epsilon_2)_c \tag{2.23}$$

by assuming that coating strains are equivalent to prototype strains

$$(\epsilon_1 - \epsilon_2)_c = (\epsilon_1 - \epsilon_2)_p \tag{2.24}$$

where subscript 'p' represent the prototype, equation 2.23 and 2.24 can be combined to form

$$(\epsilon_1 - \epsilon_2)_p = N \left[\frac{\lambda}{2Cd}\right] \left[\frac{1+\nu_c}{E_c}\right] \tag{2.25}$$

equation 2.25 is often written in terms of strain-optic coefficient K.

$$(\epsilon_1 - \epsilon_2)_c = (\epsilon_1 - \epsilon_2)_p = \frac{N\lambda}{2dK} \tag{2.26}$$

The strain-optic coefficient of the photoelastic coating is either provided by the manufacturer or calculated through calibration, see chapter 7. In order to calculate the principal stress difference within the prototype, equation 2.27 is used, assuming the prototype is linearly elastic.

$$(\sigma_1 - \sigma_2)_p = N \left[\frac{\lambda}{2Cd}\right] \left[\frac{1+\nu_c}{E_c}\right] \left[\frac{E_p}{1+\nu_p}\right] \tag{2.27}$$

Many industries employ RPE due to design optimisation processes only requiring reasonable estimates of surface stresses or stress concentrations [43]. Even though RPE is more useful than transmission photoelasticity for many industrial applications, it does possess a number of inaccuracies within stress and strain data. One such error is the angle of oblique that has been discussed. Another issue, which is discussed in more detail in section 2.4, is that the prototype can be reinforced by the application of the coating changing the overall strain field [45]. Out-of-plane bending also creates inaccuracies by causing the coating to inaccurately render the strain at the specimen surface. Finally, consider a hole in a prototype, the correspondence of coating strain and prototype strain, at the edge of the coating, will be poor because the deforming traction is applied only at the bottom side of the coating, not at the edge. Therefore, strains at the edge of the coating might not be the same as the prototype strain. These final issues can be solved by adopting thinner and/or low modulus coatings but suffer from reduced sensitivity in the yield of fringe order with applied load. RPE is also limited by its own sensitivity; it can only detect up to around 3 fringe orders when a coating is applied to metal and both are in the elastic range. As a result, careful methods of interpolation and/or fractional fringe measurements must be employed to obtain quantitative precision.

2.3.7 Simultaneous capture

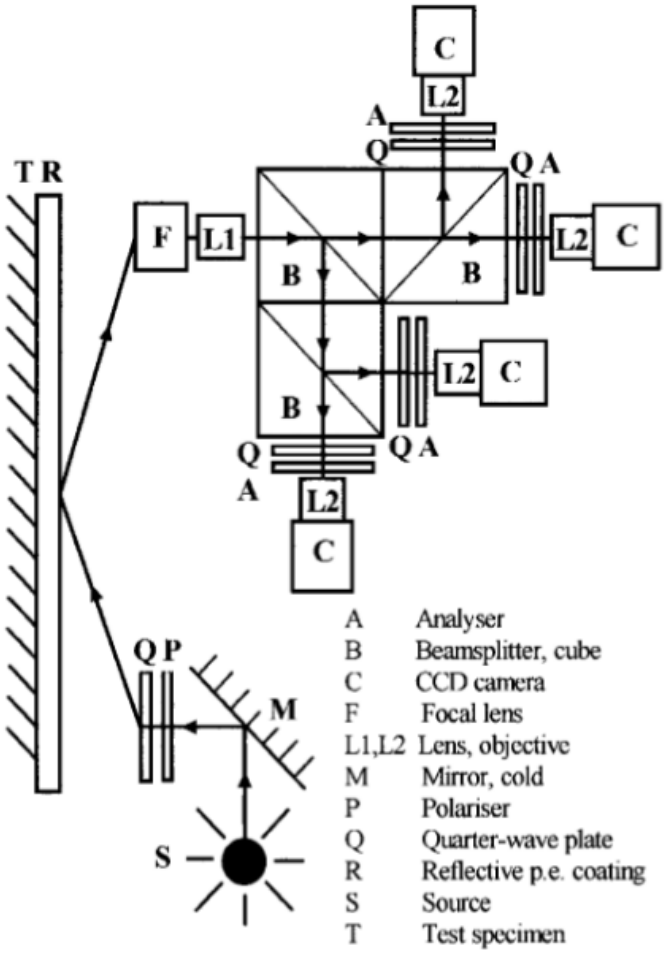


Figure 2.14: Schematic of the PSIOS system. Here light is reflected off a sample of interest with a photoelastic coating applied. Light enters the camera array and is split into four separate components with their intensities recorded by one of four CCD cameras [46].

Phase-stepping methods benefit from being able to capture the required multiple images simultaneously. The time for capture is a lot less and can be applicable in dynamic situations. A solution was to create a device in which light entering a camera setup would be first split into four components and recorded separately and simultaneously. In a setup designed by Patterson and Wang [46], figure 2.14, circularly polarised light is reflected off a photoelastic specimen. The reflected light enters the polariscope structure through a lens arrangement that collimates the light entering the camera array. A set of beamsplitters divides this collimated light into four which then passes through separate output quarter-wave plates and analysers before striking a CCD camera. The orientations of output optics are predetermined and different to generate different intensities for each image

when can be combined in a similar manner to equations 2.18 and 2.19. To ensure identical images are being taken, the path lengths for all beams must be made the same and the number of splits made by the beamsplitters must be equal for each beam. This ensures, prior to phase-stepping, the intensity of each beam is equivalent. Another thing to consider is the beamsplitters' effect on the polarisation of light. The polarisation characteristic of the beamsplitters should be known and accounted for in data processing. This device is condensed through the advent of the poleidoscope.

2.3.8 The Poleidoscope [47]

The poleidoscope is a more advantageous device for several reasons. The need to source, match and align expensive optics and provide four high speed CCD cameras is now redundant. This is because beamsplitters have been replaced with a kaleidoscope lens that returns four identical images to a single CCD camera. This also allows the device to be compacted down and easily transportable. Data collection is a lot faster using a poleidoscope as intensity data is captured in as little as $\frac{1}{25}$ of a second [33].

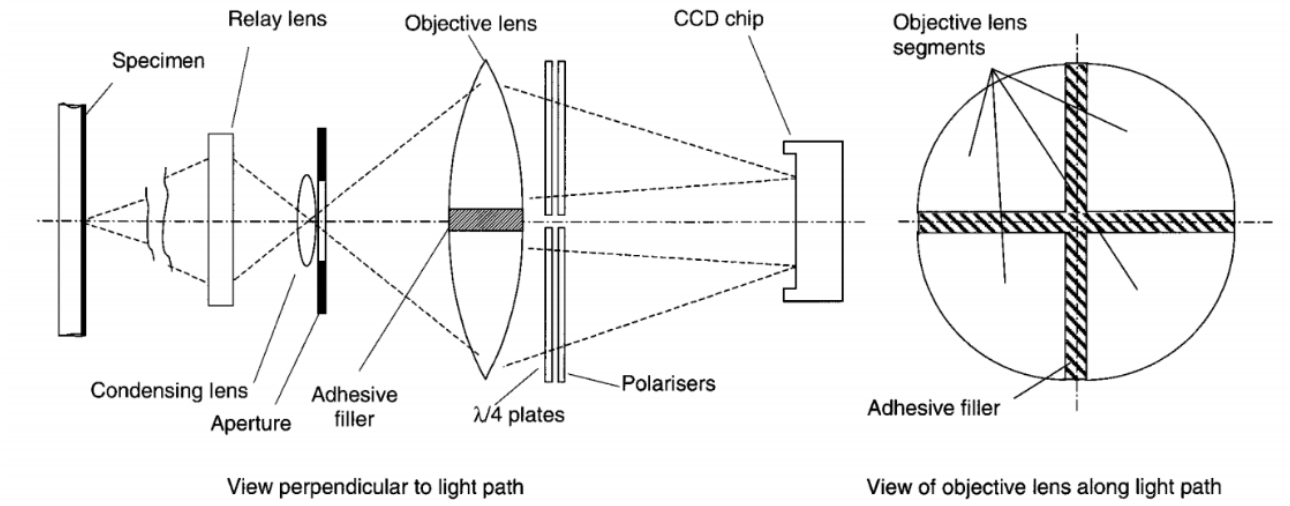


Figure 2.15: Schematic of the a poleidoscope. Light that interacts with a photoelastic specimen is incident into the poleidoscope setup. Four separate images are formed and processed by a single CCD camera [47].

Figure 2.15 illustrates the setup of a poleidoscope. Light that interacts with a photoelastic specimen is directed towards the poleidoscope structure. An input CCTV lens allows for the light entering the poleidoscope to be focused onto the objective kaleidoscope lens. This allows the device to be positioned freely to suit the needs of an experiment. The kaleidoscope lens was manufactured

out of four individual 1 inch diameter lenses each forming a quadrant of the resultant 1.2 inch kaleidoscope lens. Each lens was positioned and glued together creating a 0.25mm glue-line. Four separate images are formed and differ in intensity due to the different polariser and quarter-wave plate arrangements used directly after this lens.

Image Number	Φ	κ	Light Intensity
1	$\frac{\pi}{4}$	$\frac{\pi}{4}$	$i_1 = I_v(I_m - cos2\theta sin\alpha)$
2	0	0	$i_2 = I_v(I_m + sin2\theta sin\alpha)$
3	0	$\frac{-\pi}{4}$	$i_3 = I_v(I_m - cos\alpha)$
4	$\frac{\pi}{2}$	$\frac{\pi}{2}$	$i_4 = I_v(I_m - sin2\theta sin\alpha)$

Table 2.2: Four optical arrangements with the corresponding intensity equations used to determine principal stress direction and the relative retardation when using a Poleidoscope [47]

The light intensities in table 2.2 are combined in the following manner to generate the isoclinic angle and relative retardation functions

$$\theta = \frac{1}{2} tan^{-1}\left(\frac{i_2 - i_3}{i_2 + i_3 - 2i_1}\right) \tag{2.28}$$

$$\alpha = tan^{-1}\left[\frac{i_2 - i_3}{sin2\theta(i_2 + i_3 - 2i_4)}\right] \tag{2.29}$$

Like the previous apparatus the isoclinic and retardation parameters are periodic in nature. These arctangent functions can be unwrapped to provide continuous full-field data by applying algorithms devised for earlier devices [46, 48]. These algorithms locate points in which the periods of the arctangent function begin and end and combines them to generate the continuous data. This unwrapping procedure is performed in the data processing software used on a personal computer connected to the poleidoscope.

2.3.9 The GFP1600

This research makes use of a commercially available grey-field polariscope (GFP) by Stress Photonics Inc [49] to analyse photoelastic data. The GFP combines multiple methods, phase-shifting and Fourier methods [33], to calculate both absolute fringe order and isoclinic angle. This then translates to a possible detectable relative retardation of better than 0.1 nm and an isoclinic angle resolution

of 0.01 ^{o} as claimed by Stress Photonics. The resolution on the measured retardation translates to a 20 $\mu\epsilon$ sensitivity. This device possesses a very high sensitivity with individual spectral analysis and phase-stepping are found to have sensitivities of 0.005 and 0.007 fringes respectively [33] which is a magnitude higher than the GFP. Micro-measurement's LF.Z-2 reflection polarisation claims a sensivity of $\sim$10 $\mu\epsilon$ however at coating thicknesses of 3 mm and does not posses automated capability. The decision to utilise this apparatus was based on availability as well as it being used by Airbus allowing for better knowledge exchange. It is important to note that the GFP cannot be used in dynamic applications due to the function of the device. Where dynamic capture is used, the poleidoscope was utilised.

The GFP has a similar layout as the circular polariscope, figure 2.13b, but with the output quarter-wave plate removed. Using a circular polarised light source, light is incident on the coated sample and reflected into the first input lens of the GFP. The light then passes through two imaging lenses in which a rotating analyser is positioned in between. A motor rotates the analyser continuously with an encoder measuring its angular position. At certain orientations the encoder will trigger the camera to capture the light emerging from the analyser.

Circular polarised light is generated by transmitting linear polarised light through a quarter-wave plate (QWP). The components of light are described as being parallel to a fast, E_1, and a slow, E_2, axis which describes the different refractive indices that they past through. In the GFP setup the fast axis light component is orientated β degrees with respect to a reference direction. When passing through or reflecting off a photoelastic medium, a further phase difference, α, is induced within these components of light which can be expressed as

$$\begin{aligned} E_1 &= \frac{A}{\sqrt{2}} cos\left(\omega t + \frac{\alpha}{2}\right) \\ E_2 &= \frac{A}{\sqrt{2}} sin\left(\omega t - \frac{\alpha}{2}\right) \end{aligned} \tag{2.30}$$

these components of light emerging from the sample are elliptically polarised and can be expressed further as

$$\begin{aligned} E_{maj} &= Acos\left(\frac{\pi}{4} - \frac{\alpha}{2}\right) cos\left(\omega t + \frac{\pi}{4}\right) \\ E_{min} &= Acos\left(\frac{\pi}{4} + \frac{\alpha}{2}\right) sin\left(\omega t + \frac{\pi}{4}\right) \end{aligned} \tag{2.31}$$

where E_{maj} and E_{min} describe the amplitude of the major and minor axes of an ellipse. It is important to note that the major axis of the ellipse is always shifted $\frac{\pi}{4}$ radians from the direction of the first principal strain for odd fringes and $-\frac{\pi}{4}$ for even fringes. An analyser angled at ϕ degrees from the major axis produces a resultant light amplitude equal to

$$E_{\phi} = E_{maj}cos\phi + E_{min}sin\phi \tag{2.32}$$

the resultant light intensity, after several trigonometric manipulations, reduces to the following expression.

$$I = \frac{A^2}{2}[1 + cos(2\phi)sin\alpha] \tag{2.33}$$

As the analyser moves with a constant angular frequency, ϕ can be rewritten as

$$\phi = \omega t - \beta - \frac{\pi}{4} \tag{2.34}$$

assuming the analyser is parallel with the reference orientation at t=0, equation 2.33 can be expressed as

$$I(t) = \frac{A^2}{2}[1 + \sin 2(\omega t - \beta)sin\alpha] \tag{2.35}$$

for sub-fringe photoelastic stress analysis this equation is further reduced by utilising the small angle approximation.

$$I(t) = \frac{A^2}{2}[1 + \alpha \sin 2(\omega t - \beta)] \tag{2.36}$$

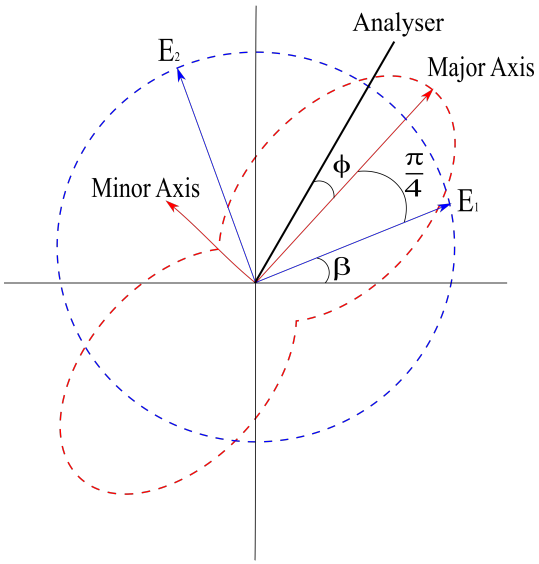


Figure 2.16: A diagram illustrating the two components of circularly polarised light that travel parallel to the fast axis, E_1, and slow axis, E_2. The fast axis is at an angle β to a reference direction. The peanut shaped ellipse is the resultant shape from squaring the amplitude of the ellipse. The orientation of the analyser is highlighted with respect to the major axis.

Figure 2.16 illustrates equations 2.35 and 2.36 with the peanut shaped ellipse representing the square of the amplitude of the elliptical light. It is shown that if the analyser is positioned along the major axis, the measured intensity would be at its highest whilst the measured intensity would be at its lowest if the analyser was orientated parallel to the minor axis. Therefore, the output signal oscillates between a bright and dark region as the analyser element rotates. This bright and dark intensity occurs about a mean grey level, hence the name grey-field polariscope. The periodic elements to these expressions are zero when the axis of the analyser coincides with the principal stress or strain axes [14].

A video lock-in algorithm is able to translate the captured intensities of light passing through or reflecting off a photoelastic specimen into useful data. The constant rotation of the analyser continuously changes the intensity of output light. At set angles of analyser position the GFP camera is triggered to capture an image. Eight images are captured per half revolution of the analyser which represents a full period of amplitude oscillation. Understanding how the eight images are combined to calculate desirable data stems from applying Mohr's circle, figure 2.17.

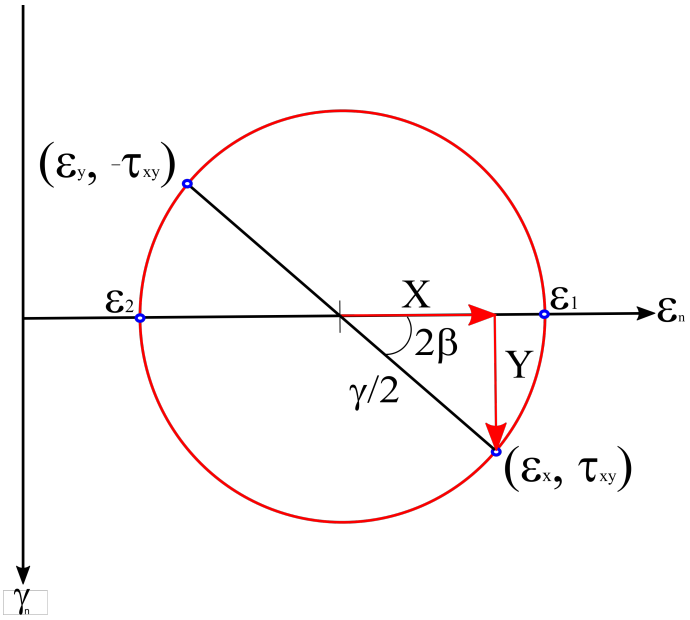


Figure 2.17: Mohr's circle for plane strain. It is a geometric representation of the 2D transformation of strains at a point in a specimen. It can be used for the determination of the relationship between normal, ϵ, and shear, γ, strains. The principal strains are denoted at ϵ_1, maximum strain and ϵ_2, minimum strain.

Mohr's circle is a graphical representation of the stress/strain transformation equations. It is used to determine the normal and shear stresses/strains at any angle at a certain point of a sample. Parameters within figure 2.17 are found via the combination of the eight captured images that produce separate X and Y images through the following expressions

$$\begin{aligned} X(x,y) &= \frac{2}{N_i}\sum_{n_i=1}^{N_i} J_{n_i}(x,y)\sin(\theta_{n_i}) \\ Y(x,y) &= \frac{2}{N_i}\sum_{n_i=1}^{N_i} J_{n_i}(x,y)\cos(\theta_{n_i}) \end{aligned} \tag{2.37}$$

where N_i is the number of images taken, n_i the image number, J_{n_i} the sampled image intensity and θ_{n_i} the angle of the analyser which triggers the image capture. From this, the phase can be calculated via the expression

$$\alpha = tan^{-1}\left(\frac{Y}{X}\right) \tag{2.38}$$

the orientation of the first principal strain direction to the reference direction, η, is related to equation

2.38 by

$$\alpha = 2\beta \tag{2.39}$$

and finally the magnitude of the shear strain, equivalent to the difference of the principal strains, can be calculated by the expression

$$\gamma = K_{GFP}\sqrt{X^2 + Y^2} \tag{2.40}$$

where K_{GFP} represents the calibration constant including system gains, light intensity variations and residual stresses in the coating [14, 49].

So far the descriptions and expressions only discuss how the magnitude and direction of shear strains/stresses are calculated. However, within this research and in industrial applications it is useful to be able to define and visualise normal strains and stresses acting on a component. In the GFP software a user can choose from a number of different image processes to generate different output data. The process labelled 'light' displays the transmission of light averaged over all analyser orientations, figure 2.18.

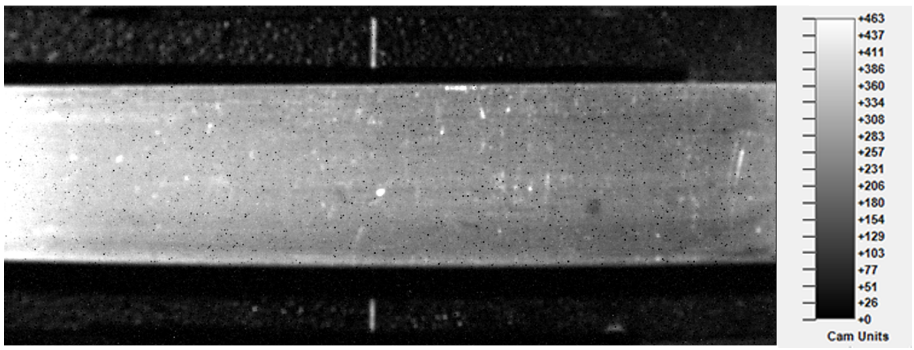


Figure 2.18: Light output image taken by a GFP1600 with corresponding intensity key demonstrating light intensity in arbitrary units.

The process 'Direction' displays the direction of the first principal stress/strain across the whole coated surface, figure 2.19.

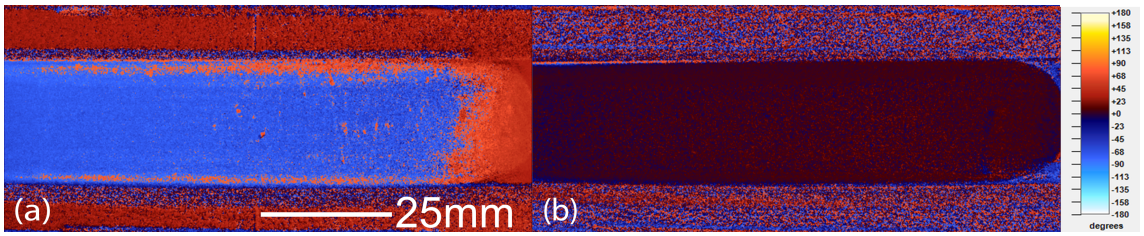


Figure 2.19: Direction output image taken by a GFP1600 with corresponding key demonstrating first principal stress direction. ***(a)*** *represents a beam coated with a thin UV curable resin with zero applied stress.* ***(b)*** *the same beam as image (a) however a load is applied at one end of the beam whilst the other is fixed. As observed, the first principal stress direction is orientated parallel to the long face of the beam.*

The final three, and arguably the most useful, are the 'Shear0' (γ_0), 'Shear45' (γ_{45}) and 'ShearMax' (γ_{max}) outputs. The terms Shear0 and Shear45 represent the orientation of the shear strains. Shear0 is the term to describe shear strains orientated in the 0/90 degrees reference frame. In equation 2.37 and figure 2.17 this is demonstrated by the term Y. This shear strain is equivalent to normal strain magnitudes orientated ± 45 degrees. Shear45 is the term used to describe shear strains orientated in the 45 degrees reference frame. In equation 2.37 and figure 2.17 this is demonstrated by the term X. This shear strain is equivalent of normal strain magnitudes orientated 0/90 degrees. The GFP utilises Shear0 and Shear45 outputs to then generate ShearMax, the maximum in-plane shear strain, equivalent to the difference of the principal strains.

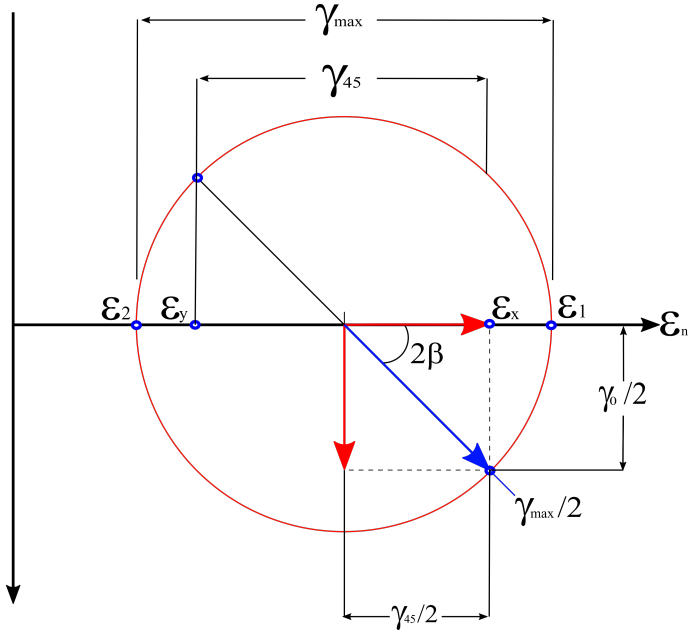


Figure 2.20: The same Mohr's Circle as figure 2.17 however altered to demonstrate the Deltavision software outputs Shear0 (γ_0), Shear45 (γ_{45}), and ShearMax (γ_{max}).

Figure 2.20 displays the three outputs on Mohr's circle. Within this diagram it is easy to see how certain parameters are calculated. The maximum in-plane shear strain magnitude is simply

$$\gamma_{max} = \sqrt{\gamma_{45}^2 + \gamma_0^2} \tag{2.41}$$

and the direction of the first principal strain is

$$\beta = -\frac{1}{2} tan^{-1}\left(\frac{\gamma_0}{\gamma_{45}}\right) \tag{2.42}$$

The image sets X and Y, Shear0 and Shear45, are best presented as vectors. This allows for determination of whether the loads on a sample of interest are in compression or in tension; an attribute unavailable when using a plane or circular polariscope.

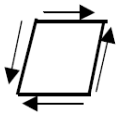
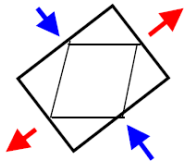
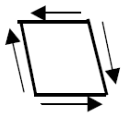
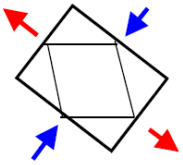
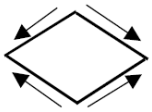
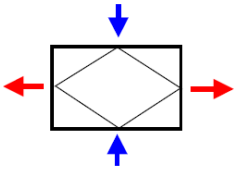
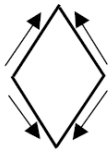
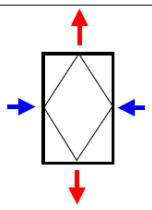
Component	Description	Sign	Shear Strains	Normal strain
γ_0 (Shear 0)	Shear strains acting in horizontal and vertical planes	+		
		-		
γ_{45} (Shear 45)	Shear strains acting in planes at 45 to horizontal and vertical	+		
		-		

Figure 2.21: Table highlighting the GFP output and what the corresponding sign translates to in terms of normal strain.

Figure 2.21 is a table taken from the GFP1400 operator's manual [50]. It highlights the shear strains and the equivalent corresponding directions of the first and second principal strains. The first principal strain being the most tensile strain and second principal strain being the most compressive strain. This information will be used to determine initial residual stresses/strains in the coating which can be calculated in the software.

To visualise the data output from the GFP1600 and Deltavision when measuring principal strain difference, appendix F features an example of a specimen subjected to uniaxial loading.

2.3.9.1 The subtraction facility

Within Deltavision a subtraction processing facility is called upon in order to extract accurate photoelastic data. Whilst this procedure is a built-in feature, it has a profound effect in correcting certain application issues with photoelastic coatings and light sources. When a coating is applied if it is subjected to any stress inducing deformation, such as shrinkage, there will be an undesirable residual stress within the coating that distorts the true photoelastic response. This subtraction is also necessary to account for additional discrepancies such as light source polarisation misalignment where presumed circularly polarised light is actually slightly elliptical. If misaligned, the GFP1600 will misinterpret the polarisation change as induced retardation caused by the coating. The subtraction facility corrects these issues by removing the residual retardation prior to the output of each loaded sample's GFP acquisition. It performs this facility by subtracting the Shear45 and Shear0 image sets onto the loaded image sets prior to calculation of the magnitude. The facility will often be used during the analysis of data in this research.

2.4 Photoelastic coatings and applications

Having a device that allow users to visualise stress and strain distributions in components and/or assemblies is one of two major important elements of RPSA. The other is a suitable photoelastic coating that can cover the entire area of a component of interest with constant thickness, minimal reinforcing effects and can provide enough of a relative retardation that is detectable by the used photoelastic measurement device. This section discusses and reviews a selection of photoelastic coatings and applications.

2.4.1 Current coating materials

The first example of a photoelastic coating was explored by Mesnager [51] in 1930 using glass fragments to cover a sample of interest. However, though photoelastic and sensitive to changing loads, the material was deemed unsuitable for practical applications. This was due to the high elastic modulus that glass possesses, 50 — 90 GPa [52], which significantly reinforces the component that the glass is bonded to. Early coating development was also limited by the lack of appropriate adhesives to bond the coatings to various shaped structures [3]. With the availability of epoxy resins

increasing in the 1950s, the development of practical photoelastic materials began. Epoxy resins allowed for the production of high-strength adhesives which could bond flexible photoelastic sheets onto various materials with different geometries [53]. Ideal properties of photoelastic materials were established early on and are listed below [53, 54].

1. High sensitivity to strains to maximise the number of fringes for a given coating thickness per unit of strain.
2. Low modulus of elasticity to minimise reinforcing effects.
3. High resistance to creep effects that cause relaxation of mechanical stress within the material over time.
4. High bondability to typical engineering materials. This ensures optimal stress and strain transmission from the sample to the coating.
5. Stress-optic coefficient independent of temperature to remove the need to correct for temperature effects.
6. Negligible moisture absorption. Prevents parasitic birefringence in the coating.
7. Good machinability to allow for applications to complex configurations.
8. Conformability to curved surfaces to allow for applications to three-dimensional components.

A list of common photoelastic coating materials with typical properties is shown in table 2.3

Photoelastic Material	Strain-Optic Sensitivity	Elastic Modulus (MPa)	Strain Limit (%)
Polycarbonate	0.16	2200	10
PS - 1*	0.15	2500	5
Glass	**0.14**	**70,000**	**0.1**
PS - 2*	0.13	3100	3
Epoxy-anhydride	0.12	3300	2
Epoxy-amine	0.09	3100	3
PL-1 Liquid*	0.10	2900	3
PS - 3*	0.02	210	30
PS - 4*	0.009	4	>40
Polyurethane	0.008	3	100

*Table 2.3: Table of a number of photoelastic coatings with their typical properties [7,53]. *Highlights commercially available photoelastic coatings, products of Vishay Measurement Group [7].*

Table 2.3 presents a number of photoelastic materials with glass as a comparison. The large majority of these common photoelastic materials are commerical products of Vishay Measurement Group [7] that have been used with minimal development for over 50 years. These materials exist as flat and rigid polycarbonate sheets and contourable plastics at thicknesses between 0.25 — 3.2 mm. The wide range of materials with differing sensitivities and thicknesses requires users to pick an appropriate material for the investigation being performed. For example, PS-1 is highly sensitive and best suited on metals, PS-3 would be used on non-metallics and PS-4 on high-elongation materials such as rubber. The variation on materials prevents reinforcement effects whilst maintaining the highest possible sensitivity. These products also benefit from being supplied with either a reflective backing applied to the coating or with a reflective adhesive, made with fine metallic particles, that provides a dispersive layer that minimises "hot-spots" in the image that occur if using highly reflective surfaces [55]. Additionally, pre-cast sheets benefit by having a uniform thickness to enable accurate calculation of strain using RPSA methods. However, methods for the application of photoelastic sheets onto components follow complicated instructions that require skill and patience [11, 12]. Contourable plastic sheets follow detailed mixing procedures with multiple polymerisation stages that follow "subjective" guidelines which become "apparent with practise." When shaping, issues such as overhanging the material can stretch the coating and unnoticed air pockets between the component and coating can obscure the photoelastic response, resulting in inaccuracies in the strain measurement. Further issues may occur during the adhesion and machining processes. In the former, a two-part reflective adhesive is spread uniformly over the component surface. The coating is placed on top and pushed down into the adhesive. Improper application again can create pockets of air between them resulting in further misrepresentation of the photoelastic response. Machining processes can inadvertently introduce undesirable edge birefringence through the generation of heat build-up producing subsequent residual strains within the coating. Additionally, processes need to be treated with care to prevent any damage through cracking and chipping. Once the coating has been applied, the complete curing time can take upwards of 24 hours before any analysis can take place. Finally, removing these coatings is also not trivial with users having to resort to hammers, chisels and power tools to remove the coating often resulting in assemblies needing to be retreated with any primers or protective coatings.

Other commonly used materials include liquid two-part epoxies such as Devcon 2-ton epoxy [56] for example utilised by Foust *et al* to perform RPSA on a pinned wood joint, further reviewed

in section 2.4.2. This coating is applied directly onto the sample material. The sample maybe pretreated with a silver paint, powder coated or a bare metal surface [57]. These types of coatings require careful mixing through either mixing nozzles or manual approaches. Discussions with the photoelastician Geoff Calvert (formerly VisEng Ltd) described that mixing this particular coating could provide difficult with mixing nozzles providing inadequate combination with bubbles forming relatively easily. Manual mixing with the adhesive heated beyond room temperature was suggested as the best approach. These coatings are applied to a target thickness of 0.3 — 0.5 mm with values of K between 0.5 — 0.12. Another liquid based coating is Stress Photonics' Tintcoat. The photoelastic performance of this coating is not widely available however its key attribute is its ability for thickness corrections. Designed for use with their range of GFP products the Tintcoat coating has a coloured tint that induces differences in the intensity of captured light at different wavelengths. Relationships can then be formed between thickness and intensity changes to correct for thickness. Detailed description of the technique is highlighted in chapter 6. Epoxy coatings have flexibility in their design as their properties can be altered widely through the selection of base resins and hardeners combined with a desired amount of diluent, modifiers and plasticisers. Even changing the curing process changes the photoelastic performance of the material, chapter 4.

2.4.2 Example applications

An early application example using a photoelastic sheet was conducted by Zandman in 1960 [58] performing stress analysis on the aluminium fins of a missile tail structure. The structure had a static load applied that simulated various in flight conditions. The coating material used was not named but stated to have a strain-optic sensitivity of 0.098. Sheets 2.03 mm thick were applied to the structure and a circular polariscope with a microscope device was used to observe the fringe pattern. Isoclinic and isochromatic fringes were measured by direct observation whilst fractional isochromatic fringes were measured using Babinet compensators in conjunction with the microscope. The Babinet compensator can be thought as an adjustable wave-plate allowing for Tardy compensation, a simpler form of phase stepping [59]. Integral and fractional isochromatic fringes were traced onto the coating with a grease pencil and photographed. The accuracy of locating integral and half-order isochromatic fringes was $1/30$ of a fringe and isoclinic fringes were determined to with $\pm 2^o$. The report concluded with suggestions of how to improve the missile structure by reporting that components should be removed, connections with the main body should be reinforced and that even the fins are too rigid.

These suggestions highlight the importance of RPSA techniques to visualise areas of concern early in the design process.

In 1982 Staab and Richard [60] used photoelastic coatings to investigate cog-root strains in V-belts. The RPSA technique was used in conjunction with linear-elastic finite element analysis (FEA) to compare results. The coating used was a PS-4 sheet, 1.016mm (0.040 in.) thick, applied to the vertical side of the cog. The belt was subjected to a series of user defined deformations and data collected using a reflection polariscope collecting isoclinic and fractional isochromatic fringes. Tangential axial strain and shear strain were presented at different belt depths. The report concluded that FEA predictions of tangential strain distributions were shown predict the PSA trends but not the magnitude. The correlation between FEA and RPSA is much worse in the shear strain data set. This report highlights PSA's strengths when comparing to numerical based strain predictions.

A more recent investigation in 2014 by Foust *et al* [8] utilised a two-part epoxy (Devcon 2-ton epoxy [56]) as a photoelastic coating alongside a grey field polariscope. The objective was to analyse and determine the individual full field stresses of a pinned wood joint through using photoelastic data alongside an Airy stress function. The aims of the research were achieved by using the experimentally measured value of principal stress difference as the values of an unknown within the Airy stress function that was used to separate the individual stresses. A similar experiment was achieved by Foust *et al* on an aluminium pinned joint [61]. These investigations demonstrate the capability of the grey field polariscope and its use within research. Moreover it demonstrates the use of a two-part epoxy as a current 'thin' coating. This material is not designed directly for RPSA applications, it is an epoxy commonly found in hardware stores, however it has some beneficial qualities. Firstly, the coating within these investigations was spread to a thickness of 0.33 mm which is within the lower range of thicknesses for commonly used RPSA coatings. This thickness allows for reduced reinforcement effects. The strain-optic coefficient is 0.055 which is a medium sensitivity coating which will work with sensitive devices such as a GFP. Additionally, the epoxy is claimed to cure without shrinkage which would remove the effects of residual stresses in the coating once cured. However, this coating is not optimised for RPSA applications and possesses some large disadvantages. Firstly, the full cure time is 16 hours with a working time of 8 - 12 minutes which limits the application area. Paired with initial sample preparation (e.g. application of a reflective surface) it could take up to two days before data collection. The final viscosity of the mixed epoxy

is 8000 cps, similar to syrup, would make the manoeuvrability of the coating difficult and paired with the short working time the application would require careful consideration if applying to large areas. Finally, the Devcon 2-ton formulation differs between US and UK versions. From discussions with experienced photoelasticians (Geoff Calvert and Stress Photonics), the UK version does not function well as a photoelastic coating and should not be used.

An important comparison for this research are luminescent photoelastic coatings (LPC) developed by Hubner *et al* that are outlined in various articles and within a patent [10, 62, 63]. The LPC technique utilises a luminescent dye as either an underlayer with a photoelastic overcoat (dual-layer coating) or incorporated into the photoelastic coating itself (single-layer coating). The inclusion of the luminescent dye allows the technique to monitor and measure the photoelastic response through the luminescence from the dye rather than capturing the reflection of the initial polarised light. The dye is able to allow this by retaining the initial polarisation state of the illuminating light. The coatings are first irradiated by blue circularly polarised light (centre wavelength 465 nm) that excites the luminescent dye causing redshifted emission within wavelengths between 500 - 700 nm. Imaging devices filter out the excitation light only capturing the emission of the luminescent dye. The advantages of LPC over traditional RPE coatings include a diffused emission field on the surface of complex geometries, thus creating a more uniform spatial measurement; the ability to measure off-axis regions of high incidence angle with respect to the image optical axis; and the separation of excitation light from the LPC's emitted light allows for elimination of specular reflections from the top surface of the coating. There are differences between the choices of coatings. A dual-layer coating is created first by an application of a black primer to provide a uniform backing prevent reflection of the luminescence, then the luminescent undercoat (a polymer binder with a dissolved luminescent dye) and finally the application of the photoelastic overcoat applied in multiple thin layers. The singe-layer coating is created by application of a black primer then application of the photoelastic coating that contains the luminescent dye. The dual-layer coating possesses higher sensitivity whilst the single-layer provides better adhesion; easier preparation and application; improvements in the thickness correction capabilities; and increase in the maximum subfringe strain level due to the distribution of the dye throughout the coating rather than underneath the coating. The LPC shares many attributes of the coating developed in this research. The LPC can be sprayed using conventional apparatus, the materials are UV curable, the optical sensitivity of the LPC is high and has thickness correction capabilities. The ability of the LPC to be sprayed is a major desirable property as it

enables increased ease-of-application over precast sheeting and thick two-part epoxies. It provides evidence to suggest that similar materials, such as those used in this research, would be sprayable. However, the UV curable aspect of the LPC puts into question the feasibility of this research and its contribution to the wider field. Two photoelastic materials were outlined by Hubner *et al*, which were bis-(4-glycidyloxyphenyl) methane (BGM) monomer and bisphenol-A glycerolate diacrylate monomer that both contain similar substructures (a double aromatic ring core) as polycarbonate that results in high performing photoelastic materials. These formulations have been quoted a strain-optic coefficient of 0.1 - 0.12. Further information on the chemical structures are described in chapter 3.1. These monomers are included in a formulation that contains various additives such as chloroform, toluene and thixotropic additives to aid application during spraying. The inclusion of solvents most likely reduces viscosity to enable spray application. However, the combination of these monomers with the choice of solvent produces issues. Firstly, the curing time for these materials and formulation is over 1 hour with a formulation requiring continuous UV light exposure of 1 hour to complete cure. Whilst improving application times, continuous UV exposure for these periods of times would limit application onto large assemblies and structures. There is possibility to improve upon these curing times as outlined by chapter 3.1. Additionally, the inclusion of chloroform and toluene are volatile organic compounds (VOC) that would need to be carefully handled whilst introducing challenges in storage and the curing process. Formulations would require proper storage to prevent significant volume loss over time. The application of the formulation and the initiation of cure would occur in an initial expanded state and as the solvents evaporate a reduction in volume would develop inducing residual strain. There will also be a diffusion gradient to the solvent leaving the top "cured" layer as solvent will first leave from the top downwards. There is also the problem of trapped solvent in this layer, this may make repeat measurements over time problematic, as the layer may undergo long term changes due to solvent leaving over longer periods. However, this could be improved by the application method of applying sequential coats to build up the overall photoelastic coating, however the time for application increases. The thickness of the overcoat ranges between 50 - 500 μm with overall coating thicknesses targetted $\sim$300 μm. The ability to correct for thicknesses differ between the coatings. The dual-layer coating measures the variation of intensity of the luminescent light due to coating thickness. However due to spatial variations of emission intensity differences between emission at 600 nm and 700 nm were observed. By taking a ratio the thickness was mapped and correction however the error induced for thinner coatings

(130 μm) was calculated to be 11 % & demonstrating not complete correction of thickness effects. However, utilising the single-layer coating improves this as the coating is described as being thickness independent once a threshold thickness was achieved, between 200 - 250 μm. This is a result of the penetration depth of the excitation light is being limited by the addition of the dye, at a certain thickness the emitted light then becoming independent of the thickness of the coating. The ability to remove thickness dependency or correct for thickness differences enables further ease-of-use as the coating can simply be applied without the need to achieve uniformity that is challenging with direct application coatings. This property must be achieved by the coating developed in this research to enable accurate strain measurements. Other important factors of this coating provide further scope for improvement. The single-layer coating is quoted to have a practical working range between 2000 - 10000 $\mu\epsilon$ with the dual-layer coating possessing a resolution of 50 - 100$\mu\epsilon$. The practical working range has scope for improvements at lower applied strains for the single-layer coatings. The resolution provides a target for the developed coating to achieve. The overall timescale for coating application and data collection was outlined as being between two - three days. This does not consider any removal procedures that could provide challenges depending on the overall adhesion properties of the coating. The major limiting factor of LPC is the requirement for RPSA to be performed in a darkened environment to avoid disruption in the capture luminescence. This has real limitations within a large range of scenarios as certain environments would be challenging to combat ambient light. For example, large structures and or assemblies in well lit hangers and/or in-situ testing outdoors or brightly lit spaces.

2.4.3 Airbus

Airbus makes use of PhotoStress photoelastic sheets and liquid plastic as their photoelastic coatings, section 2.4.1. Flat sheets would be selected for coating a flat surface whilst a liquid plastic allows for the coating to be moulded to a particular shape. Bonding both types is a multi-step process requiring time, up to two days for one component, and skilled operatives. Detailed instructions for bonding flat and contoured sheets can be found in Vishay Precision Group's application notes B-221 and B-223 [11, 12]. These materials and bonding procedures will be used, within this research, to understand further why an updated material and procedure would benefit industry. These materials can then be used during the same tests as the bespoke new coatings to provide benchmark measurements on important properties. These benchmark properties can then be used as a comparison for the

potential new coatings that aim to be quicker, easier and more insightful than what is currently used.

2.5 Mechanoluminescence

Mechanoluminescence (ML) is a phenomenon where spontaneous emission of light, luminescence, is observed when a material undergoes a mechanical action. An early example of ML was noted by Francis Bacon in 1605 [64] where lumps of sugar would emit light when scraped. ML can be described in several different ways depending on the excitation process of the material. Common processes include pulling, rubbing and crushing but ML can also be triggered through thermal shocks, light induced shock waves from powerful laser pulses and acoustic cavitation by irradiating crystal slurries with ultrasound [65,66]. These physical processes cause ML to fall under two categories, deformation mechanoluminescence (DML) and tribomechanoluminescence (TML). The former depends only on the material that is being deformed and not on the material used to cause the deformation. The latter depends on the nature of the material under deformation and the material used to create it [65]. For example, Bacon's observation of rubbing sugar falls under DML whilst TML depends on the contact between two dissimilar materials that produces such contact phenomena as triboelectrification and tribochemical reactions that generates ML. ML is of interest within this research, as it can be used to visualise stress distributions as the intensity of emitted light is linked to the intensity of a component's stress field [67]. An important aim of this research is to use ML in conjunction with photoelasticity to increase the technique's insightfulness.

Luminescence is referred to as 'cold light' as the production, emission, of light occurs with little to no heat. When electrons are subjected to an energy source, they can be promoted from their lowest energy ground state to a higher excited state. By transitioning back from an excited state to a lower state there is a release in energy in the form of a photon. This is the basis of luminescence. Explanations for why ML occurs depends on the type being investigated. DML can be divided into three types: fracto-ML, plastico-ML and elastico-ML [65, 68]. These mechanisms produce light through the fracture, plastic deformation and elastic deformation of solids respectively.

As photoelasticity operates within the elastic region of the coating and component elastico-ML (EML) will only be considered.

2.5.1 Materials

Literature states that 50% of all inorganic salts and organic molecular solids exhibit fracto-ML whereas only a few demonstrate plastico-ML or elastico-ML [69,70]. A report by Feng and Smet [67] has tabulated a large quantity of inorganic solids that present a form of ML. Although if focusing on EML, materials that demonstrate the greatest intensity, when subjected to stress, are rare-earth ion doped alkaline aluminates and silicates [70–80], and doped zinc sulphide crystals [68, 69, 77, 81–83]. The former is used in this research and shall be the focus of this section.

2.5.2 Mechanoluminescence in tridymite structures

The classification of the structure of rare-earth ion doped alkaline aluminates and silicates are tridymite structures - a high temperature polymorph of silica. Within this research the materials are strontium aluminates doped with rare earth metals such as europium and dysprosium. The exact origins of the ML phenomenon is not completely understood and there exists various proposed mechanisms and models [84]. However, the process mainly involves the release of trapped carriers at defects due to application of a load.

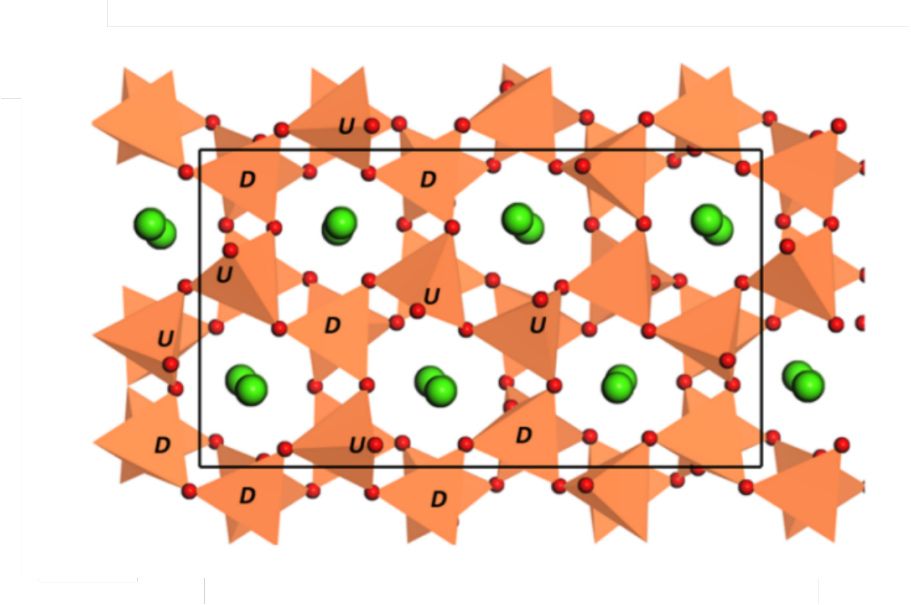


Figure 2.22: The crystal structure of the tridymite $SrAl_2O_4$ along [010]. The black outline represents the unit cell and the direction of the tetrahedra are marked as U(up) and D(down). Red represents O^{2-} and green Sr^{2+} [84].

Figure 2.22 illustrates the ring-like structure, or stuffed tridymite structure, of the type of materials

used in this research. The structure contains rings with corner sharing AlO_4 tetrahedra in which Sr^{2+} ions fill the large cavities. Sr^{2+} ions can occupy two non-equivalent sites with nine adjacent oxygen ions. When doped with europium and/or dysprosium the ML intensity is high and has resulted in these materials being widely researched for ML applications. As mentioned, it is widely accepted that ML is caused by transitions of trapped carriers at traps within the crystal structure. The band gap energy between valance and conduction bands for $SrAl_2O_4$ is 6.5 eV [73]. By introducing dopants, such as europium, energy levels then exist within the band gap effectively reducing the energy needed for electrons to transition into the conduction band. Exciting the europium through the emission of UV light or thermal activation, electrons are excited into the conduction band of the crystal. The electrons are then trapped within energy levels that are close to the conduction band caused by oxygen vacancies. There are various mechanisms that describe the detrapping process of these carriers and are discussed in great detail in a review by Feng [84]. A report by Chandra *et al* [72] summarises the elastic ML process of $SrAl_2O_4$:Eu as a piezoelectric effect. Under the influence of a mechanical load, a piezoelectrric field is produced and is high close to dopant ions due to the change in the local structure. This production of this local piezoelectric field may reduce the trap-depth (trap to conduction band) or cause band bending. These processes make it easier for the trapped carriers to move back into the conduction band. As a result, the carriers become captured by an excited state of the dopant ions in another energy level close to the conduction band thus exciting the ion. The de-excitation of the dopant ion gives rise to light illumination. This mechanism can by visualised in figure 2.23.

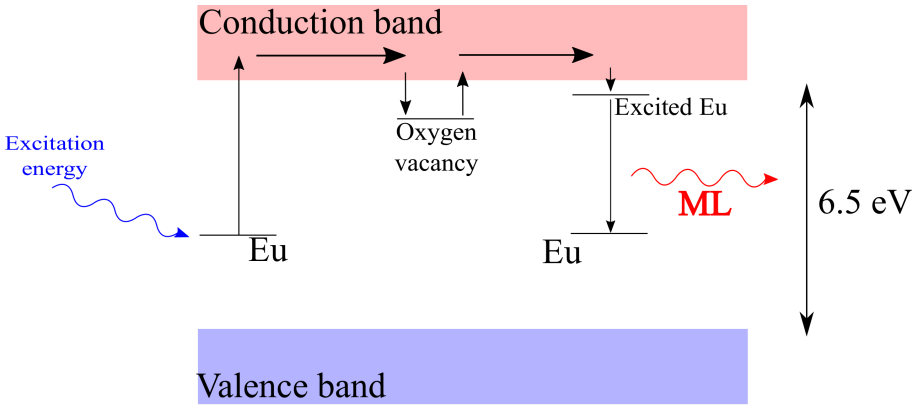


Figure 2.23: The elastico-mechanoluminescent (EML) process shown in an energy level diagram of $SrAl_2O_4$:Eu. The electrons within the Eu dopant ions are excited into the conduction band which are then trapped by the oxygen vacancies. The application of a mechanical load detraps the carriers back into the conduction band and into the excited state of the dopant. The de-excitation process then emits the observed ML light.

2.6 Visualising and interpreting stress distributions

An important topic of this research is the combination of photoelasticity with ML. Photoelasticity is a well understood technique that provides the user with information on the principal stress and/or strain difference. The research aims to demonstrate that a photoelastic coating could be made more insightful by introducing an ML material that would provide new stress and strain data. It is therefore important to understand what the production of ML light represents. The majority of ML research refers to stress when comparing to ML. This section stays consistent with the research highlighted in this section.

Initial observations performed at Airbus were conducted prior to the research start. These observations stated that the light could represent a principal stress sum as the light distribution looked similar to those captured during thermoelastic stress analysis. However, a detailed literature review does not support this initial theory. Research conducted by Jongchansitto *et al* [85] performed compression tests on epoxy cylinders with $SrAl_2O_4$:(Eu^2,Dy^{3+}) mixed into the epoxy at a 19:1 epoxy-to-powder ratio. The captured ML light distribution was compared against various FEA models demonstrating different stress relationships, figure 2.24.

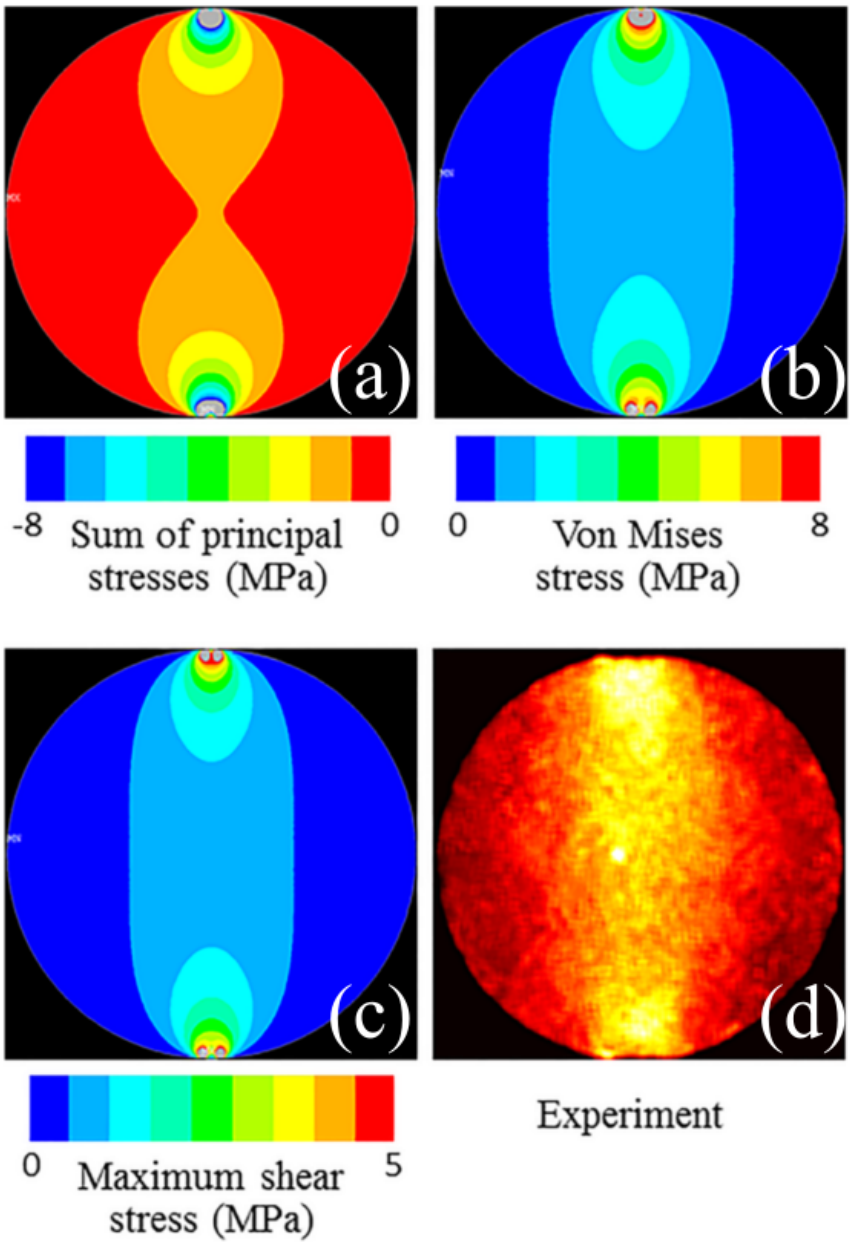


Figure 2.24: Comparisons of finite element analysis models of various stress distribution with experimentally recorded mechanoluminescent light distribution shown in a pseudo colour [85].

Figure 2.24 demonstrates distinct differences from an expected principal stresses sum, figure 2.24)(a), and ML light distribution , figure 2.24)(d). The research demonstrated that the light matched closely to that of either the Von Mises stress or maximum shear stress (equivalent to principal strain difference). The former has been used to interpret the ML light in various articles [67, 74, 79, 80, 86]. Wang et al [74] compared the light distribution of a disk sample under compressive load to the FEA. The disk sample featured an ML film of 1mm thickness made of a $SrAl_2O_4$:Eu epoxy mixture

bonded to a separate epoxy disk 25mm in diameter and 3mm thick. The intensity of emitted light was captured using a CCD camera at an applied load of 10N. The report discussed that the visual light distribution of the disk was similar to both strain energy distribution and Von Mises equivalent stress distribution simulations. Strain energy density, e_{strain}, can be expressed as follows

$$e_{strain} = \frac{1}{2E}[\sigma_1^2 + \sigma_2^2 + \sigma_3^2 - 2v(\sigma_1^2\sigma_2^2 + \sigma_2^2\sigma_3^2 + \sigma_3^2\sigma_1^2)] \tag{2.43}$$

where σ_n is one of three principal stresses, E Young's modulus and ν the Poisson's ratio of the material. This equation can be expressed as the sum of the distortion energy density, $e_{distortion}$, and volume change energy density, e_{volume},

$$\begin{aligned} e_{strain} &= e_{volume} + e_{distortion} \\ e_{distortion} &= \frac{1+\mu}{6E}[(\sigma_1 - \sigma_2)^2 + (\sigma_2 - \sigma_3)^2 + (\sigma_3 - \sigma_1^2)] \\ e_{volume} &= \frac{1-2\mu}{6E}(\sigma_1 + \sigma_2 + \sigma_3)^2 \\ where\ \mu &= \frac{E}{2(1+v)} \end{aligned} \tag{2.44}$$

The report states that a relationship between the distortion energy density equation and the Von Mises equivalent stress, σ_s, equation can be made. The Von Mises equivalent stress is used to evaluate the yielding stress of isotropic materials and can be expressed as follows

$$\sigma_s = \sqrt{\frac{1}{2}[(\sigma_1 - \sigma_2)^2 + (\sigma_2 - \sigma_3)^2 + (\sigma_3 - \sigma_1^2)]} \tag{2.45}$$

Equation 2.45 is proportional to the square root of the distortion energy density and with this connection, the report states the Von Mises equivalent stress can be used to analyse ML light intensity distributions. Kanamaru and Utsunomiya [80] further reported a linear relationship between experimental ML intensity and computational Von Mises stress. Kanamaru and Utsunomiya performed ML investigations by screen-printing a 5 μm film onto 1 mm aluminium alloy dogbone specimens. The ML light intensity was recorded as the sheet underwent ductile fracture using an industrial camera (model name not stated). The significance of this study demonstrates that thin coatings with ML materials are able to produce observable light that was recorded using relatively simple

full field imaging devices. As a result, the research documented in this thesis can focus on simple camera setups rather than photon counters or photomultiplier tubes.

A report by Li *et al* [71] investigated the application of a $SrAl_2O_4$:Eu (SAOE) film on an aluminium sample (225 x 35 x 3mm). This report further demonstrates ML in practice as a coating onto a sample surface. The film consisted of an SAOE paste, co-doped with Ho to enhance the ML intensity, which was adhered to the metal sample. The thickness of this coating was not defined. Under tensile and compressive loads, inflicting stresses between 40-170MPa, the ML intensity was linearly proportional to the applied stress. This data set was then be used as a calibration curve to relate ML intensity to stress. In order to demonstrate how ML visualised stress distributions within a metal sample, a 10mm diameter hole was bored into the centre of the aluminium specimen with the film surrounding it. The sample was then placed into a tensile loading machine which applied an uniaxial load along the length of the sample. The load applied was a triangular wave up to 5kN at a rate of $5kNs^{-1}$. A high speed camera was set at 250 fps to capture the emitted light. FEA was used as a comparison for the ML light distribution. The FEA model simulated a quarter of the axial symmetry of the specimen. By utilising the calibration curve, the ML image was corrected and displayed in pseudo-colour where the ML intensity is transformed into stress.

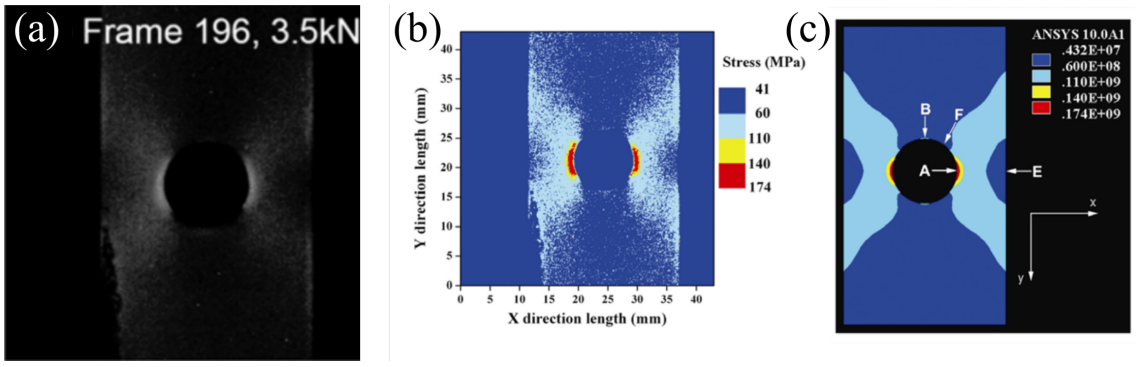


Figure 2.25: ***(a)*** *The measured light distribution at a tensile load of 3.5kN.* ***(b)*** *The same light distribution image as (a) but transformed to illustrate stress according to the calibration curve.* ***(c)*** *FEM model of the same setup demonstrating that it is in agreement with image (b) [71].*

Figure 2.25b demonstrates this corrected image and can be directly compared to the FEA model, figure 2.25c. The FEA model is stated to be in complete agreement with the corrected image. However, there are various issues with this report. Firstly, the thickness of film was not directly mentioned. A thickness dependency on the ML intensity has been demonstrated recently by Chen *et al* [87] where intensity increased up to an upper limit of 240 μm before decreasing. The captured

decrease in intensity was attributed to an attenuation effect as a result of coating thickness preventing light emission from deeper within the coating. Furthermore, it is not stated what the FEA model represents. Regardless of these issues, it is shown that ML light was recorded using high speed cameras which would be limited in exposure. This provides confidence that a simple camera setup can be used without issues such as exposure being a limitation in the capture of ML light. Furthermore, the investigation demonstrated an observable ML light distribution with the elastic limit of the sample. Finally, paired with the article by Kanamaru and Utsunomiya, a thin film (50 - 100 μm) containing ML particles is enough to generate sufficient light.

By establishing an understanding of ML light distributions and its relationship to stress, combining with photoelasticity would allow a user to potentially have two techniques that could be used to assist in the validation of any structural health monitoring test. Conducting photoelasticity and mechanoluminescence simultaneously has yet to be researched and provides a novel concept dual-technique coating for full field strain imaging. However, its practicality will need to be investigated within this research.

2.7 Conclusions

This chapter has reviewed the relevant theory and provided examples of currently used coatings for reflection photoelastic strain analysis. Within this review there exists the potential to produce a photoelastic coating that improves application performance whilst maintaining sensitivity utilising well developed and commercial imaging devices.

The crucial property that is omitted from all the outlined photoelastic coatings are application and data collection efficiency. Current commercially available photoelastic coatings dissuade users due to their overall difficulty to apply and remove. The long and complicated application procedures of precast sheets are improved by direct application coatings however the curing time remain high taking over an hour to perform with certain coatings requiring direct UV irradiation for one hour. LPC [10, 62, 63] provide unique detection methods that enable increased ease-of-use (sprayable, thickness independent and thickness correction) however the curing time remains high with problematic formulation qualities with an overall timescale of two - three days. Furthermore, the LPC can only be performed in low light environments that limits it use within industry. Through

consideration of available materials that possess fast curing with high photoelastic sensitivity it is proposed, in this research, that the overall timescale for application, data collection and analysis, and removal could be reduced to a single day.

Furthermore, reflection photoelasticity has scope for combination with additional imaging techniques in order to provide further detail. Introducing mechanoluminescence materials to a photoelastic coating is a novel concept that can provide validating data to support captured photoelastic responses. The novelty of combining these two techniques will be simultaneous capture that promotes further ease-of-use and increased efficiency.

Chapter 3

Coating development

This chapter reviews the theory of UV curing mechanisms and introduces the UV curable materials used in this research. The UV curable materials are presented with their chemical structure with their properties outlined. A summary of preliminary research will be discussed that utilised these materials and demonstrated potential in their photoelastic performance. The preliminary research was then expanded upon through conducting formulation screening investigations that reviewed optical, physical and chemical properties of the materials used in this research. Upon establishing between properties and material selection, rational coating optimisation was performed through statisical design packaging, Design of Experiments, to attempt to formulate the optimal coating material. Finally, the coating went through intial calibration experiments to determine the strain-optic ceofficient of the proposed optimal formulation.

3.1 UV curable resins and preliminary research

This research makes uses of various liquid UV curable resins to create a variety of different formulations, to be used as coatings, which can be applied and cured in a matter of minutes. Two types of cationic resins are used separately or combined to produce various formulations of differing properties. The types of resins used include cycloaliphatic epoxy and oxetane resins. The former creates cured coatings with high adhesive, low shrinkage and chemical resistance whilst the latter provide benefits such as increased speed of cure, viscosity control and hardness. Coating properties can be changed by blending these epoxies and oxetanes together.

An epoxy resin is defined as a molecule which contains more than one epoxide group, a three-membered

ring consisting of one oxygen atom and two carbon atoms. A cycloaliphatic epoxide is described as having an epoxide group that is appended to an aliphatic ring structure, a non-aromatic organic compound of only single bonds, figure 3.1. This is unlike other epoxies which are independent of ring structures that make up their chemical structure.

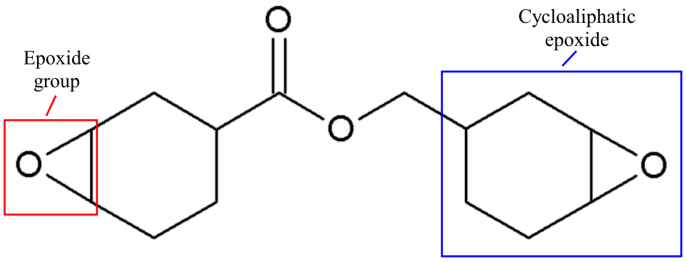


Figure 3.1: Chemical Structure of Lambson's UviCure S105 [88] a cycloaliphatic epoxide resin. The cycloaliphatic epoxide can be seen at either end of the structure.

The structure of a cycloaliphatic resin provides low viscosity allowing for application onto difficult surfaces, good exterior weatherability, heat resistance and high potential T_g materials [89, 90].

An oxetane's structure, figure 3.2, is closely related to that of an epoxide but is made up of a four-membered ring with three carbons and one oxygen [91].

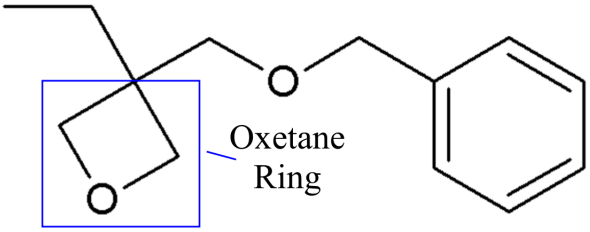


Figure 3.2: Chemical Structure of Lambson's UviCure S140 [92] an oxetane resin. The four-membered ring structure of the oxetane is highlighted. A benzene ring structure can be observed at the far right of the structure.

Oxetane resin chemical structures often feature certain structures, such as benzene rings to increase stiffness and refractive index and can be monofunctional which reduces crosslinking density in order to increase flexibility of a formulation.

Both epoxy and oxetane resins cure through photoinitiated cationic polymerisation with the aid of a liquid onium cationic photoinitiator added to each formulation. This photoinitiator acts as a

catalyst for the curing process to a produce a chemical reaction in which the liquid formulation turns into a hard insoluble crosslinked polymer network. These types of photoinitiators feature two key elements in their chemical structure, known as moieties, which are the cation and anion portion of the compound. The cation portion describes the UV absorbing characteristic of the photoinitiator. It describes if the photoinitiator can be photosensitised, the quantum yield of the photoinitiator and the thermal stability which has a direct relationship to the latency of polymerisation. The anion moiety describes the strength of Brønsted acid formed during photolysis, the separation of molecules by the action of light, which initiates and determines the rate of polymerisation [93]. These moieties are presented in figure 3.3.

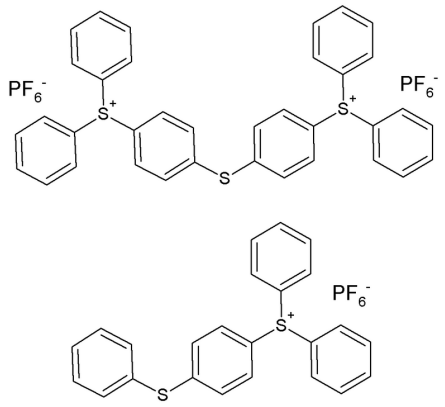


Figure 3.3: Chemical Structure of Lambson's SpeedCure 992 [94] a sulfonium hexafluorophosphate cationic photoinitiator. The cation sulphur atom is surrounded by benzene ring structures with the hexafluorophosphate, PF_6^6, anion moiety.

The curing process commences by illuminating the liquid formulation with UV light. UV light is chosen because the peak quantum yield, or photosensitivity, of onuim salt photoinitiators is usually a wavelength between 230 - 300nm. Cationic polymerisation for epoxide and oxetane monomers follows the same mechanism. The onium salt absorbs the UV light producing an excited singlet state. This then causes cleavage of the bond between, in the case of figure 3.3, carbon, of the ring structure, and the sulphur which produces an aryl cation. A hydrogen donor, from the resin/s used in the formulation, causes the aryl cation to produce a proton which, when coupled to the PF_6^6 anion, produces a Brønsted acid. This acid then catalyses a chain-growth polymerisation known as cationic ring opening polymerisation. This forms the crosslinked polymer network [91, 95].

The benefit of using UV curable resins with the assistance of cationic photoinitiators, compared to thermoset resins, is to produce rapid, energy efficient, low cost chemical reactions with epoxides

and oxetanes without the use of solvents [96]. These benefits also demonstrate improvements upon the materials used within the luminescent photoelastic coatings (LPC) [10, 62, 63]. The materials used in this research are fully solid and emit no VOC, unlike the additives within the formulations that create LPCs. As a result, the cationic resins will be the sole contributor to the crosslinked polymer network that results in less shrinkage and increased adhesion. Furthermore, cycloaliphatic epoxy groups are characterised by greater ring strain compared to aliphatic oxetanes (used in LPCs) that contributes to accelerated cationic ring-opening polymerisation, thus much faster curing times. These cationic resins will cure in a matter of seconds rather than hours.

3.1.1 UV curable resins

This section presents all the materials utilised in this research and preliminary experiments. Material properties will be outlined per resin and photoinitator to provide insight into why they might be used to form a photoelastic coating.

- **S105** – A difunctional cycloaliphatic epoxide resin which which will give a high crosslink density resulting in high hardness and T_g.

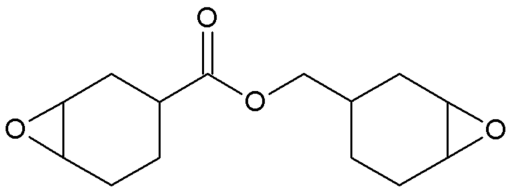


Figure 3.4: Chemical Structure of the epoxide resin UviCure S105 [88].

- **S128** – An adipate based difunctional cycloaliphatic epoxide with increased flexibility compared to S105 due to the adipate spacer between cycloaliphatic epoxide groups. This will give a lower crosslink density than S105.

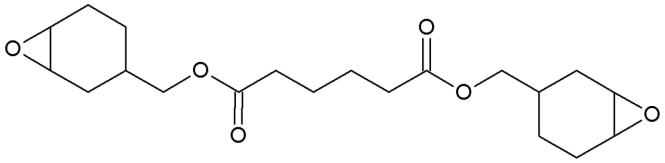


Figure 3.5: Chemical Structure of the epoxide resin UviCure S128 [97].

- **S160** – A difunctional aromatic oxetane. The rigid aromatic core (the two benzene ring structures) will give increased stiffness to the coating and the high refractive index aromatic segment will increase the sensitivity of the photoelasticity measurements. This double aromatic ring structure is present in polycarbonate and LPCs that are representsive of high performing photoelastic coatings.

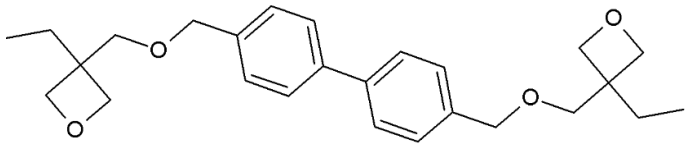


Figure 3.6: Chemical Structure of the oxetane resin UviCure S160 [98].

- **S150** – Another aromatic difunctional oxetane.

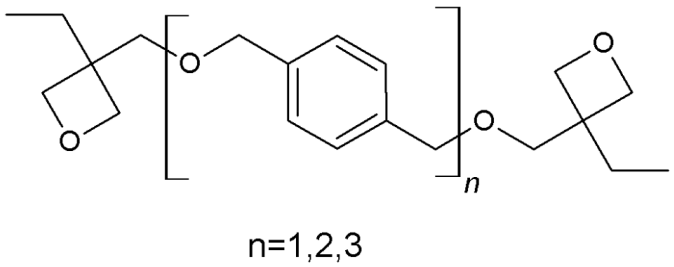


Figure 3.7: Chemical Structure of the oxetane resin UviCure S150 [99].

- **S140** – A low viscosity monofunctional oxetane that will reduce crosslink density of the coatings increasing flexibility and reducing T_g.

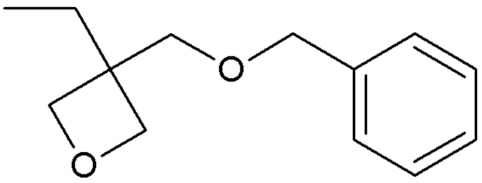


Figure 3.8: Chemical Structure of the oxetane resin UviCure S140 [92].

- **S130** – A hydroxy functional mono oxetane. Hydroxy groups can increase reaction rate via chain transfer. The monofunctional oxetane will reduce crosslink density reducing T_g therefore increasing flexibility.

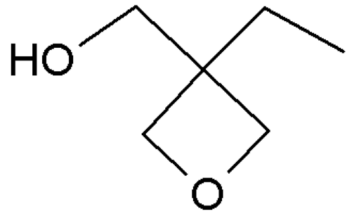


Figure 3.9: Chemical Structure of the oxetane resin UviCure S130 [100].

- **976** - a 50% active liquid cationic photoinitiator of the sulfonium hexafluoroantimonate family, with absorption maxia at 279 and 291 nm. It provides high reactivity in cationic systems when used at 0.5-5 wt% in UV formulations.

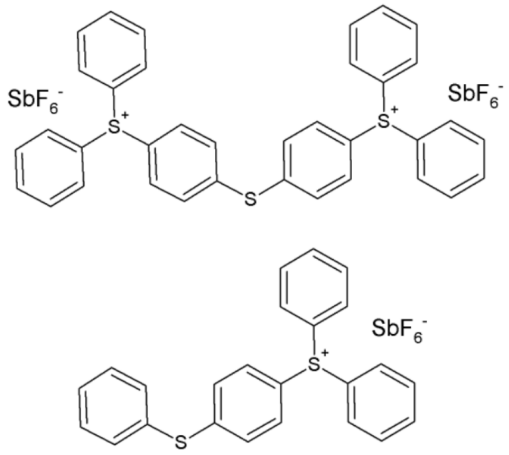


Figure 3.10: Chemical Structure of the photoinitiator SpeedCure 976 [101].

- **992** - A 40% active liquid cationic photoinitiator of the sulfonium hexafluorophosphate family. When used with cationic systems, at 0.5 - 5 weight%, it provides high reactivity during UV curing with a quantum yield peak at 230nm. This photoinitiator is not as efficient as 976 and more cost effective.

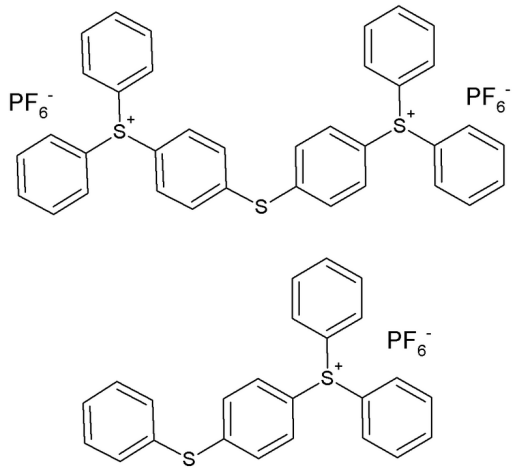


Figure 3.11: Chemical Structure of the photoinitiator SpeedCure 992 [94].

3.1.2 Preliminary research

Preliminary research into the use of these UV curable materials was first conducted by Geoff Calvert, of VisEng Ltd, in 2017 and Warwick Manufacturing Group (WMG) in 2018. Both reports have not been published and not widely available so a summary will be conducted with permission granted by Geoff Calvert. This research follows on from their findings. Calvert investigated the photoelastic capabilities of various materials including two-part epoxies, vinyl wraps, PVA water based materials and UV curable resins. The report concluded with no instant solution to replace existing RPSA materials but that UV curable resins had potential and should be investigated further. WMG continued this research by measuring the photoelastic properties of various films, epoxies and UV curable resins. WMG's findings demonstrated the potential of UV curable resins by comparing their birefringence and response to applied loads to existing and used photoelastic materials, PS-1D (PS-1 at a thickness of 0.5 mm) and Devcon 2-ton epoxy. WMG explored 11 different coating formulations, designed by Arkema UK, using different cationic resins which were all products of Arkema UK [102] as highlighted in section 3.1.1. These formulations are presented in table 3.1.

Formulation	S105 (wt.%)	S128 (wt.%)	S160 (wt.%)	S140 (wt.%)	S130 (wt.%)	976 (wt.%)
F1	88				10	2
F2		88			10	2
F3			88		10	2
F4			88	10		2
F6	10			88		2
F7	10		88			2
F8	20		78			2
F9	30		68			2
F10		30	68			2
F11			68	30		2
F12			68		30	2

Table 3.1: The table of formulations created for previous experiments. There are five resins, S105, S128, S160, S130 & S140, and one photoinitiator, 976 [88, 92, 97–101]. Different combinations of resin with 2% photoinitiator make up the 11 formulations.

The rationale for the determination of weight percentages were based on Arkema's expertise. For example, the resins S105, S128 and S160 function well at high weight percentages (> 60 %) whilst the diluents S140 and S130 can drastically alter certain properties, such as viscosity, at lower percentages (≤ 30 %). Photoinitiator content at 2 % provides sufficient reactivity. Experimental procedures were reproduced and are outlined in greater detail in section 3.2.3. In summary all formulations were applied as $\sim$100 μm thick coatings to an aluminium beam (300 x 25 x 6) mm. The coating were applied as (70 x 25) mm strips applied 50 mm away from one end of the coating. The beams were cured by passing the coating under a 850 W mercury bulb five times at as belt speed of 10 m min^{-1} then placing in an oven for 40 hours at 50 ^{o}C. The baking stage is not a necessary part of the curing process however it guarantees that the coating has become fully cured. The beam was then subjected to cantilever loads by fixing the end closest to the coating and keeping the opposite free with a micrometer able to push down onto the beam producing a cantilever load. The beams were subjected to sequential static loading with a GFP1600 measured the induced retardation with the residual retardation accounted for in the post-processing. The conclusions that are of interest to this research were the captured photoelastic responses of the formulations using the GFP1600. It confirmed that these materials possess a suitable photoelastic response at relatively low thicknesses. Additionally, it demonstrated that S160 majority formulations were the highest performers as proposed. However, the research was conducted with uncertainties

within the methodology and production of results. Firstly, the calculated sensitivities were suspect in their determination. Quoted values between Devcon 2-ton epoxy and PS-1 placed Devcon higher which based on strain-optic coefficient comparisons between Devcon 2-ton epoxy, Foust [8], and published values for PhotoStress coatings, [7], put PS-1 at almost three times higher. Additionally the measurement of the coating's thickness was not made clear. Finally, the PS-1D sheets were applied with generic superglue rather than the manufacturers recommended adhesive. This work will be repeated within preliminary investigations, section 3.2, to provide further confidence on WMG's analysis.

3.2 Formulation screening

This research followed on from WMG's research by conducting a more in-depth investigation with a larger range of coating formulations. A larger sample set was created in order to establish a greater understanding of the resin's effect on various optical, physical and chemical properties. In total, 27 formulations were created based on WMG's findings. These formulations were made by combining various quantities of cationic resins with a photoinitiator, all products of Arkema UK. The formulations were then applied and cured onto aluminium beams, steel Q-panels and strips. These samples were then placed through a number of experiments to determine various properties of interest. The properties measured were:

- Birefringence (photoelastic sensitivity)
- Viscosity
- Solvent resistance
- Adhesion
- Flexibility
- Glass transition temperature (T_g)

By investigating these properties the resins that contribute to desirable outcomes will be used to create an optimised formulation through rational formulation design. The aim was to measure how resin changes influence these properties to determine overall usability, for example application, appearance and removability. The property of most importance was photoelasticity with detailed

methodology, results and analysis featuring in this section. A summary of all remaining properties will be provided in this section with detailed methodologies and results provided in appendix A. Experiments to determine these properties were conducted at the University of Sheffield and at Arkema UK by the author. Results were compared against benchmark measurements calculated from testing an existing commercial coating material, PS-1E, used at Airbus for their RPSA testing.

3.2.1 Formulations

The majority of formulations created for this research features the resin S160 based on WMG's findings that this was the most optically sensitive resin. The formulations used in this research are highlighted in table 3.2.

Formulation Reference	S105 (wt.%)	S128 (wt.%)	S160 (wt.%)	S150 (wt.%)	S140 (wt.%)	S130 (wt.%)	992 (wt.%)	Group Reference
Structure	NA	NA	CA	CA	NCA	NCNA	n/a	n/a
WF1			98				2	**a**
WF2				98			2	
WF3		98					2	
WF4	98						2	
WF5	88					10	2	**b**
WF6	68					30	2	
WF7	48					50	2	
WF8	88				10		2	**c**
WF9	68				30		2	
WF10	48				50		2	
WF11	88		10				2	**d**
WF12	68		30				2	
WF13	48		50				2	
WF14	28		70				2	
WF15	8		90				2	
WF16			88		10		2	**e**
WF17			68		30		2	
WF18			48		50		2	
WF19			88		5	5	2	**f**
WF20			68		15	15	2	
WF21			48		25	25	2	
WF22	48		40		10		2	**g**
WF23	28		60		10		2	
WF24	8		80		10		2	
WF25	48		40			10	2	**h**
WF26	28		60			10	2	
WF27	8		80			10	2	

Table 3.2: NA = Non-aromatic, CA = Connected and aromatic, NCA = Not connected but aromatic, NCNA = Not connected and not aromatic. The table outlines the formulations created for the research. There are six resins, S105, S128, S150, S160, S130 & S140, and one photoinitiator, 992 [88, 92, 94, 97–100]. Different combinations of resin with 2% photoinitiator make up the 27 formulations. The table is spilt into eight groups, within each group the formulations are related with each other.

Table 3.2 presents 27 formulations, each with a reference WF#, which are made from six different cationic resins (S105, S128, S150, S160, S130 & S140) and one photoinitiator (992) [88,92,94,97–100]. These resins feature in WMG's formulation set, apart from S150 and the photoinitiator 992. Quantity rationale followed the same as within WMG's investigations following Arkema's advice.

The replacement photoinitiator 992 is more cost effective but not as efficient in the curing process as the 976, however for initial testing it will suffice. In the future this component can be changed in order to increase curing speed if required. Table 3.2 also splits the formulations into eight groups. Within a group the formulations are related to one another by the resins they are comprised of. Data is displayed within these groups with individual component formulations, group a, included where necessary.

In order to better decribe the selection of each group, table 3.3 provides a description of the properties each formulation group possesses.

Group reference	Group properties
a	Group a features formulations with a single resin to act as a reference for other groups. For example WF4 can be compared within group b to determine the effects of additional materials on S105.
b	Group b combines S105 with the diluent S130. The addition of S130 will act to reduce the hardness of S105 introducing increased flexibility to the formulations.
c	Group c combines S105 with the diluent S140. Similar to the addition of S130, S140 with act to reduce the hardness of S105 introducing increased flexibility to the formulation. The Benzene ring structure of S140 could impact the refractive index of the formulation thus affecting photoelastic sensitivity.
d	Group D combines S105 with S160. Introducing S105 to S160 will increase the flexibility of the rigid structure of S160. The connected aromatic core of S160 will provide stiffness whilst introducing high sensitivity to the photoelastic measurements.
e	Group e combines S160 with the diluent S140. S140 will drastically reduce the viscosity of the formulation increasing flexibility and reducing T_g & hardness. The diluent will enable better hand-ability of the formulation. The effects of S140's benzene ring structure will be monitored during photoelastic measurements.
f	Group f combines S160 with the diluents S140 and S130. The addition of the diluents will drastically reduce the viscosity of the formulation ncreasing flexibility and reducing T_g & hardness. The diluents will enable better hand-ability of the formulation. The addition of S130 will increase reaction rate to enable fast cure times.
g	Group g combines differing amounts of S105 and S160 with 10 wt% of the diluent S140. S140 will dilute the formulation to control viscosity whilst S105 will increase flexibility and S160 will control the photoelastic sensitivity.
h	Group h combines differing amounts of S105 and S160 with 10 wt% of the diluent S130. S130 will dilute the formulation to control viscosity whilst S105 will increase flexibility and S160 will control the photoelastic sensitivity. S130 promotes increased reaction rate.

Table 3.3: A table to describe the properties each formulation group possesses that result from the materials featured in each group.

3.2.2 Coating applications

3.2.2.1 Methodology - UV curable materials

The procedures used to apply and cure the UV curable materials were provided by operators at Arkema UK.

Formulations were created by selecting a desired final volume, e.g. 100 g, and introducing each resin as a weight percentage (wt. %) as described in table 3.2. By using an accurate top pan balance,

resolution 10^{-5}g, each resin was carefully weighed into a single container. The liquid resins were added individually using a 5mL pipette to reduce the chance of spoiling the formulation by adding excess resin. The completed formulation was then stirred continuously for a minimum of ten minutes using a heated (50 ^oC) magnetic stirrer set at 200 rpm. The more viscous resins, S150 and S160, required heat, 40 - 50 ^{o}C, to allow the stirrer to effectively mix the formulation by reducing their viscosity.

Each formulation was applied to three aluminium flat beams, five steel Q-panels and six steel strips. The aluminium beams were RS component's 6082 - T6 aluminium flat beams which were cut to (300 x 25 x 6) mm. The Q-panels were Q-Labs Type QD-46 (102 x 152 x 0.81) mm smooth finish panels [103]. These panels were also used to produce the steel strips at dimensions of (20 x 152 x 0.81) mm. Before application onto the surface of each sample, acetone was used to clean the curing area. This was a important step as any dust, oil or water would cause the wet formulation to separate and cause large holes to appear. Using a pipette, a small quantity of formulation, less than 5 mL for the panels and less than 1 mL for the strips and beams, was applied at one end of the coating area. For the panels and strips, the entire area was covered whilst the aluminium beams only required a (100 x 25) mm strip at one end of the beam. The liquid coatings were spread using a K-bar which is a manual applicator that features a close-wound wire across a metal rod. Using a number 5 K-bar [104] the formulation was spread across the coating area leaving an approximate 50 μm thick wet coating.

The samples were then cured, at Arkema UK, by passing through either a Dymax UVC - 5 UV conveyor curing system [105], for all strips and panels, or a Jenton UV JA2000 VPXI UV conveyor curing system [106], for aluminium beams. Both systems operate in the same way by directing UV light perpendicular to the conveyor belt. The Jenton replaced the Dymax system late 2019 as an upgrade. The Jenton system benefits by having a friendlier user interface with the possibility to alter the intensity of the UV light source. Both curers utilised 850 W mercury bulbs to produce UV-C light with high relative intensities between 200 — 300 nm. The bulb within the Jenton curer was set to a 30 % intensity, no data available, to provide a cure that matched the Dymax. If set too high, the top surface of the coating cures much faster than that underneath forming a 'skin' which would move freely from the uncured formulation underneath. Each system's conveyor operated at 10 m min^{-1} and samples were passed under the UV light 10 — 15 times to achieve a hard-to-the-touch

coating. The sample's curing performance was initially tested using a firm thumb twist to gauge roughly the degree of cure. All samples were then placed in a dark oven overnight, at 50 - 60^{o}C, to ensure the coating reached maximum cure conversion. The appearance of each sample was recorded as well as any difficulties in curing the sample.

3.2.2.2 Results and analysis - UV curable materials

Curing occurred in two separate multi-day sessions. Firstly the panels and strips were coated and cured in July 2019 using the Dymax UV conveyor system and the aluminium beams were coated later in January and March 2020 with the Jenton apparatus. The laboratory was temperature controlled however the effects of ambient temperature would have had little influence on the resultant cured coating due to the temperatures within the curer and the oven where samples were kept to complete their cure.

The majority of all panels and strips, immediately after curing, produced a clear, hard and glossy coating. However, there were a number of issues that presented themselves early on. Firstly, the formulation WF21 was deemed unsuitable as severe shrinkage occurred during the curing process leaving large holes throughout the sample. WF20 also had problems in curing by remaining liquid after 15 passes under the mercury lamp. By placing these samples in a dark oven overnight (50 - 60^{o}C), the coating then became hard-to-the-touch. Secondly, samples that were placed in the oven for over 48 hours developed a cloudy appearance with a brown tinge. As a result, these were redone and samples were left in the oven no more than 24 hours. Thirdly, the first batch of S160 was contaminated and left noticeable pitting within the formulations, figure 3.12.

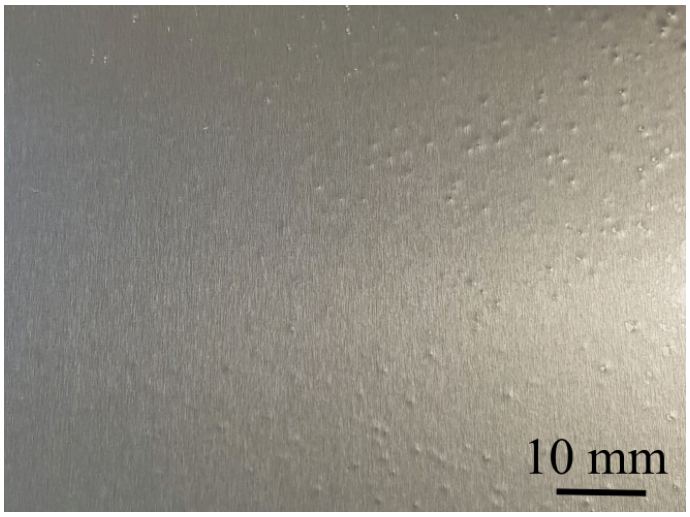


Figure 3.12: Example of pitting within a test sample, WF19. Pitting of this sample appeared after curing. This was the worst case out of all 27 formulations.

This was observed before curing and in some cases increased after the curing process. No solution was found to remove the cause of the pitting and due to time constraints and limited supply, the existing S160 was used to make all panel and strip samples. Care was taken to try to avoid areas of pitting in testing. A second and non-contaminated batch of S160 was used to coat the aluminium beams for photoelasticity investigations. A description of each coating is as follows with images showing the most severe appearances:

- **WF1** - Clean and clear coating with no observable pitting or shrinkage.
- **WF2** - No signs of shrinkage and mostly clear. However, some strange artefacts present on the coating. Likely to have an effect on photoelastic measurements.
- **WF3** - Severe shrinkage around the edge of the coating where thicker regions naturally occur. These thicker regions did not fully cured. The appearance is presented in figure 3.13.



Figure 3.13: WF3 applied to an aluminium beam. The appearance of shrinkage is severe within the thicker regions of the coating demonstrating a rippling within the coating.

- **WF4** - Moderate Shrinkage observed throughout the sample however hard-to-the-touch. The appearance is presented in figure 3.14.

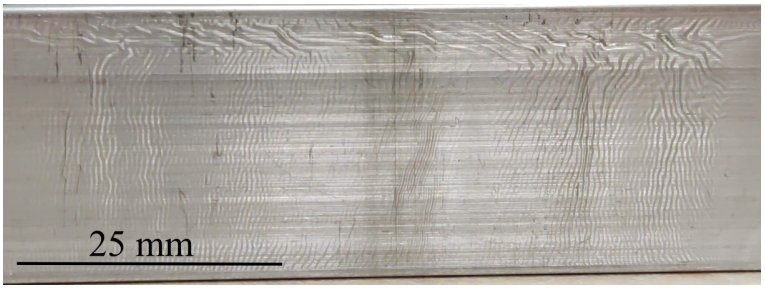


Figure 3.14: WF4 applied to an aluminium beam. Shrinkage is observed throughout the main bulk of the coated region.

- **WF5** - Moderate Shrinkage observed in thicker regions such as the edges and point of application.
- **WF6** - Clean coating however some artefacts observed in the coating.
- **WF7** - Coating unusable, smears and pitting in the coating. Potentially due to beam not being cleaned effectively prior to coating.
- **WF8** - Small amount of shrinkage visible around the edges and thicker section where the rod was removed after coating.
- **WF9** - Clean and clear coating with no observable pitting or shrinkage.
- **WF10** - Clean and clear coating with no observable pitting or shrinkage.
- **WF11** - Severe Shrinkage observed in the middle of sample, at edges and thicker regions where resin was applied and where the K-bar was removed. The appearance is presented in figure 3.15.



Figure 3.15: WF11 applied to an aluminium beam. Severe shrinkage around the edges and ends of the coated region with shrinkage also observed in the main bulk.



Figure 3.16: WF22 applied to an aluminium beam. Clear coating however the effects of a failed thumb twist test presenting rippling at one end.

- **WF12** - Small amount of shrinkage visible around edges and where the coating was first applied.
- **WF13** - Severe shrinkage around the edge of the coating where thicker regions naturally occur.
- **WF14** - Slight shrinkage visible around the edges.
- **WF15** - Clean and clear coating with no observable pitting or shrinkage.
- **WF16** - Clean and clear coating with no observable pitting or shrinkage. Slightly thicker regions observed throughout the coating.
- **WF17** - Clean and clear coating with no observable pitting or shrinkage.
- **WF18** - Clean and clear coating with no observable pitting or shrinkage.
- **WF19** - Clean and clear coating with no observable pitting or shrinkage.
- **WF20** - No signs of shrinkage and mostly clear. However some strange artefacts present on the coating.
- **WF22** - Clean surface, slight defect in coating due to thumb twist test. The appearance is presented in figure 3.16.
- **WF23** - Clean coating, possible shrinkage on edges and thicker ends. Wave appearance observed in starting region.
- **WF24** - Clean coating very even throughout. However starting region is thicker with some strange artefacts.
- **WF25** - Clean coating apart from a strip of what appears to be shrinkage. The appearance



Figure 3.17: WF25 applied to an aluminium beam. Mainly clear coating however a strip of shrinkage is observed at one end of the beam.



Figure 3.18: WF27 applied to an aluminium beam. Clear coating however thicker regions at one end demonstrated artefacts in the coating appearance.

is presented in figure 3.17.

- **WF26** - Clean coating. Thicker regions shrunk leaving uncured resin underneath a layer of cured formulation.
- **WF27** - Clean coating but thicker region at start of application has artefacts similar to WF24. The appearance is presented in figure 3.18.

The application of the UV curable formulation onto the beams was a very quick process with the liquid formulation being applied, spread then initiated cure all under 2 minutes per sample. The management of formulations was trivial with fast clean up of any spillages and on the applicator.

3.2.2.3 Methodology - PS-1E

A common RPSA coating material is a precast polycarbonate flat sheet that are applied to flat geometries. This coating material will be used as a reference point mainly for photoelastic investigations of the UV curable materials. Additionally, it provides experience in applying these types of materials and why the application has been described as challenging. The coating and adhesive used as a comparison was Vishay Precision Group's PS-1E flat sheet, thickness of (0.25 $\pm$ 0.06)mm, and PC-10 a two part epoxy resin [7]. These materials were supplied by Airbus. The flat sheet was

bonded to the same materials as the UV curable resins. All tests, apart from T_g and viscosity, will be performed on these samples. The bonding procedure takes four hours, however advice from experienced photoelasticians suggested an overnight cure to prevent creep issues.

Firstly, the desired sheet size was cut using a sharp blade and laid onto the bonding surface. Masking tape was then used to mask off an open space around the sheet leaving an approximate 6 mm gap between the tape and sheet if possible. Using acetone, this open space was cleaned prior to application of the two-part epoxy. One gram of adhesive covers an approximate area of 10 cm^2 so an estimate of the total adhesive required was made. The curing process was started by mixing the PC-10 resin with 15 parts per hundred of PC-10 hardener. The required amounts were weighed using a weighing scale resolution 10^{-3}g. Once weighed, the mixture was thoroughly mixed for two minutes. The adhesive has a working time of 10 — 15 minutes which limited the amount of samples that could be prepared at once. Due to inexperience of the user only two samples at a time were made. The adhesive was then applied to the bonding surface with a small flat plastic spatula spreading it as evenly as possible. The adhesive was required to be between 0.8 — 1.6 mm thick before coating application. This enabled the adhesive to spread and fill any voids when the sheet was placed on top. Two 0.032 in (0.813 mm) feeler gauges were placed either side of the sample to ensure the target coating thickness was met. A flat object, such as a metal ruler, then spread the adhesive across the bonding area creating a uniformly thick layer by removing any excess adhesive. If needed, more adhesive was applied in areas where the thickness was below the feeler gauges. These steps are shown in figure 3.19.

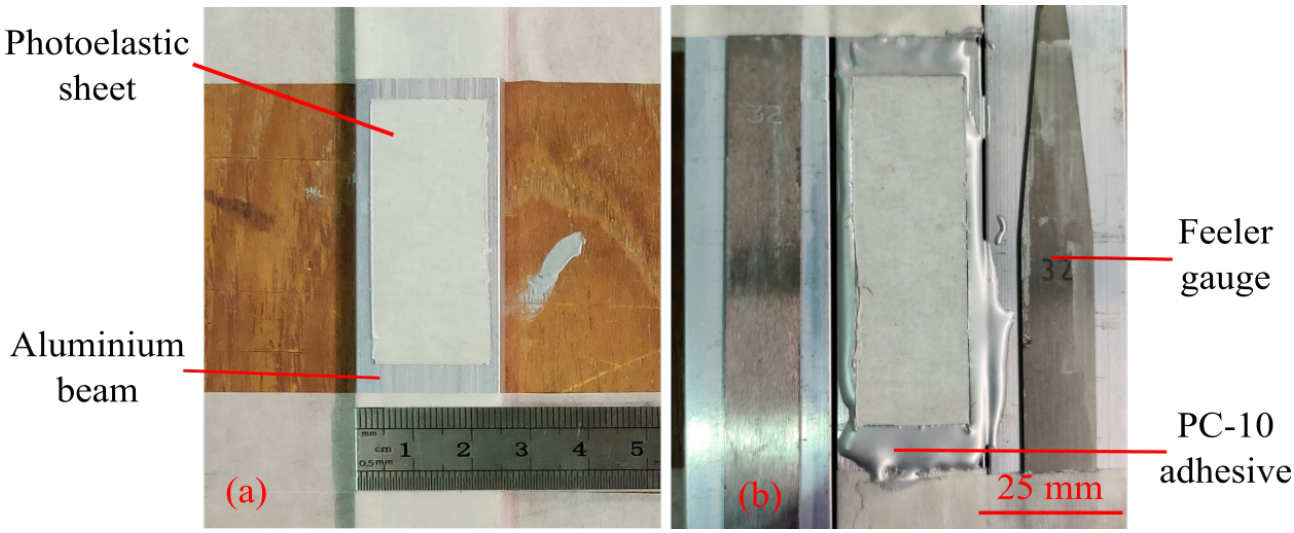


Figure 3.19: ***(a)****: An aluminium beam being prepared for bonding a PS - 1E sheet to the open area. The cut-out of the sheet is observed on the left beam with a protective cover. The area surrounding is masked off.* ***(b)****: Two 0.032 in feeler gauges were used to ensure that the spread of the silver adhesive is uniform across the open area.*

The sheet was then placed on top of the adhesive and moderate finger pressure was used to push down on the sheet. This action removed any air bubbles that were present by allowing them to flow out with the excess adhesive. Once excess adhesive was removed, a thin coating of adhesive is left around the edges of the sheet to provide a seal against moisture absorption. After 30 minutes the adhesive has a putty consistency and adhesive bevels were built. This required a flat object, positioned at an angle to the bonding surface, to form an angled lip to prevent peeling of the sheet. At this point the masking tape was removed and the protective cover of the photoelastic sheet peeled away. The samples were then left to cure overnight. The completed sample is shown in figure 3.20.



Figure 3.20: The finished sample. The masking tape was removed leaving a clean adhesive boundary around the sheet. The protective cover was also removed from the sheet and is now ready for testing.

3.2.2.4 Results and analysis - PS-1E

In total four aluminium beams and two steel Q-panels were bonded with the PhotoStress coating. The area covered on these samples were (70 x 15) mm for the aluminium beams and (70 x 60) mm for the Q-panels. When laying the sheet onto the adhesive the relatively long working time, 15 minutes, caused the sheet to slip easily when squeezing out the excess adhesive. Care was taken to gently squeeze out the excess adhesive over a period of time allowing for the adhesive to cure slightly to create stability in the sheets position. A large amount of excess adhesive was pushed out and removed using a flat edged tool angled with respect to the flat surface. The finished result is demonstrated by figure 3.21.

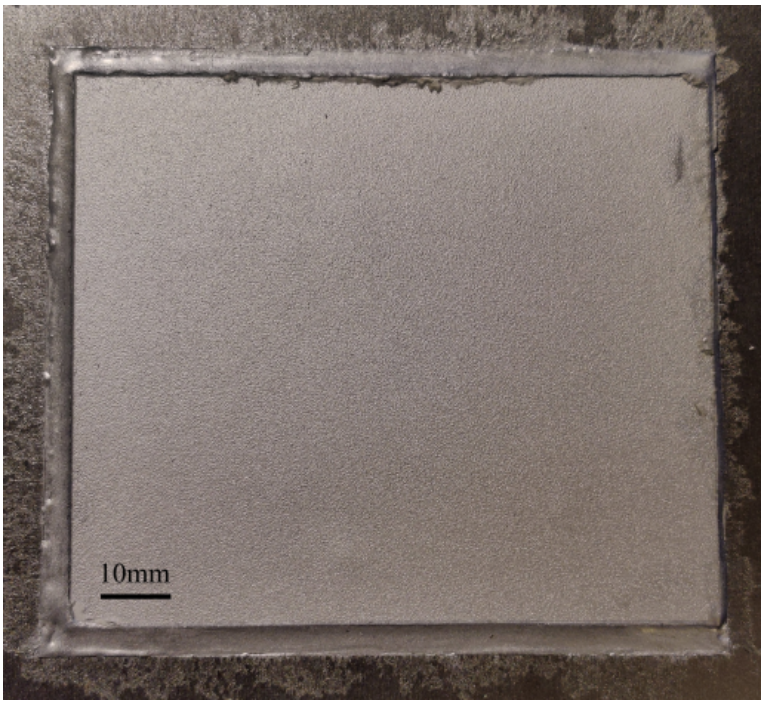


Figure 3.21: PhotoStress PS - 1E bonded to a steel Q panel with a PC - 10 adhesive. The sheet is surrounded by an adhesive border which is angled to create a bevel.

The samples were not perfectly applied as bumps were often present around the edges of the sheet due to the surface tension of sheet. Its effect on the photoelastic properties of the coating will be investigated. Overall the application of PS-1E was a very involved process that required careful preplanning. Only two samples were worked at a time to allow for easy management of the application that would contribute to the long total application time. Per pair of samples it took upwards of 15 minutes to get it into a state that they could be left to cure. The handling of the adhesive was difficult with it being incredibly viscous and difficult to clean.

3.2.3 Photoelastic response of UV curable formulations

3.2.3.1 Methodology

Measuring the photoelastic response of each formulation was the most crucial parameter as it determined the coating's suitability for performing strain analysis. As a large sample size of formulations were tested, the individual strain-optic coefficients were not calculated to increase efficiency. However, the photoelastic response was monitored by measuring the sensitivity to changes of induced retardation with different applied load to the sample. Formulations deemed to possess

the greatest performance were normalised per coating thickness to enable direct comparisons.

In order to generate repeatable and known deflections in all the samples, the aluminium beams were mounted into a 010-B Vishay photoelastic calibration rig, figure 3.22.

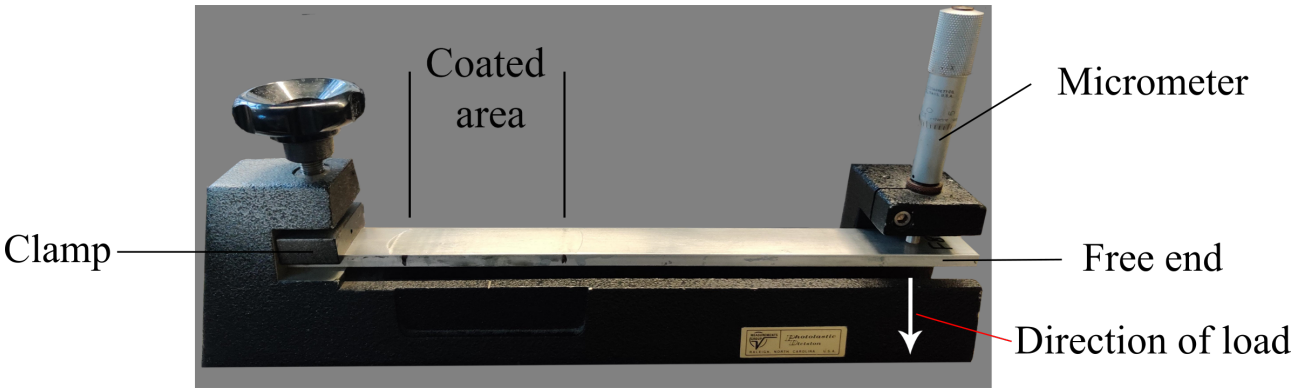


Figure 3.22: Image of the Vishay photoelastic calibration rig with an aluminium beam mounted. The aluminium beam has a coating applied between the markings close to the securing end. A micrometer applies a load to the free end of the beam causing it to act like a cantilever.

The rig secured the beam at one end, closest to the coated area, whilst the opposite remained free. A micrometer arm was positioned at the free end and was able to push down to create a deflection in the beam simulating a cantilever. Knowing the deflection at the free end allowed for calculation at the point of measurement. Beams were deflected at the free end to a maximum of 0.8 in (20.32 mm) in intervals of 0.05 in (1.27 mm). Incremental steps in inches were used due to the imperial scale on the micrometer. At each interval the GFP1600 with the image acquisition and processing software DeltaVision was used to measure the induced retardation. The GFP1600 was mounted looking directly down onto the coated region of the beam. A single circular polarised light source illuminated the coating also from above at an angle. The determination of the light source's placement was not measured and was placed upon advice from Geoff Calvert, an experienced user of this apparatus. Consideration of light source angle was not a concern, this procedure was backed with advice by Airbus. The apparatus setup is shown in figure 3.23

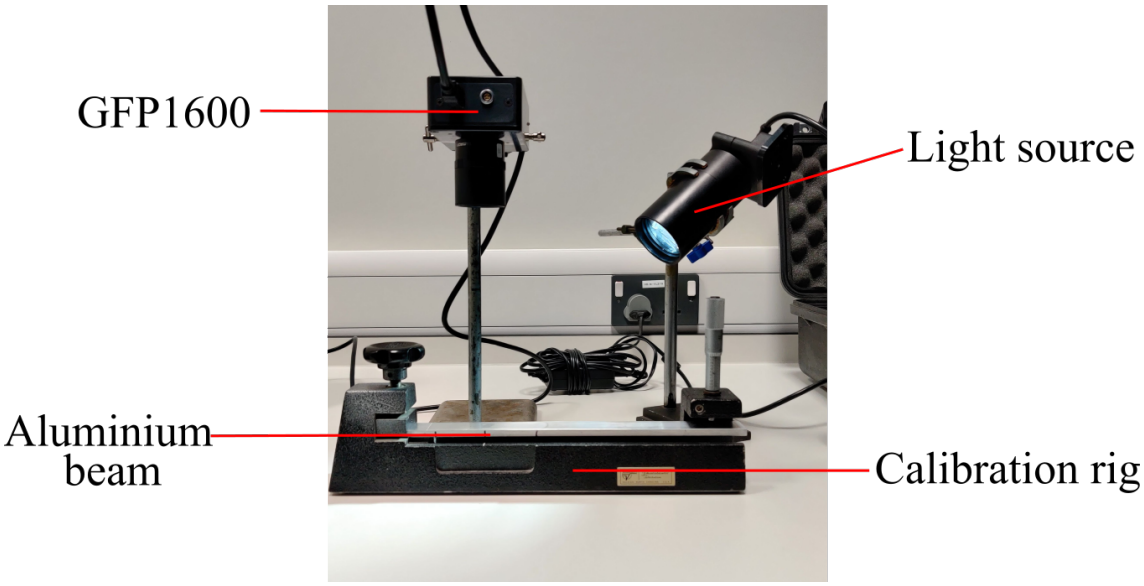


Figure 3.23: The experimental setup for the initial measurements of photoelastic performance of the 27 formulations. A GFP1600 looks directly onto the coated region of an aluminium beam mounted in a calibration rig that inflicts cantilever loads onto the beam. A circularly polarised light source illuminates the coated region.

The output of the GFP1600 is presented in figure 3.24.

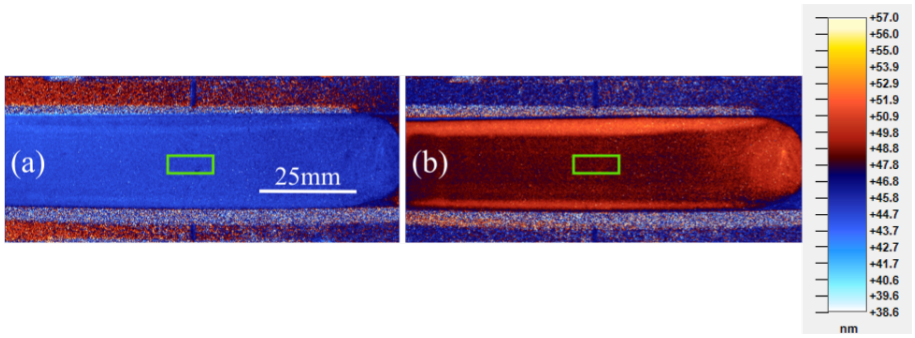


Figure 3.24: Shear 45 output images of the same aluminium beam coated with WF23. The green box highlights the area birefringence data were extracted from. The key relates the observed colour with a relative retardation in nm. ***(a)*** *Zero deflection image.* ***(b)*** *Maximum deflection (20.32 mm) image.*

Figure 3.24 illustrates the change in birefringence from zero to maximum deflection. The retardation of each individual pixel was analysed separately and highlighted with a colour that allowed for visualisation of the birefringence change. A full size image is 1280 x 960 pixels. The green box represents the user defined area in which data were extracted from. The box's location could be saved and recalled by the software allowing for consistent measurements in the same spot between

deflection intervals and samples. Also, the location of the area ensured that any thicker regions of coating, which usually resided on the beam's edges due to excess formulation causing a meniscus effect, were ignored, observed clearly in figure 3.24b. Correction and control of thickness will be discussed in chapter 6.

Firstly, experiments using PS-1E were performed. Each of the three samples had three individual tests performed to quantify repeatability within the sample and the coating. The resultant dataset was used as a benchmark for the individual formulations. Each UV curable formulation had only one repeat run to determine their initial performance using data extracted from the GFP's Shear 45 output only. The Shear 45 image was assumed to contribute the majority of the resultant retardation as the beam was positioned in the 0 degree plane of the GFP. Focusing on the Shear 45 image allowed for the analysis of the residual retardation within the coating. Formulations that possessed strong linear responses to deflections were chosen and further repeats were performed on a further two samples to calculate repeatability within the sample and the coating. At this point, the Shear max image was used to provide the resultant retardation with the residual retardation subtracted from each data point following procedure outlined in section 2.3.9.1. Finally, to compare formulations with each other and with the existing material, all retardation values were normalised with coating thickness. The published thickness of the PS-1E sheets is (0.25 ± 0.06) mm and the formulations were measured using a micrometer of resolution 0.001 mm. The thickness was measured by first measuring the thickness of the beam then the beam with the coating.

3.2.3.2 Results and analysis

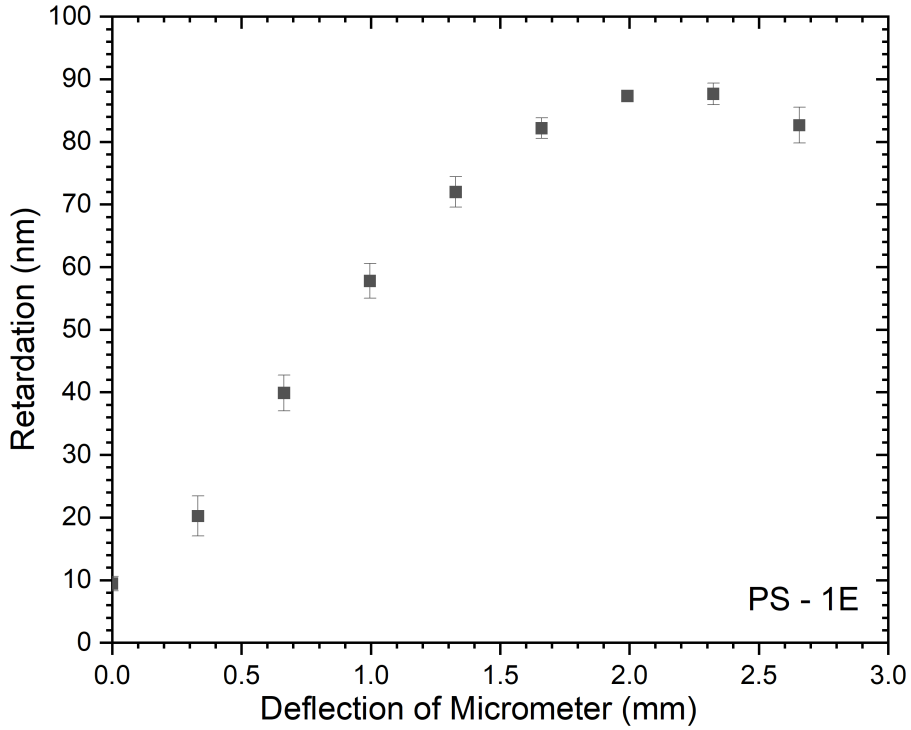


Figure 3.25: The measured retardation of three PS-1E coated beams whilst analysing the shear 45 output within Deltavision. The response starts to curve due to limitations of the GFP1600.

Figure 3.25 demonstrates the combined response of three PS-1E coated beams within the shear 45 output. Error bars are the standard uncertainty from three repeat measurements with the data point being the average retardation at each point. The average uncertainty calculated was (7.4 $\pm$ 6.0) %. Notable observations include the presence of residual retardation at zero deflection and the curve in the response towards $\sim$2 mm. The shape of the response is a limitation of the GFP1600. At the point of apparent decreasing retardation a wrapped phase response, section 2.3.8, was being observed and the calculations were unable to correct for this automatically. These data were not unwrapped as the UV curable coatings were predicted to be much lower in magnitude. However, the initial linear response of figure 3.25 will be the desired response for the UV curable materials as the applied stain is proportional to the applied bending moment. The following data will present each group individually and single component formulations (group a), table 3.2, will be included in other groups as a comparison where necessary.

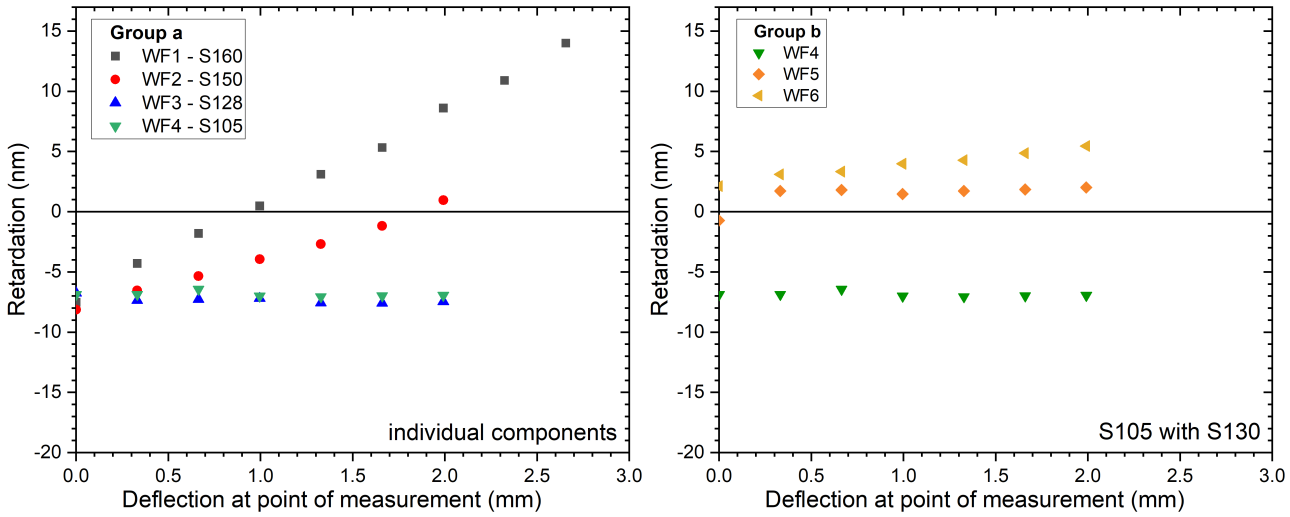


Figure 3.26: Both graphs plot the shear 45 dataset. ***Group a****: Individual resin component formulations.* ***Group b****: Combinations of S105 and S130 with WF4 (S105) as a comparison.*

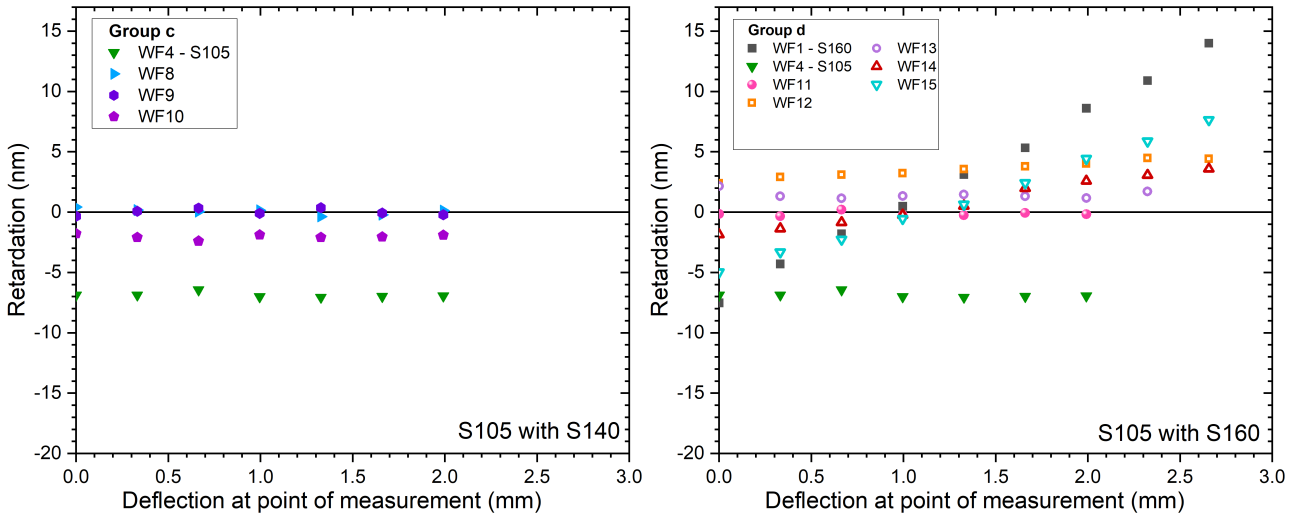


Figure 3.27: Both graphs plot the shear 45 dataset. ***Group c****: Combinations of S105 and S140 with WF4 (S105) as a comparison.* ***Group d****: Combinations of S105 and S160 with WF1 (S160) and WF4 (S105) as a comparison.*

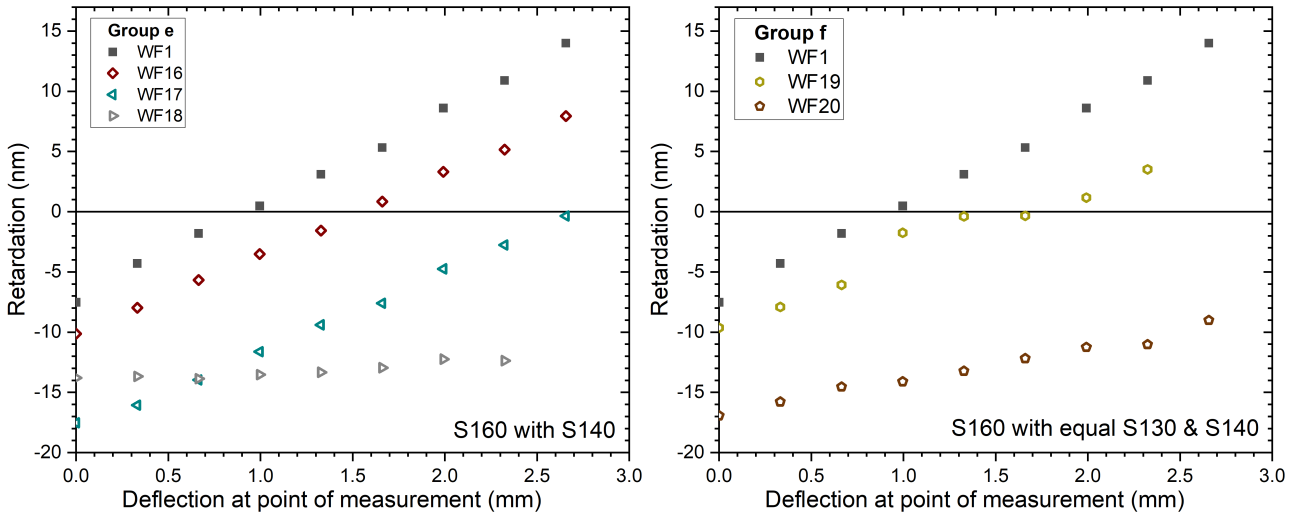


Figure 3.28: Both graphs plot the shear 45 dataset. ***Group e****: Combinations of S160 and S140 with WF1 (S160) as a comparison.* ***Group f****: Combinations of S160 with equal parts S140 and S130 with WF1 (S160) as a comparison.*

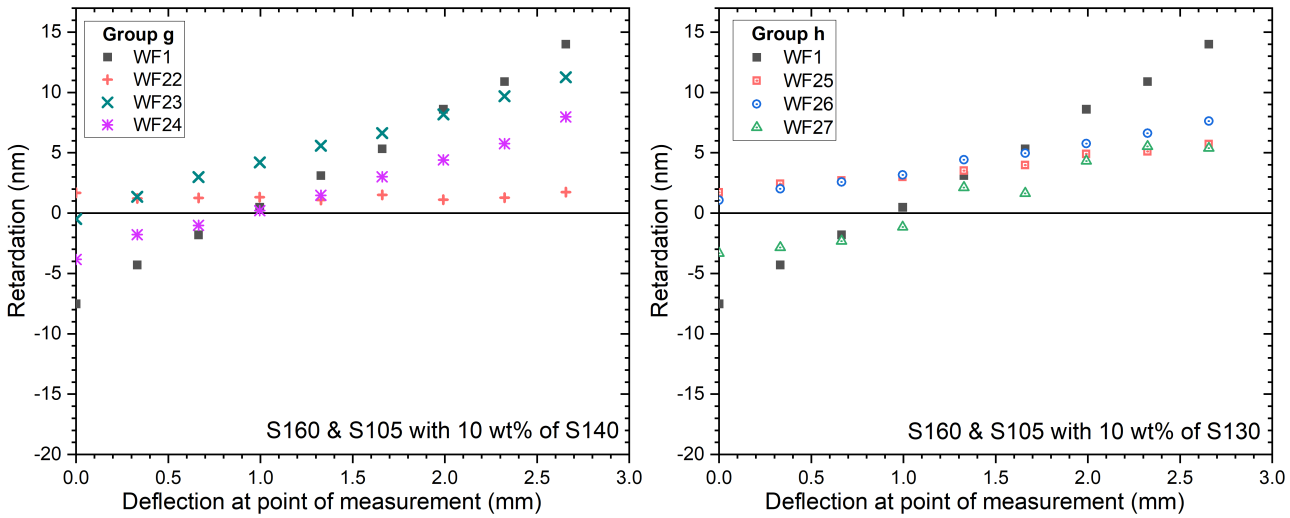


Figure 3.29: Both graphs plot the shear 45 dataset. ***Group g****: Combinations of S160 and S105 with fixed 10 % of S140. WF1 (S160) plotted as a comparison.* ***Group h****: Combinations of S160 and S105 with fixed 10 % of S130. WF1 (S160) plotted as a comparison.*

Figures 3.26 — 3.29 presents the retardation (from the shear 45 images) datasets for each group. No error bars were included as only one repeat per sample was performed to gather an initial understanding of the formulation's photoelastic response. Figure 3.26, group a, demonstrates that the resin S160 possesses the greatest birefringence whilst S128 and S105 feature no observable birefringent effects. Whilst S140 possesses a benzene ring structure, the free dangling end of the material has shown to have no benefit to the photoelastic sensitivity. The large majority

of formulations (WF1-5, WF9-11, WF14-20, WF23-24 & WF27) initially possessed a negative residual retardation which signified compression within the coating. This demonstrates the effects of shrinkage within the coating as a result of the curing process. A selection of four formulations were highlighted as having the best performance: WF1, WF16, WF17 & WF23. By focusing on these four formulations, their repeatability was investigated and compared directly to PS-1E by normalising the coatings for thickness. The ShearMax output dataset was now used with the effects of residual retardation subtracted following the procedure outlined in section 2.3.9.1. The four formulations were repeated three times.

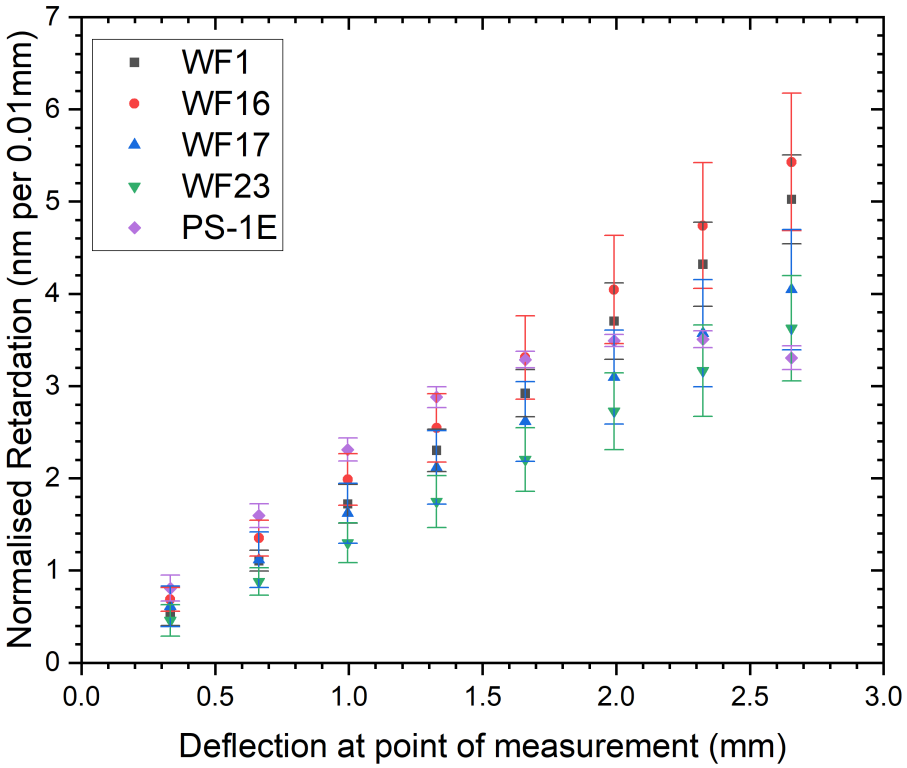


Figure 3.30: Four UV curable formulations plotted alongside the commercially available PS-1E sheet for a comparison. The ShearMax output is plotted with the retardation normalised per 10 μm of thickness.

Figure 3.30 presents all four potential formulations with the benchmark PS-1E. WF16 possessed the highest magnitude of photoelastic response measured by the value of the gradient. WF16 demonstrated that a combination of resins can increase the photoelastic response of the base resin S160 that was thought to be the highest performer due to its chemical structure containing the double aromatic core that exists within polycarbonate and other high sensitivity coatings [10,62,63]. This finding was significant as WF1 was solid at room temperature and required heat to melt the

formulation prior to curing. The initial magnitude of PS-1E's response was comparable to that of WF16's which demonstrates that the UV curable formulation possesses a similar sensitivity. However, the main differences between the coatings are the size of error bars associated with each data point.

The majority of the UV cured coating's uncertainty, was contributed by thickness measurements. Thickness measurements increased the uncertainty of the coating's retardation by approximately 36 % when comparing against the uncertainty associated with PS-1E. Thickness measurements of the coatings were performed with inaccuracies. The measured thicknesses for all coatings within this sample set was between 29 — 150 μm demonstrating an incredibly wide range of thicknesses for the same application method. Compared to direct methods of thickness measurement that were only performed in later investigations, chapter 5.2, there was a measured difference between measurements on the beam and the direct approach. This was only discovered in this later investigation. As a result, the confidence surrounding the accuracy of the measurement of the thickness is low. Therefore, the normalisation has not been performed with accurate values for thickness thus the measured response has a wide variance as demonstrated by the large increase in uncertainty. Furthermore, differences in the uniformity of the thickness is shown in figure 3.31.

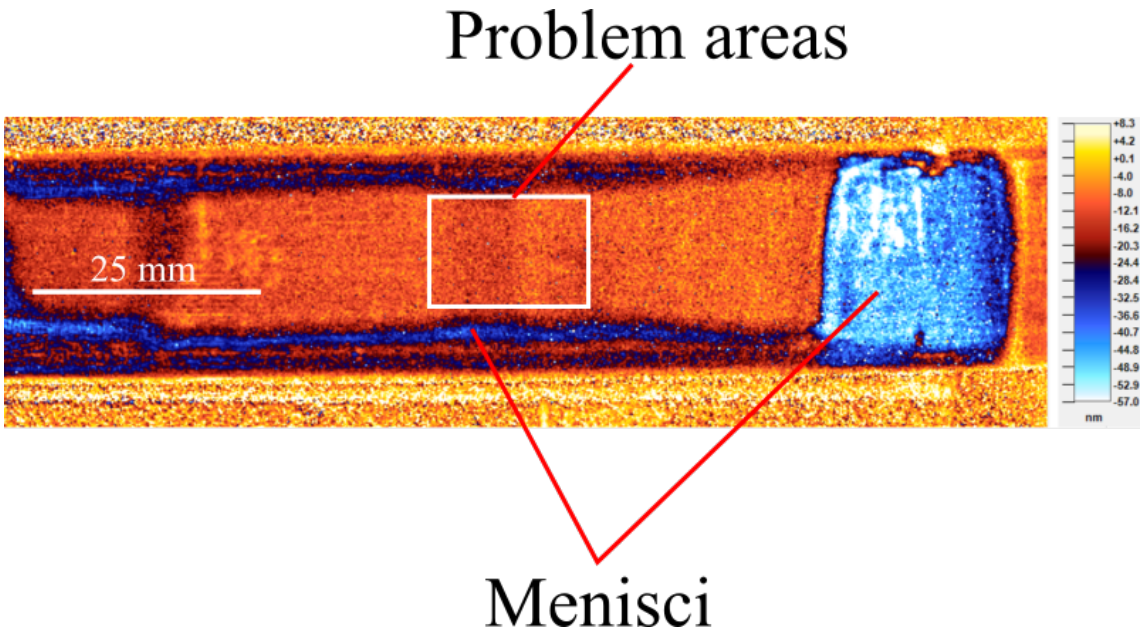


Figure 3.31: Shear45 image of the sample WF16a demonstrating multiple regions of differing thickness.

Figure 3.31 presents multiple regions of problematic increases in measured retardation. The increase in retardation magnitude were a result of differing thicknesses through menisci on the edges and

slight variations of retardation in the main bulk. As a result, measurement of the thickness using the manual approach would be measuring variations of the thickness. Due to the coating being relatively thin, these changes have large impacts on the measured retardation. Another cause of the formulation's uncertainty is result of the non-uniform reflectivity of the bare aluminium beam, figure 3.32.

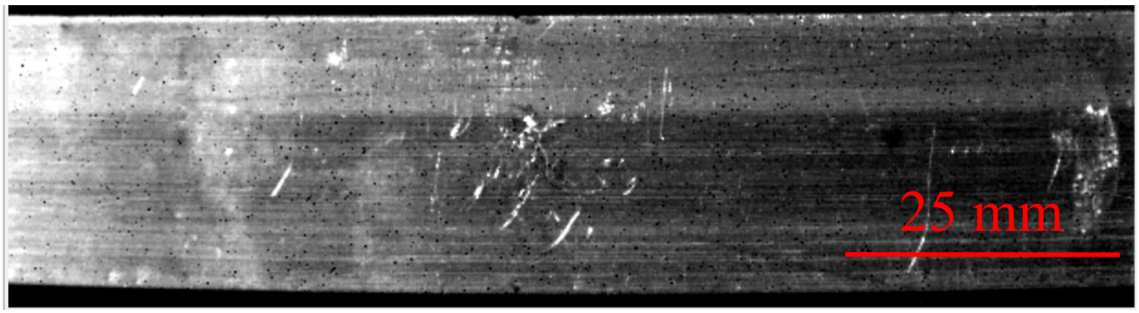


Figure 3.32: Light image of the sample WF17b demonstrating a non-uniform reflective backing.

Figure 3.32 is an example of the coating WF17 applied to an aluminium beam. Many markings were observed which produced bright hotspots as the light reflects off them at different angles. These markings possessed retardation data that were higher than surrounding areas. Care was taken to avoid these markings when extracting photoelastic data but an error is thought to be produced by this non-uniform reflective surface. The decision to utilise no reflective backing came from suggestions in published work [57, 107] and from experienced photoelasticians. One conclusion from WMG's work was significant delamination of the UV coating when applied on top of a silver paint. As a result, this was avoided by direct application onto the metal surface. However, the variations in light intensity caused by the specular reflections has negative impact on the collected data. PS-1E has a reflective backing applied onto the surface that provided a uniform reflective backing. This highlighted an area for development which was investigated and discussed in chapter 5.2.

3.2.4 Viscosity

Viscosity was investigated as it will play an important role when developing the sprayable capability of a formulation. Learning how effective different resins are in changing the formulation viscosity is important when designing the final formulation makeup. In summary, the data collected provides insight that will assist the applicability of a formulation. An article from the American Coating Association [108] states that an ideal viscosity for spray painting is approximately 100 cP yet it

is possible to spray at viscosities up to 500 cP but not without issues. The major issue is the atomisation of the fluid which describes how the liquid breaks into fine droplets during the spraying process. An article by Lechler [109], a spray technology company, demonstrates the limitations of spraying at high viscosities (up to 2000 cP) using various nozzle configurations. By considering the nozzle type and how the liquid is mixed with the pressurised air, it is possible to spray at high viscosities (500 - 1000 cP) but the finish will be affected. As a result, a target viscosity of 200 - 500 cP would allow for spraying with the correct configuration of spraying equipment. It is possible to achieve these viscosities with introduction of a diluent resin. It was shown that S130 and S140 have the greatest effect on the reduction of viscosity when paired with S160. As a result, the addition of these diluents would be favourable for spray applications. Viscosity can be further reduced by heating the formulation and there is potential to introduce a solvent to thin the formulation without changing the formulation's photoelastic properties.

3.2.5 Solvent resistance

This test was a guide to determine the chemical resistance of each cured formulation. This is important when considering how the cured coating will be removed from a component after RPSA. If it is decided that the coating is to be removed by a chemical, then these results will be useful to refer to. In summary, it was difficult to establish clear observations between resin amounts and the resulting chemical resistance. However, S160 appears to increase the resistance whilst S130 and S140 degrades it. By increasing the amounts of a single diluent, it appeared that solvent resistance decreased considerably. If the coating is to be removed by a chemical then focusing on using S160 to provide photoelastic performance with a diluent, e.g. S130, could benefit from being sprayable and removable.

3.2.6 Adhesion

Adhesive testing explores how well a coating bonds to a surface as well as providing details on how well they can be physically removed. If a coating can be taken off a component easily, without damaging or marking the component, then a removal procedure could be constructed from reviewing these measurements. It is important to note after curing the formulations did not slip on top of the metal substrates nor could they be easily picked off with minimal effort e.g. using a fingernail. To

summarise, by following the test procedure, formulations with majority S160 exhibited poor adhesion. This is a beneficial quality as procedures could be developed for manual removal of the coating. However, further investigations are required to understand if poor adhesion equates to undesirable responses to sample deformation as discussed next.

3.2.7 Flexibility

Flexibility provides information on the maximum bend a formulation can withstand in terms of radius of curvature. If a component is being analysed under dynamic conditions a suitable coating must be chosen to ensure the coating does not break or delaminate from a surface. To summarise, many coatings could withstand when the sample were bent back close to completely upon themselves. When failure was observed, the precision of repeat measurements was low or not replicated in subsqeuent samples. The main observation from this investigation was that S160 cures to become a glassy/brittle coating that can exhibit failure at certain deflections. The failure occurs suddenly with the coating delaminating from the sample surface and snapping. This observation further supports the cause of S160's high photoelastic performance as stiff coatings are used to visualise strains in stiff materials as their sensitivity is greater [55]. Ultimately, the UV curable formulations demonstrate high resistance to extreme deformations and are predicted to remain adhered to a sample during elastic loading scenarios.

3.2.8 Glass transition temperature

Glass transition temperature (T_g) is the temperature region for amorphous materials, such as epoxies, where the polymer transitions from a glassy state to a soft and rubbery state. It is an important property to explore as if conditions are above the T_g of a coating the structure changes which could alter other properties. A proposed scenario would be if RPSA was conducted on a runway on a hot day, the surface temperatures of the aircraft could be relatively high thus affecting the photoelastic properties. The T_g of all formulations varied from -4 — 84 ^oC. However, the confidence of these results is unclear as Arkema UK flagged concern over these values being lower than once thought. As a result, no conclusions can be made from this dataset and T_g should be investigated in future experiments, chapter 4.

3.2.9 Screening conclusions

The conducted preliminary research and development demonstrated high potential for UV curable materials to act as a well-functioning photoelastic coating. After experiencing both procedures for RPE coating application, the UV curable formulation was a lot easier to manage and apply than the flat PS-1E sheet. By using a small quantity of coating formulation, the sample was coated and cured in a matter of minutes requiring very little skill. Whilst application of the PS-1E sheet was relatively straightforward, the timescales for application were a lot longer and it was harder to avoid issues with the final sample. Moreover, these issues will be harder to control and somewhat amplified when applying to bigger areas with geometries with greater complexity. Additionally, larger areas will result in increased amount of excess adhesive being wasted. This comparison helps further demonstrate why this research is being conducted.

UV curable coatings possess an observable photoelastic response to changes in applied load comparable to the highly sensitive PS-1E sheet, figure 3.30. The resin S160 was found to be the dominant contributor to the birefringence with majority S160 formulations being the best performers for photoelastic response. Therefore, it is apparent that an optimised formulation must be constructed mostly of this resin. It was observed that the majority of formulations initially measured a negative retardation via the analysis of GFP1600 images. Negative retardation within the software indicates compressive stresses within the coating. This was a result of shrinkage that occurred during the curing process as the crosslinked polymer network forms when exposed to UV light. The shrinkage can be accounted for when applying the subtraction facility that removes the effects of the initial residual birefringence from each loaded image. Although possessing desirable sensitivities, the UV curable formulations exhibited poor precision when compared to PS-1E. The uncertainty associated with the PS-1E sheet was calculated to be (7.4 $\pm$ 6.0) % whilst the UV curable coatings had an average uncertainty increase of 36 %. Two contributing factors are believed to be the cause, the measurement of the coating thickness and the surface finish quality. The former issue was shown to be a result of the application using a K-bar to spread the formulation across the beam. It was challenging to produce a uniformly thick coating and any imbalance of the applicator would cause non-uniformity across the coated surface. As a result, measuring the thickness manually from the sample proved to inflict large uncertainties in the measurements. This then demonstrated a main concern with these materials as the thickness of the coating is required for RPSA investigations. The

surface finish quality spends on the effects of specular reflection of the beams on the photoelastic measurements. The location of direct reflections altered the measured retardation. The beams were not treated in any way prior to coating application. In future investigations efforts to remove surface scratches will be applied to reduce the increase of uncertainty caused by specular reflections. Coating preparation in this manner follow from findings with WMG's research that suggested poor adhesion between paint and the UV curable coating. Delamination was recorded as the shrinkage removed the paint underneath. Whilst literature states the use of a reflective underlayer [3, 55] it was not a requirement and the research favoured efficiency in coating optimisation. The effects of surface finish are explored further in chapter 5.2.

Investigations into the formulations' viscosity, solvent resistance, adhesion, flexibility and glass transition temperature all demonstrated potential desirable properties that effect the applicability of the coating. S160 alone is a very viscous resin which should be thinned by a diluent resin (S105, S130 and/or S140) in order to achieve a viscosity that would support spray applications. Including diluents was shown to not dramatically affect the photoelastic response, figure 3.30. The requirement for the coating to be easily removable was provided by investigations into solvent resistance and adhesion. Both chemical and physical removal methods could be adopted depending on the formulation of the optimised coating. If S160 is the majority component, the data suggested that physical removal may be the best course of action due to S160 contributing to relatively poor adhesion and high solvent resistance. Flexibility investigations then provided an understanding into a formulation's ability to withstand geometry changes of the sample. Whilst an optimised formulation is predicted to have poor adhesion, the findings from flexibility testing showed that all formulations are able to withstand large deflections thus able to be used effectively in RPSA investigations. Finally, investigations into T_g were not successful as the outcomes were not supported by Arkema's understanding of their products. Initial discussion with Arkema indicated that the methodology was not analysing a bulk sample but reviewing a small volume of a formulation built from multiple materials. Repeat measurements were not conducted and future investigation into T_g will be performed on a smaller sample size to save time and resources, chapter 4.

A good understanding of the UV curable formulations' capabilities have been achieved. As a result the next stage in this research will be to determine an optimised formulation for future RPSA investigations. Optimisation will be performed using design of experiment statistical packages to

provide a rational optimisation approach.

3.3 Coating optimisation

The next stage in the research was to formulate an optimised coating by building on the knowledge gained on the outcomes of preliminary coating development. The objective will be to perform rational design by adopting statistical packages to analyse data and output a proposed best solution. Design of experiments (DOE) statisical packages will analyse a selection of formulations and, based on user defined properties, will calculate an optimised formulation. The DOE process will be described in section 3.3.2.1. Prior to DOE implementation, a study into the curing performance was performed to determine if a baking stage is required after UV light irradiation to determined if the application of heat was required for curing.

3.3.1 Reviewing the curing process

This section reviews the curing performance for two high performing formulations highlighted in section 3.2. These formulations, WF17 and WF23, possessed suitable photoelastic responses with a linear relationship between retardation and deflection and an intercept close to 0 nm for a zero load. However, these properties were only achievable through the use of the subtraction post-processing facility. For this investigation, the formulation's other properties, e.g. high viscosity and apparent low T_g, will not have an effect as further formulation optismation will occur, section 3.3.2.

Their raw retardation demonstrated significant initial retardation due to compression in the coating which was explained by the shrinkage that occurs during the curing process. However, according to the manufacturer's specifications the resins should possess minimal shrinkage (< 5 %). Whilst this value seems small its effect of the photoelastic response is unknown. Furthermore, it was proposed that another process could be inflicting an unknown amount of residual stress within the cured coating. This was thought to be a result of placing samples in a dark oven immediately after being subjected to UV light. As the metal substrate contracts with the removal of heat, the coating will shrink along with it inflicting parastic birefringence. Moreover, the inclusion of a heating stage increases the application time by several hours which goes against the desired criteria for the coating. The heating stage becomes even more problematic if considering its use in industry when coating

large components such as sections of an aircraft's wing. Heating such large structures would not be feasible and not possible in indsutrial settings. Ultimately the heating stage must be removed for this coating to have an impact on the wider field of research utilising RPSA for structural health monitoring. Additionally, by eliminating the heat cycle a significant amount of time can be saved from the coating application. Due to the coating thickness ($\sim$50 μm) and its appearance after the irradation of UV light it was proposed that the heating stage might not have a significant effect after all. The effects of the photoelastic response for two formulations, WF17 and WF23, were reviewed with and without a heating stage to explore this hypothesis.

3.3.1.1 Methodology

In order to review the effects of heat treatment on UV curable coatings, further samples needed to be created. Five aluminium beams per formulation were coated with WF17 and WF23. A new pretreatment step was to use 200 grit sandpaper to polish the aluminium surface to produce an approximate uniform reflective backing. This was an important step as any surface defects could cause direct reflections of light into the GFP1600 resulting in distortion in the measured retardation as observed in figure 3.32. The beam thickness was measured using a micrometer, resolution of 0.001 mm, at the point of measurement used for photoelastic measurements. Acetone was then used to clean the metal surface thoroughly to remove all traces of dust and oil. Approximately 0.5 mL of formulation was applied per beam and a number 6 K-bar was used to deposit an approximate wet film thickness of 50 μm. Samples were then placed in a Dymax UVC-5 UV conveyor system for 10 passes. A thumb twist on the cured surface determined if the coating was sufficiently cured by roughly determining its adhesion to the metal surface.

The new samples were subjected to photoelastic investigations using the same methodology as the heat treated sample. A cantilever calibration rig, figure 3.22, applied a static load to the free surface of a beam whilst the opposite end was clamped securely, thus simulating a cantilever beam. The samples were illuminated with circularly polarised light and the GFP1600 measured the retardation between the two components of light after interacting with the coating. A micrometer then measured the thickness of the coated sample to enable coating thickness calculations. Retardation data were normalised per 0.01 mm of coating thickness to enable direct comparisons between samples.

3.3.1.2 Results and analysis

Formulations WF17 and WF23 were efficiently cured just using UV light irradiation. Each formulation was hard to the touch after 10 passes under the UV light and produced clear and glossy surfaces. The retardation data from five of each the UV only cured samples were compared to the corresponding dataset from section 3.2 where heat-treatment was used. Averages were produced with their standard uncertainties as shown in figure 3.33.

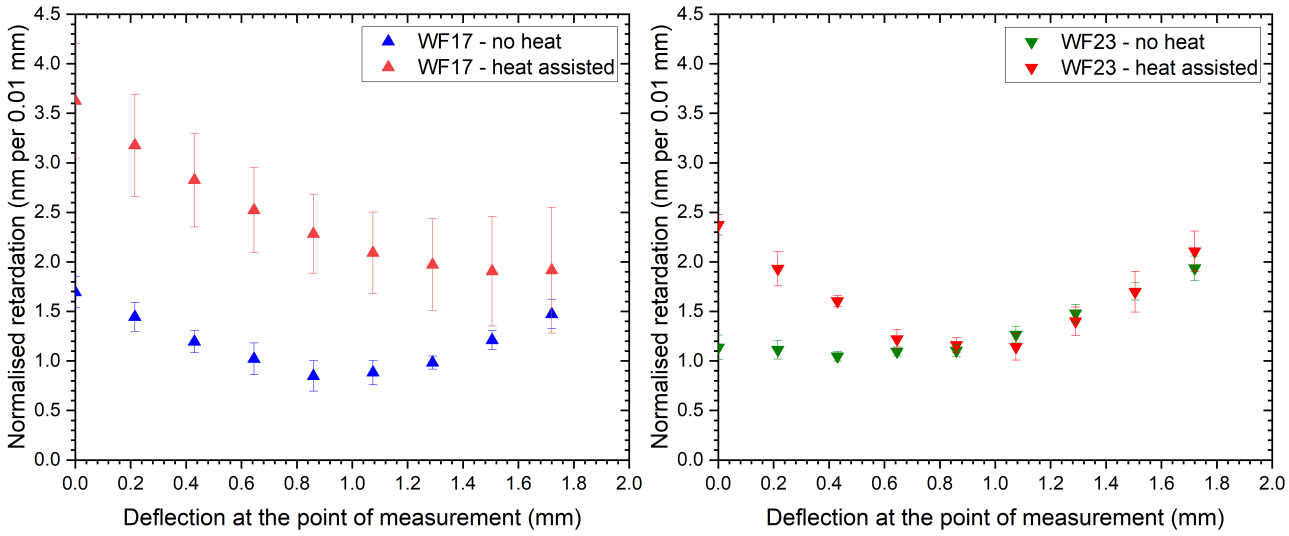


Figure 3.33: The comparison between non-heat treated and heat treated samples for the formulations WF17 and WF23. The retardation data were extracted from the Shear Max output of the GFP1600.

The data shown in figure 3.33 was the ShearMax normalised per 0.01 mm of coating thickness without the subtraction post-processing. The ShearMax is the resultant of the Shear 0 and Shear 45 datasets calculated as the hypotenuse of a right-angled triangle with Shear 0 and Shear 45 acting as either the opposite or adjacent. Therefore, as the Shear 45 dataset approaches 0 nm from an initial compressive state, the resultant ShearMax appears to decrease in photoelastic magnitude. Shear 45 datasets are demonstrated in figures 3.26 - 3.29. Shear 0 datasets are not included due to their contribution to ShearMax being low. Only when the coating increases from 0 nm does the response return to the desired positively linear response. This demonstrates the importance of the subtraction facility.

Comparing samples using the two different curing methods, it was discovered that removing the oven stage reduced the initial retardation in both formulations by (54 $\pm$ 20) % and (52 $\pm$ 12) % for WF17 and WF23 respectively. However, a source of compression was still present and that was

attributed to the shrinkage of the coating. Another observation from figure 3.33 was the reduction in the uncertainty present in the non-heated treated samples. This was a result of preparing the sample's surface finish prior to coating. This investigation has further demonstrated the ease of application of the UV curable formulations. Removing the oven stage allows samples to be created, ready for use, after a number of minutes rather than hours. All future photoelastic samples did not feature an oven in the curing process.

3.3.2 Optimising the formulation

The design of the optimised formulation will focus on only three resins — S160, S105 and S140. S160 was discovered to be an essential major component to generate a sensitive photoelastic response. By introducing S105 and S140, both the viscosity, figure A.1, and presence of residual stresses were reduced, figures 3.27 - 3.29. By focusing on just these three resins, utilising statistical packages to optimise formulations becomes more feasible as the information required will take a lot less time and resources to gather.

3.3.2.1 Design of experiments

Design of experiments (DOE) is an applied statistics tool that assists in planning, analysing and interpreting data in a set of controlled tests to determine factors that control the value of parameters [110, 111]. It is a tool that can be used to speed the process of optimisation when compared to trial-and-error and one factor at a time approaches. DOE simultaneously reviews changes in various input factors and determines their effect on desired outputs.

In the context of this research DOE will analyse how changes of the three resins effect properties of interest and will design a formulation that best matches a set of user defined targets of those properties.

3.3.2.2 Methodology

For this research a mixture DOE design, using the software Minitab [112], was utilised. Minitab first required the lower and upper limits of the individual resins as a percentage. These ranges were determined through the outcomes of section 3.2. Formulations with lower than 60 % S160 often had no photoelastic response thus a suitable DOE range was chosen to be 60 — 98 % for S160. S140,

a diluent resin, had a DOE range of 0 — 38 % whilst S105 was restricted to 0 — 30 % as above this value formulations did not demonstrate a photoelastic response. The design was fixed so that the total weight percentage of the combined resins would be 98 % to allow for the inclusion of the photoinitiator. With this information, the software designed nine new recommended formulations with different percentages of each resin, table 3.4.

Formulation Reference	S160 (%)	S140 (%)	S105 (%)	992 (%)
DOE1	60	38	0	2
DOE2	60	8	30	2
DOE3	98	0	0	2
DOE4	68	0	30	2
DOE5	71.5	11.5	15	2
DOE6	65.75	24.75	7.5	2
DOE7	65.75	9.75	22.5	2
DOE8	84.75	5.75	7.5	2
DOE9	69.75	5.75	22.5	2

Table 3.4: Formulations outputted by the Design of Experiments mixture design. These formulations were subjected to photoelastic investigations. Numerical data were then inputted back into the design in order for formulation optimisation based off user requests.

DOE required that these new formulations, shown in table 3.4, were put through experimental testing to extract certain data. The data of interest were selected by the user following discussions with Airbus. Three properties of interest were chosen: photoelastic sensitivity, initial retardation and graph y-intercept. Each property was measured utilising the cantilever bending rig described in section 3.3.1.1. Aluminium beams were coated with the DOE formulations, three beams per formulation were coated and cured by passing under a mercury bulb ten times. The cantilever bending rig applied sequential loads and a GFP1600 was used to take images at each load. Photoelastic sensitivity was a measure of the response to loads applied to the aluminium beam in the cantilever bending rig. It was measured by calculating the gradient of the graph of normalised retardation, with initial retardation subtracted, against deflection. Graph intercept observed the value of the y-intercept between a graph of normalised retardation, with initial retardation subtracted, against deflection. This parameter analysed the shape of the response. Examples of both properties are shown in figure 3.34.

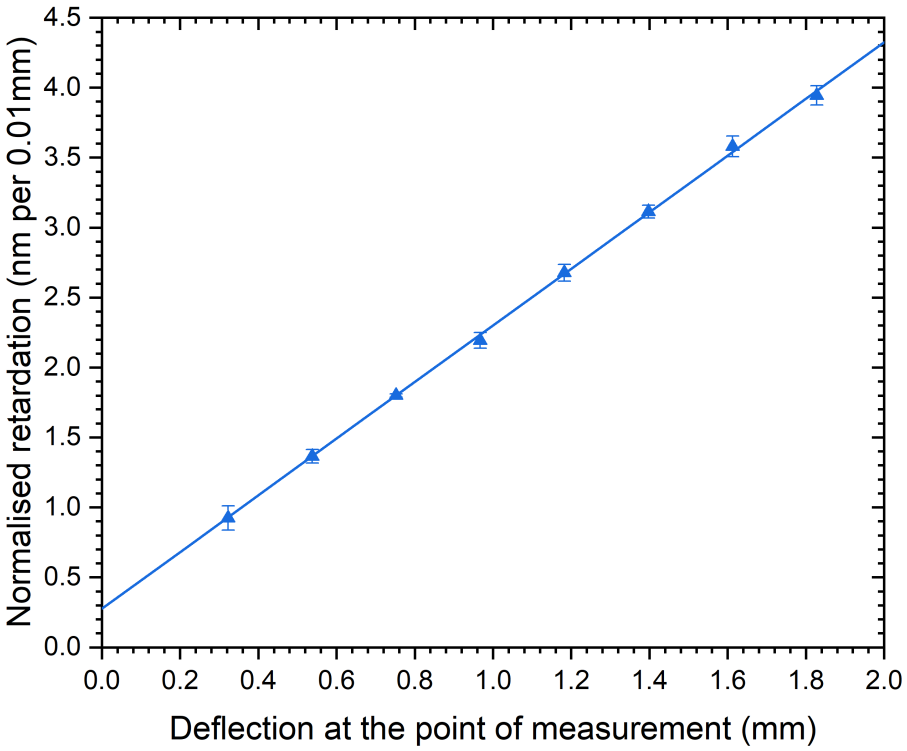


Figure 3.34: Normalised subtracted retardation of DOE3, the solid line represents the gradient with the value used as photoelastic magnitude. The line extends to the y-intercept that was used to determine the shape of the response.

Finally, Initial retardation, normalised for direct comparison, was measured from a zero-load image from the GFP1600. This analysed residual strain within the coating and is demonstrated in figure 3.35.

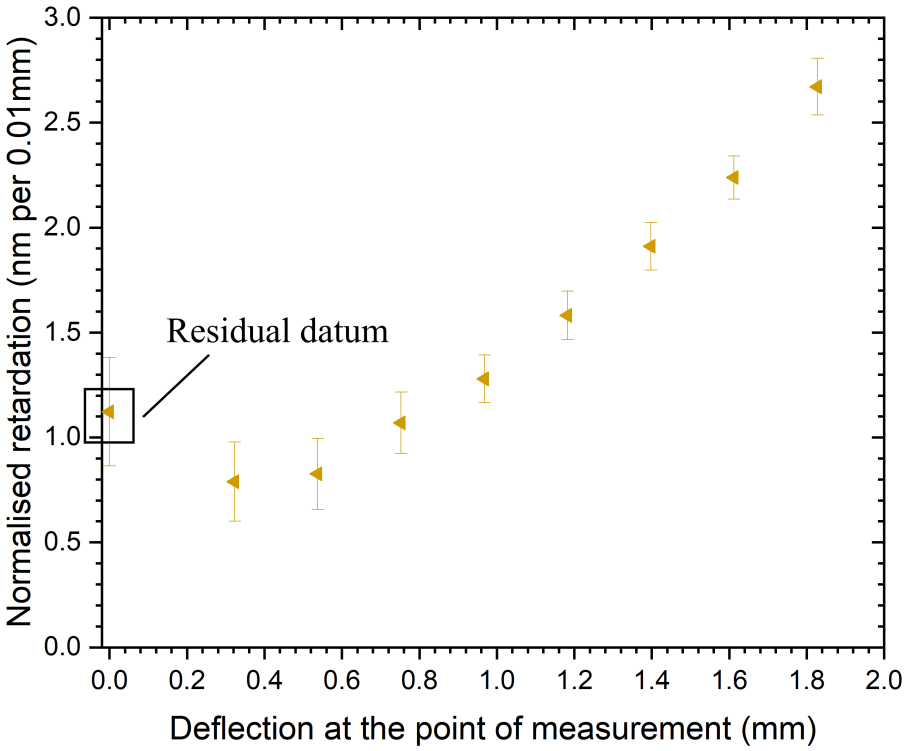


Figure 3.35: Normalised retardation without the subtraction applied for DOE6. The highlighted datum point indicates where initial retardation measurements were taken from.

These properties were then allocated a desired target within the DOE design. Photoelastic sensitivity was set to be as high as possible whilst initial retardation and graph intercept were set a target value of 0 nm per 0.01 mm. DOE also allowed the user to determine which property was more important by applying weighting to the properties. Due to the resolution of the GFP1600 being high (0.01 nm) the latter two properties were given a higher importance. Three samples per DOE formulation were created following steps highlighted in section 3.3.1.1. This resulted in three datasets which were all inputted into the same DOE design. A response optimisation facility was called upon which outputted the weight percentage of the resins to create what it evaluated to be the optimised formulation. Five samples per optimised formulation were made and subjected to photoelastic investigations. To determine the compatibility of the optimised formulation, its photoelastic response was measured and analysed.

3.3.2.3 Results and analysis

The DOE formulations cured effectively achieving a hard to the touch coating after 10 passes under the UV light. The entire photoelastic measurement procedure had to be conducted twice as it was

noticed that the micrometer was loose within the cantilever testing rig. This resulted in the applied load being less than expected as the micrometer was shifting in position. Data inputted into the DOE design were extracted from the datasets presented in figure 3.36.

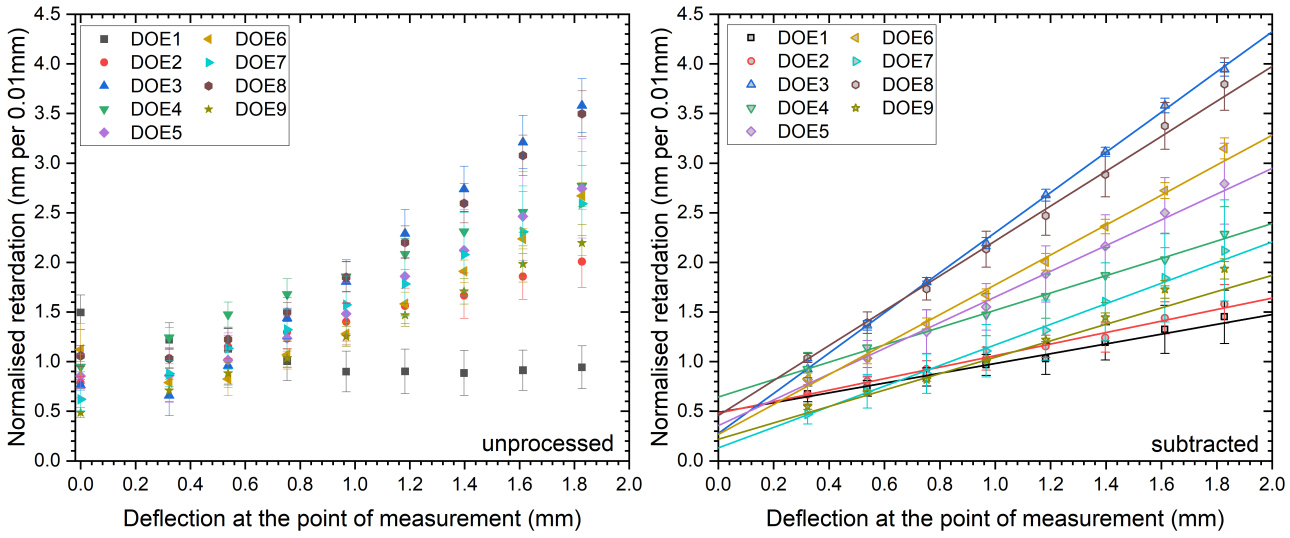


Figure 3.36: Photoelastic responses for all nine Design of Experiments (DOE) formulations. Unprocessed and subtracted ShearMax datasets are observed with the initial retardation, gradient intercepts and slopes.

Both unprocessed and subtracted datasets are observed with retardation values being extracted from the ShearMax images. Uncertainties attributed to each data point are the standard uncertainties calculated from three repeat measurements using three different samples. The standard uncertainty was chosen to aid clarity of the graphs. Initial normalised retardations are observed and the subtracted data set had linear analysis performed with the lines of best fit extending towards the y-intercepts. Linear analysis was performed with errors weighted instrumentally. Numerical values for initial retardation, gradient slope and gradient intercept were recorded and inputted into the DOE package.

The mixture design produced a formulation, OptDOE2, with composition shown in table 3.5.

Formulation Reference	S160 (%)	S140 (%)	S105 (%)	992 (%)
OptDOE2	80.7273	0	17.2727	2

Table 3.5: Composition of the predicted optimum formulation, OptDOE2, as calculated by a Design of Experiments statistical package utilising a mixture design.

OptDOE2 is a high majority S160 based formulation paired with only S105. The formulation was then made and tested following the same methodology. The formulation's photoelastic performance is presented in figure 3.37. The data represents the normalised retardation data without subtraction post processing and with subtracted post processing. The error bars represent the expanded uncertainty of three repeat measurements.

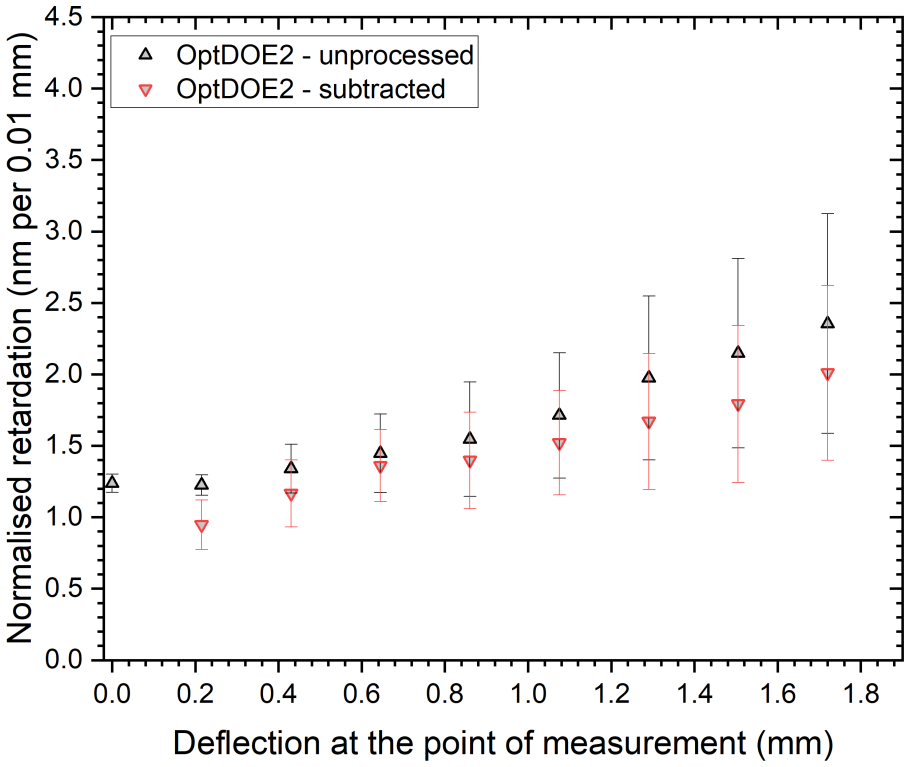


Figure 3.37: The photoelastic response of OptDOE2, a formulation designed through a DOE statistical package. Both unprocessed and subtracted datasets are visible.

Initial observations of OptDOE2, figure 3.37, demonstrated no noticeable differences from a number of DOE formulations, figure 3.36. In fact a number of DOE formulations possessed a response that more closely met the desirable end objectives than the statistically designed formulation.

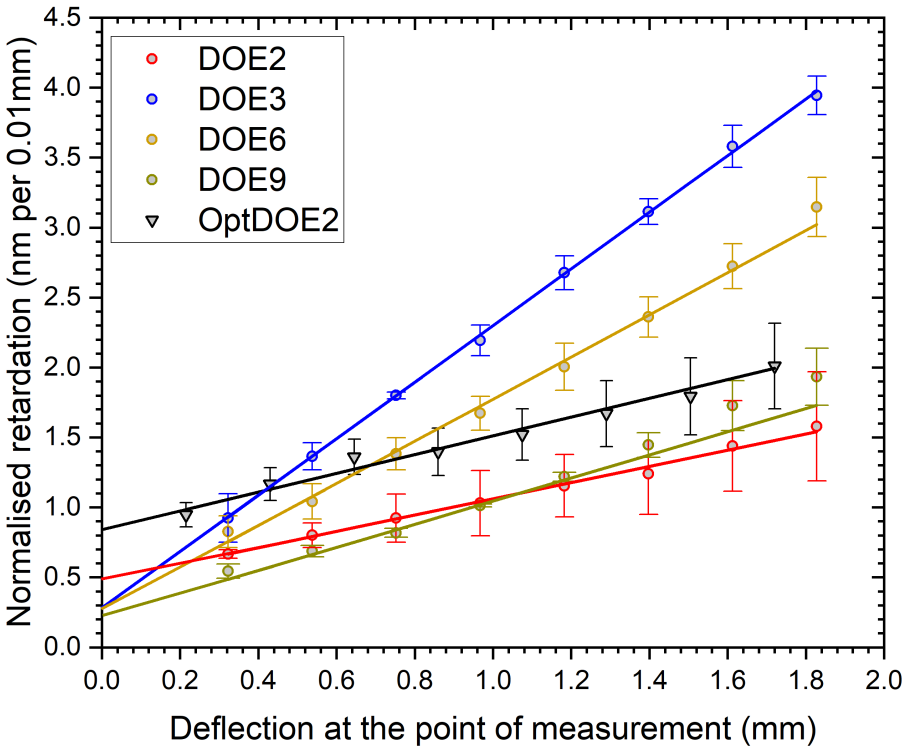


Figure 3.38: Comparisons of subtracted normalised retardation between DOE2, 3, 6 & 9 and OptDOE2.

Figure 3.38 compares OptDOE2 with the formulations DOE 2, 3, 6 & 9. The majority of these formulations (DOE3, 6 & 9) exhibited greater RPE sensitivity shown by the steeper slopes and all possessed an intercept closer to 0 nm than OptDOE2. Figure 3.38 presents all data with the expanded uncertainty with DOE 3, 6 & 9 demonstrating lower variance between data points. The normalised non-subtracted data set is presented in figure 3.39 with the expanded uncertainty was applied to all data points.

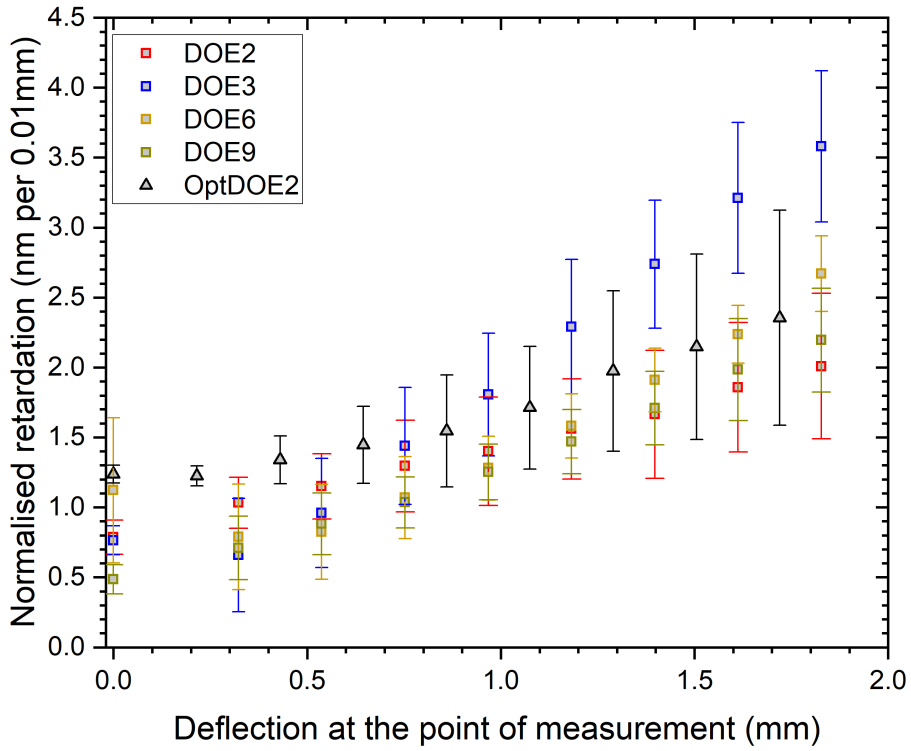


Figure 3.39: Comparisons of unprocessed normalised retardation between DOE2, 3, 6 & 9 and OptDOE2.

OptDOE2, DOE3 & 6 demonstrated relatively high residual retardation that indication initial shrinkage, DOE2 & 9 possessed slight residual retardation which demonstrated no initial shrinkage. The apparent zero compressive residual retardation of DOE2 & 9 were unique observations that provided potential RPSA efficiency improvements that were desirable to Airbus following dicussions of the analysis. It was proposed that a coating that exhibited a linear response without subtraction would speed the data collection time. Practical applications of OptDOE2, and DOE 3, had issues with the formulation being a solid paste at room temperature which would further increase the time of application. Furthermore, the residual retardation of DOE9 was similar to that of PS-1E, figure 3.40.

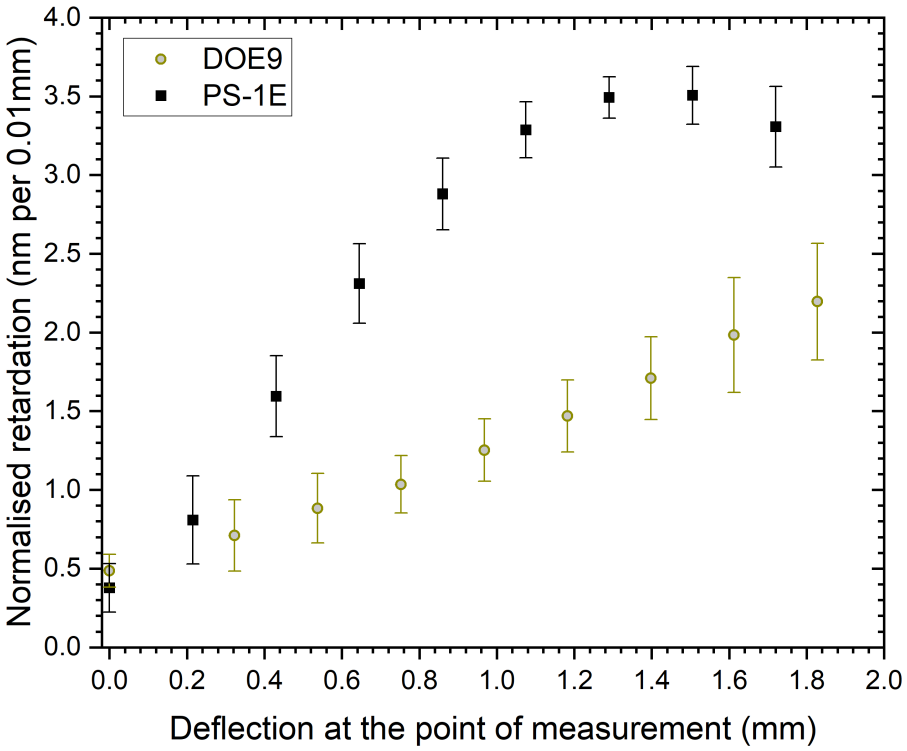


Figure 3.40: Comparisons of unprocessed normalised retardation between DOE9 and PS-1E.

Figure 3.40 compares normalised retardation without post-processing. PS-1E data was taken from section 3.2 with the shape of the response a limitation of the upper limit of the measurable retardation from the GFP1600. Comparisons demonstrated similar uncertainties between DOE9 and PS-1E with the former having an average expanded uncertainty of (19.8 $\pm$ 3.5) % and the latter (14.7 $\pm$ 8.5) %. DOE9 demonstrated possessing various desirable qualities of a photoelastic coating. Whilst not being the most sensitive of the DOE formulation set, changes to applied loads can easily be detected by the GFP1600 and its performance on other attributes of interests outweigh the slight decrease in sensitivity. It was decided to focus on using DOE9 as the 'optimised' formulation.

Overall DOE did not output an optimised formulation due to a number of suspected reasons. Firstly, inexperience of the user may have created a non-optimised design focusing on desirable outputs that were hard to control. For example, controlling the residual retardation was challenging in repeat measurements as demonstrated in chapter 4. Additionally, further mechanisms were investigated that demonstrated that procedures must be followed in order to extract data with high confidence. These included curing time, chapter 4, and surface finish of the sample, chapter 5.2. DOE within this investigation did not factor in these procedures as their effects were unknown at this time.

Optimisation also hasn't considered other important qualities such as application, spray capabilities, or other additives that may assist the formulations application. Future work on optimisation is outlined in chapter 12. The decision not to continue with DOE investigations at this time was due to time constraints and the efficiency of testing OptDOE formulations. Each new formulation required Arkema UK to make and ship to the University slowing down considerably data collection.

In conclusion DOE9 was decided to be a suitable formulation for this research due to properties such as its high photoelastic sensitivity and hand-ability during application. By focusing on one such formulation the research focused on the calibration of the coating in order to translate retardation data into principal strain difference.

3.3.3 Coating calibration

A crucial investigative topic was being able to translate retardation data into principal strain difference. Focusing on one formulation, DOE9, allowed for a more efficient investigation of this topic. Whilst procedures exist to determine the strain-optic coefficient of a material [113,114], they do not account for coating thicknesses of less than 508 μm. This section describes how the use of strain gauges enabled the translation of formulation retardation data into useful principal strain difference.

3.3.3.1 Methodology

In order to determine the strain-optic coefficient K, equation 2.26 was utilised.

$$(\epsilon_1 - \epsilon_2)_p = \frac{N\lambda}{2dK} \qquad \text{(2.26 revisited)}$$

Coating calibration is the evaluation of the parameter K for the photoelastic material of interest. GFP retardation data provided the product of the wavelength of captured light and fringe order whilst a micrometer provided measurements of the coating thickness. The only parameter preventing calculation of K was the principal strain difference. Additional techniques were required to calculate this parameter.

In order to calibrate DOE9, the cantilever beam test rig, figure 3.22, was again used. In order to measure the principal strains, strain gauges were applied to an aluminium beam and the strains were

measured at each deflection where photoelastic data was captured. Due to the COVID pandemic, there were delays and restrictions in the equipment used in this investigation. Only certain types of strain gauge configurations were available and the most suitable was multiple $0/45^o$ planar rosette gauges [115]. These gauges possessed a small gauge length (0.6 mm) that allowed for accurate measurements of the strain at the point that they were adhered. As a result, multiple gauges were needed to measure each individual principal strain. A standard application process was utilised for strain gauge application onto the top surface of the beam. This surface would be where a photoelastic coating was applied.

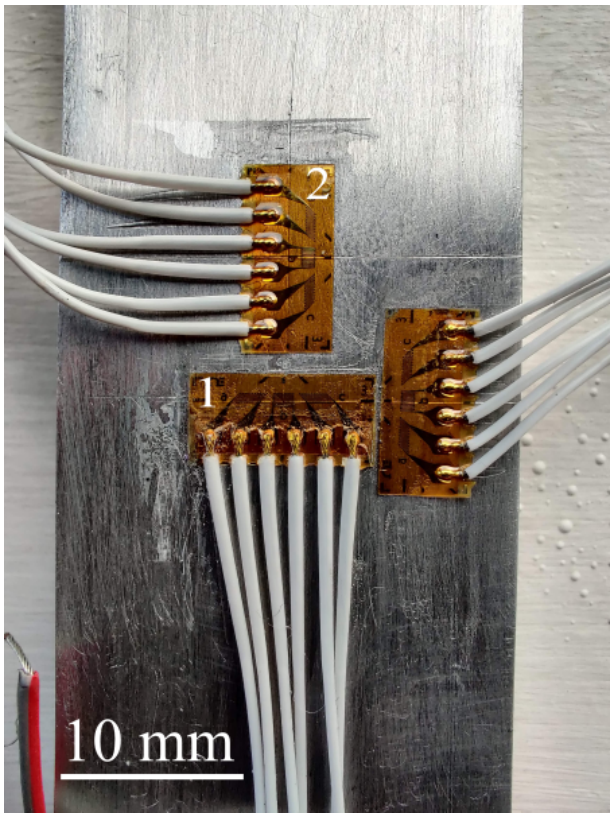


Figure 3.41: Configurations of strain gauges used the measurement of the principal strain difference. Gauges labelled 1 and 2 were used.

Figure 3.41 presents the strain gauge configuration used to measure principal strain difference. Only gauges 1 and 2 were used as it was deemed that edge effects could have induced inaccuracies in the measurement. The middle gauge was used to record the principal strains within the beam however due to the size of the gauge (10.5 mm) the space between them was $\sim$ 8 mm. Therefore the measurement of the exact principal strain difference could not be made accurately and a degree of uncertainty was present in the data. However, as the first principal strain was deemed to have

the most impact on the principal strain difference, the configuration was predicted to give a good indication of the value of K. A slight error was noticed as gauge 2 was positioned slightly off-centre in relation to gauge 1's middle gauge. In spite of this observation, as the middle gauge was relatively far from an edge the measurement of the strain value was deemed acceptable.

To gather strain data, terminal wires from the strain gauges were connected to a NI-9235 input module [116] that outputted the strain data through the use of a LabVIEW program on a personal computer. At each deflection interval, data was collected for several seconds at a sample rate of 1000 Hz. The captured data were reduced to a single average value for each principal strain which were then subtracted from one another to produce the principal strain difference at that deflection. This was repeated three times to calculate the uncertainty in the measured strain.

In order to calibrate the coating, equation 2.26 was rearranged to equate K to a single fraction, equation 3.1.

$$\begin{aligned} K &= \frac{x}{y} \\ where \quad x &= N\lambda \\ y &= 2d(\epsilon_1 - \epsilon_2) \end{aligned} \tag{3.1}$$

Both x and y were calculated separately for each deflection. Retardation data included in x calculation were taken from subtracted GFP datasets. A graph of x against y was constructed with the value of the gradient being the strain-optic coefficient. This method was conducted for both DOE9 and the commercially available PS-1E sheet.

3.3.3.2 Results and analysis

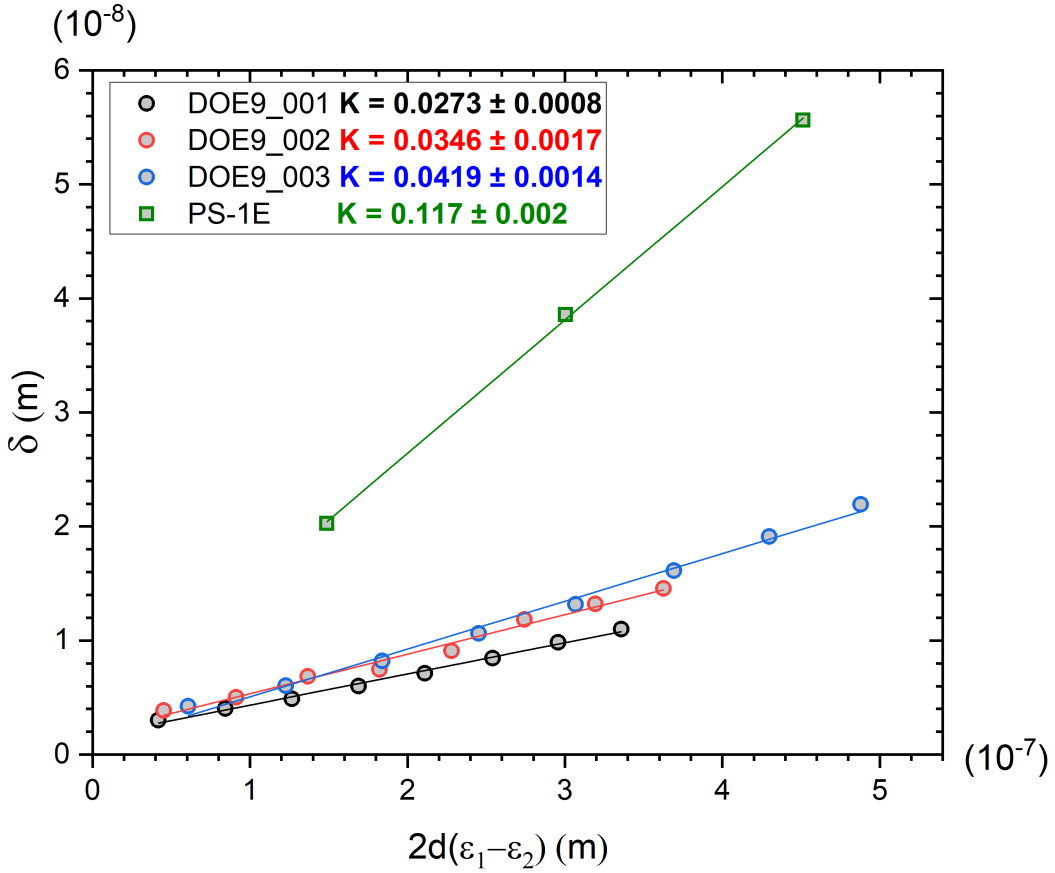


Figure 3.42: Calculations of the strain optic coefficient for DOE9 and PS-1E using the cantilever beam test rig

Figure 3.42 presents the calculations of K for both DOE9 and PS-1E. Three separate samples of DOE9 were analysed whilst the average retardation of three PS-1E samples was calculated. PS-1E was combined as the thicknesses were the same throughout the samples. Uncertainties have not been included in the data points due to issues with the overall results. The error associated with each value of K was calculated through the graphing software's linear analysis function that provides confidence in the linear fit of each dataset. Issues with the outcomes of figure 3.42 are present within PS-1E and DOE9. With the former, only three data points were usable as the GFP1600 was unable to unwrap the retardation at loads greater than 0.8 mm, figure 3.40. Additionally, the measured value for strain-optic coefficient of PS-1E was lower than the stated published value of 0.15. However, the published value does not take into account the material this calibration was performed on as material differences and problems need to be accounted for [55].

3.3.4 Discussion and conclusions

The calculations of K for DOE9 demonstrated a large spread between the three values. By combining the three values with their uncertainties the average value was 0.0346 $\pm$ 0.0073. The calculated value had uncertainty of 21.1 % without taking into account errors associated with each data point. Comparing to published values of K for polycarbonate sheets [7], LPCs [10, 62, 63], and other epoxy coatings [8], the value for K for DOE9 is much lower than expected. Due to the double aromatic ring structure of S160 and its similarities to polycarbonate and LPCs the value for K would be expected to be over a factor two greater than calculated in this research. Overall, the experimental procedure to calibrate DOE9 had reason for concern as the confidence surrounding the calculated values for K was low. Various experimental procedures need to be reviewed in order to extract accurate data that can be used for the calculation of DOE9's K value. For example, the effects of curing will be reviewed, chapter 4; the measurement of coating thickness will be improved upon, chapter 6; and changes experimental procedures explored, chapter 7. All these factors impact the accuracy of the data that is used to calculate K.

Within this section the extensive list of formulations has been narrowed down to a single formulation that possess various desirable properties. The design of this single formulation was performed rationally by adopting statistical packages. Observations made in section 3.2, with regards to resin amounts and their effects on the formulation's physical and chemical properties, made it possible to create an efficient design of experiments mixture optimisation. However, whilst DOE provided a supposed optimised formulation (OptDOE2) the performance was not nearly as desirable as certain formulations used in the design process. Four DOE formulations (DOE2, 3, 6 & 9) demonstrated greater photoelastic sensitivity, closer to 0 nm intercepts and/or greater precision between repeat measurements. The exact reasoning for the failure of DOE in this investigation was not clear. It was suspected that the design itself was not fully optimised not factoring the procedure, developed throughout the following chapters, that generated data of high confidence. Unfortunately due to time constraints, no further plans have been made to repeat DOE optimisation.

The best performing formulation was DOE9 possessing an intercept close to 0 nm, suitable sensitivities to applied load, and confidence surrounding experimental data similar to PS-1E. However, DOE9's standout property was the observed zero compressive shrinkage demonstrated in figure 3.40. The need for the removal of residual retardation within the coating could be omitted allowing for efficient

data extraction. The efficiency is further improved upon by the finding that heat treatment during curing is not necessary. Airbus demonstrated interest in these observations and potential outcomes. As a result, DOE9 will be the focus for the remainder of the thesis. DOE9 will be referred as WF31 going forward.

Chapter 4

The effects of curing time on photoelastic response

This chapter investigates the effects of curing time on the measured photoelastic response of WF31. Repeat measurements showed that the photoelastic response varied significantly between repeat samples, figure 4.1. By reviewing the experimental procedure it was hypothesised that changes to curing procedure had an adverse effect and that an outlined curing procedure needed to be developed.

4.1 Repeat WF31 photoelastic measurements

This section further explores the photoelastic response of WF31 for additional samples. During DOE investigations three samples were created per formulation. As a result, WF31 was originally tested three times using the cantilever beam testing rig on coated aluminium beams. The aim was to produce additional data to calculate WF31's strain-optic coefficient with increased confidence following the same procedure documented in section 3.3.3.1.

4.1.1 Methodology

Eight further samples were created for the repeat measurements and were labelled WF31e-l. To explore alternative coating methods an automated coater [117] was used to try and produce consistently thick samples with a micrometer adjustable applicator.

However, this change in application did not yield consistency but increased the variation in the

measured coating thickness. Setting the thickness of the coating with respect to the sample was easily influenced by user error due to the difficulty of manually calibration the applicator onto the surface of the sample. Additionally, applicator draw speeds affected the final thickness with higher speeds producing thinner coatings. The applicator had to be removed each time for cleaning which considerably increased the time of application. Finally, the coating thickness variation still resembled manual methods with the K-bar. Consequentially, manual application was determined as the preferred method and will be utilised in the remaining investigations. The method used in section 3.3.1.1 was used to coat the remainder of the beams. Curing occurred by passing the beams under a mercury bulb for 10 passes. The photoelastic response was measured by using the cantilever bending rig with the GFP1600 capturing images at certain deflections.

4.1.2 Results and analysis

For WF31d the final coating thickness was manually measured to be 7.5 μm using the automated coater. The coating at this thickness produced no photoelastic response which provided evidence that suggested that there is a limiting thickness required in order to produce measurable data. Taking repeat measurements on the new samples and recording the unsubtracted photoelastic response, the following was observed in figure 4.1.

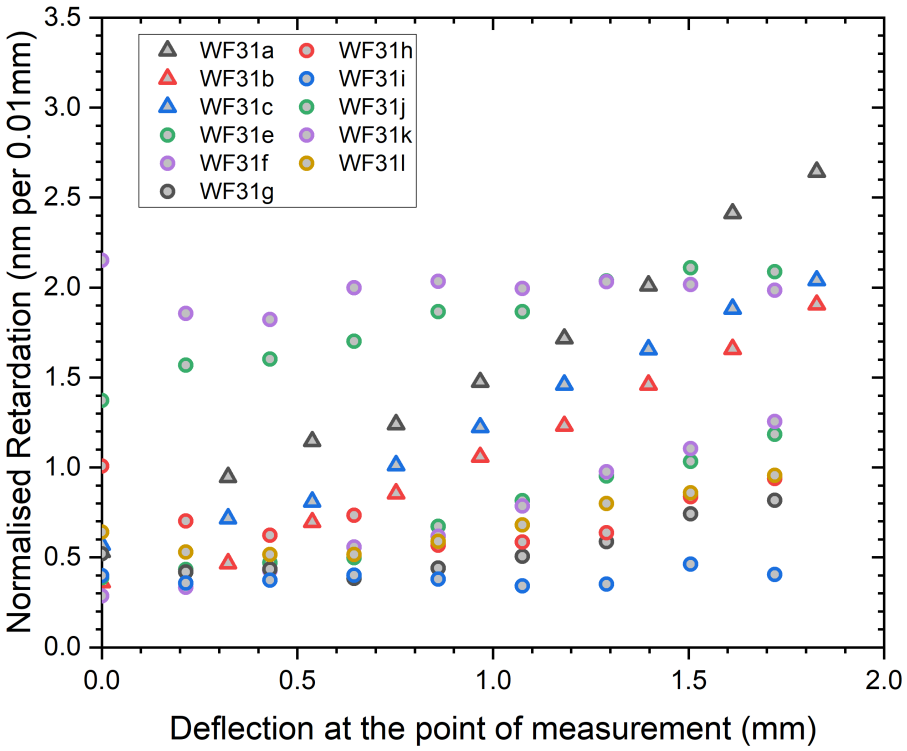


Figure 4.1: The photoelastic responses of all eleven WF31 samples. The measurements demonstrate a variety of unexpected responses.

By reviewing the responses in figure 4.1 it was clear that there were inconsistencies between the samples. Samples WF31a-c demonstrated three separate responses that possessed linear relationships with no residual compression — the desired response. These repeat findings created a strong argument that these responses were not subject to chance occurrences. However, samples WF31e-l presented eight vastly different responses in terms of shape and sensitivity. The cause for these inconsistencies was unclear and required further investigations to determine the cause. As the methodology for sample creation and photoelastic investigation was kept the same, it was believed the cause may occur within the procedures that have been overlooked. One such procedure was the curing time.

4.2 The effects of curing time on photoelastic response

Within this investigation the effects of curing time on a formulation's photoelastic response was explored. These investigations were made to determine if a link could be established between curing times and the inconsistencies discussed in section 4.1.

It is hypothesised that curing time has an effect on the photoelastic response of a formulation as the level of cure completion, known as cure conversion, would change the mechanical properties of the coating [118, 119]. UV curing at different times has an effect on the cross-link density of the formulation. As the coating time increases the material would become more rigid as the cross-link density increases. This change could result in differences within the photoelastic response of the material by changing the coating's strain-optic coefficient thus changing its sensitivity [55]. These investigations have not been previously discussed due to differences in cure mechanisms. Two-part epoxies retain the curing process as the components are mixed together. The majority of the cure progress of the UV curable formulations is a result of UV light irradiation. Whilst the formulation has dark cure capabilities, curing after irradiation of light, these processes are slow in comparison as demonstrated in section 4.2.2. Reviewing Hubner's research on LPCs [10] a much involved curing process was utilised with baking stages to ensure completion of cure.

4.2.1 Methodology

Investigating the effects of curing time followed the same sample creation and photoelastic experiment procedures as summarised in section 3.3.3.1. However, within this experiment the time that sample was held under the UV light was measured rather than passes under the UV light. The conveyor belt of the UV curer was stopped and the sample was placed underneath the Hg bulb to cure for a set amount of time. Using a stopwatch, samples were cured for 5, 10, 15, 30, 45, 60, 90 and 120 seconds. Five sample sets were created resulting in 40 total samples. These samples were then subjected to wait times of between 1 — 4 hours and 24 hours. The 1 — 4 hours wait time was to simulate how industries would potentially use the coating in their reflection photoelastic stress analysis. The 24 hours wait period was to determine if there was any change due to additional curing that may occur after the initial UV light irradiation. If the effects of a longer wait period are noticeable then any repeat measurements would possess errors due to the changing photoelastic response.

The responses were normalised per coating thickness and deflection of the aluminium beam. These calculations were performed to allow for statistical analysis in the form of paired and independent t-tests. By performing t-tests on a variety of dataset combinations, the population means can be compared and determined if they were statistically significant or insignificant. The former

describes the situation where the datasets **reject** the null hypothesis, there was no difference between comparisons. The latter describes the situation where the datasets **accept** the null hypothesis, there was a difference between comparisons. T-tests were performed using excel and origin graphing software.

4.2.2 Results and analysis

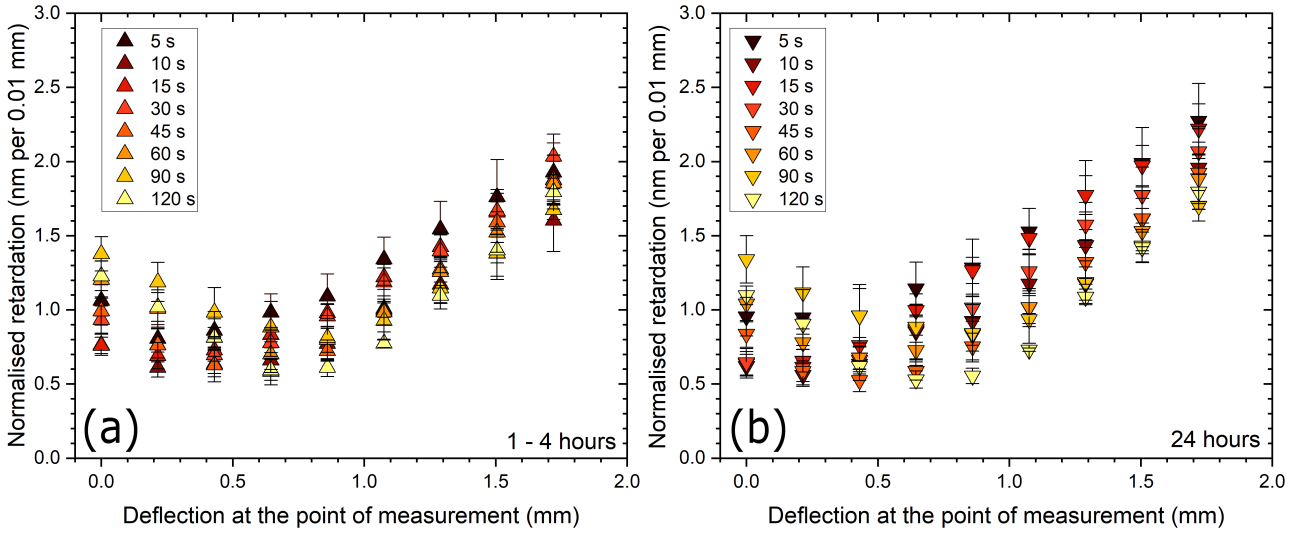


*Figure 4.2: The photoelastic responses of five sample sets at various cure and wait times of either 1 — 4 hours **(a)** and 24 hours **(b)**. Subtraction post-processing has not been performed.*

Figure 4.2 presents the photoelastic responses of the five sets at both wait time periods. The data points represent the mean of the five sets with the error bars representing the standard uncertainty. Prior to normalising for beam deflection, a subtraction facility, section 2.3.9.1, was called upon to remove initial retardation values from the deflected datasets, figure 4.3.

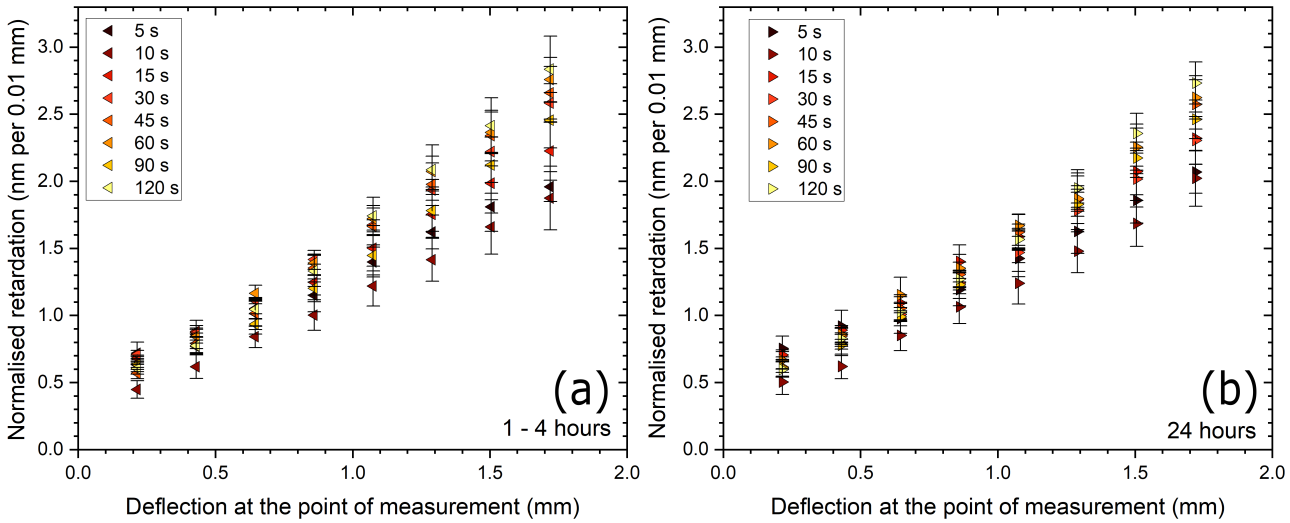


*Figure 4.3: The photoelastic responses of five sample sets at various cure and wait times of either — 4 hours **(a)** and 24 hours **(b)**. The resdiual retardation has been subtracted from each data point.*

Paired and independent t-tests were performed on the subtracted responses that were normalised per deflection. In total 18 comparisons were made between two datasets. These included comparisons between the 1 — 4 hour and 24 hour wait times and individual curing times with the same wait periods. These were then conducted for each sample set individually resulting in 90 paired t-tests being performed. The t-tests of the most significant comparions is presented in appendix D.

Figures 4.2 and 4.3 illustrate a number of photoelastic responses that are similar in shape but appear to possess variable photoelastic sensitivities. Statistical analysis is an important tool as it removes the human bias of believing that these responses are similar and insignificant. By performing paired and independent t-tests two conclusions were made:

1. No difference was observed in the photoelastic responses for longer curing times (>30s) between the wait periods.

2. By performing t-tests on samples within the same sets and comparing the verdicts, no clear trend was observed.

The former conclusion was an important finding. Given cure time is long enough, the wait period between repeated experiments should not affect the photoelastic results. This is important if repeat experiments are required over a certain time period. The latter conclusion does not present a clear finding. However, it described that differences do exist between different cure times, although the

differences are not enough to fully account for the inconsistencies presented in section 4.1. These differences include significant changes in the photoelastic response demonstrated in figures 4.2 and 4.3. Nevertheless, it has shown that samples need to be made with a procedure that enables maximum cure conversion to achieve more consistent samples. This will be explored next.

4.3 Maximising cure conversion

This section reviews various techniques used to determine the cure conversion of the UV curable formulation WF31. As discussed in section 4.2, different cure times can produce variations in the measured retardation resulting in increased uncertainty. A procedure that produces a coating with a consistent cure conversion must be established to remove this imprecision. During this investigation Differential Scanning Calorimetry (DSC), Attenuated Total Reflection Fourier-Transform Infrared spectroscopy (ATR-FTIR) and real-time ATR-FTIR were all used to determine when maximum conversion was achieved. Real-time infrared spectroscopy was determined to be the most appropriate technique with both DSC and ATR-FTIR providing no conclusive data. Methodology and results for DSC and ATR-FTIR investigations is documented in appendix B.

4.3.0.1 ATR-FTIR

Attenuated total reflection (ATR) is used alongside infrared spectroscopy to enable the collection of an infrared spectrum of a sample, in a liquid or solid state, without the need for further sample preparation. Within ATR the changes that occur to an internally-reflected infrared beam as it makes contact to a sample material are quantified. An infrared beam, from the FTIR spectrometer, first interacts with a crystal, located within the ATR accessory attached to the spectrometer, which has a high refractive index. At a certain angle of incidence the light internally reflects within the crystal creating an evanescent wave which extends into the sample material positioned above. This wave penetrates at different depths depending on the beam's wavelength and angle of incidence. The information on how the evanescent wave interacts with the sample is carried by the internally-reflected infrared beam which is directed to a detector which processes the infrared spectrum. This is illustrated in figure 4.4.

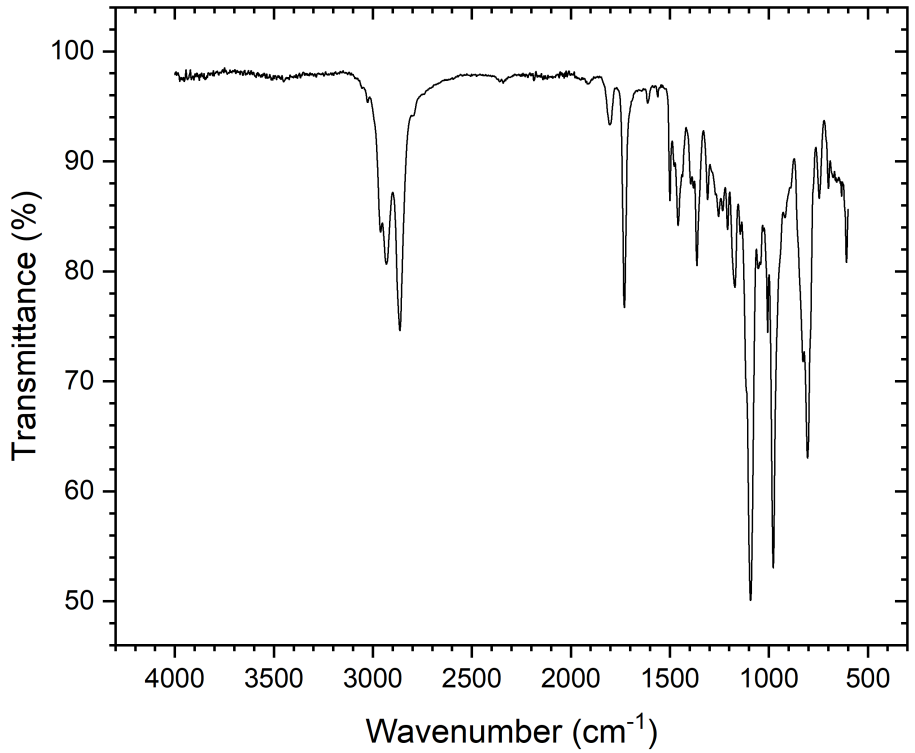


Figure 4.5: Example infrared spectrum of the uncured UV curable formulation WF31. Various peaks are observed at different wavenumber ranges

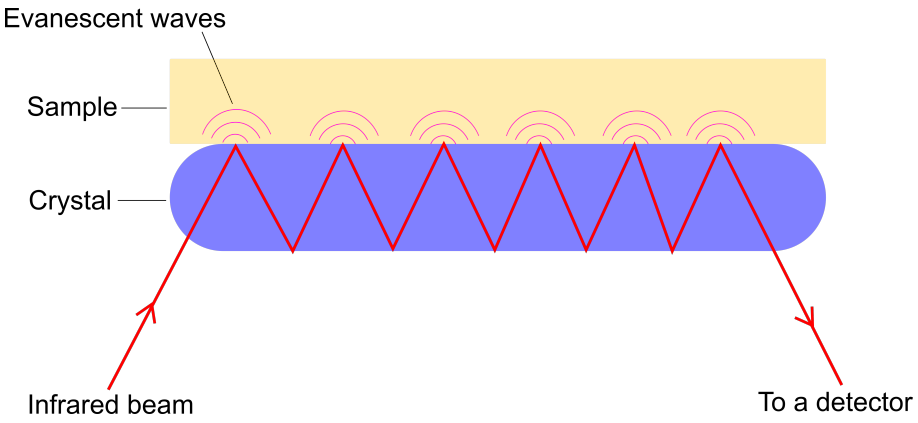


Figure 4.4: A diagram of the attenuated total reflection (ATR) sampling technique used alongside infrared spectroscopy. An infrared beam internally reflects in a crystal and produces evanescent waves at the surface of the crystal. These evanescent waves penetrate into the sample at different amounts depending on the incident angle and wavelength of light. The information of the interacting wave is passed along the beam to a detector.

ATR-FTIR spectra provide users with a 'molecular fingerprint' of a sample of interest. As the apparatus cycles through wavenumber the transmittance is recorded and peaks will occur at various wavenumber ranges. An example spectrum of uncured WF31 is shown in figure 4.5.

The peaks demonstrated in figure 4.5 express different functional groups. In the context of this research the functional groups of interest include the epoxy conversion, 770 — 820 cm^{-1}, and the oxetane conversion, 950 — 1000 cm^{-1}. As the sample material varies in cure conversion the peaks of interest will diminish or increase in size. In order to calculate cure conversion, the peaks of interest are first normalised by a peak that resembles a reference functional group that will not change during the curing process [120]. This is to account for any transmittance changes that may occur due to issues with contact between samples and the FTIR crystal. One such group is a carbonyl species that is observed at 1720 cm^{-1}. The following equation is then used to calculate cure conversion for either epoxy conversion or oxetane conversion

$$C\% = \left(1 - \left(\frac{A_{interest}/A_{carbonyl}}{A_{initial}/A_{initial\,carbonyl}}\right)\right) \times 100 \tag{4.1}$$

$$where\ A = 2 - log(\%T)$$

where $A_{interest}$ is the absorbance of a group of interest (epoxy or oxetane) of a partially cured sample; $A_{carbonyl}$ is the absorbance of the carbonyl peak measured using the partially cured sample and $A_{initial}$ describes the absorbance peak of interest of an uncured sample. For this equation, transmittance, $\%T$, has been converted to absorbance.

Real-time ATR-FTIR is an extension to ATR-FTIR and is used to study the kinetics of cure reactions triggered via light. In this research, resin formulations undergo a photopolymerisation reaction through the irradiation of UV-C (100 - 280 nm) light. In real-time ATR-FTIR setups, a light source is positioned above the crystal of the ATR attachment of a FTIR spectrometer. An uncured sample is placed on top of the crystal and a light source triggers the curing process of the sample. Using the same principles of ATR-FTIR, the reaction can be monitored in real-time to provide a detailed account of the cure conversion through the irradiation time.

4.3.1 Methodology

This investigation took place at Arkema's Photoinitiator Centre of Excellence [121] using a Nicolet iS50 FTIR spectrometer from ThermoFisher [122] with a modified Specac Golden Gate ATR acccessory [123]. The Golden Gate accessory allowed for the output lens of the UV light source's fibre cable to

be securely positioned where the sample clamp would usually be. There were panels of tinted glass to reduce stray UV light. The light source was an OmniCure Series 2000 spot UV curing system from Excelitas [124] which housed a mercury bulb. The light from the bulb was directed directly above the ATR crystal through the use of a fibre cable. The entire setup during operation is shown in figure 4.6.

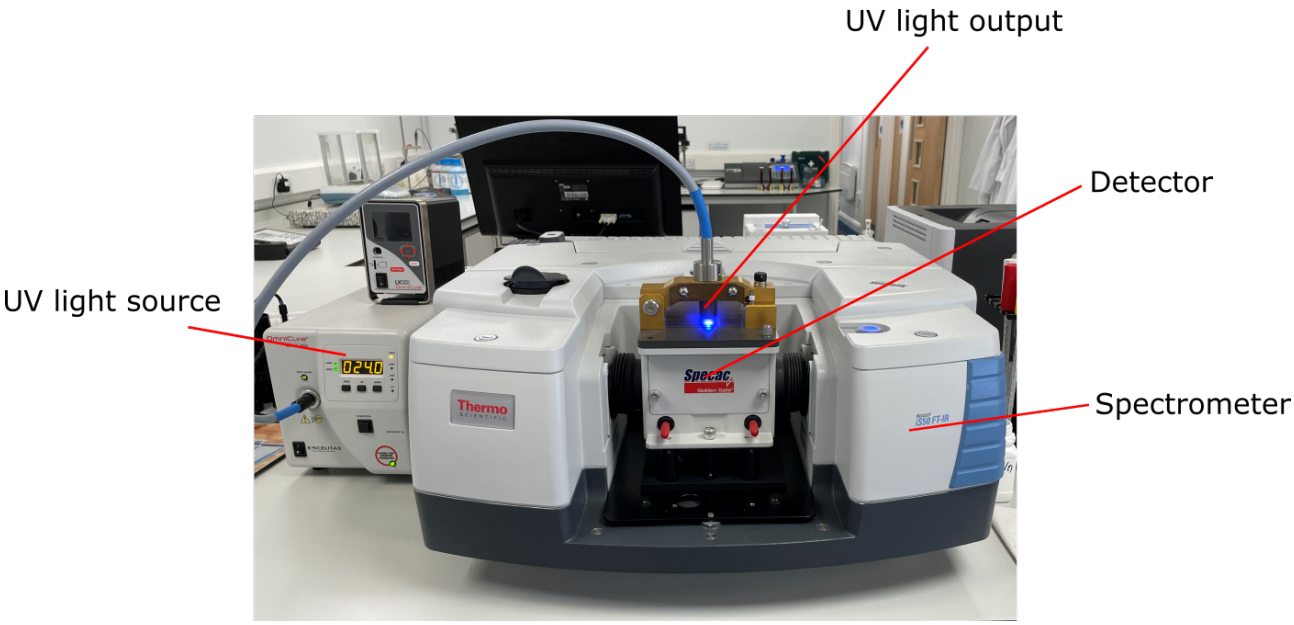


Figure 4.6: Real-time ATR-FTIR apparatus. The modified ATR accessory is positioned in the FTIR spectrometer. A fibre cable is directing the light from an external UV light source.

Prior to operation, the FTIR spectrometer needed to be filled with liquid nitrogen to provide cooling to the sensor. Real-time FTIR scans at very fast speeds required liquid cooling to remove noise. Also, if high temperatures were present in the detection housing an increased moisture content would be present resulting in reduced sensitivity, resolution, inaccuracies in the gathered data and potential malfunction of the equipment. The external light source required ten minutes for the lamp to heat up and the operation of the light source was controlled via a computer programme. The user controls, for the light source, included the exposure time and iris control. Exposure time was the time in which the lamp would remain on, this was kept to 100 s in this investigation. Iris control allowed the user to roughly change the intensity of the light by restricting the light output by closing the iris by a certain percentage. This effectively changed the dosage of the bulb, however the exact dosage amount could not be extracted without a specialised radiometer which was not available at the time of investigation. For this research, iris percentages of 30, 50, 80 and 100 % were chosen.

This was to generate a range of cure conversions using various dosages. This information could then be used to assist in the design of curing procedures in an industrial setting.

After the initial setup, a background scan was performed by the spectrometer which occurred before every sample. The ATR crystal was first cleaned with acetone and, using a pipette, a small amount of liquid formulation was placed a short distance from the ATR crystal. A number 6 k-bar then spread an approximately 50 — 80 μm thick layer over the crystal and the light source was positioned above awaiting user input. A spectrometer scan was performed, scanning a range of 650 — 4000 cm^{-1} every 0.05 s for just over 100 s. As there was no internal trigger between the FTIR software and light source software, the light source was turned on manually once the FTIR scan was running. Once complete, the cured coating was scraped carefully from the crystal using a sharp razor blade.

Due to equipment issues and time constraints the experiments were performed on two separate occasions by the author and technicians at Arkema UK. Analysis was performed by the author.

4.3.2 Results and analysis

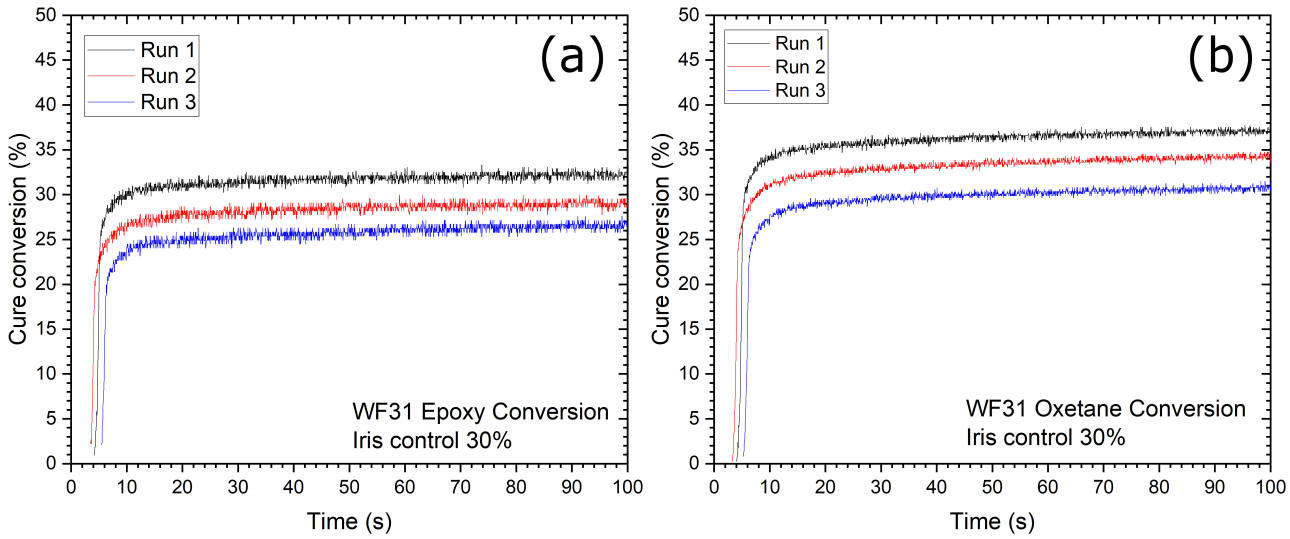


Figure 4.7: Graphs of epoxy and oxetane cure conversions using real-time ATR-FTIR spectroscopy. The UV light output was reduced with an iris aperture of 30 %.

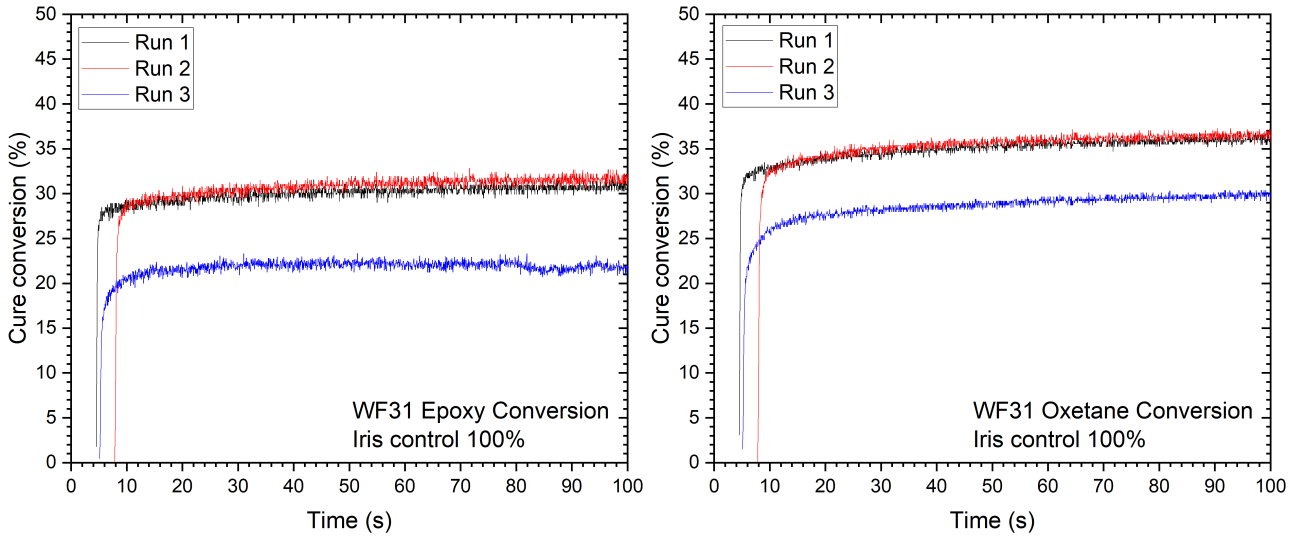


Figure 4.8: Graphs of epoxy and oxetane cure conversions using real-time ATR-FTIR spectroscopy. The UV light output was reduced with an iris aperture of 100 %.

Figures 4.7 and 4.8 presents the change in epoxy and oxetane cure conversion during 100 s of UV light irradiation. The dosage of UV light was altered by an iris control of 30 % and 100 % openness respectively. At each user defined iris control percentage, three runs per formulation were conducted and presented. The important findings were that the max cure conversion, for each resin type, was achieved in approximately 10 — 20 s and that the max conversion appeared to be unaffected by the dosage of the light source. However, the results demonstrated poor precision in certain runs with a max achievable conversion of only 35 %.

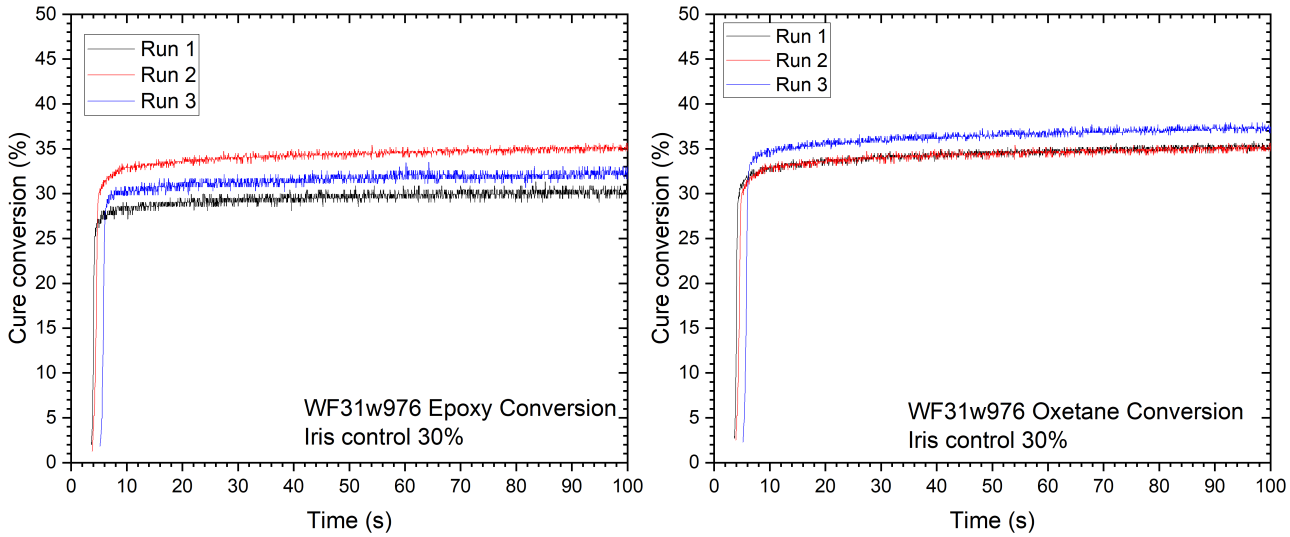


Figure 4.9: Graphs of epoxy and oxetane cure conversions using real-time ATR-FTIR spectroscopy. The formulation's photoinitator was changed to the more efficient SpeedCure 976. The UV light output was reduced with an iris aperture of 30 %.

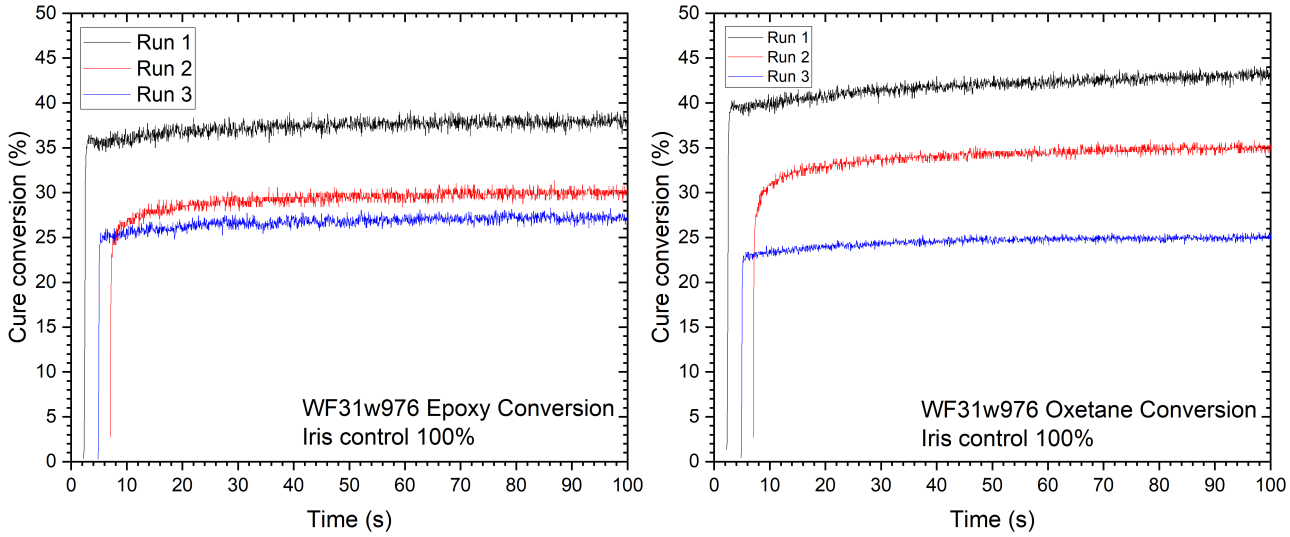


Figure 4.10: Graphs of epoxy and oxetane cure conversions using real-time ATR-FTIR spectroscopy. The formulation's photoinitator was changed to the more efficient SpeedCure 976. The UV light output was reduced with an iris aperture of 100 %.

Figures 4.9 and 4.10 present the cure conversion changes when a more efficient, but more expensive, photoinitator was used. The photoinitator was Arkemas's SpeedCure 976 [125] and the decision to use this photoinitator was to determine if the max cure conversion could be increased. However, the results remain unchanged. Max cure conversion was met within the same time period; dosage had a small influence on the maximum achievable cure conversion; max cure conversion remained,

on average, at ∼35 %; and the precision differs between runs.

4.4 Discussion and conclusions

Real-time ATR-FTIR spectroscopy was the most ideal analytical technique used to measure cure conversion. Its primary advantage was how the spectrometer could record the change in cure conversion every 30 ms throughout a user defined time period. With these data, the exact moment maximum cure conversion was achieved could be quantified. Figures 4.7 — 4.10 demonstrated that the UV curable formulations achieved maximum cure conversion quickly and were not affected by the dosage of UV light. The data demonstrated that maximum cure was achieved after 20 s of UV light irradiation. This finding was kept consistent throughout repeat measurements and between changes of UV light dosage. This provides evidence that these coatings are fast curing, an essential criterion for this research. Another benefit is that dosage was not important which would allow industries to use lamps of lower power resulting in easier and safer curing in any environment. However, the results demonstrated a lack of precision between the calculated quantity of maximum cure conversion for both oxetane and epoxy groups within each formulation. For WF31, epoxy max conversion was between 21 — 32 % and oxetane max conversion was between 27 — 36 %. For WF31 epoxy max conversion was between 25 — 37 % and oxetane max conversion was between 24 — 42%. The exact reasons for this imprecision was unknown however several factors could be the cause. The analysis was performed on two separate occasions by two people due to time constraints on using the equipment. As a result, runs 1 and 2 was performed by the author whilst the remaining run, run 3, was performed by technicians at Arkema. Human error could be the result of such differences seen in figure 4.8. Also, the small area of the ATR crystal, 4 mm^2, could potentially be an issue as prior to curing, there are several kinds of monomers, PLS chemical components and oligomers within the UV curable formulation. After curing, there will more polymers added to the matrix of the sample as not all the starting materials will be converted. Any of these could contribute to variation in the cure conversion measured using this technique.

As discussed in section B.0.3.1, the UV curable formulation contains many substructures that change into polymers or exist with newly formed polymers as the cure progresses. It could be possible that the small area of analysis of the ATR accessory was not capturing the bulk of the formulation as it cured. As a result, more repeats would be necessary to extract an accurate average of maximum cure

conversion percentage. The percentage range are also not near to 100 %. This is understandable considering the length of the monomers and the introduction of the mono-functional S140 that would essentially prevent the polymer chain increasing in length during curing. Increasing cure conversion would increase the coating stiffness and therefore photoelastic sensitivity [55]. However, this research is limited by the materials available. Removing S140 could potentially increase the stiffness but the viscosity would increase. There needs to be a balance between sensitivity and ease of application. This is discussed in future development, chapter 12.

This chapter has successfully determined the time required for the UV curable formulation to achieve its maximum cure conversion. By performing real-time ATR-FTIR investigations the cure conversion percentage was calculated three times per second until saturation resulting in an exact time period for completion. It was determined that the formulation WF31 requires upwards of 20 s of UV light irradiation to achieve maximum cure conversion. Furthermore, this time period remains constant irrespective of the dosage of the UV light resulting in increased compatibility with UV curing systems.

Previously, samples were made without regard to the exact time of cure in favour of using passes under a UV light. Whilst these procedures enable consistent cure times, the exact time needs to be calculated taking into account light illumination area and belt speed. When transiting into industry, a conveyor system will most likely not be the most appropriate curer to use especially when considering large components and assemblies such as aircraft wings. Therefore establishing a guideline for time of cure is an important measurement. Additionally, due to the curing behaviour of the applied coating the physical appearance and feel at cure times as short as 2 s gives the impression of cure 'completion'. By not understanding the concept of maximising cure conversion, a user could infer that a hard-to-touch feel and high adhesion to a sample surface from a short cure time would yield optimum photoelastic responses. However, it has been found that cure times do have an unpredictable effect on the photoelastic response. The photoelastic response becomes more consistent at higher cure times ($>$30 s) that is coherent with the formulation achieving maximum cure conversion at 20 s of UV light irradiation. An interesting observation made in section 4.3.2 is the inconsistency in the percentage of maximum cure conversion between repeats. Currently, it is proposed that the small crystal of the spectrometer was not capturing the main bulk of the material during the curing process. However, an important question emerges from these data — how important is quantifying maximum cure conversion? If the maximum cure conversion does

fluctuate, will this have a negative impact on the measured photoelastic data? This was monitored in the following investigations, chapter 5.1 - 8.2.

Chapter 5

Light source placement and reflective backings

This chapter reviews the effects of light source placement on the measured photoelastic data extracted from the GFP1600. It was discovered that for any given deflection, the measured response changed depending on the location of the light source around the sample. It was important to discern what the correct configuration was to guarantee that the correct data was being analysed. This chapter outlines the importance and necessity to post-process captured data to account for parasitic birefringence induced by the coating and apparatus.

Additionally, this chapter focuses on the effects of surface finish to explore the improvement of the signal-to-noise ratio for the UV curable coating. A desirable attribute of reflection photoelasticity is a reflective backing that provides uniform reflectivity with no specular reflections that negatively effect the photoelastic response. This chapter investigates any changes to the photoelastic response as a result of changing the reflective backing. Further investigations then quantified the reflective qualities with an aim to determine an analysis that enabled measurement of an appropriate backing. There is no published literature that explicity states that changes in a reflective backing will alter the measured response. This investigation aims to provide valuable practical information to users performing RPSA.

5.1 Light source placement - preliminary testing

At this point of the research, it was decided to prepare samples for tensile testing. Tensile testing increases the dynamic range of the gathered photoelastic data when compared to the cantilever beam testing rig which was limited to a 0.8 inches (20.32 mm) of deflection at the point of load. Utilising tensile testing would also keep the surface the sample within the same plane throughout the loading scenario instead of it changing when the beam was deflected in the cantilever beam testing rig. This is important as the light path will stay the same throughout the load and any inaccuracies associated with coating bending will be avoided [114].

Tensile testing required the samples to be orientated with its longitudinal axis perpendicular to the ground. Initially one light source was used, positioned above the GFP1600 angled down onto the sample to prevent any direct reflections that occurred whilst positioning the light source at either side of the GFP1600. By analysing the zero-load image of the tensile samples, the measured retardation was much higher than previous zero-load images. Tensile samples had initial retardation values between 15 - 18 nm. This magnitude of retardation was greater than coated aluminium beams that underwent a maximum deflection subjected by the cantilever beam testing rig.

To investigate the cause of these differences the experimental setups were compared. The most noticeable setup difference, that was thought to affect the measured retardation, was the location of the light source that would alter the light path of the reflected light into the GFP1600. The effects of light source placement are reviewed in the following sections.

5.1.1 Methodology

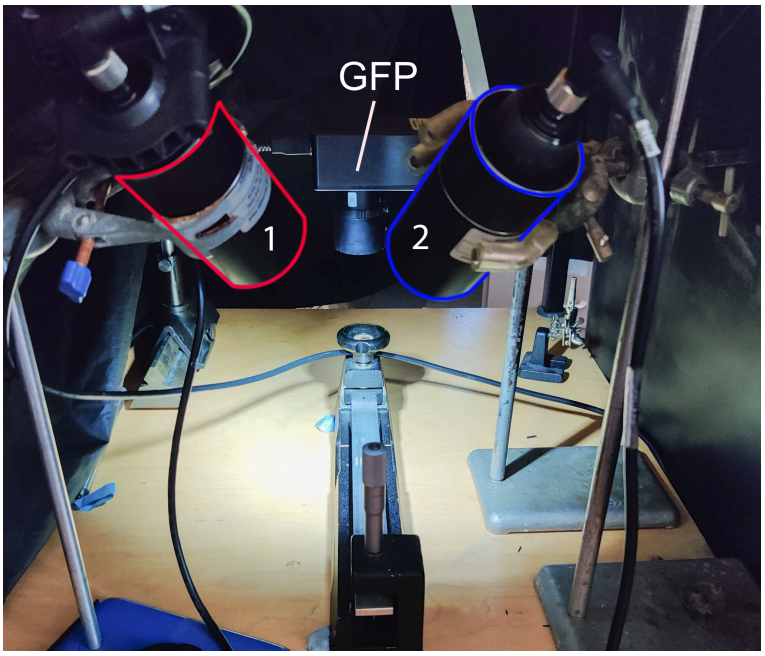


Figure 5.1: The experimental setup for light source placement investigations. The GFP was positioned so the beam was in a horizontal orientation. Two light sources can be seen, labelled 1 and 2. These numbers represent the two positions that were used.

Figure 5.1 demonstrates the experimental setup for light source placement investigations. The GFP1600 was positioned with the imaging lens capturing the coated region of an aluminium beam mounted in the cantilever beam testing rig. Two light sources were positioned at opposite sides of the beam and were labelled 1 and 2. The investigation consisted of performing photoelastic analysis, as documented in section 4.1, for three separate light source configurations. The configurations were light 1 only, light 2 only and lights 1 & 2 together. The shutter speed of the GFP1600 was changed to keep the light levels approximately within 50 camera units (a measurement of light intensity).

Previously analysed samples were used for response comparisons. WF31b, WF31c and WF31e were selected due to their photoelastic responses being comparable in trend - they all possessed linear responses. Responses were only compared within the same sample, due to differences in coating thicknesses, to determine the effects of light source placement. The samples were subjected to bending deflections, at the free end, from 0 to 0.8 in in 0.1 in intervals (chosen due to the scale of the micrometer). At each interval the GFP1600 took an image and the photoelastic data were analysed.

5.1.2 Results and analysis

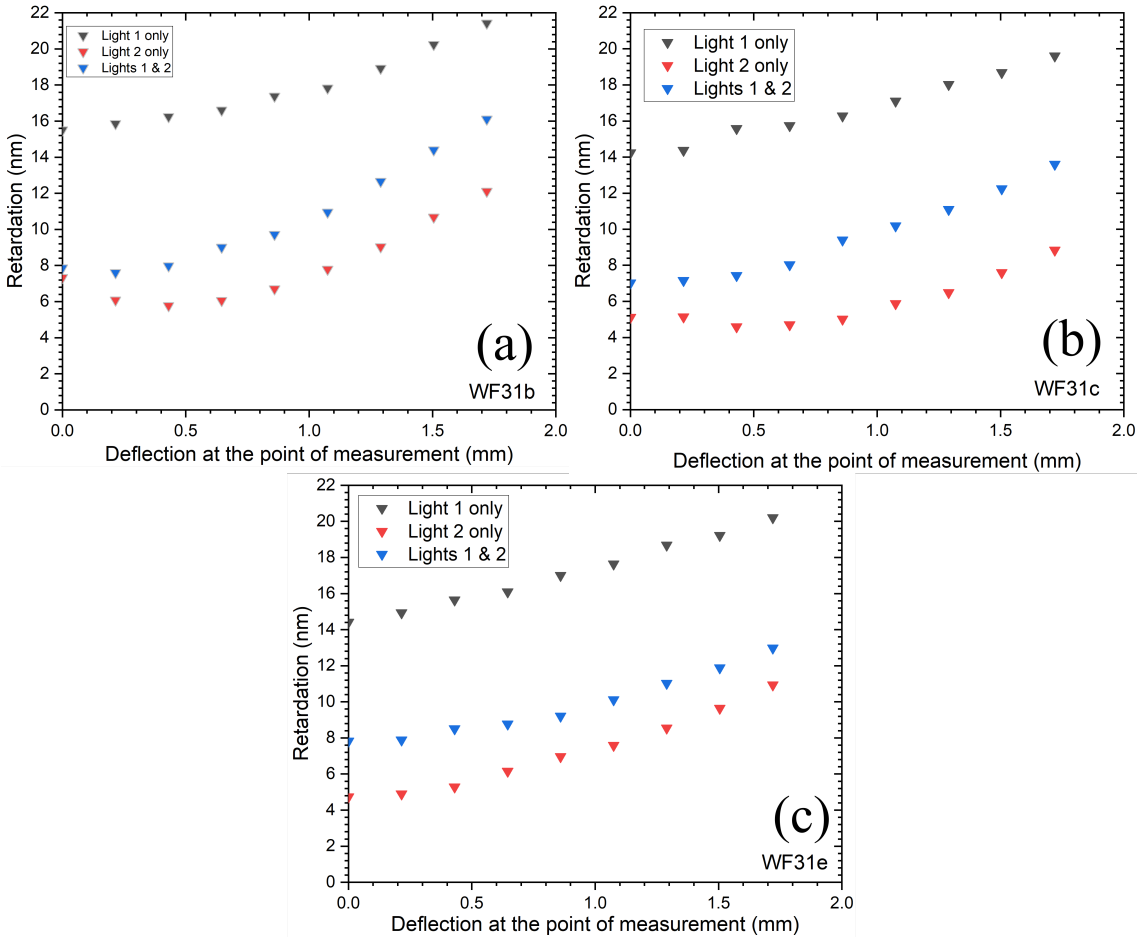


Figure 5.2: The unprocessed retardation data of samples WF31b ***(a)****, WF31c* ***(b)*** *& WF31e* ***(c)*** *using various light source configurations during photoelastic investigations.*

Figure 5.2 presents the retardation data of three different samples using the same UV curable formulation, WF31. Unprocessed retardation is shown on the y-axis and represents the data that was extracted straight from the GFP1600 acquisition software, no post-processing was performed. The x-axis represents the deflection within the beam from which the retardation was extracted from. Three responses per sample were observed with response shape, within the same sample, being relatively similar. However, the retardation values differ considerably when the light source placement changed.

Subtracted retardation data is demonstrated in figure 5.3.

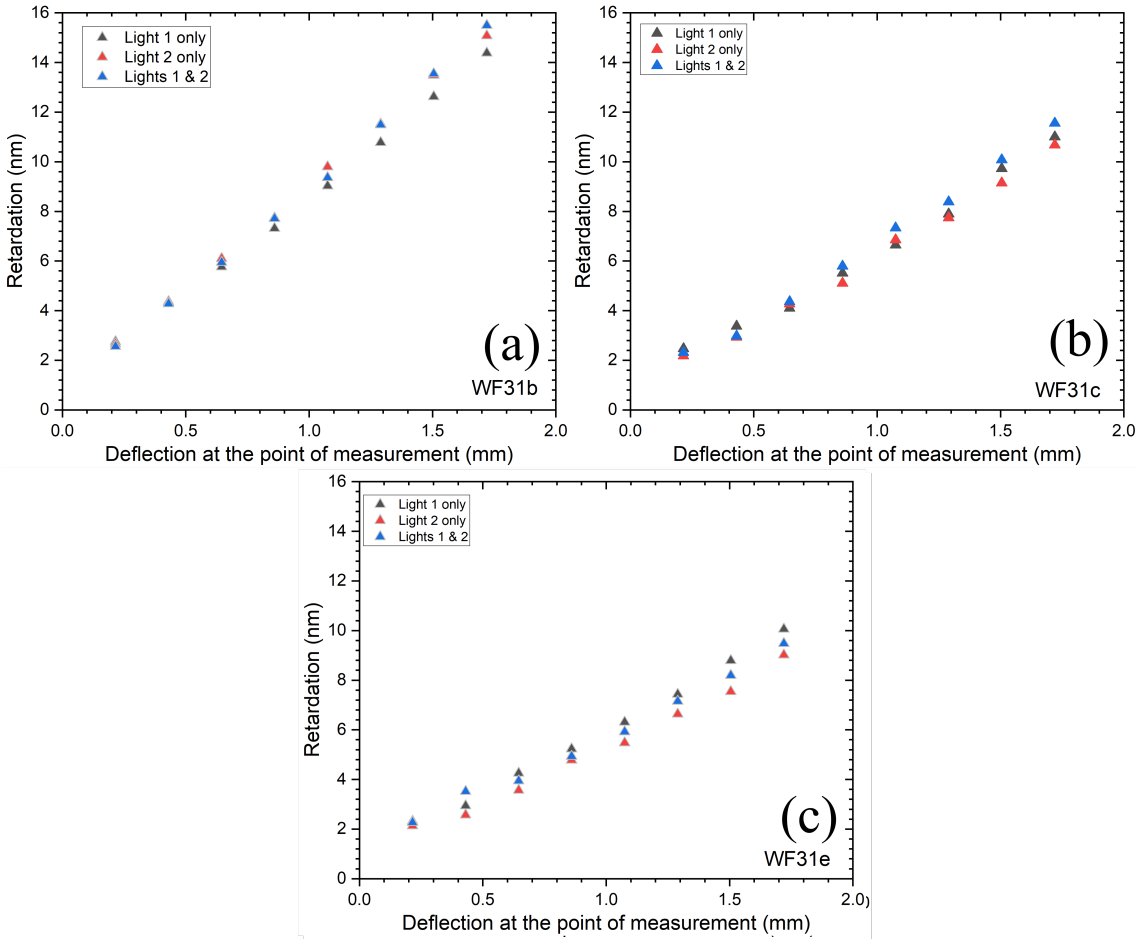


Figure 5.3: The subtracted unnormalised retardation data of the samples WF31b ***(a)****, WF31c* ***(b)*** *& WF31e* ***(c)*** *using various light source configurations during photoelastic investigations. The subtraction post processing facility was performed to remove the initial retardation from each loaded image.*

Figure 5.3 presents the same data as figure 5.2 but with the subtraction post processing facility applied. The responses are now linear with retardation values that are approximately the same.

It was initially determined from figure 5.2 that light source placement matters when using UV curable formulations. Depending on the location of the light source, the measured retardation was different for the same loading scenario. Tests were also performed on PS-1E coated samples to determine the effects of light source placement and the variation of unprocessed retardation was also measured in figure 5.4 towards the lower deflection ranges.

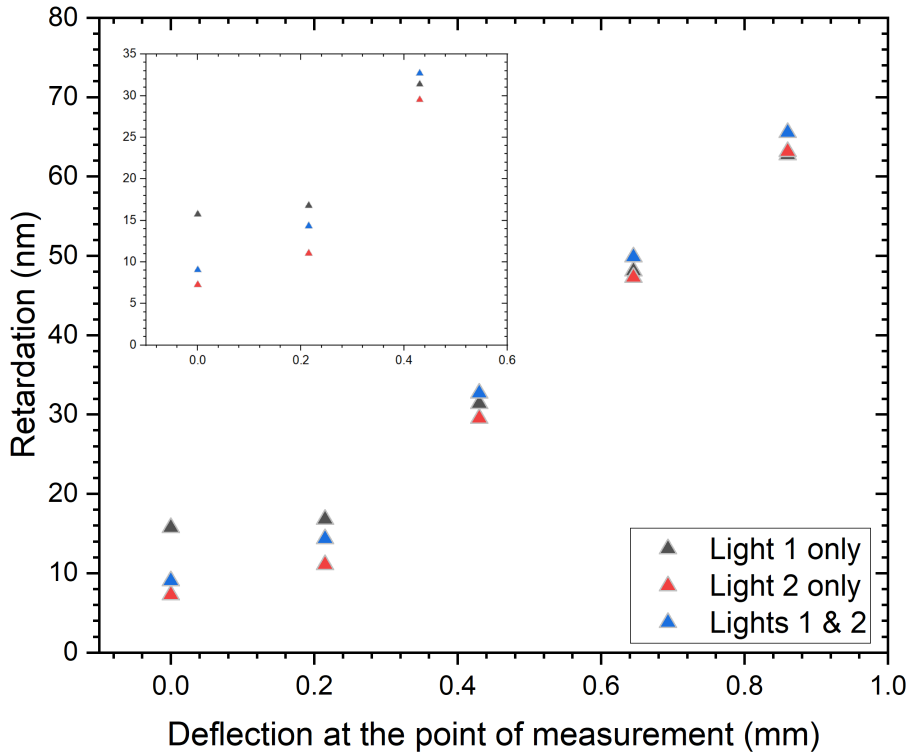


Figure 5.4: The retardation data of an aluminium beam coated with a photoelastic sheet, PS-1e. PS-1e is a polycarbonate sheet, 0.25 mm thick, that was bonded to the aluminium beam through the use of a two-part epoxy adhesive. The retardation data has had no post processing applied.

It is therefore crucial that the correct configuration was established in order to extract the most accurate retardation data. However, the solution to this issue was presented in the form of the subtraction post processing facility.

5.1.3 Discussion and conclusions

Performing subtraction as a solution does not explain the cause but provided a direction to explore. Figure 5.3 demonstrates how subtraction equalises the PE magnitude of the three light positions. As result there must have been a consistent factor to the setup that was providing different photoelastic responses. Initially it was proposed that light path length differences through the coating were attributed to discrepancies in the photoelastic response. Being relatively thin, small changes to path length difference would have a great impact on the resultant retardation. Reflection photoelasticity needs additional consideration to the setup as it is the best practise to achieve normal incidence to avoid introducing inaccuracies in the results [3]. In reality, normal incidence is challenging to achieve without the use of partial mirrors that themselves require corrections complicating the

procedure. It has been stated that angles of incidence and reflection be kept to below 4^o [3] to prevent introducing inaccuracies to the photoelastic response. In practice this is difficult to achieve with the size of the camera and light sources. However, a wide dispersion of light in the current setup satisfies these conditions and discussions with experienced photoelasticians (Airbus, VisEng Ltd and Stress Photonics) did not provide concern for not achieving this setup. However, figure 5.4 still demonstrates the same difference in PE response at low deflections. PS-1E is approximately five times thicker than WF31 at 0.25 mm so it would be expected that the same differences in path length difference would not have much as an effect on the photoelastic response. As a result, the only other factor to consider are the light sources. It has been assumed that the light sources are perfectly circularly polarised especially as they are supplied with the GFP. It is easily overlooked that the light sources could be emitting elliptically polarised light of differing ellipticity. By performing a quick experiment through a reference piece of birefrigent material with a known retardation, it was shown that the light sources are emitting differing degrees of the elliptically polarised light. By switching between the light sources used in this investigation the values of retardation were significantly different. The GFP therefore records the ellipticity as contributions to a photoelastic response and due to its sensitivity (less than 0.5 nm) the slightest change will be detected. Errors due to quarter-wave plate mismatch with incident light wavelength have been reviewed in research by Ji [126]. In this research it was determined that inaccuracies are introduced if the target wavelength of a quarter-wave plate, the optical media forming the circularly polarised light, differs from the outputted light. The introduced error was stated to be less than 0.015 fringes which equates to a retardation value of 9.75 nm (using red light of 650 nm) that is of the order of the differences observed in figure 5.2. It is unclear how the light sources used in this investigation were manufactured however due to them being white light sources it is obvious to understand that mismatch between outputted wavelengths and the optical media must be occurring. Therefore it is vital to correct these issues by performing the subtraction facility in all cases to remove the effects of light source polarisation misalignments. Additionally, the use of the facility enables the user to place the light source in the most optimum position that suits the scenario rather than being constrained to a certain position. This is a very important discovery as it further supports the ease-of-use criterion of the research. By calling upon the subtraction facility a user will not have to correct for placement and repeat measurements can be performed without the need for complicated setup procedures that would require a fixed light source placement. As a result of these findings, the subtraction facility

will be called upon in all future loading tests to ensure the most accurate data is being analysed.

This section demonstrates that in order to extract accurate photoelastic data a user must account for the polarisation state of the light sources used their RPSA investigations. Initially it was proposed that light source placement was a parameter that needed to be controlled based on the results shown in figure 5.2. However, it was determined that the light sources themselves were outputting elliptically polarised light of differing states that were being interpretted as induced retardation. The outcomes of this investigation seem trivial yet would be overlooked by many users especially if the apparatus was supplied with 'circularly' polarised light sources. Furthermore, the quantity of elliptically polarised light disguises itself with the effects of coating residual stresses requiring further work to separate. Within Deltavision, the software used to control the GFP1600, the use of the subtraction facility was able to counteract the inclusion of the parasitic birefringence enabling a user to illuminate a sample in a location that satisifies the needs of the experiment. As a result, a user is not constrained to a certain setup if using this post processing facility. This procedure will be used in all future investigations.

5.2 The effects of surface finish

The aims and objectives was to review the effects on photoelastic response due to changes in the reflective surface. Currently, aluminium samples have been coated utilising only the bare metallic surface as a reflective backing. These surfaces produced non-uniform reflections with surface scratches causing direct reflections that introduce inaccuracies to the photoelastic response. Reviewing existing commercially available coatings such as PhotoStress sheets 2.4.1, these products possess reflective backings with desirable properties. These properties include uniform reflection with no specular reflections dependent on the light source position. PS-1E was used as a comparison and target to various surface finishes determining their effects with an aim to improve signal-to-noise ratio when imaging the UV curable coating.

5.2.1 Methodology

Aluminium samples, alloy 6082 — T6 at dimensions (300 x 25 x 6) mm, were prepared in a selection of different ways to generate unique reflective backings. The surface of three samples were roughly

polished using 220 grit sandpaper. This removed the majority of light surface scratches but left a noticeable grain on the surface. An additional three samples were sandblasted with 60 grit sand to dull the bare metal surface and provide a uniform finish. Three samples were coated with a common commercially available silver metal paint [127]. The paint was chosen to provide a uniform reflective finish whilst being able to withstand the shrinkage effects of the coating during cure. Additionally, the paint is widely available and cost effective. WMG's preliminary research found that acrylic paints was unable to withstand shrinkage during curing causing delamination between the coating and the sample surface. An approximate 150 mm strip at the centre of the samples was painted. A number 3 K-bar (wet film deposit of 24 μm) was used to spread a small amount paint across this section creating a smooth uniform layer of paint. The paint was left for 24 hours prior to a UV curable formulation application to allow the paint to fully dry. Finally, another set of three samples were coated with PS-1E, 150 mm x 20 mm strips following the application instructions provided with the material [12].

Prior to application of WF31 the samples were cleaned with the solvent acetone. The painted surface was cleaned carefully to avoid stripping the paint. Before applying the UV curable formulation and PS-1E, each sample's thickness was measured using a micrometer to provide the sample with a unique identification number based on their measured thickness. All the prepared samples were coated using the same process. A number 6 K-bar deposited a $\sim$60 μm layer onto the sample. The sample was then placed under a Hg lamp for 20 s and stored in a dark place until ready for photoelastic analysis.

The loading procedure for this investigation now switched to a tensile experiment to increase the dynamic range of the strain inflicted on the sample by approximately double that of the cantilever beam testing rig. Utilising tensile testing would also keep the surface of the sample within the same plane throughout the loading scenario instead of it changing when the beam was deflected in the cantilever beam testing rig. The aluminium samples were mounted into a Mayes 100 kN tensile tester with the GFP1600 facing directly at the coated section of the sample. The light sources were positioned both above the coated sample, figure 5.5(a), and either side of the GFP staying within the same lateral plane of the imaging lens, figure 5.5(b).

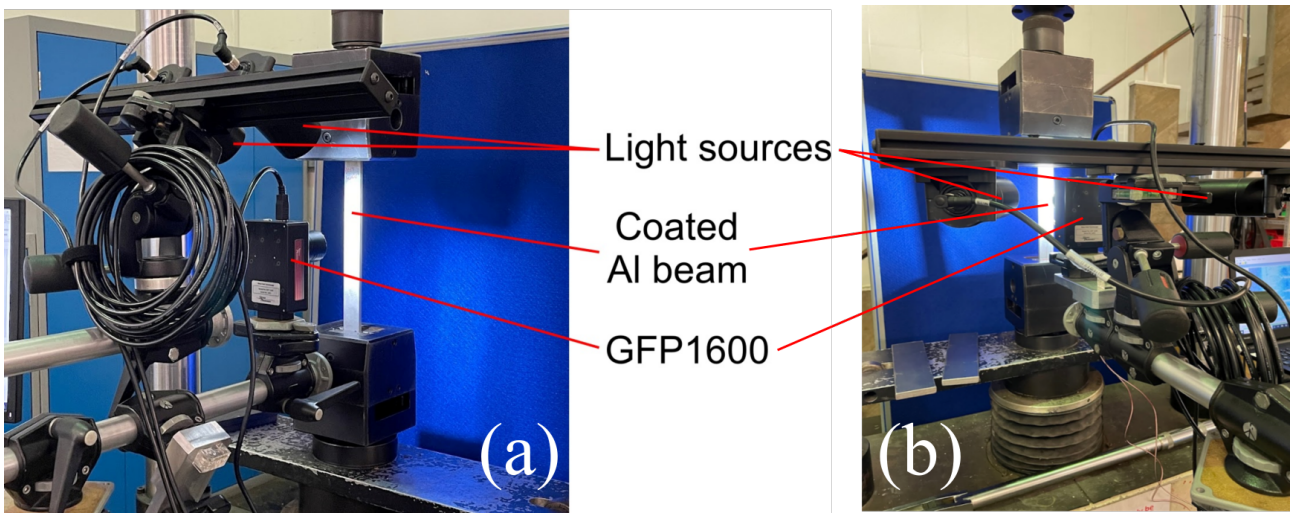


Figure 5.5: Two experimental setups investigating the effects on the signal-to-noise ratio of photoelastic response. The light sources were positioned above the sample and side-by-side within the same imaging plane of the GFP1600's imaging lens.

The choice of light placements were chosen based on the reflection effects observed on the samples. For example, imaging above the GFP1600 would allow for a more uniform reflection for bare metal surfaces, figure 5.8(a). Imaging in plane either side of the GFP1600 allowed for better control of the illumination on the samples. Angles of light placement were not recorded and placed to satisfy a requirement of not achieving saturation due to direct reflections. This procedure was supported by photoelasticians at Airbus and a consultant.

These two setups were used to explore the effects light direction had on the signal-to-noise ratio of the photoelastic response. Prior to load the GFP1600's exposure was altered to achieve a light level between 300 — 1000 arbitrary light units which prevented any areas of saturation within the captured images. Once the desired exposure was set, the sample at zero load was captured with just the top grip engaged to avoid the loads applied when both grips were securing the sample. The Mayes 100 kN tensile tester was electronically controlled using a LabView script and the applied force and the measured deflection were monitored. At force intervals of $\sim$ 5 kN, the machine would be paused and an image captured using the GFP1600. However, pausing the machine caused the applied load to drop rapidly for several seconds until it remained at a consistent value at which an image was captured. The tensile yield strength for aluminium 6082 — T6, the alloy of the samples, was 250 MPa [128]. By measuring the thickness and width of each sample using a micrometer and calliper, the upper force limit of the sample can be accurately calculated to ensure the sample remains

elastic throughout the load. The upper limit for the sample was between 35 - 40 kN. A number of these samples were loaded beyond the yield strength to investigate the coating's performance through photoplasticity. The tensile tester used was difficult to control. Initially, a speed could be manually inputted so that the machine would approach the first 5 kN interval at a controlled pace and then paused. However, once restarted, the machine would revert to its fastest jog speed resulting in a sudden increase in force. The stop and go command would be flicked on and off in less than 1 s periods to ensure the force did not go beyond the desired value. This made repeat measurements impossible for certain loads. As a result, retardation values can be collected with the stated standard deviation calculated through the Deltavision software that acquired and processed the GFP1600 images. Three repeats per sample were used to provide a more accurate representation of the photoelastic response of the coating.

It was clear in the captured images that as the load increased the position of the sample would shift from its zero-load position as shown in figure 5.6.

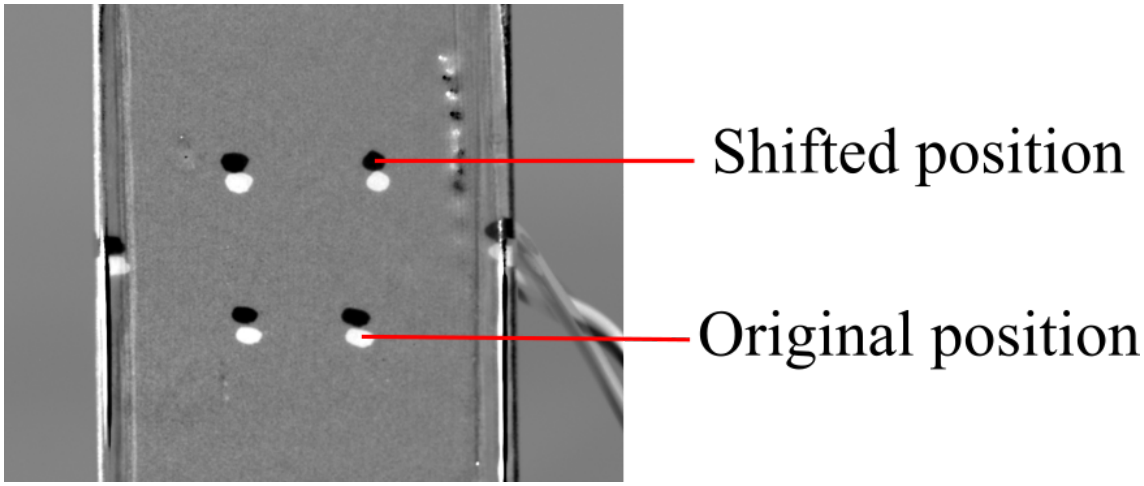


Figure 5.6: Superimposed image of two aluminium samples. The original position was an image at the sample at 0 kN whilst the shifted position was at an applied load of 31 kN. The image was capturing during the image translation facility in Deltavision.

Extracting the data manually would be time-consuming, requiring the user to manually open each image and carefully reselect the area in which information was captured. Most importantly, the subtraction facility would not be able to be called upon due to the shift of the entire sample across the different loads. However, the Deltavision software contains an analytical facility known as 'Image Translation' which can shift the position of a certain image so that easily identified features are in

the same position as a reference image. To aid this process, a black marker was used to apply several dots on the cured UV coating. These acted as identifiable features within the images so the image translation could be effectively applied. Once image translation was performed, the zero-load image was subtracted from each loaded image and each file was analysed through a batch command to speed the analysis process.

Data from each image was extracted from an area roughly (100 - 200) x (50 - 100) pixels ([3 - 6] x [1.5 - 3] mm) that was set in the very centre of each samples, an example is shown in figure 5.7.

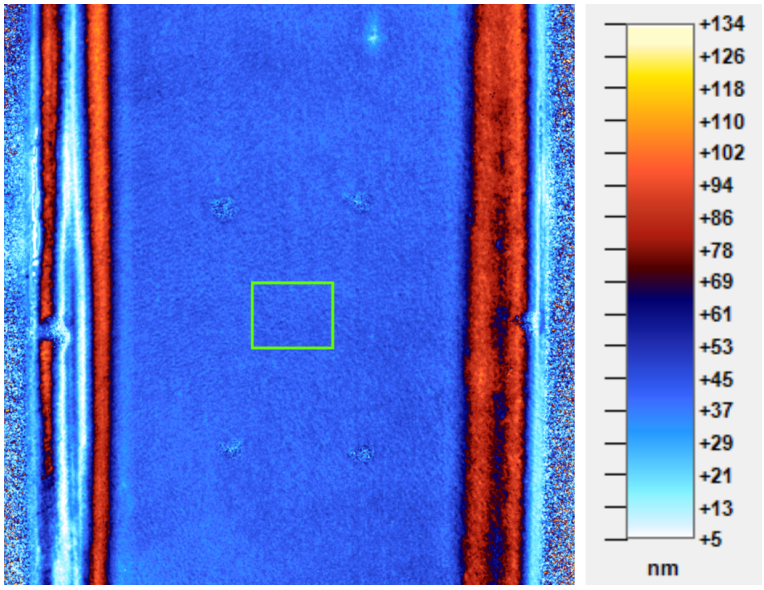


Figure 5.7: GFP1600 image of a sandblasted sample in tension. The green area represents where photoelastic data was taken between samples. Here the retardation is dominated by one colour.

Deltavision supplied both the average and standard deviation of the data within the area which was measured and recorded automatically between all images. For this investigation the measurement of the coating thickness was performed directly by manually extracting the coating from the sample after photoelastic analysis. This was achieved by using a sharp blade to get inbetween the coating and the sample which would then release the coating relatively easily. Using a micrometer, each coating's thickness was measured at the point of data extraction. With an accurate measurement of thickness, the samples could be directly compared to one another by normalising the subtracted retardation with thickness.

5.2.2 Results and analysis

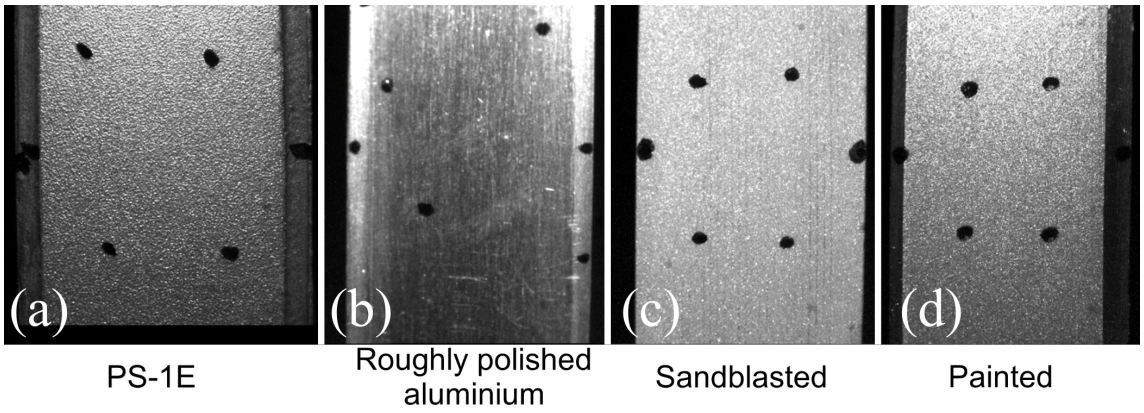


Figure 5.8: Light output images captured by the GFP1600. The light sources were positioned above the GFP1600 angled down onto the aluminium samples.

Figure 5.8 demonstrates the light output images of each surface finish, coated with a photoelastic coating, with the light sources positioned above angled down. Within the PS-1E and painted images, the light intensity decreases from top to bottom. All images possess regions of high contrast in the form of speckled patterns or direct reflections off surface scratches.

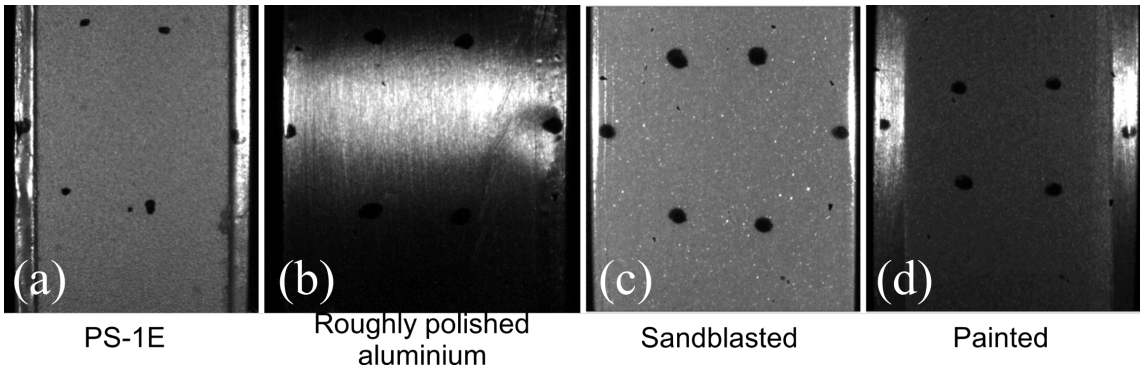


Figure 5.9: Light output images captured by the GFP1600. The light sources were positioned either side of the GFP1600 in the same horizontal plane as the imaging lens.

Figure 5.9 demonstrates the light output images of each surface finish with the light sources in plane with the image lens. The light intensity remains consistent throughout the image when the surface was painted, sandblasted and coated with PS-1E. On the roughly polished sample, the light sources could not be manipulated to illuminate the sample uniformly and as a result, a 'band' of light was observed. However, the light levels within the strip of light were at an appropriate level to extract data from.

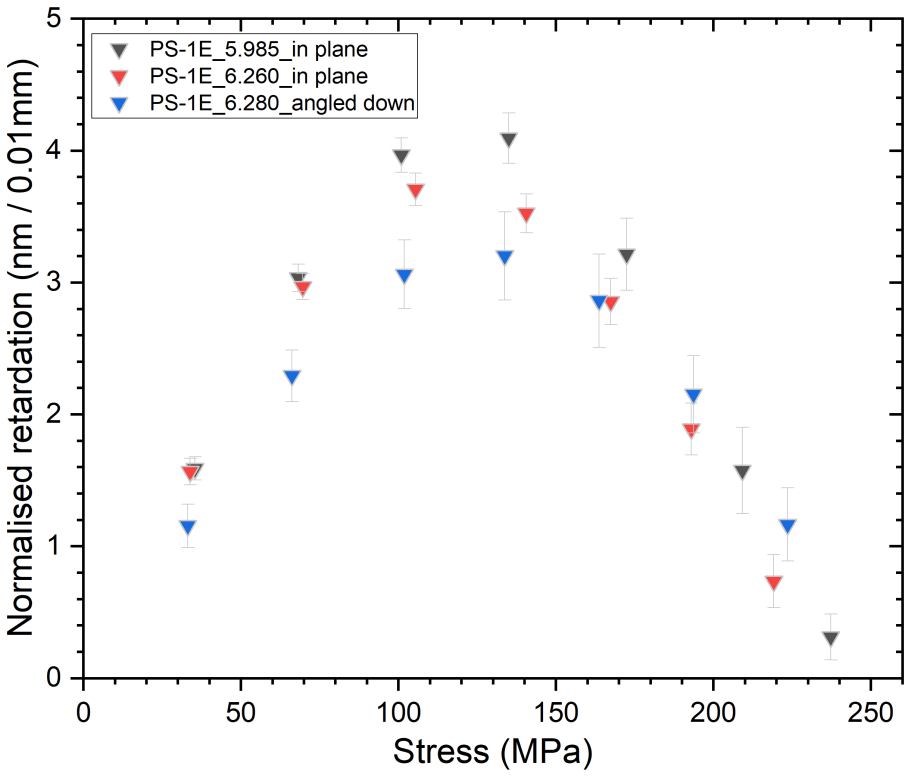


Figure 5.10: Normalised retardation against stress for aluminium samples coated with PS-1E, a commercially available photoelastic coating. The data points represent the average retardation values and the error bars represent the corresponding standard deviations. This data was extracted from an area drawn within the images taken by the GFP1600. Each sample was labelled with thickness measurements and is presented in the legend.

Figure 5.10 presents normalised retardation (zero-load image subtracted) vs the applied load calculated as stress. Within this graph one aluminium sample was analysed with the light sources angled down and the remaining two with the lights sources in the same horizontal plane as the GFP1600's imaging lens. An initial linear response was observed to a point at which the retardation decreased. This was due to the fringe order limit of the GFP1600 being breached.

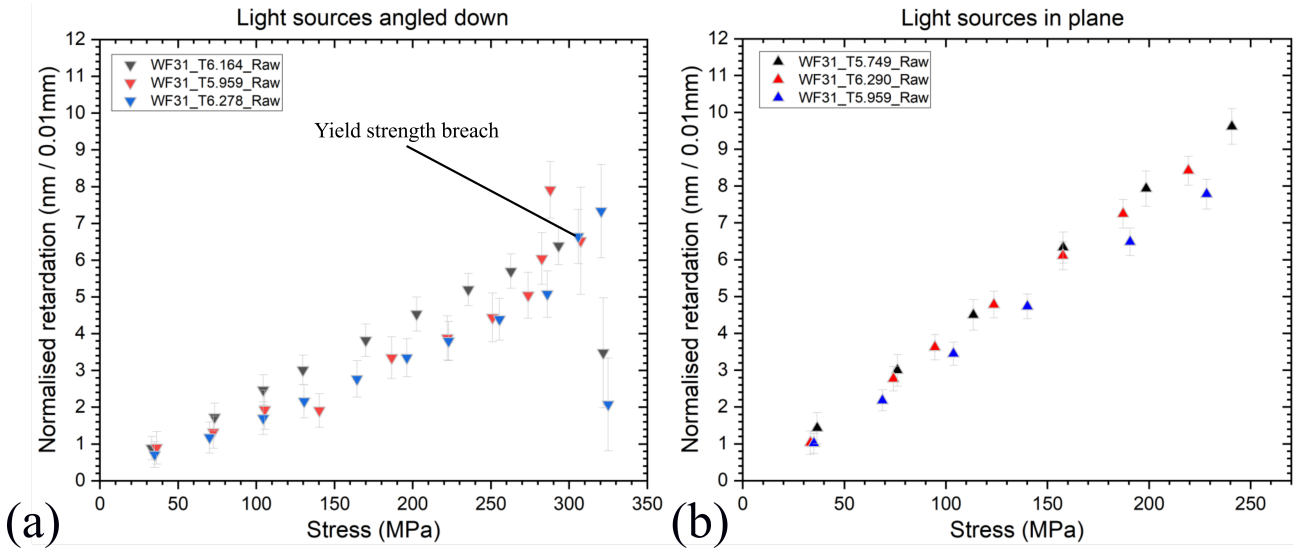


Figure 5.11: Normalised and subtracted retardation against stress for aluminium samples coated with the UV curable formulation. The aluminium samples were initially roughly polished with sandpaper. The data points represent the average retardation values and the error bars represent the corresponding standard deviations. These data was extracted from an area drawn within the images taken by the GFP1600.

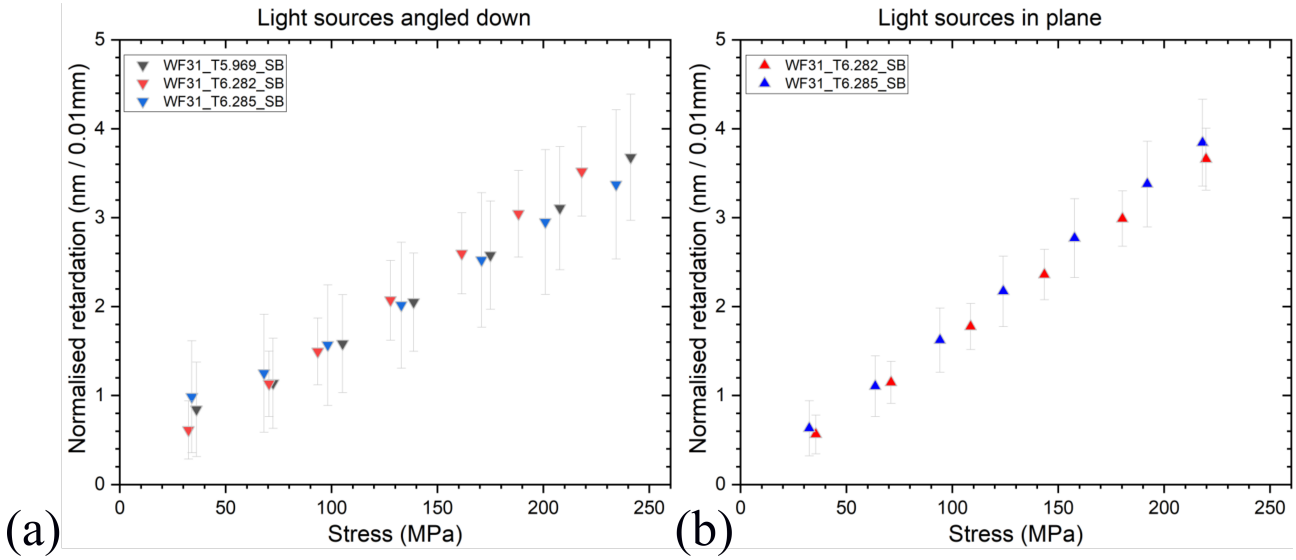


Figure 5.12: Normalised and subtracted retardation against stress for aluminium samples coated with the UV curable formulation. The aluminium samples were initially sandblasted with 60 grit sand. The data points represent the average retardation values and the error bars represent the corresponding standard deviations. These data was extracted from an area drawn within the images taken by the GFP1600.

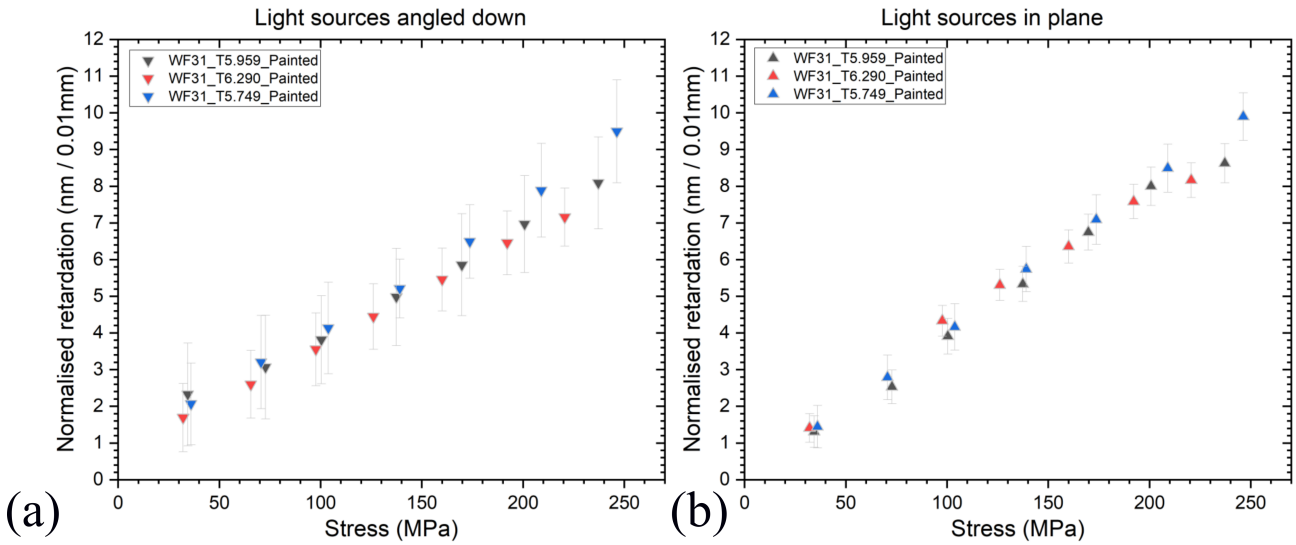


Figure 5.13: Normalised and subtracted retardation against stress for aluminium samples coated with the UV curable formulation. The aluminium samples were initially coated with a silver paint. The data points represent the average retardation values and the error bars represent the corresponding standard deviations. These data was extracted from an area drawn within the images taken by the GFP1600.

Figures 5.11 — 5.13 represent the normalised retardation against stress for aluminium samples coated with WF31 initially prepared with different surface finishes. Figure 5.11(a) light sources angled down data sets features data for when the samples went beyond the aluminium's yield strength. The samples did not return to their original lengths and were discarded, a further three samples were prepared for light source in plane investigations. Figure 5.12 light sources in plane features only two data sets due to a previous sample inadvertently going beyond its yield strength causing damage to the sample. An additional sample was not prepared due to equipment accessibility. All responses demonstrated the same linear response through the applied load. Measured magnitudes of the responses also remained consistent when comparing responses between samples prepared in the same way. The size of the error bars decreased when the light source configuration was within the same horizontal plane as the GFP1600's imaging lens, figures 5.11(b) — 5.13(b), due to a decrease in specular reflection improving signal-to-noise ratio.

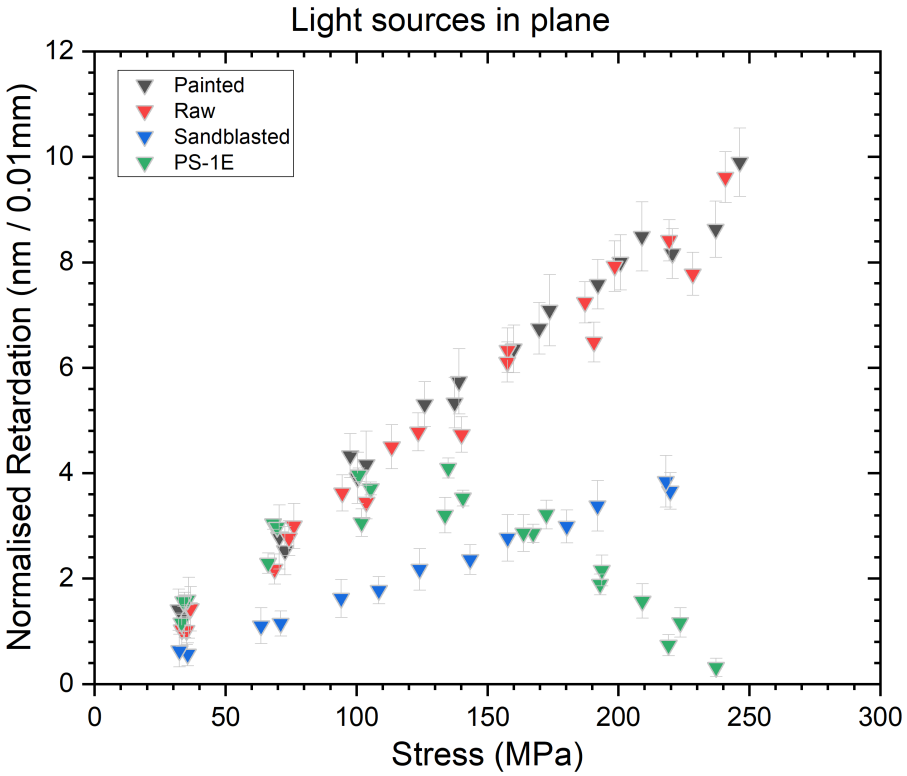


Figure 5.14: Comparisons of all four surface finishes when the light sources were in plane. A difference in response magnitude was observed.

Figure 5.14 focuses on the in plane light configuration. By bringing the responses of the different surfaces together, a difference in magnitude was observed between the surface finishes. The painted samples have a response gradient that coincided with PS-1E's until the commercially available coating started to fall off. Sandblasted had the lowest magnitude photoelastic response.

By reviewing the data shown in figures 5.10 — 5.13 an improvement in signal-to-noise ratio was observed when the light sources were moved next to the GFP1600. This can be justified by observing the differences between the light output images, figures 5.8 and 5.9. When the light sources are in plane with the imaging lens, the speckled patterns were removed resulting in a uniform shade of grey. As a result, the light source will remain in the in plane configuration in future investigations.

By comparing and analysing the responses together, in figure 5.14, the magnitude of the gradient in response differed between the surface finishes. The most noticeable difference was between the painted and sandblasted samples as these possessed the greatest and lowest gradients. To understand further the cause of these differences, the painted samples were stripped of all paint and sandblasted samples were painted with the same silver paint. The samples were then re-coated with the UV

coating and photoelastic analysis performed again.

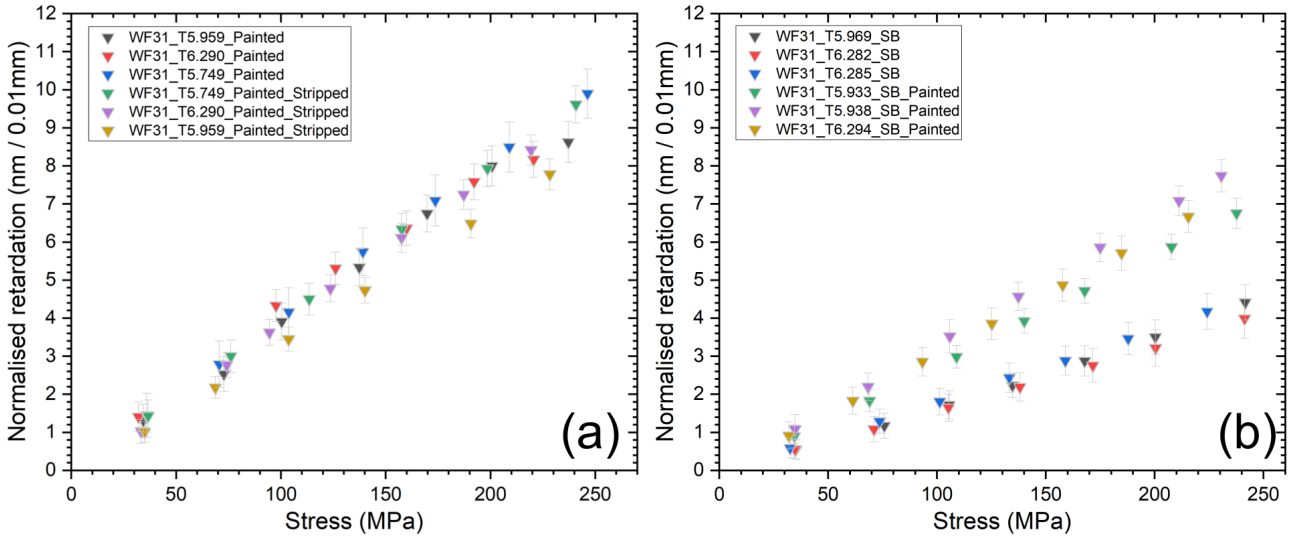


Figure 5.15: Comparisons of measured retardation for painted and sandblasted samples with different surface finishes. The light configuration was in plane. This was to determine if surface finish affected the measured retardation.

Figure 5.15 demonstrates how a change in surface finish affected the measured retardation. Figure 5.15(a) showed that removing and reapplying the paint had no effect on the measured retardation. This coincided with the findings presented in figure 5.14 when comparing painted and raw samples. However, by painting the sandblasted samples the measured retardation increased, figure 5.15(b). This suggests that the surface reflectivity has an effect on the measured retardation. To explore this claim further, photoelastic analysis was performed on aluminium samples coated with a green aerospace primer with a matt finish. The appearance was duller than that of the sandblasted samples. The data for this comparison is documented in appendix C with the results confirming that dull surfaces impact photoelastic sensitivity with application of a consistent reflective backing necessary for recovering the sensitivity loss.

Whilst a connection between surface finish and photoelastic response has been outlined the cause has not been investigated systematically to try and quantify why certain surfaces are more suitable than others. It is proposed that surface reflectivity investigations will provides some solutions to these observations.

5.2.3 Surface reflectivity

This section utilises UV-Vis spectrometry to quantify the surface reflectively of each surface with the aim of quantifying why changes in surface finish are affecting the photoelastic response. A spectrometer measured the diffuse reflectivity of all reflective backings used in section 5.2 and appendix C. The objective was to outline the differences between the reflective backings, to assist the discussion of why dulled surfaces can negatively impact the sensitivity of the photoelastic response. The information in this section will provide useful insight into the limitations of the photoelastic response as a result of surface finish.

5.2.3.1 Methodology

To quantify the surface reflectivity, consideration of the photoelastic setup was taken into account when designing the following experiment. The light sources were positioned either side of the GFP1600 angled towards the coated region of a sample. The GFP1600 was then positioned parallel to the surface with the imaging lens perpendicular to the coated region. The light source emits from an 2 inch aperture forming a wide cone of emitted polarised light in which some is reflected from the sample to the GFP1600. Therefore, to retrieve signal, the GFP relies on the diffusive reflection performance of the sample's surface finish. This setup was recreated using an optical goniometer that would direct light down a path and record the reflected light down another path. Both paths could be angled from the surface individually, figure 5.16.

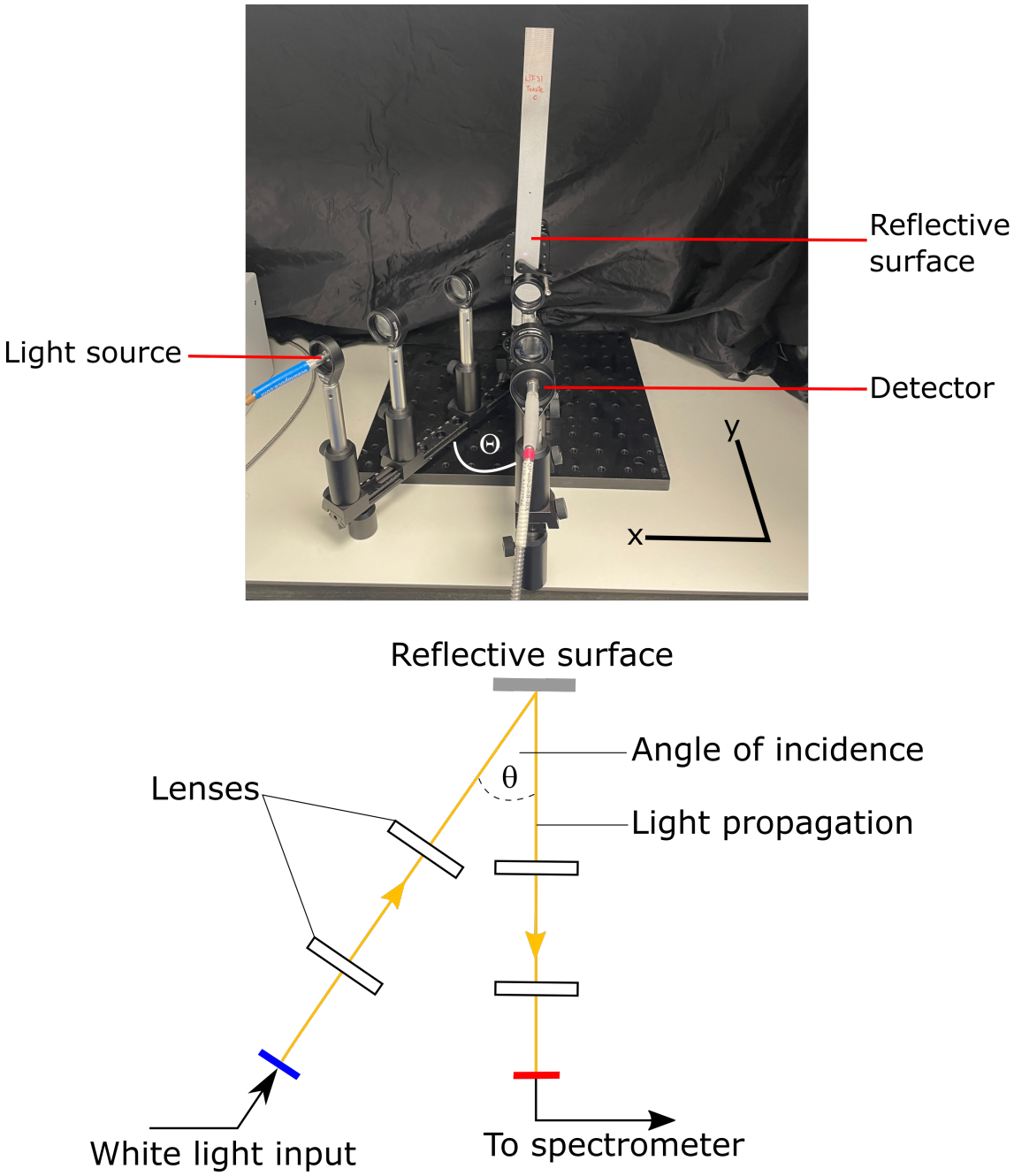


Figure 5.16: The setup used to quantify surface reflectivity performance of the various surface finishes. An optical goniometer was used that direct lights down one rail and the reflected light is captured by a detector positioned along the other rail.

A white light source was directed through an optical fiber that emerged and was directed across the rail shown in figure 5.16. The light was focused to a sample positioned at the end of the rail that was secured and positioned so its flat surface was parallel to the x-axis. A second rail then focused the reflected light to another optical fiber, connected to the detector, that was positioned parallel to

the y-axis. The detector used was an Ocean Insight (Ocean Optics) HR2000+ spectrometer [129]. The detector rail was kept fixed parallel to the y-axis (zero degrees) whilst the incident light rail was orientated across its full range between 20 - 60 ^{o} in 4 ^{o}. These increments were selected due to the resolution of the goniometer's scale being 2 ^{o}. The spectrometer would measure the intensity in the form of counts across the entire visible spectrum of light but for this investigation the wavelength of 650 nm was focused on as that is the wavelength used by the GFP1600 in the capture of red light. The software used to control the spectrometer and extract data was setup for five scans to improve the statistical accuracy of the data. The exposure time was fixed when the incident light rail was at 20 ^{o}, to prevent saturation of the spectrometer across the higher angles of incidence. The intensity values were stable with one repeat sufficient for data collection.

5.2.3.2 Results and analysis

The reduction in intensity due to increasing angle of incidence is shown in figure 5.17. The reflective coating of PS-1E was used as a reference.

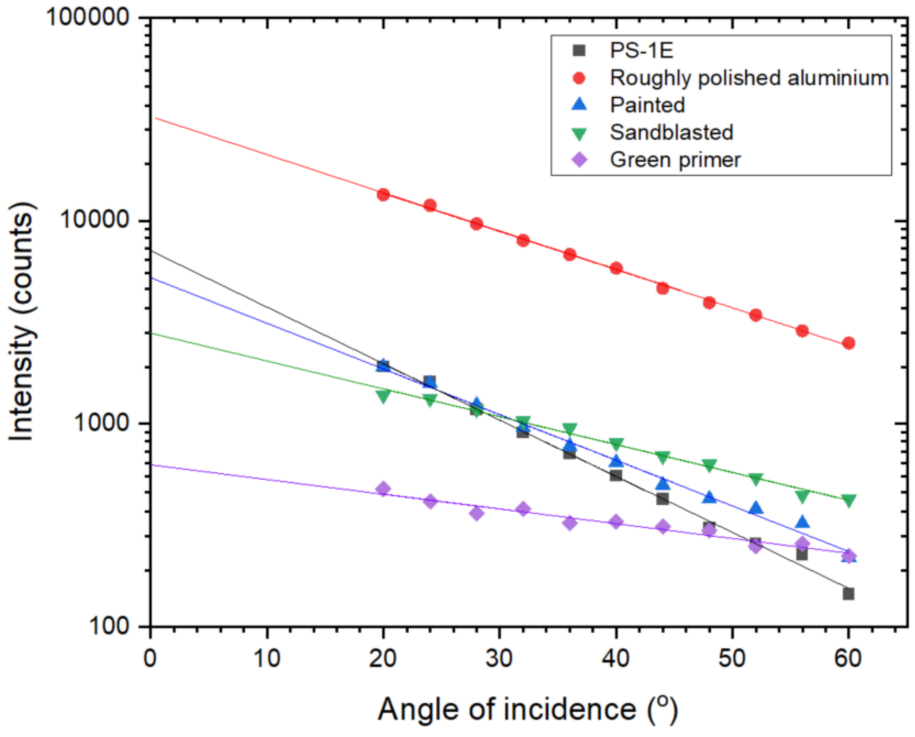


Figure 5.17: The intensity of the reflected light from various surface finishes at a fixed detector position.

Figure 5.17 demonstrates that the angular intensity relationship differed in gradient depending on

the reflectivity of the surface finish. Bare aluminium was significantly more reflective than the other backings with the green primer being the least. The intensities of PS-1E and silver paint were comparable. Linear analysis was performed on each dataset with the line of best fit extrapolated over the 0 - 20 ^{o} range. The sandblasted surface possessed a reduction in intensity towards lower angles. This suggests that during photoelastic investigations insufficient signal was extracted preventing collection of the full magnitude of the response as shown in the painted and roughly polished samples. This observation was further reinforced by applying WF31 onto samples coated with a low gloss (20 GU) aerospace green primer. The reflectivity at shallow angles was further reduced (480 counts at 20 ^{o}) which resulted in a photoelastic response that was barely discernible. Reviewing the effects of surface reflectivity also explain the effects on the photoelastic response of the highly reflective roughly polished samples. The configuration in figure 5.8 was initially deemed suitable due to the uniform appearance of the light output image. However, this was achieved by positioning the light sources so that the edge of the bulk illumination was falling upon the coated region. It is now apparent that this configuration was too severe of an angle for the highly specular reflective backing which inadvertently caused a reduction of the photoelastic response - an effect similar to low surface reflectivity was observed. Consequentially from this investigation, the painted surface was deemed the most suitable choice due to its reflection profile being similar to PS-1E's reflective backing allowing for extraction of the full photoelastic response. However, the paint used does maintain areas of specular reflection which introduce inaccuracies in the gathered response. Specular reflections should be avoided in reflection photoelasticity [55].

5.2.4 Discussion and conclusions

This section provides important considerations a user must make when designing a photoelastic investigation. Furthermore, the data within this section has not been published or mentioned in studies using photoelastic coatings. This is understandable as the majority of previous applications have used the PhotoStress range of commercial photoelastic coatings that come supplied with reflective adhesives and/or backings on their products. However, if users want to utilise thermoset resin coatings (such as Devcon 2-ton epoxy) then the surface reflectivity becomes a parameter that must monitored but might be overlooked as the information has not been published. The outcome of this investigation demonstrates that not all reflective surfaces are equal and can hinder the photoelastic sensitivity and the signal-to-noise ratio. For example dulling the sample surface

by methods such as sandblasting or applying a low gloss paint reduces the magnitude of the photoelastic response. Alternately, using a highly reflective surface the magnitude is high however the signal-to-noise ratio is poor. The best solution was to apply a silver metal paint to slightly dull the reflective bare surface but retain enough reflective properties in order to maintain the magnitude of the bare surface. The silver metal paint (Hammerite smooth silver) will be applied to all samples to keep a consistent reflective backing. However, it must be noted that the application of the paint increased the total time for application by upwards of 12 - 24 hours as the paint was left to dry completely prior to WF31 application. However, the ease-of-application remains and the fact that the paint has not been designed specifically for this research must be taken into account. It was decided that developing an ideal reflective backing for this research was beyond its scope and should be considered in any further work, discussed in chapter 12.

Chapter 6

Tinted coatings for thickness measurements

There exists a major application concern of using liquid photoelastic coatings that limits its usability for RPSA investigations. This concern is the strict control of the applied thickness of the coating when applied to a sample. Thickness measurements are required in order the extract strain and/or stress information from photoelastic experiments, equation 2.26. Pre-cast photoelastic sheets possess uniform thickness resulting in accurate extraction of data providing an advantage over the UV curable material in its current form.

Thin, planar and simple geometry samples have been the only subjects for the application of the UV curable coating thus far. Even these simple geometries are challenging to coat uniformly as demonstrated in figure 6.1.

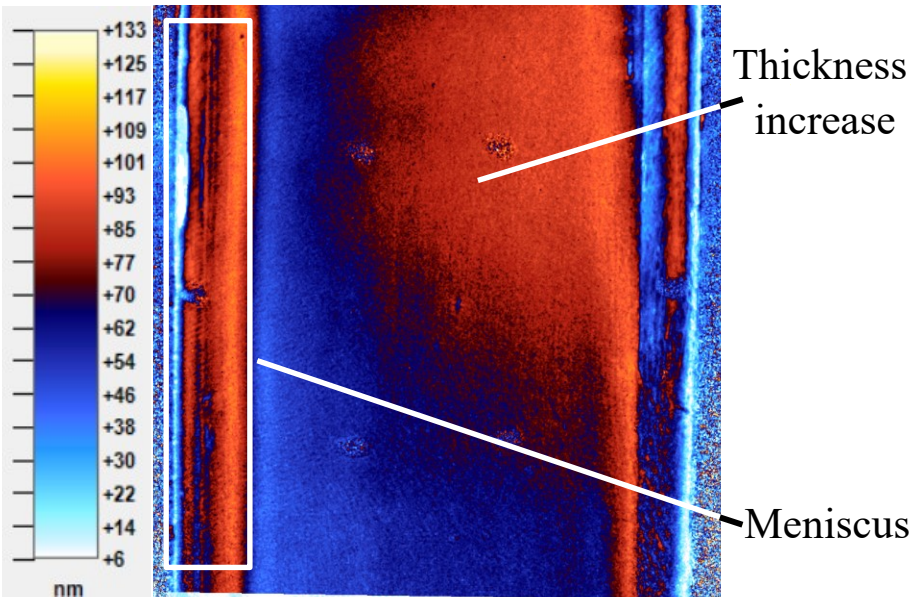


Figure 6.1: An aluminium sample coated with WF31 that has been placed in tension. The grey field polariscope was used to analyse the image to measure the induced retardation. The orange areas represent an increase in retardation due to increased thickness only.

Figure 6.1 shows an aluminium sample coated with WF31, placed in tension and analysed using the GFP1600 that measured the induced retardation. Several orange/red regions are observed that demonstrate an increase in retardation. A user could interpret these areas as increased strain on the surface however it is just an increase in retardation due to thickness differences alone. When using an applicator, such as a K-bar, to spread the coating, the relatively low width of the sample causes a meniscus to form at the edges. This effect would also be observed if the sample had features such as holes or slits. Another issue with spreading occurs when there is an imbalance along the K-bar's length causing one end of the applicator to be raised slightly higher than the other. The cause of this issue can be due to both human error and/or differences in the geometry of the coating face of the sample. If the application process transitions to spraying, the thickness control would be presented with more issues as maintaining consistent thickness would be extremely challenging. Furthermore, applications onto more complicated geometries and/or large surfaces would also present challenges when trying to achieve consistent thickness.

Techniques to try to tightly control the thickness would be complicated and remove the easy-to-use aspect of the coating. The solution comes in the form of a thickness measurement facility within the software, Deltavision, used to acquire and process images from the GFP1600.

6.1 Theory

The ability to measure thickness from a tinted coating is not a new technique. Within the software used alongside the GFP1600, a facility can be called upon which can measure the thickness of a specifically designed photoelastic coating produced by Stress Photonics. This coating, named TintCoat, is a two-part adhesive designed with various tints. Documentation on its use is not widely available but the theory has been explained by Jon Lesniak of Stress Photonics. This report will document the theory alongside the procedure used to create a bespoke tinted coating for thickness measurements.

The GFP1600 captures light in RGB (Red, Blue and Green) monitoring around three wavelengths: 650 nm (red), 551 nm (green) and 449 nm (blue). The Full width half maximum around these wavelengths is not specified in the camera's documentation. If imaging a PE sample using the default GFP setting, the intensity of these individual colours would vary depending on several factors such as the attenuation and destruction of certain wavelengths when the light interacts and reflects off the sample. However, the software can apply gains onto the individual colours to bring each wavelength to the same captured intensity. Introducing a tinted coating would disrupt the intensities between the three colours. If a red tinted coating was used then the red light would be transmitted whilst the blue absorbed. The reduction in blue light intensity compared to red would allow for a relationship to be formed between thickness and the ratio between blue and red light. As thickness approaches zero, the ratio approaches 1 and reduces as the thickness increases. The connection between ratio and thickness can be modelled by a 4^{th} degree polynomial equation and is utilised by the software in its calculations. This theory was applied to the new UV cured photoelastic coating, the challenge being to introduce a tint to the coating without significantly affecting the birefringent properties.

6.2 Methodology

Several options were discussed when introducing tint into raw WF31. The objective was to choose a tint that would provide enough signal for thickness measurements at approximately 50 — 100 μm. The thickness facility within the software has been coded to monitor the ratio between blue and red light. The necessity of a reflective backing made this choice relatively simple as a red tint

would provide the greatest difference between the measured red and blue light. A simple approach for determining an appropriate dye was favoured over an extensive investigation to demonstrate the concept. Three types of tint were used: food colouring, widely available and cheap; red inkjet ink, a common additive to UV curable resins; and red transparent resin dye [130], utilised by Stress Photonics in their TintCoat product. The amount of tint was kept between 0.5 — 2 % to minimise the reduction in photoelastic sensitivity as the dye dulled the coating surface. A weight percentage of each red tint to WF31 within this range produced a deep red colour that was maintained when spread to $\sim$60 μm, as shown in figure 6.2.

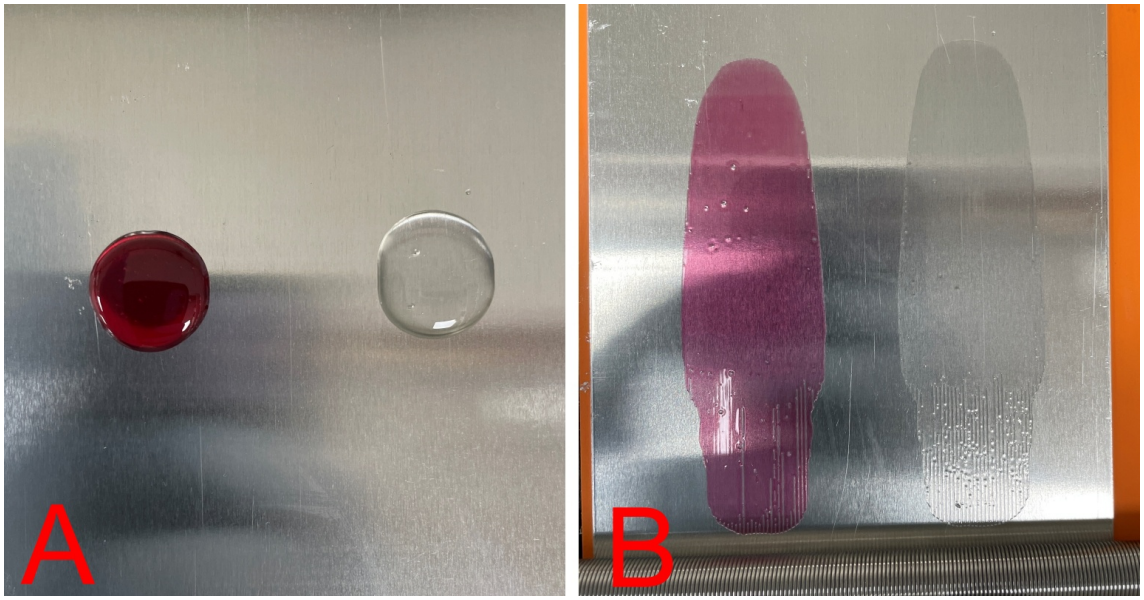


Figure 6.2: Comparison between clear WF31 and red tinted WF31 with a red transparent resin dye. ***a*** *demonstrates the initial deep red colour.* ***b*** *demonstrates the colour after being spread to a wet film thickness of approximately 60 μm.*

To calibrate a tinted coating for thickness measurements, a wedge sample was created as shown in figure 6.3.

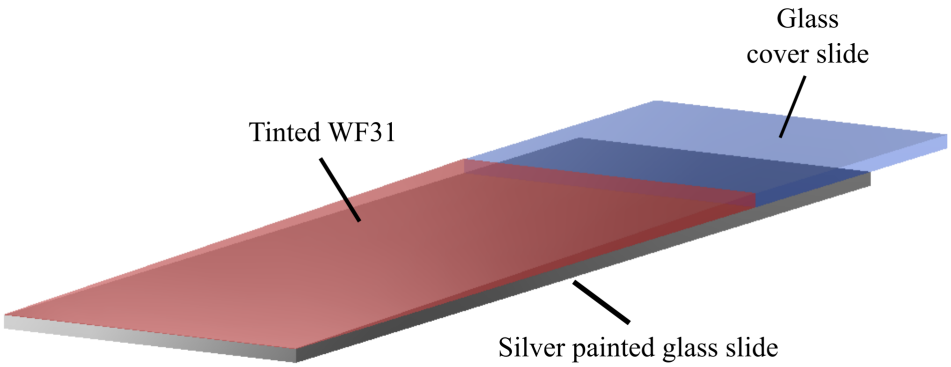


Figure 6.3: A schematic (not to scale) of the wedge sample used to calibrate the tinted WF31 formulation. Two glass slides with a glass cover slide spacer forms the wedge with a thickness range of (18 - 40) — (150 - 240) μm. One slide was painted silver to provide a reflective backing. The other slide has been omitted from the diagram for clarity.

The wedge creates a thickness gradient that can be used to image changes in the ratio of blue and red light across the wedge's length. Glass slides were used to create the wedge as it is an ideal flat surface whilst enabling sufficient UV-C light to penetrate to the liquid formulation triggering cure. A glass cover slide was used as the spacer as they are relatively thin (150 - 250 μm) and easily available. Keeping the maximum thickness of the wedge as close to the target coating thickness ($\sim$ 50 μm) was an important step. If using a thicker spacer then the dynamic range of the appropriate data is reduced and the calibration does not perform as well. The thicknesses of the glass cover slides were sufficient in these experiments. Prior to wedge formation, a glass slide was spray painted with silver paint (Hammerite smooth silver). To form the wedge, the cover slide was adhered to a clear glass slide using petroleum jelly to create a temporary bond. Approximately 0.5 mL of red tinted WF31 was applied to the painted surface of the reflective glass slide covering the total length of the slide. A clear slide with the spacer was placed on top and light finger pressure was used to ensure all the painted slide was covered. The wedge was transferred to the UV curer and cured for 20 s producing a solid wedge. There was no disturbance to the curing performance of the formulation by the top glass slide. Once cured, a sharp blade was used to carefully peel the top clear glass slide off without de-bonding the cured formulation from the painted slide. It was easier to remove the top slide immediately after curing. Leaving the slide would degrade the signal-to-noise ratio of the gathered intensity data from the GFP1600.

Once the wedge had been formed, it was analysed using the GFP1600. Firstly, the GFP captured an

image of just a reflective glass slide using two circular polarised light sources to uniformly illuminate the slide. This enabled a crucial step where the intensities of blue and red light were made equal, by adjusting the individual light gains in the software, on the reflective surface being used. The gains were adjusted either automatically or manually via the software. A combination of both was the most effective and efficient. It is important to note that this step would have to be repeated if the reflective backing was changed as the intensities of the two wavelengths would change. Consequentially, it is vital to keep the reflective backing consistent across all samples and applications. The reflective slide was replaced with the tinted wedge and analysed with the GFP1600 using three image sequence repetitions to achieve an average value for light intensity.

Within the software a line was drawn across the length of the wedge covering the entire thickness gradient, figure 6.4.

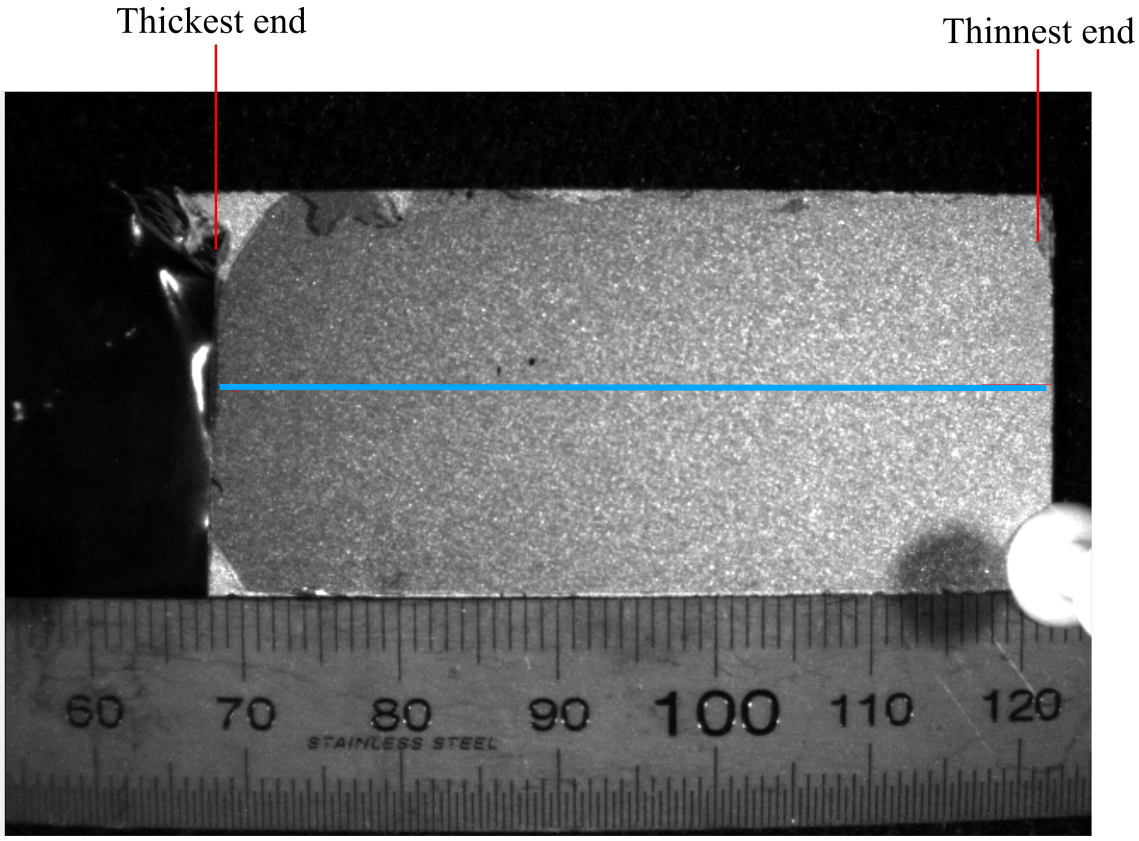


Figure 6.4: The light intensity output of the GFP1600 imaging a wedge of WF-Red1 to calibrate the coating for thickness measurements. Along the blue line each red and blue light pixel value was recorded. The difference in light intensity was observed due to change in formulation thickness.

The intensity values for both red and blue light were taken at every pixel within the line. Before this

point it was necessary to apply a median filter before extracting this data. This removed some noise and assisted in the calibration procedure. The ratio of blue and red light was then calculated. The next step was to remove the tinted wedge from the glass slide and use a micrometer to measure both ends of the wedge. By applying simple geometry the angle of the wedge can be calculated as well as the thickness at any point across the wedge's length. A graph of thickness against blue:red light was formed and the data were fitted to a 4^{th} degree polynomial equation

$$y = \mathbf{A}x^4 + \mathbf{B}x^3 + \mathbf{C}x^2 + \mathbf{D}x + \mathbf{E} \tag{6.1}$$

with A, B, C, D & E as coefficients to be stored in the software.

6.3 Results and analysis

It was identified that both food colouring and inkjet dyes were unsuitable for this investigation. In the former, red food colouring produced a weak tint and would vanish after the UV curing stage. Inkjet ink had the opposite issue, where the tint was too strong and opaque and would prevent curing of the coating at weight percentages between 1.5 - 2 %. The resin dye performed the best, producing a strong tint at lower percentages whilst maintaining curing performance. Arkema conducted real-time ATR-FTIR, as outlined in chapter 4, and the time to reach maximum cure conversion was not effected at a weight percentage of 1.5 %. The data for the time to reach maximum cure conversion is presented in appendix E. The addition of 1.5 % of red resin dye to WF31 will be referred to as WF-Red1.

Preliminary investigations were performed to determine a suitable tint weight percentage of the resin dye. Creating samples was time-consuming and challenging and it was determined to establish a consistent amount of dye to improve the efficiency of systematic testing. The aim was to have the thickness measurement facility output data within the expected thickness range of the coating, for example figure 6.5.

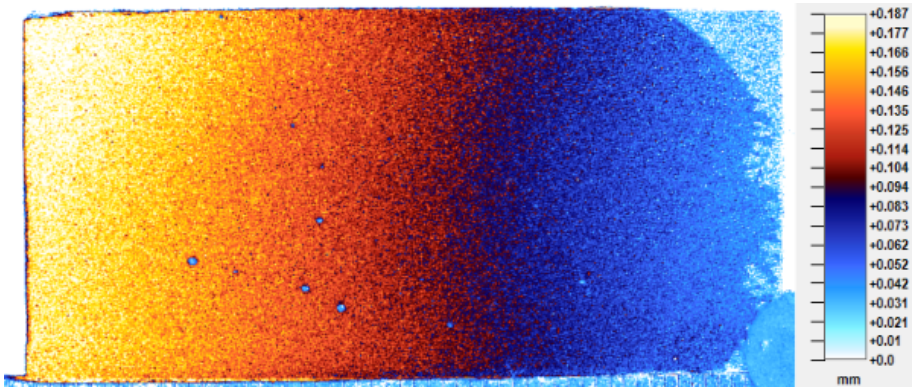


Figure 6.5: A wedge of tinted WF31 calibrated for thickness. The colours within this image represent different thicknesses.

The thickness facility was found to perform optimally when the values of the polynomial coefficients were $-5 < x < 5$ with values outside this range producing obvious inaccuracies within the facility. For example unrealistic thickness measurements or no output signal. A weight percentage <1.5 % produced coefficient values outside the range whilst increasing from 1.5 % had no beneficial effect. As a result, a weight percentage of 1.5 % was used throughout systematic investigations.

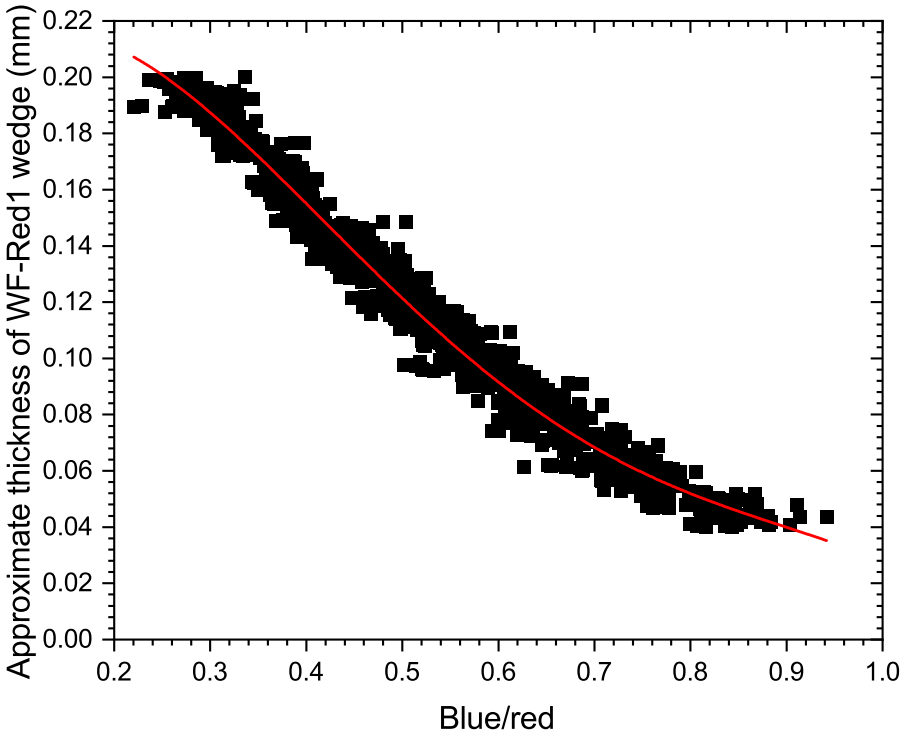


Figure 6.6: Calculated thickness across the wedge against the ratio between blue and red light intensity. A 4^{th} polynomial has been fitted onto the curve. The calculated coefficients are then used within Deltavision to measure thickness using the tinted UV curable formulation.

Figure 6.6 presents a graph of calculated thickness across the wedge against the ratio of blue and red light. A 4^{th} degree polynomial was fitted and presented as a red line through the curve. The resultant polynomial equation was:

$$y = \textbf{(-1.04)}x^4 + \textbf{(2.74)}x^3 + \textbf{(-2.34)}x^2 + \textbf{(0.48)}x + \textbf{(0.18)} \tag{6.2}$$

Equation 6.2 features four coefficients and an intercept value to two decimal places. These coefficients were saved and inputted into Deltavision, figure 6.7.

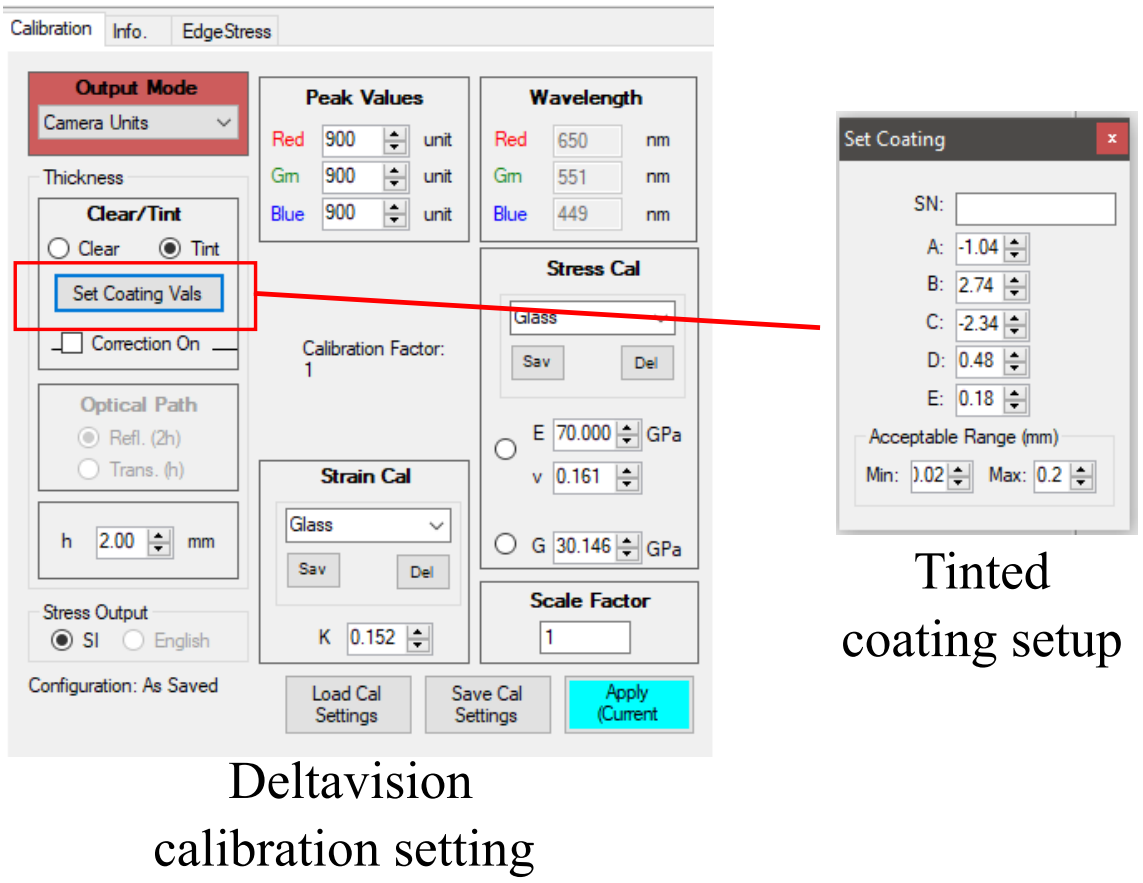


Figure 6.7: The input of calibration coefficients into Deltavision. The five coefficients A - E were calculated through a 4^{th} polynomial equation that equates the ratio of blue and red light to thickness.

The calibration coefficients were then used to produce a thickness output image, figure 6.5. At each pixel value the software has associated the intensity of blue and red light to a thickness through equation 6.2. The analysis setup was then used on a reflective slide that had WF-Red1 applied using a K-bar that spread the formulation, within its main bulk, to an approximate uniform thickness.

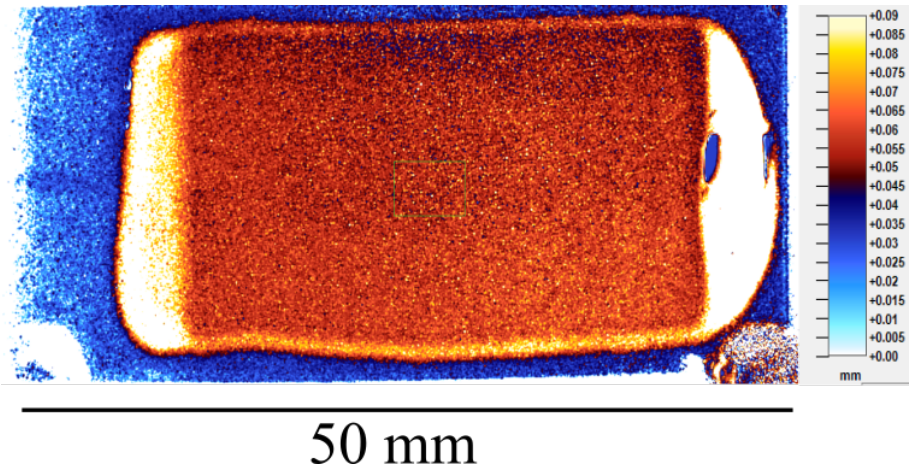


Figure 6.8: A slide to validate the calibration data of WF-Red1. The slide was applied with WF-Red1 using a K-bar and cured using UV light. The calculated thickness value was close to the measured value using a micrometre.

Figure 6.8 demonstrated the validation of the software's thickness measurement facility. The calculated thickness within the middle of the coating was 0.056 $\pm$ 0.008 mm whilst the measured thickness using a micrometer was 0.055 $\pm$ 0.004 mm. These comparisons were also measured in all samples within chapter 7 and 8.

However, the main issue with the calibration procedure was the repeatability of results. In total seven samples were created and within three samples the cured coating did not adhere to the painted slide whilst the remaining four did. The three unbonded coatings were adhered to the slide using a thin application of petroleum jelly in several locations where data extraction would not take place. This was to prevent any distortions of the captured light intensity. The seven samples were analysed and fitted with a 4^{th} polynomial fit with their individual coefficient values shown in table 6.1.

Calibration wedge	Polynomial coefficients				
	A	B	C	D	E
001 - Not Bonded	-0.16	0.42	-0.23	-0.35	0.33
002 - Not Bonded	-3.38	7.96	-6.39	1.74	0.052
003 - Not Bonded	-0.36	1.76	-2.38	0.96	0.054
004	-3.08	8.06	-7.31	2.44	-0.091
005	0.36	-0.93	1.11	-0.89	0.37
006	-1.04	2.74	-2.34	0.48	0.19
007	-0.12	1.21	-1.82	0.62	0.15

Table 6.1: The five coefficients used in the thickness correction facility within Deltavision for seven calibration samples. The coefficients A — E are observed in equation 6.1.

The polynomial coefficients for the seven sample vary considerably in value. Their effects on the resultant polynomial curve is presented in figure 6.9.

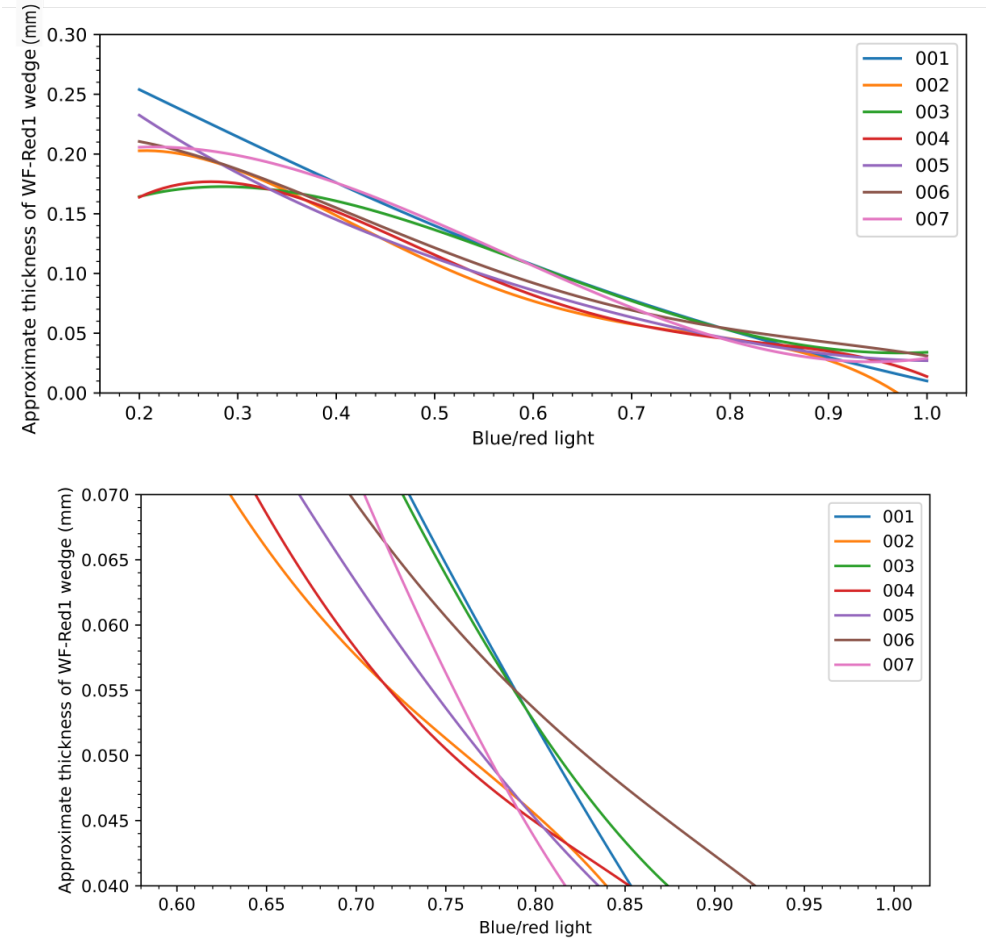


Figure 6.9: Seven 4^{th} degree polynomial fits using coefficients calculated from seven WF-Red1 wedge samples. The thickness ranges are both the entire wedge and a thickness range that the cured coating usual exists within after application.

The seven polynomial fits deviate at various locations which would result in considerable differences in calculated thickness. At certain ratio values the calculated thickness can vary between $\sim$ 10 μm. As a consequence, the precision of the tinted coating calibration procedure was relatively poor however the accuracy of calibration wedge 006 has shown to be high at the thickness range that the coatings usually exist between (40 - 60 μm). The source of the imprecision is evident when observing the large spread of data shown in figure 6.6. Within figure 6.4 there exists a high density of hot spot pixels which contribute to poor signal-to-noise ratio resulting in the large spread of data. This effect was reduced by applying a median filter however not removed completely. Perfect uniform illumination was not possible due to the lack of diffusion of the bright light sources and the

reflectivity of the silver paint. Designing an optimum reflective backing is beyond the scope of this research and considerable time would be needed to find a better alternative. However, several other experimental changes could be made to assist the optimisation of the calibration process. Firstly, the wedge could be made smaller to increase the dynamic range between a thickness range that the coating would be expected to be between. Secondly, methods of illumination need to be changed to achieve uniformity with ease-of-use. A simple addition would be to use diffusing material to assist the spread of the light sources whilst keeping light intensity high. The final potential solution would be to apply further data processing techniques such as data binning which is used to minimise the effects of small observation errors. Data binning groups intervals within the dataset essentially smoothing the dataset and preventing overfitting of data. An example of data binning being performed on figure 6.6 is shown in figure 6.10(b).

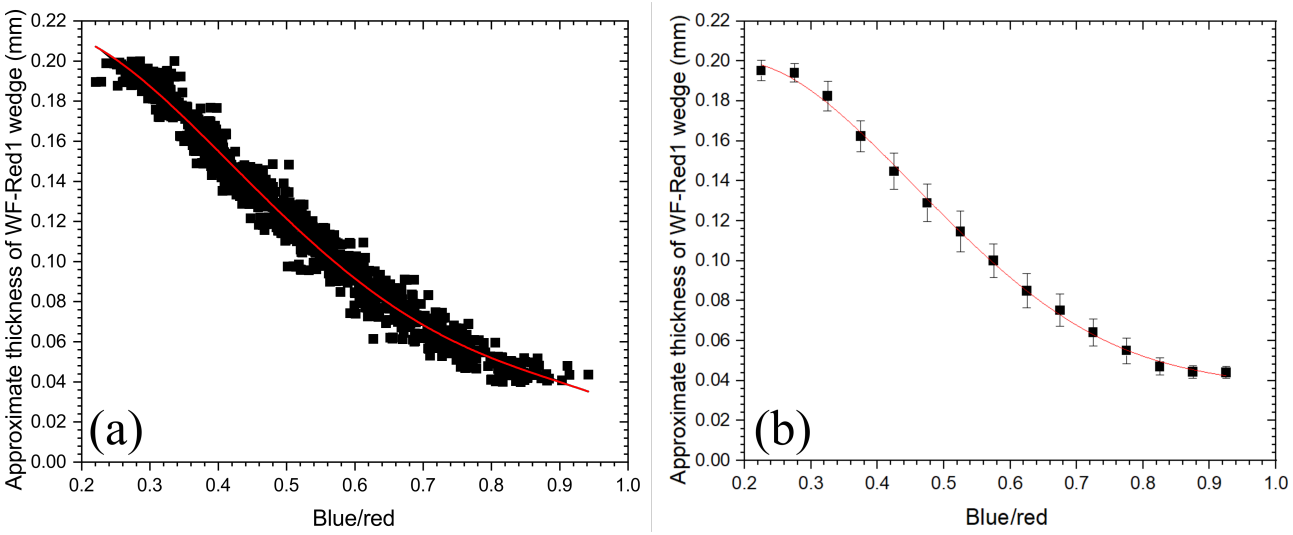


Figure 6.10: Data binning performed on figure 6.6 which smooths the data preventing overfitting.

The effects of data binning on the bonded calibration wedge's polynomial coefficients are presented in table 6.2.

Calibration wedge	Polynomial coefficients				
	A	B	C	D	E
004	-0.85	2.19	-1.70	0.14	0.25
005	-0.72	2.10	-1.98	0.46	0.16
006	-1.19	3.35	-3.09	0.84	0.13
007	-0.50	2.06	-2.51	0.85	0.12
Average	-0.81 $\pm$ 0.25	2.43 $\pm$ 0.54	-2.32 $\pm$ 0.53	0.57 $\pm$ 0.30	0.16 $\pm$ 0.05

Table 6.2: The five coefficients used in the thickness correction facility within Deltavision for four calibration samples. The pre-processing was applied to the data before polynomial fitting. The coefficients A — E are observed in equation 6.1.

Data binning has improved upon the repeatability between the wedge samples when compared to table 6.1. However, the standard deviations of the averages were high. Nevertheless these changes had minimal effect within the thickness measurement facility with no observable difference in the outputted thickness.

6.4 Discussions and conclusions

There has been successful implementation of automatic thickness measurements using the software that controls and analyses GFP1600 data. Whilst the facility exists and is functional with Stress Photonics coatings, the methodology has been adjusted to work with coatings at thicknesses between 30 — 150 μm which has not before been attempted. Tinted coatings have been used in research [8], however the thicknesses applied was 0.33 mm. Recommendation by Stress Photonics on their TintCoat photoelastic coating was to apply at thicknesses between 0.3 — 0.5 mm. Furthermore, the original methodology, outlined by Jon Lesniak, was to form calibration wedges with a maximum thickness of 1 mm. The ability for the coefficients within equation 6.2 to produce accurate measurements, when compared with physically destructive measurements, provides significant improvements of the coating's ease-of-use. A user is now to apply a coating without a requirement of achieving uniformity across the coating surface. Subsequently, this allows for easier application management on larger coating areas and/or areas with difficult features such as bolt heads, bolt holes and curved surfaces. The Deltavision software can now perform and apply the thickness measurements to correct calculations of principal strain difference at any point within the image. The next stage is to calibrate the coating to calculate its strain-optic coefficient to extract the desired strain data.

Chapter 7

Coating calibration

Coating calibration is a crucial procedure in RPSA. Determination of the principal strain difference from measured retardation requires knowing a photoelastic coating's strain-optic coefficient (K). To calibrate the UV curable formulations, the findings of chapters 4 — 6 were implemented into an experimental procedure. The aim was to determine both WF31's and WF-Red1's K value with an associated uncertainty to provide confidence in the overall method and approach.

7.1 Methodology

The test method used for calibration follows the simple tension test as described by Cloud [131]. The aluminium samples, used in chapter 5.2, were reused for this investigation alongside the Mayes 100 kN tensile tester. The samples had constant cross section through the test area and were a suitable match for calibration tests. Two separate experiments were performed at different times to determine the K value of both WF31 and WF-Red1. The creation of samples was dictated by the availability of strain gauges that were utilised in this investigation. WF31 was coated onto three aluminium samples that were painted silver on one side prior to the coating application. The samples were reused for repeat measurements however the coatings were removed and reapplied. For calibrating WF-Red1 five aluminium samples were used without repeats. UV curable coatings were applied using the method in section 5.2.1.

On all samples, the uncoated opposite face of the samples were applied with strain gauges to allow for easy and accurate measurement of the principal strain difference at the point of PE data extraction. A single rectangular rosette strain gauge was adhered to the centre of the (300 x 25) mm face of

each sample. The gauge used was a general purpose gauge from Micro-measurements [132] and featured three stacked elements, 1.52 mm in length, in a 0, 45 & 90 ^{o} orientation, figure 7.1.

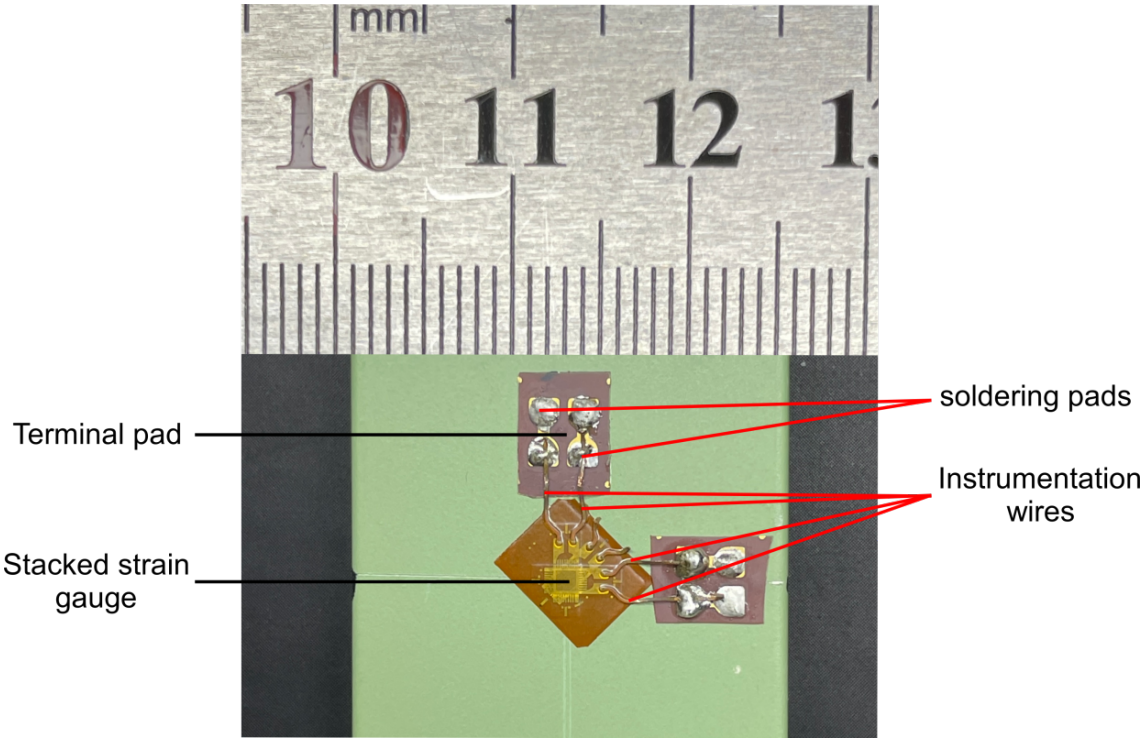


Figure 7.1: A primed aluminium sample adhered with a stacked rosette strain gauge. The instrumentation wires are soldered onto terminal pads which would also be connected to leadwires. The leadwires connect to a P3 strain indicator and recorder for testing.

The 0^{o} gauge was positioned perpendicular to the sample's longitudinal axis and the 90^{o} gauge positioned parallel to the longitudinal axis. The 45 degree gauge was ignored for this experiment. Gauges were applied following the manufacturer's instructions. Lead wires then attached to a P3 strain indicator and recorder [133] with both gauges setup in separate quarter bridge arrangements. The sample was held by the top grip and the gauges were balanced using the P3 indicator and recorder. The bottom grip was applied and loading commenced. Each sample was carefully mounted into the rig using guidelines on both the sample and the grips to ensure that the load was applied along the longitudinal axis of the sample.

A stepwise loading scenario was again used, as described in section 5.2.1, and recommended for this calibration test. The tensile tester enabled constant applied load at various intervals to ensure no drop in load during the capture of photoelastic data by the GFP1600. Once the maximum load was applied and the images taken, the load was removed and the values of the strain gauges were

checked to observe if the values went back towards zero.

In order to calibrate the samples, the strain-optic law was rearranged in order to calculate K.

$$K = \frac{\delta}{2d(\epsilon_1 - \epsilon_2)} \tag{7.1}$$

A graph of retardation (δ) against the product of double the thickness of the coating (d) and principal strain difference ($2d(\epsilon_1 - \epsilon_2)$) was constructed to calculate the average strain-optic coefficient throughout the load by performing linear analysis on each individual response. By including the uncertainty associated with the measured retardation and thickness, the linear analysis was performed taking into account the uncertainty in each data point. With values for K calculated, the measured retardation could be translated into principal strain difference.

WF31 coatings were manually removed from the aluminium sample surface and the thickness at the location of photoelastic data extraction was measured using a micrometer. WF-Red1 made use of the thickness measurement facility within Deltavision. Manual extraction was applied to confirm the analysis measurements.

7.2 Results and analysis

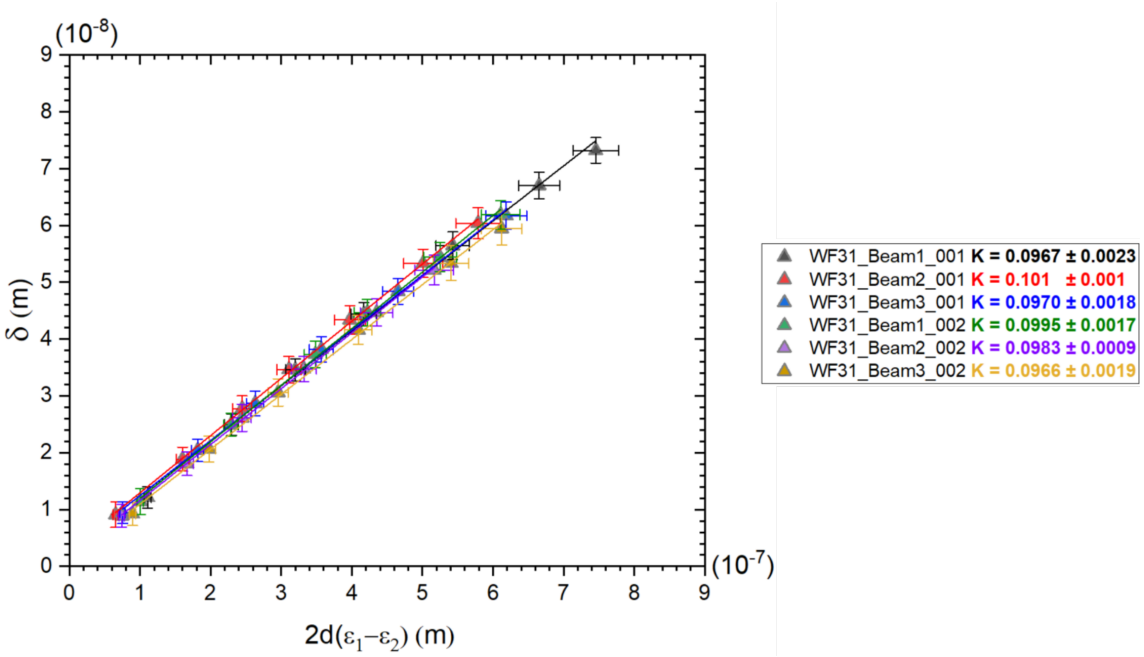


Figure 7.2: Calculations of strain-optic coefficient for WF31. Retardation (δ) against double the coating thickness (d) multiplied by the principal strain difference (($\epsilon_1 - \epsilon_2$)). Each solid line represents the linear analysis formed on each sample. The value of each line's gradient is the corresponding strain-optic coefficient as highlighted in the legend.

Figure 7.2 presents calculations for the strain-optic coefficient of WF31 using six separate coatings. Each dataset had linear analysis performed and is demonstrated by the solid line in the same colour as the corresponding dataset. The gradient of each line represents the K value for each dataset and is presented in the legend along with the uncertainty in the gradient's value. Each datasets' K value was combined to calculate an average value of 0.0982 ± 0.0018. The assigned uncertainty equated to a precision of 1.84 %. The newly calculated value was also ∼180 % greater than the previously measured value of 0.0346 ± 0.0073 stated in chapter 3.3.

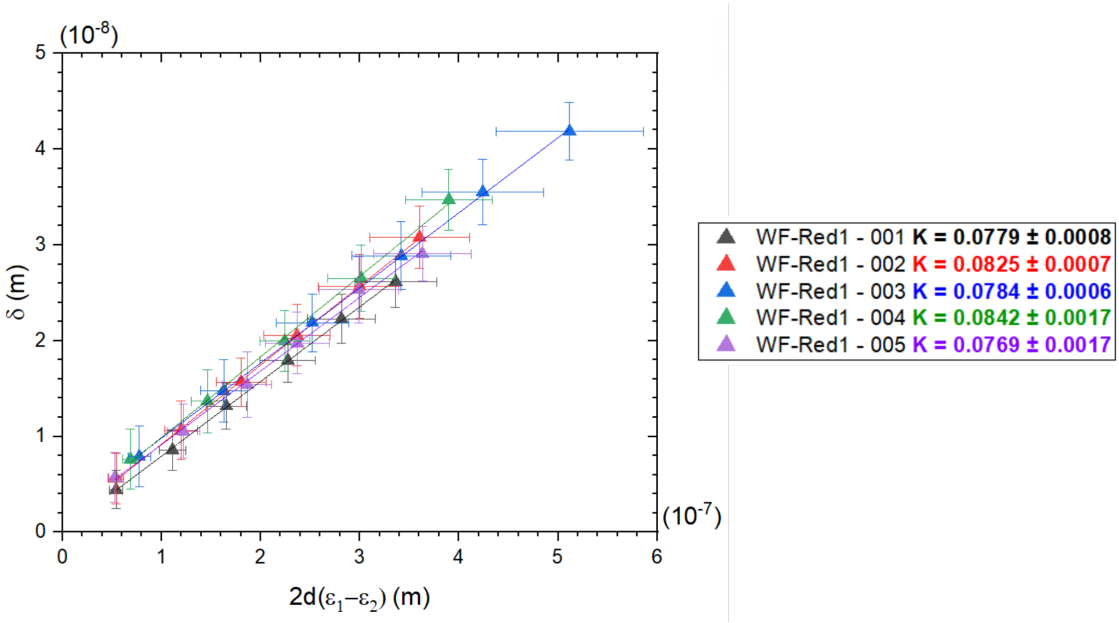


Figure 7.3: Calculations of strain-optic coefficient for WF-Red1. Retardation (δ) against double the coating thickness (d) multiplied by the principal strain difference (($\epsilon_1 - \epsilon_2$)). Each solid line represents the linear analysis formed on each sample. The value of each line's gradient is the corresponding strain-optic coefficient as highlighted in the legend.

Figure 7.3 presents the K calibration data for WF-Red1. Five individual coatings were tested and their individual K values are visible in the legend. The combined value for K was 0.08 $\pm$ 0.003. As expected the value for K was reduced from the clear WF31 formulation however it is still representative of a medium-high sensitivity coating.

The investigation was able to produce values for K with high precision for both WF31 and WF-Red1. The addition of the tint reduced the photoelastic sensitivity and these findings further support the analysis that surface reflection qualities affect the photoelastic response outlined in chapter 5.2. However, it was observed that WF-Red1 introduced increases to the uncertainty in both the captured retardation and measured thickness by the observed increase in the error. As the sensitivity is reduced the effects of the specular reflections from the silver paint, on degrading signal-to-noise ratio, have an increased effect on the measured retardation.

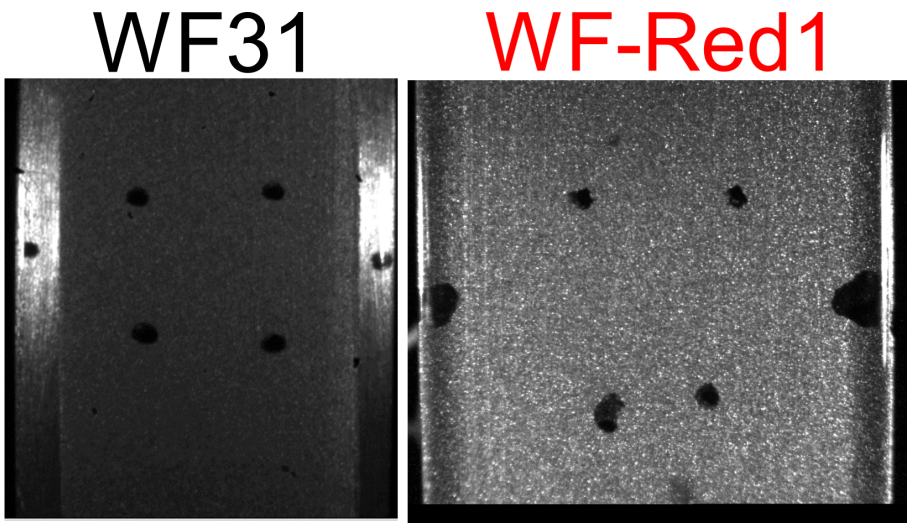


Figure 7.4: Comparisons of the light intensity output of WF31 and WF-Red1 samples. Both coatings were applied onto aluminium samples painted with the same silver paint. The high density of hot spot pixels within the WF-Red1 sample demonstrates a large reduction in the signal-to-noise ratio.

Figure 7.4 also demonstrates differences between surface finishes of the same paint. These images were taken using the same setup of two light sources either side of the GFP1600 within the same lateral plane, figure 5.5(b). The GFP1600 was also capturing similar light levels. The change in surface reflectivity was unexpected and efforts to determine the cause have not been discovered. The paint was always mixed thoroughly and applied in the same manner. This further demonstrates the need to develop an optimised reflective surface for the UV curable coatings. Subsequentially these effects are also the major contributor to the thickness measurement's uncertainty. Nevertheless, the precision associated with K for WF-Red1 remains high.

7.3 Discussions and conclusions

The values for K for WF31 and WF-Red1 were calculated to be 0.0982 ± 0.0018 and 0.08 ± 0.003 respectively. Comparing with table 7.1, these values indicate a medium-high sensitivity coating comparable to epoxy-amine based coatings.

Photoelastic Material	Strain-Optic Sensitivity	Elastic Modulus (MPa)	Strain Limit (%)
Polycarbonate	0.16	2200	10
PS - 1*	0.15	2500	5
Glass	0.14	70,000	0.1
PS - 2*	0.13	3100	3
Epoxy-anhydride	0.12	3300	2
Epoxy-amine	0.09	3100	3
PS - 3*	0.02	210	30
PS - 4*	0.009	4	$>$40
Polyurethane	0.008	3	100

*Table 7.1: Table of a number of photoelastic coatings with their typical properties [7,53]. *Highlights commercially available photoelastic coatings, products of Vishay Measurement Group [7].*

The calculated values for K in this investigation were closer to the hypothesis made in chapter 3.3. This hypothesis described WF31 having a value for K that would be comparable to LPC's ranging between 0.1 — 0.12 LPCs [10, 62, 63]. This comparison was argued due to similarities between the chemical structures of S160, LPCs and polycarbonate that all possessed double aromatic ring structures. Within chapters 3.1 and 3.2 this claim was confirmed. S160 was the resin that contributed significantly to the photoelastic response. WF-Red1 suffered a reduction in sensitivity due to the addition of the tint, hindering reflective qualities. Chapter 5.2 demonstrated differences within captured photoelastic responses due to decreases in reflection. However, WF-Red1 possesses the quality of being able to be thickness corrected within the GFP's software — a powerful tool for coating application. However, WF31 would also be useful in qualitative scenarios where a user would want to locate problem areas efficiently. The coatings are now ready to be validated in an industrial setting.

Chapter 8

Industrial focused applications

The development of a new photoelastic coating for RPSA has been achieved and the next stage is to perform validation testing. This chapter investigations the coating's effectiveness within applications that are important to industry. The aims were to scrutinise the coatings in different environments that required changes to the experimental procedure and in unfavourable settings where RPSA would take place e.g. well lit working spaces. Several applications were explored with WF-Red1 following calibration of the coating's strain-optic coefficient (K). Applications included laboratory based experiments with a focus on different sample materials and forced manufacture defects whilst another application validates the coating in a true industrial setting.

8.1 Research laboratory based investigations

Two experiments were conducted to explore the effectiveness of the application of WF-Red1 for RPSA investigations. The application of the coating was applied onto composite materials to demonstrate their usability on thinner samples. Firstly, a specimen of glass laminate aluminium reinforced epoxy (GLARE) with a hole in the centre was coated with WF-Red1 and placed in uniaxial tension. This demonstrated the thickness correction processing facility around features that provide difficulties within RPSA investigations e.g. holes and edges. The second application was performing RPSA on carbon fibre composite samples that were purposely made with defects. The objective for using these samples was to simulate industries that would be performing quality control with a main focus on qualitative data. Samples were chosen based on availability and access to materials within the University.

8.1.1 GLARE Sample

8.1.1.1 Methodology

Sample preparation followed similar procedures as described in earlier chapters. A GLARE sample (38 x 200 x 2) mm had a 3 mm hole drilled in the centre of the (38 x 200) mm face, figure 8.1.

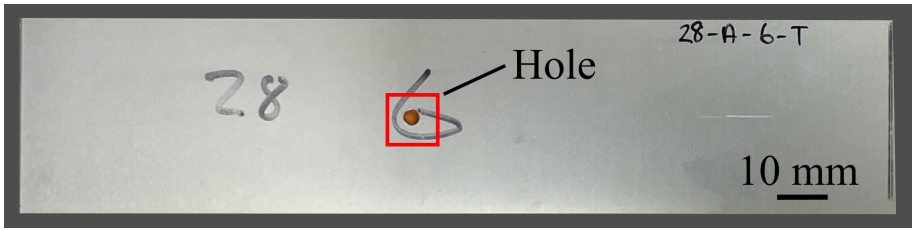


Figure 8.1: The GLARE sample prior to the application of a silver paint and WF-Red1. RPSA was performed on the sample using the GFP1600. The sample was placed in uniaxial tension with a stacked rosette strain gauge monitoring the strain away from the hole.

The sample surface was cleaned with acetone and then painted with silver aerosol paint (Hammerite smooth silver). Once the paint was completely dried, the surface was again cleaned with acetone and a number 6 K-bar (60 μm wet film thickness) applied WF-Red1. The manual application caused menisci to form around the hole and near the edges of the sample. A 20 s curing time was implemented to ensure maximum cure conversion was achieved. A stacked rosette strain gauge [132] was applied away from the hole, on the non-coated side, to validate the RPSA data using the same method described in chapter 7. Using a Mayes 100 kN hydraulic tensile tester the sample was securely gripped and a tensile load of 9 kN was applied incrementally in intervals of 1 and 2 kN. Lower load tensile testers did not possess grips wide enough to accommodate the width of the GLARE sample. However, this machine enabled secure contact with the sample and the strain from the gauges was monitored and used in the analysis rather than the load output of the tester. Photoelastic analysis was performed to observe how the effects of a meniscus around the hole and on the edges of the sample could be corrected for using WF-Red1.

8.1.1.2 Results and analysis

Figure 8.2 presents the effects of thickness correction on RPSA data performed on a sample of GLARE with a hole under uniaxial tension.

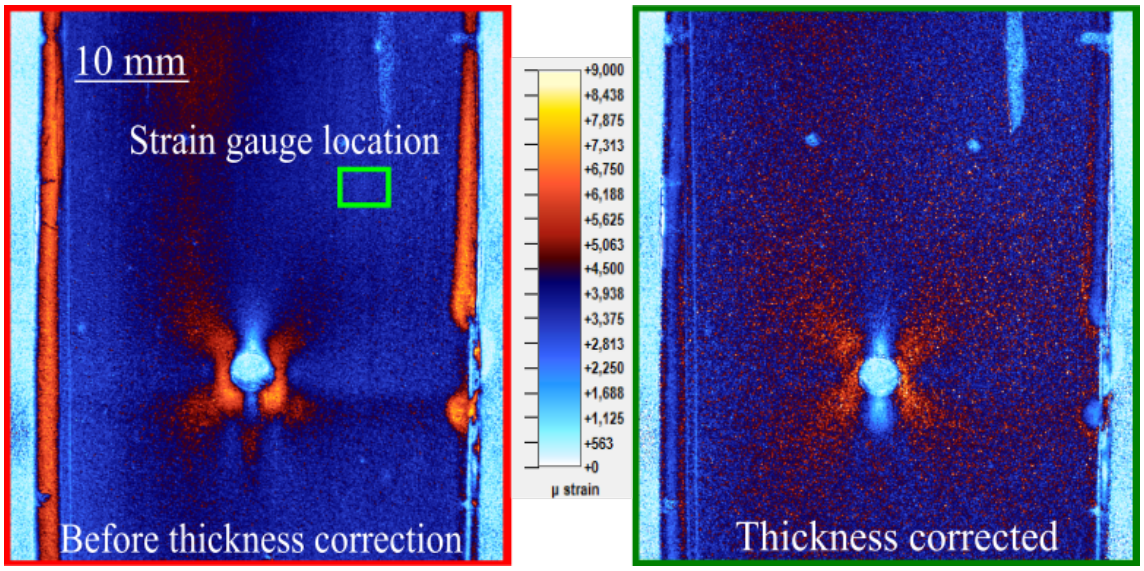


Figure 8.2: A GLARE sample with an applied load of 9 kN. A comparison between no correction and thickness correction is demonstrated. The effects of meniscus around the hole and on the edges of the sample have been removed and an expected strain map is observed more clearly in the corrected version.

The observable menisci have been removed around the hole and on the edges of the sample which resulted in a much clearer strain map of the sample under tension. The strain map matches that of well understood photoelastic investigations of a hole in a plate in tension. However, several discrepancies were observed. Firstly, considerable noise was observed in the corrected image. Secondly, the comparisons between principal strain difference values as calculated from the software and measured directly using strain gauges were not consistent. At the location of the strain gauge, the RPSA value for principal strain difference was 3972 $\pm$ 559 μstrain whilst the strain gauge measured value was 3088 $\mu\epsilon$. This indicated a difference in the value of K for WF-Red1. Recalibrating the coating using the strain gauge a value for K of 0.097 $\pm$ 0.003 was calculated. This K value was used for the translation of retardation into principal strain difference for this image only. To demonstrate the formation of the corrected pattern observed in figure 8.2, appendix F features GFP data at each applied load.

Whilst figure 8.2 demonstrates successful correction of thickness differences, the post processing facility has appeared to introduce noise in the sample. This is a result of the specular reflections of the silver paint used in the investigation as described in chapter 7. However, the calculated increase in WF-Red1's K value was problematic. The direct cause was not completely apparent until similar

observations were made in more recent investigations that are described in section 8.2. The issues arose due to the experimental setup and unforeseen inaccuracies inflicted by slight changes to the laboratory environment. Major changes were: the hydraulic tester sits beneath a skylight with the test conducted on a bright day; the tester was surrounded by perspex safety screens; finally, the tester had a large metallic frame with large pneumatic grips. All these additional elements provided reflections that have been picked up by the GFP1600 and misinterpreted as increases to the photoelastic response. Additionally the manufacture process of the GLARE sample is unknown. Strain gauges were placed on the opposite face to the coated face. As a result, orientation changes within the layers could result in different strain values being measured by the gauges that in turn causes the calculation of K to be incorrect. As further investigations were needed to understand all the causes changes to the experimental setup were minimal. Initially, it was proposed that proximity to reflections from sunlight was the only cause. As a result, the carbon fibre experiments were conducted in a dark room.

8.1.2 Carbon fibre sample

8.1.2.1 Methodology

For carbon fibre investigations strips (150 x 25 x 2) mm of carbon fibre composite with an 8 ply quasi-isotropic layup were used. During manufacture between the second and third layer a piece of PTFE tape was placed at one end of the strip, figure 8.3, and was not visible on the surface of the first layer.

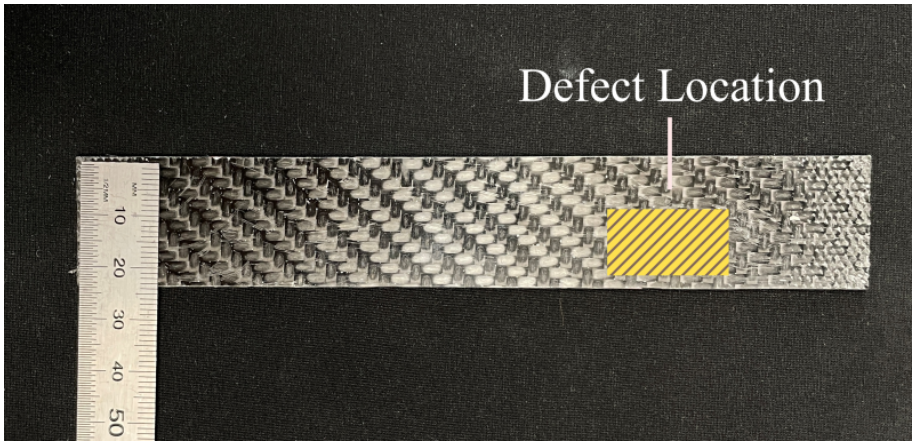


Figure 8.3: The carbon fibre sample created with an added defect. The sample has an 8 ply quasi-isotropic layup with a piece of PTFE tape placed between the second and third layer. The defect was undetectable both visibly and physically on the surface of layer one.

Three samples were prepared following similar procedures as the GLARE sample. Silver paint was first applied and dried before the application of WF-Red1 using a K-bar (60 μm wet film thickness). Strain gauges were applied to the opposite side of the sample to validate RPSA data. The samples were placed in a 25 kN Tinius Olsen tensile tester and a load of 16 kN was applied in intervals of 2 kN. RPSA was performed correcting for thickness differences using the thickness facility within Deltavision.



Figure 8.4: Carbon fibre samples applied with a silver paint and the UV curable photoelastic coating WF-Red1. Defects were purposely included between the second and third layers. RPSA was performed using the GFP1600.

8.1.2.2 Results and analysis

At a load of 2 kN the effects of the added defect on the composite sample were clear as highlighted in figure 8.5.

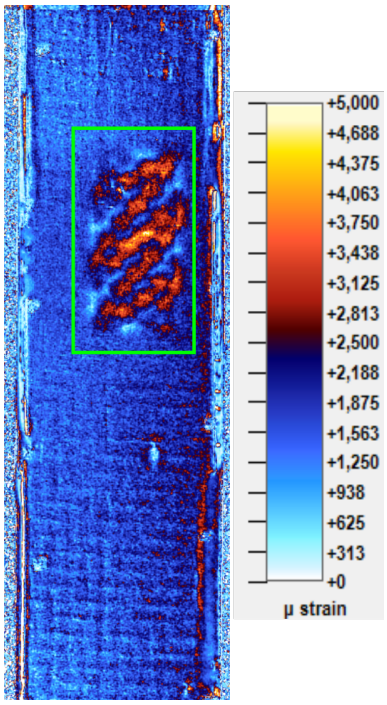


Figure 8.5: RPSA Data of a carbon fibre composite sample that was made with an added defect. The sample was loaded at 2 kN and the defect is highlighted in the green box. The red UV curable formulation was used to correct for thickness differences across the samples.

This measurement demonstrated the applicability of this coating within quality control applications. Clear identification of the defect was observed demonstrating a critical area of the sample due to the degradation of the structural integrity. Using strain gauges on the sample the calculated RPSA data was validated against the measured strain. Figure 8.6 presents the comparison where a close overlap between strain gauge and RPSA datasets exists. RPSA calculations utilised the original K value of 0.080 $\pm$ 0.003 at the higher end of the uncertainty, 0.083.

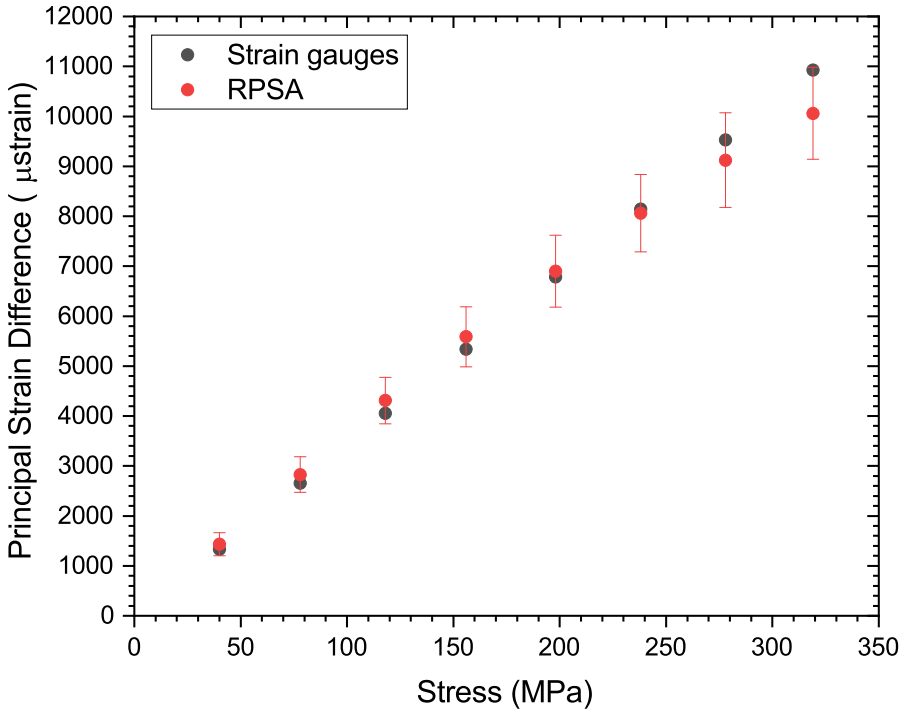


Figure 8.6: Comparisons of principal strain difference of the carbon fibre sample calculated using RPSA and measured directly using strain gauges. RPSA data was calculated using a strain-optic coefficient of 0.083.

Investigations on the composite sample demonstrated the effectiveness of WF-Red1 for quality control applications. At an applied stress of 40 MPa the location and the effects of the defect can be easily observed and also quantified. These samples were originally designed for final year undergraduate students to perform Digital Image Correlation (DIC) measurements. In its simplest form, DIC works by matching small square subsets of an undeformed image of a component to locations in an image of the surface after deformation, to produce full-field maps of deformation and strain. The technique records local "fingerprint" digital greyscale patterns of a surface. The high contrast random pattern required can be simply the texture of the surface, but it is more common to apply a speckled paint coating, or decals. Whilst the pattern generation and application still requires skill, it is much less time-consuming than the current surface preparation methods for RPSA. However, the advantage of RPSA over DIC is that it is entirely based on physics, whereas DIC needs post processing and careful subset selection. The data within figure 8.5 can be compared to DIC as shown in figure 8.7. Within the two DIC datasets the location of the defect can be observed however the clarity was poor compared to the RPSA dataset, figure 8.7(a).

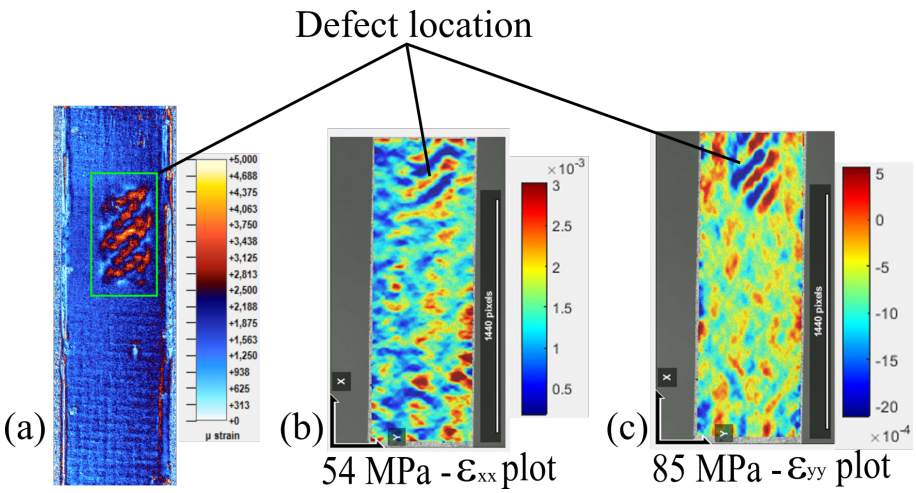


Figure 8.7: Comparisons between RPE and DIC strain analysis on a carbon fibre manufactured with a defect between the layers. The defect is mostly easily demonstrated in the RPSA data, ***(a)****, compared to DIC,* ***(b) & (c)***

8.2 Applications in industrial setting

The following applications assess the coating within an industrial environment onto structures being used at The Aerospace Integrated Research & Test Centre (AIRTeC) at Airbus Filton. Industrial trials were performed over a two-week period with an aim to apply WF-Red1 onto functional test structures that would provide unique application challenges. These applications were used to establish standard operating procedures for the application of the coating onto a wide range of structures outside lab-based research environments. Additionally, RPSA was performed on these structures to demonstrate its performance. After discussions with Airbus test engineers the following sample surfaces were used: large aluminium dogbones and a test wing structure being used for experimental development that had a total length of approximately 3 m. The former sample allowed for additional validation using Airbus expertise. The latter application provided a unique application on larger areas with problem features such as numerous bolt points. Coating locations and loading scenarios will be described in the methodology. Exact wing dimensions, detailed descriptions and images are proprietary information and cannot be shared with their full details. Additionally, there were restrictions on the images taken due to sensitive experiments being performed in proximity to the structure.

8.2.1 Coating application and curing

In order to coat larger areas, necessary modifications to the methodology were conducted. Firstly, manual applicators such as K-bars would not be applicable on the test wing structure due to large areas preventing contact between the K-bar and the wing surface and protruding bolt heads would get in the way of casting a coating. A simple solution was to use a paintbrush to spread the formulation across the desired coating area. It was found that brushing was able to produce solid coatings without major reticulation effects causing holes in the coating. A paintbrush was chosen due it being a cost effective method whilst not breaching any health and safety constraints within Airbus. Secondly, a conveyor curing system would not accommodate large samples and structures so a handheld device was utilised and selected with the assistance of Arkema. The curer used has since been discontinued and online documentation is not available. To summarise, the UV hand lamp operated at 400 W with a mercury bulb that outputted the target wavelength, 230 nm, to enable cure of WF-Red1. The lamp had an output window of dimensions (140 x 85) mm with no output filter to control wavelength emission.

The first few days of the placement were spent establishing curing procedures with the unfamiliar curing lamp. A UV cure specialist from Arkema was present for these investigations offering guidance and advice. The main concern was the height from the UV light to the coating material and its effect on the cure conversion. The handheld lamp required the user to direct the light towards the liquid formulation using the device's handle that is located underneath the lamp head. By irradiating the sample for 20 s at a distance approximately 5 — 15 cm from the surface produced coatings that had a stretchy and soft feel which is indicative of a partially cured coating. It was decided to extend the cure time to 1 minute to safeguard achieving maximum cure conversion. 1 minute curing produced glassy coatings that resembled the feel of coatings that had achieved maximum cure conversion. Due to time constraints of the placement and lack of equipment, the ability to determine the minimum time required to achieve maximum cure conversion was not able to be measured. However, previous data determined that a minute of cure time was more than enough to satisfy the requirement to achieve maximum cure.

8.2.2 Aluminium dogbones

8.2.2.1 Methodology

The first application was performed on aluminium dogbones that were placed in uniaxial tension. The dimensions of the dogbone were (797 x 305 x 40) mm and the alloy of aluminuim was 7150-T651. The significance of this test was to gain valuable insight into the altered curing procedure and how RPSA performed in the space that the test wing structure was located. Both the tensile testers and wing structures were housed in the same large hanger that was brightly lit with ceiling lights. Two dogbones were prepared with Hammerite smooth silver aerosol paint that were left overnight to dry then were cleaned with isopropyl alcohol using lint free cloths. WF-Red1 was applied to the gauge length and brushed using long strokes to form a continuous coating along the gauge length. The output window of the UV lamp was held approximately 5 cm away from the coating for 1 minute. Following cure the dogbones were adhered with TEE rosette strain gauges [134] applied by experienced engineers within Airbus. The gauges were applied on opposite face to coating application. Applying strain gauges enabled further validation on WF-Red1's strain-optic coefficient. The dogbone samples were placed into 500 kN hydraulic tensile testers secured using pneumatic grips. The top grip maintained hold of the sample and the gauges were balanced using a recently calibrated P3 strain indicator and recorder. The GFP1600 was positioned in front of the dogbone illuminated by two circular polarised light sources. Due to the size of the tester and the equipment available, the camera was positioned approximately 0.5 — 1 m away from the sample. A 28 mm macro lens enabled an appropriate field of view of the sample whilst maintaining suitable exposure. A perspex screen was positioned between the tester and operators. Load was applied in steps of 25 kN up to a target load of 400 kN to further increase the dynamic range of gathered data. The entire setup and operation of the tensile machines was performed by Airbus engineers. A value for WF-Red1's strain-optic coefficient was calculated following the procedure outlined in chapter 7.

8.2.2.2 Results and analysis

The first dogbone was placed in a 500 kN tensile tester with circular pneumatic grips. Between 230 — 250 kN the sample consistently slipped within the grips. The GFP1600 images for thickness measurements and RPSA at 225 kN are shown in figure 8.8.

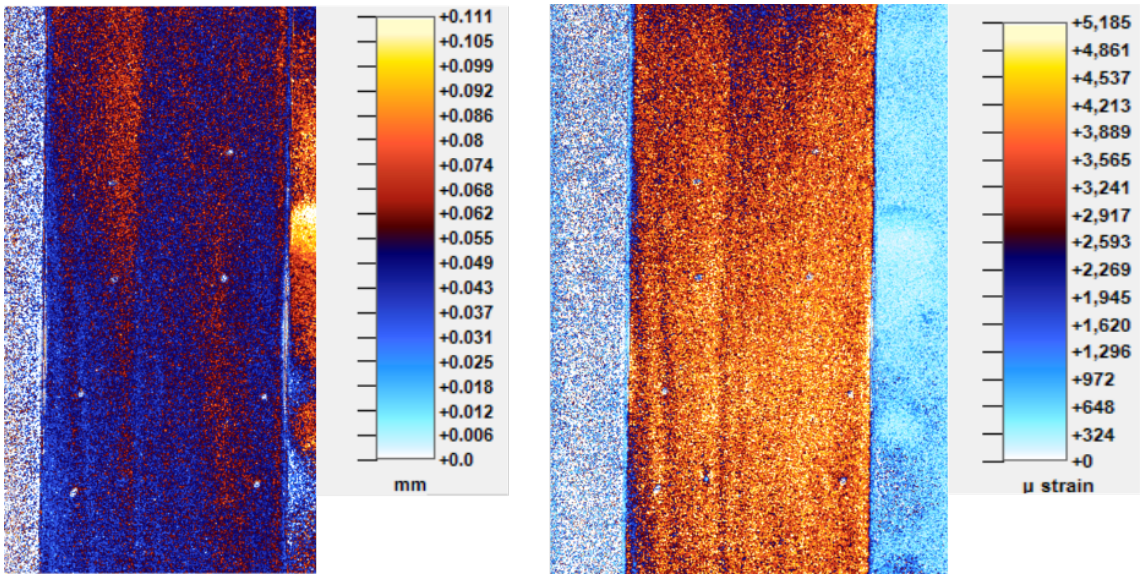


Figure 8.8: GFP1600 images, analysed by the software Deltavision, of an aluminium dogbone in uniaxial tension at a load of 225 kN. The images demonstrate both thickness measures and strain analysis with the scales indicating the values of the colours shown in the images. A strain-optic coefficient of 0.08 was inputted into the software for strain analysis.

Using a brush the coating was applied at a thickness of 0.05 $\pm$ 0.01 mm which was in agreement with manual measurements when the coating was removed from the sample. Performing RPSA with a value for K of 0.08, using the calculated value from chapter 7 for aluminum samples, the middle bulk of the sample generated a value for principal strain difference of 3678 $\pm$ 738 $\mu\epsilon$ for an applied load of 225 kN. The standard deviation of both thickness and principal strain difference was extracted from the Deltavision software. Performing median smoothing reduced the uncertainty to $\pm$ 462 $\mu\epsilon$. However, the strain gauge values for this load was 4246 $\mu\epsilon$ which is higher than the average value measured via RPSA but falls within the uncertainty. Reducing the K value to its lower uncertainty limit of 0.077 raises the principal strain difference value to 3783 $\mu\epsilon$ which enables the median smoothing uncertainty to overlap with the strain gauge value. However, manipulation of K values demonstrates a weakness in the coating's performance. Furthermore, uncertainty values of $\sim$ 20 % is very high and introduced a lack of confidence in the extracted values. By performing K value calibration on this sample the following data were calculated and shown in figure 8.9.

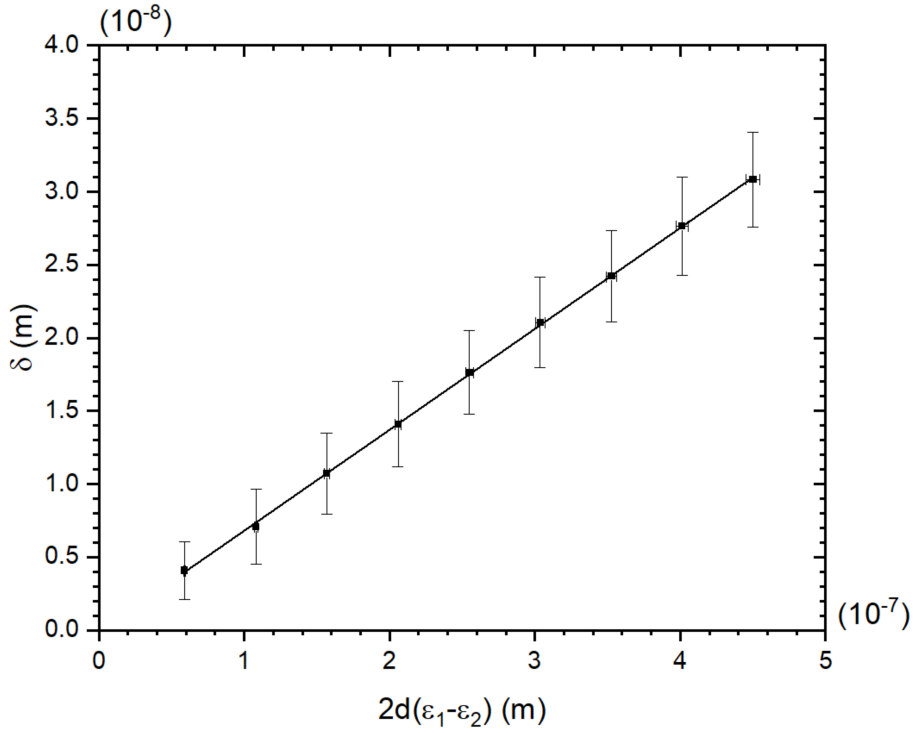


Figure 8.9: Strain-optic coefficient calculation from an aluminium dogbone applied in uniaxial tension at Airbus' AIRTeC site. The linear response produced a value for K of WF-Red1 of 0.0690 $\pm$ 0.0004. The calculated value is lower than the previously calculated value of 0.08 $\pm$ 0.03.

Figure 8.9 calculates the value of K to be 0.0690 $\pm$ 0.0004. Uncertainty bars were calculated from standard deviation values associated with retardation values and thickness values extracted from the Deltavision software.

The second Al dogbone was loaded in a different tensile tester with serrated wedge grips which did not cause the sample to slip throughout the load to a maximum of 400 kN. During analysis there was an immediate issue with captured retardation compared to the strain gauge values as shown by figure 8.10.

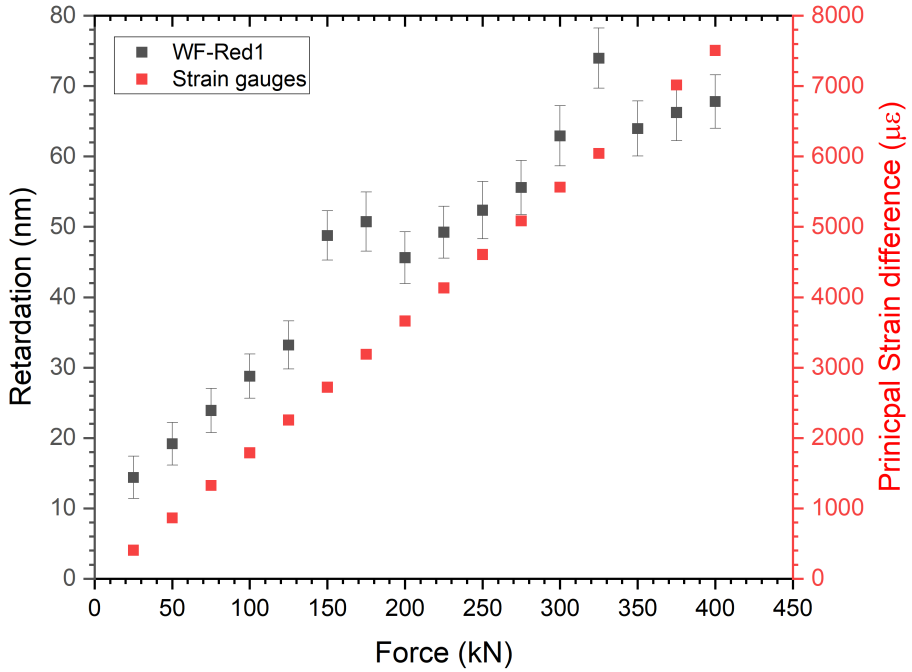


Figure 8.10: The comparison of measured retardation values with the strain gauge values of an aluminium dogbone in uniaxial tension. The non-linear response was unexpected and indicated a problem with experimental setup.

Problems with the photoelastic response in figure 8.10 is the initial high retardation values with sudden jumps in retardation that do not match the response shown by the strain gauges. Retardation values have had the zero load image subtracted. This response indicated problems with the experimental setup. Reviewing the light output images of 125, 175 and 200 kN and observed changes in the background light was observed and highlighted in figure 8.11.

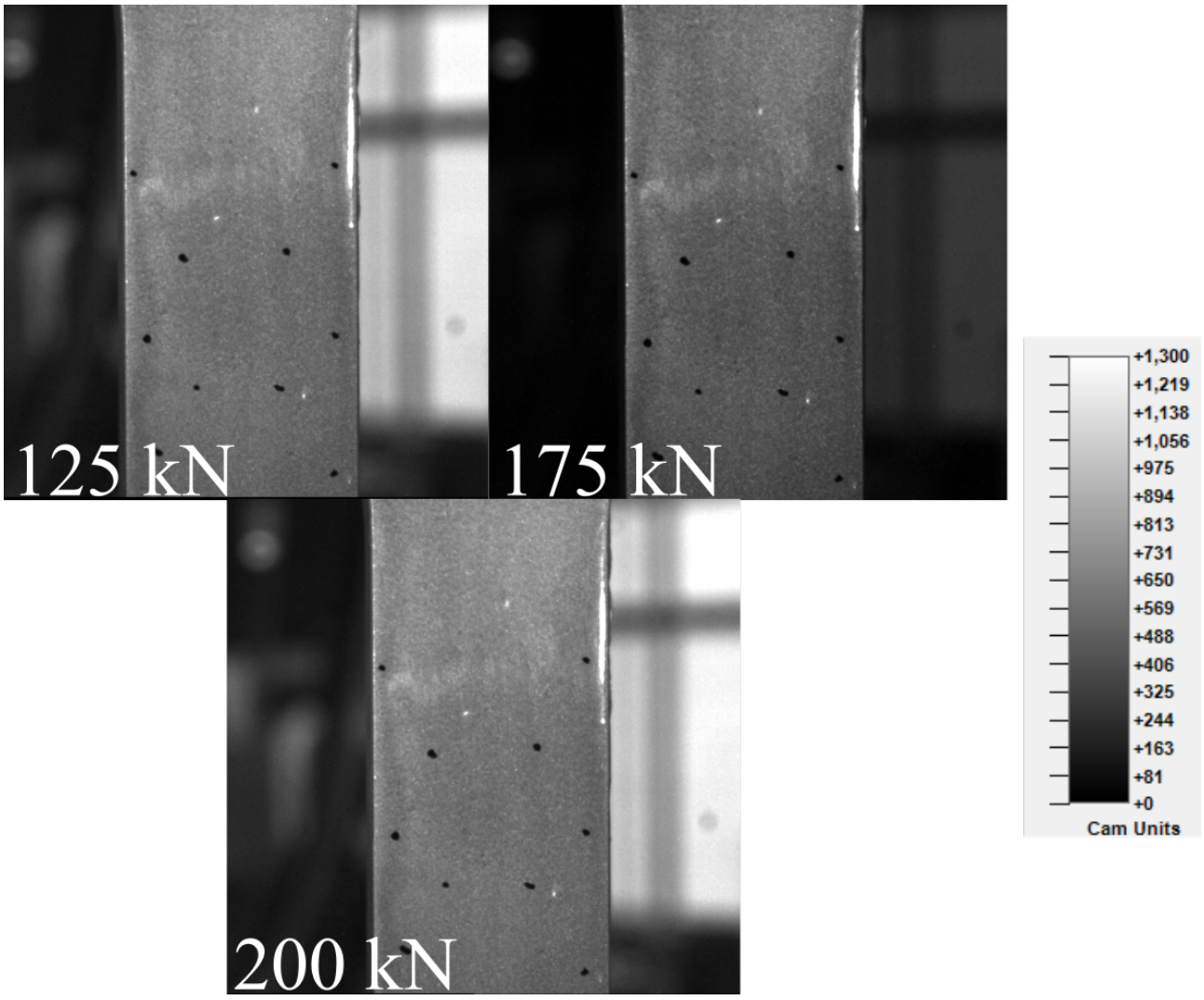


Figure 8.11: Three light images taken from the GFP1600 of the aluminium dogbone with three different loads. The light conditions change between the loads that relate to the unusual differences in retardation values demonstrated in figure 8.10.

The light intensity from 125 kN to 175 kN decreases before returning at 200 kN. This finding was also observed between 300 — 350 kN. Comparing these observations with the data in figure 8.10 indicate that lighting conditions are having an effect on the measured retardation. The exact influences on the light conditions have not been fully determined but there are several factors that would have an effect. This tensile tester was facing in the opposite direction to the tester in the first Al dogbone investigation. The space behind the second tester was more open with numerous machinery that had highly reflective metal surfaces. The side supports of the second tensile tester were closer together and the light sources were illuminating them. These supports were polished metal cylinders that would have produced a bright reflection back towards the imaging equipment. A

perspex screen was placed without regard to reflection it may be producing back towards the sample. Doors to the outside were located behind the testing area and ambient light could be captured by the GFP1600. An overhead crane was in operation that passed over overhead lighting. Due to the light intensity returning to its initial state a reversible change to the environment must have taken place. As a sudden reduction in light intensity was captured, the subtraction process would not be valid for all captured images. Further analysis had to be abandoned due to personnel and sample availability the test could not be repeated.

8.2.3 Test wing structure

8.2.3.1 Methodology

The second application was applying WF-Red1 onto various locations on the underside of a test wing structure approximately (3 x 1 x 0.15) m in dimension with the skin of the wing made from aluminium grade 7055A-T7951. The structure mimics a wing in a cantilever bend arrangement with four actuators able to apply load in both an upwards and downwards direction. There were a few limitations of this structure. Firstly, the top surface of the wing was being used for other investigations. Secondly, the space underneath the structure was limited with many mounting brackets that restricted the ease of tripod placement. Finally, due to technical issues a maximum load of 6 kN could only be applied to structure. Two locations were chosen for RPSA investigations: a $\sim$(200 x 200) mm square at the support of the wing at the edge which featured two rows of bolting points; and another $\sim$(200 x 200) mm square at the location of rib approximately at a quarter of the wing's length away from the support with bolt holes running both parallel and perpendicular to the wing. Both locations are shown in figures 8.12 and 8.13.

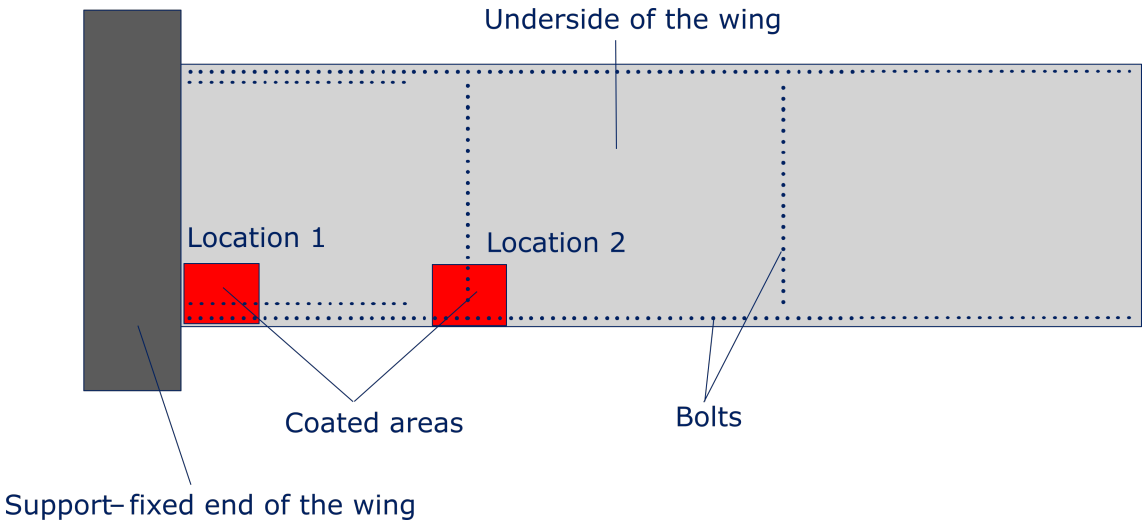


Figure 8.12: A schematic demonstrating an approximate layout of the underside of the test wing structure. Rows of bolt heads ran along the length of the wing with perpendicular rows of bolts at various locations along the wing. The two red section illustrate the locations where RPSA took place.

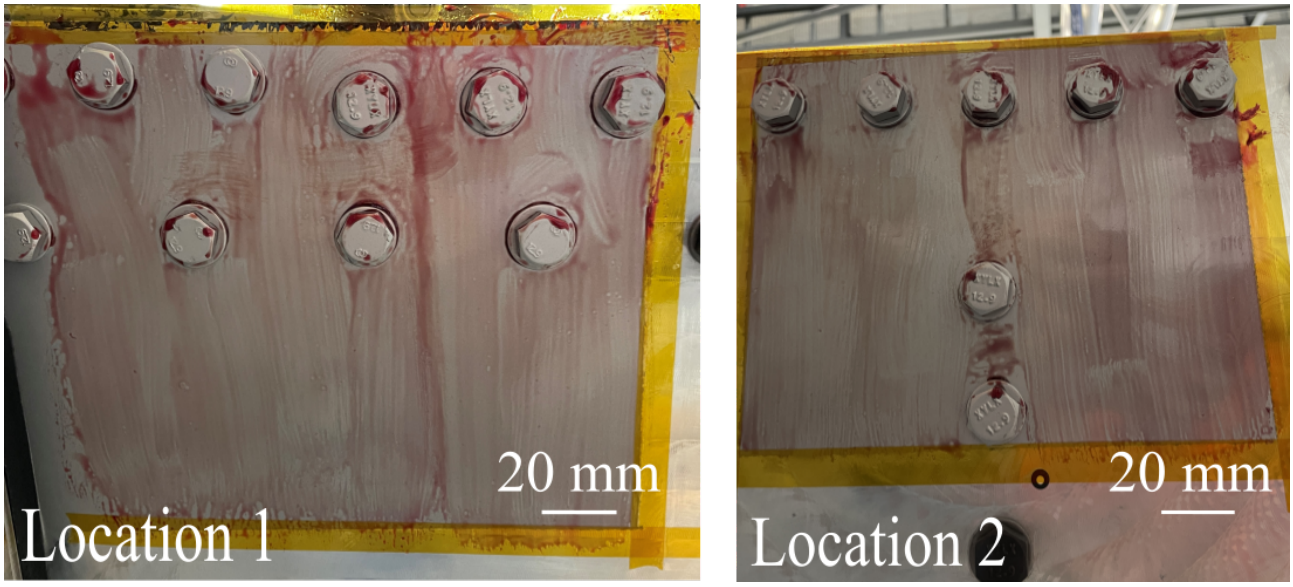


Figure 8.13: The application of WF-Red1 on a test wing structure at two different locations. WF-Red1 was brushed on and cured using a handheld curer. Curing was performed in sections due to the size of location being bigger than the output window of the curer.

Once the locations were finalised, an Airbus engineer cleaned the locations with isopropyl alcohol prior to the application of aerosol silver paint that was left to dry overnight. The curing procedure was performed in a single half hour session. Firstly the entire area was bordered with heat-resistant tape. The tape acted to protect the surrounding area whilst being used to trial methods and to

ease the removal process. The painted locations were cleaned with isopropyl alcohol and WF-Red1 was applied using a brush. Applying the coating was not straightforward, firstly the coating area was greater than the output window of the curer resulting in both locations being cured in two separate sections. Secondly, the effects of reticulation were quite severe meaning the application of the coating and irradiation of UV light had to be performed quickly in succession. This was made challenging with only one user performing both tasks. The difficulty of coating application can be observed in figure 8.13 with well-defined brush marks, obvious thickness differences and the overlap of coatings. Whilst the application of the coating is not ideal the effects of application inexperience can be determined through performing RPSA. Additionally, time constraints limited the application of the coating onto different locations on the wing structure. The GFP1600 was placed directly underneath each location with light sources on separate tripods positioned either side of the GFP illuminating the coated area. The GFP1600 was initially mounted with 16 mm lens to capture the whole area mounted approximately 0.5 — 1 m from the surface. A 28 mm macro lens was then used to zoom in on areas of interest. Two light sources were required to prevent the effects of shadows from the bolt heads that would produce low light levels resulting in no measurable photoelastic response. The angles of light were not monitored but placed to satisfy requirements of no direct reflections and to counteract any shadows produced by the protruding bolt heads. Perspex screens were positioned around the wing structure. Loading was performed in 2 kN intervals from 0 — 6 kN (underside in tension) and 0 — -6 kN (underside in compression) with an image being captured at each load interval. The wing underwent tensile or compression loading and returned to zero load where another GFP image was taken prior to loading in the opposite direction. Upon completion, analysis followed similar steps described in earlier sections. The coatings were then removed to demonstrate the ease of removability.

8.2.3.2 Results and analysis

RPSA investigations on the wing structure was successful in demonstrating observed changes in principal strain difference from RPSA using WF-Red1. All RPSA data was thickness corrected and subtraction processing performed. Compressive loading measured the greatest contribution on RPSA data on the location closest to the support is demonstrated in figure 8.14.

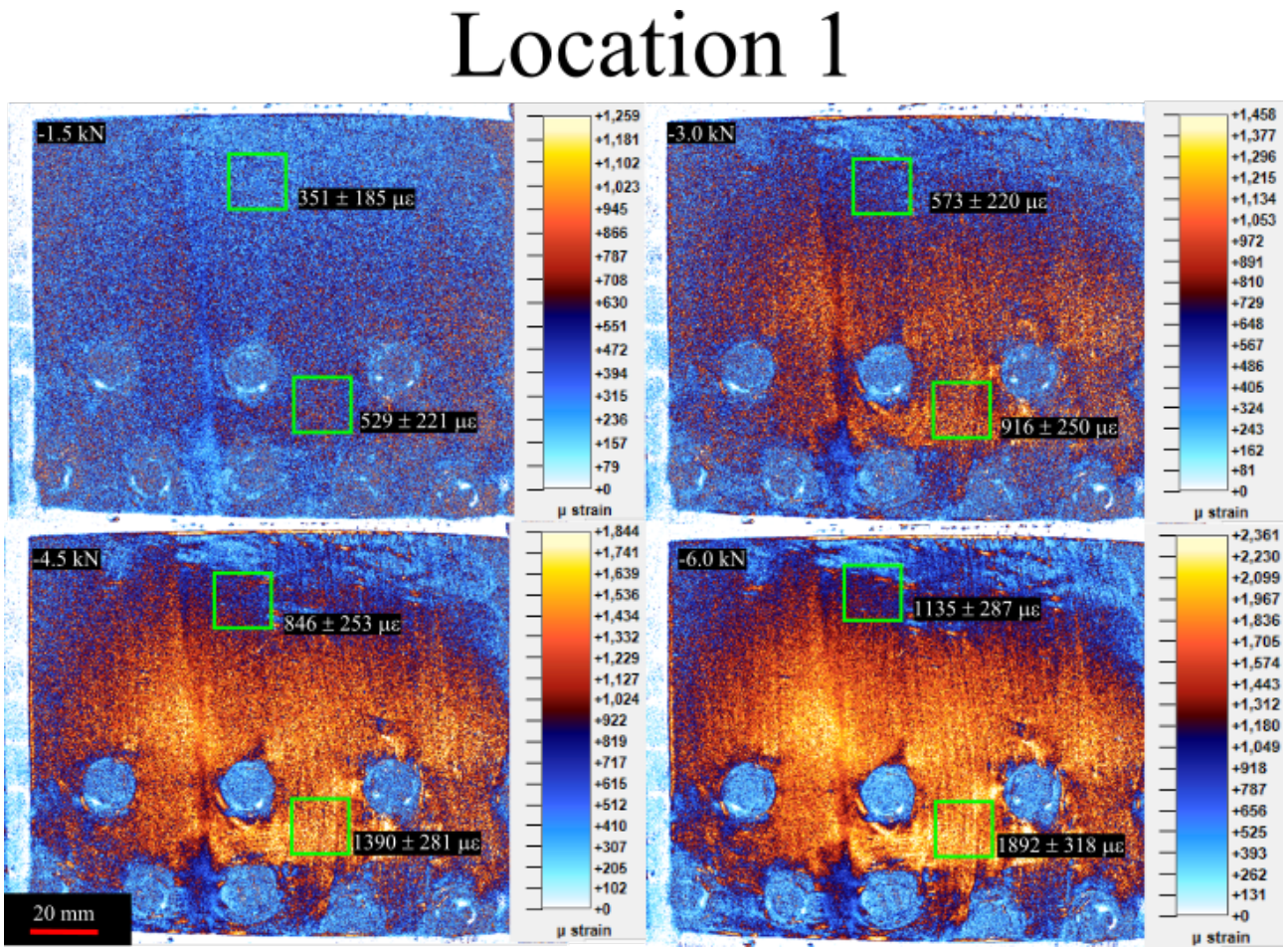


Figure 8.14: Reflection photoelastic strain analysis (RPSA) performed on a test wing structure using WF-Red1 at location 1. The location for RPSA was towards the support of the wing on the bottom of the wing at the edge. At this location the surface was in compression. The location of the support was at the right of each image.

The wing support was positioned at the right of each image. RPSA was performed using a K value of 0.069 as calculated during the Airbus dogbone experiments. This decision was made as the value was calculated in the same environment. Uncertainty values are the standard deviation of the strain values outputted from Deltavision. RPSA on the location further along the wing is demonstrated in figure 8.15.

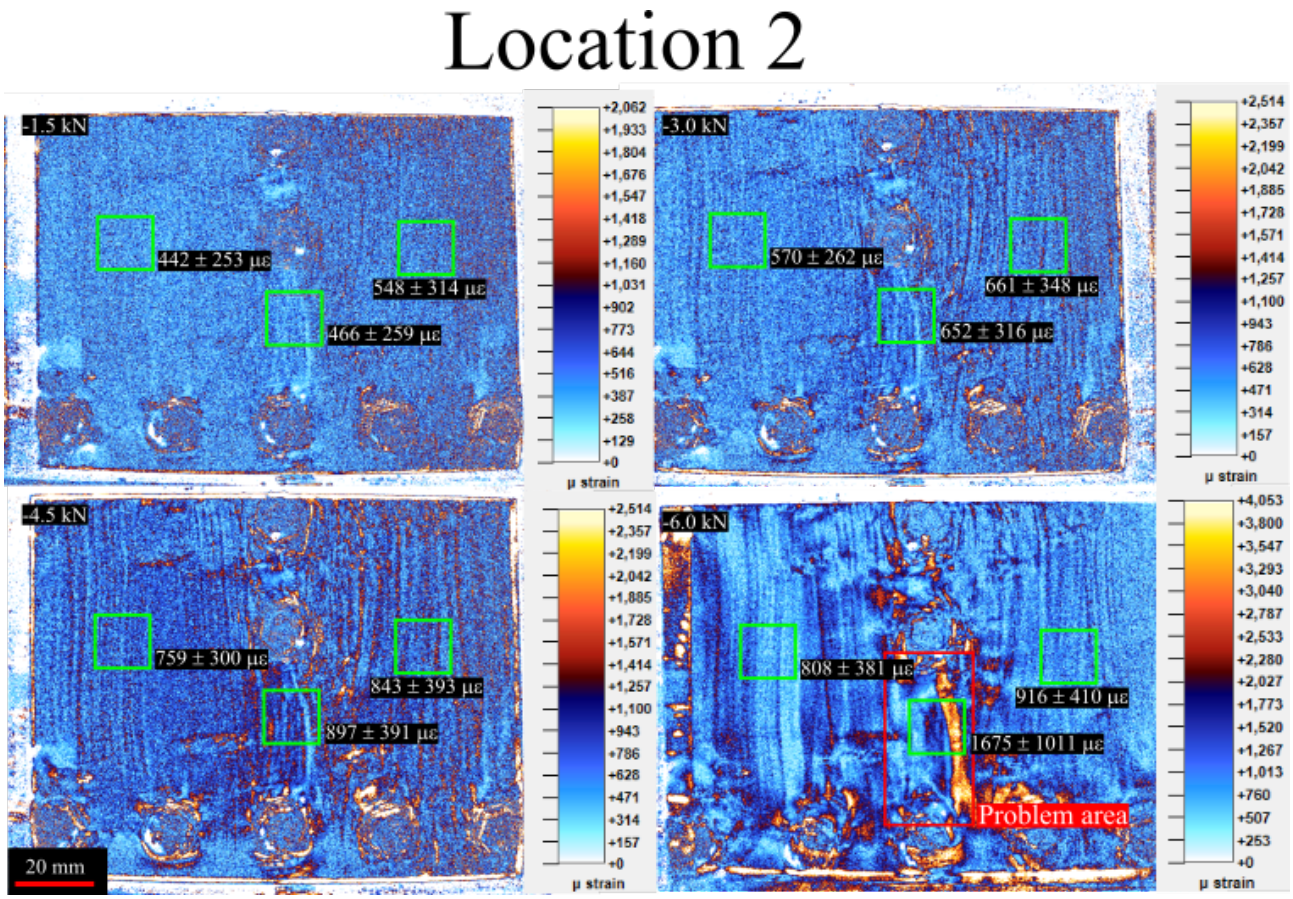


Figure 8.15: Reflection photoelastic strain analysis (RPSA) performed on a test wing structure using WF-Red1. The location for RPSA was approximately at a quarter of the wing's length closest to the support. At this location the surface was in compression. The location of the support was at the right of each image.

RPSA on location 2 featured the detection of lower increments of strain as load was increased. However, the GFP images were negatively impacted by the application procedure with the appearance of brush strokes having a detrimental effect on the signal-to-noise ratio. This was also observed in figure 8.14 however not to the same magnitude. Additionally, location 2 had inaccuracies within the -6 kN load image with a hot spot within the lower middle section of the image. This hot spot was immediately noticeable and an additional loading cycle was performed focusing on the problem area with the 28 mm macro lens.

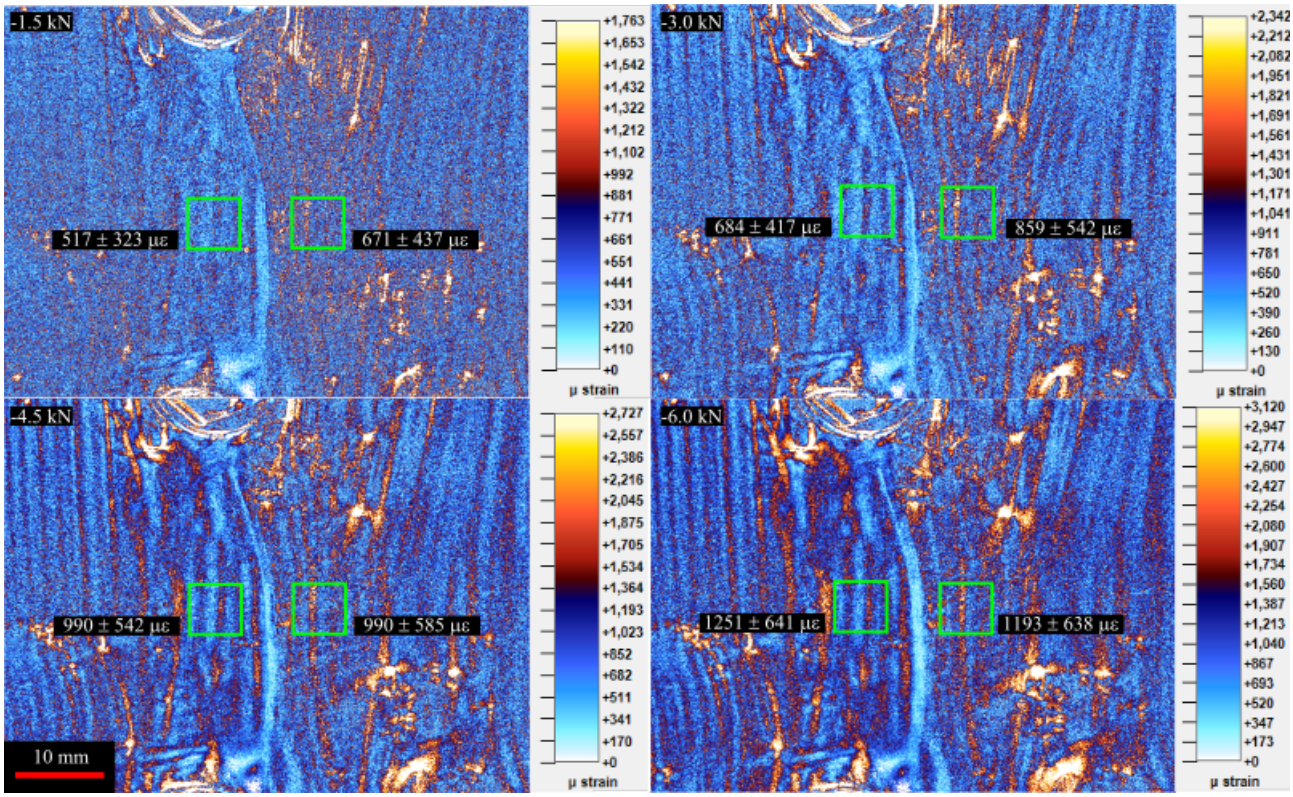


Figure 8.16: Reflection photoelastic strain analysis (RPSA) performed on a test wing structure using WF-Red1. This location focused on the problem hot spot illustrated in figure 8.15. The effects of brush strokes are drastically increasing the presence of noise.

Figure 8.16 demonstrates that the hot spot was no longer present however the effects of the brush strokes were more apparent. The brush strokes have introduced significant noise in the data with all values for principal strain difference possessing extremely high uncertainties. These findings demonstrate a limitation with either the brushing application and/or the thickness correction facility. The effect of the thickness correction facility was explored by comparing thickness measurements on both locations.

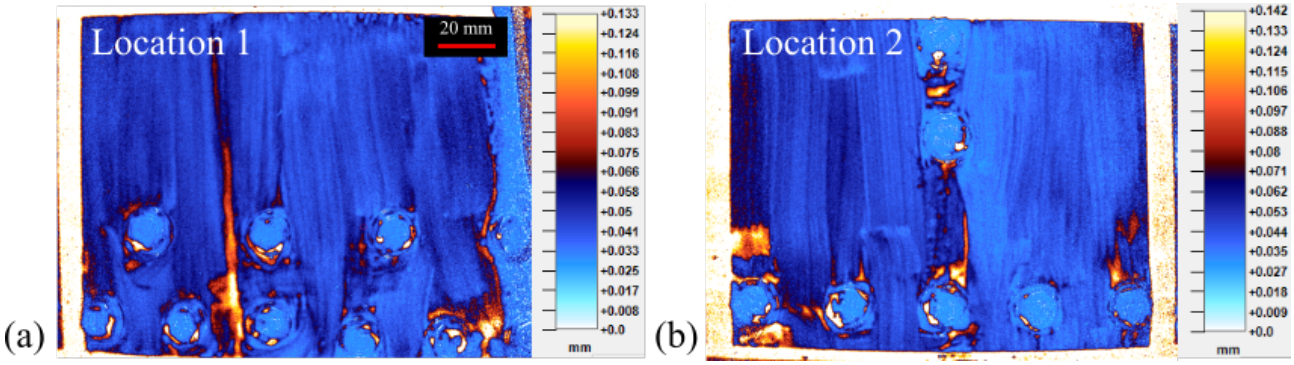


Figure 8.17: Thickness measurements on both locations performed by Deltavision. The appearance of brush marks looks similar between the locations however the photoelastic response at location 2, ***(b)****, is negatively impacted by their presence. Location 1,* ***(a)****, is not affected to the same degree.*

Figure 8.17 shows that the thickness measurement image was similar between location 1, figure 8.17(a), and location 2, figure 8.17(b). As a result, it was unclear how the thickness correction has not functioned as intended for location 2. Further work is required to investigate these findings utilising the observations made during this investigation. One outcome of this investigation was that rushing the coating application process has had a negative impact on the signal-to-noise ratio of the gathered GFP data. The urgency to cure the coating was a result of the strong effects of reticulation. This effect needs to be addressed to enable consistent application of the coating. Recent discussions with Arkema state that additives to the formulation can be added to combat this effect by reducing the coating's surface tension [135]. This combined with thorough cleaning and further consideration on the application for RPSA would improve the coating procedure. The latter comment addresses the location of the coated areas on the wing test structure. Preparing and coating the area was awkward and challenging especially with one person. Future investigations should aim to be able to apply a coating in a controlled manner and cure once ready. Additionally, curing equipment that enables consistent height control would remove uncertainty with regard to the cure conversion of the coating. Height gauges could be designed to allow the curer to rest on the surface being cured.

The coating at both areas was removed in less than half an hour using a small blade to peel the coating away from the surface. Removing the heat-resistance tape enabled the blade to get in between the wing and the coating more easily. The awkward position of the locations made it difficult to look up at the coating for extended periods of time. However, these challenging locations further tested the application procedure of the UV curable formulation.

8.3 Discussion and conclusions

This chapter has demonstrated both strengths and challenges of WF-Red1. Qualitative analysis of RPSA has shown to be effective with thickness corrections enabling clearer strain fields on samples with holes, figure 8.2, and problem areas being easily detectable on purpose made samples with hidden defects, figure 8.5. Applications onto larger structures also demonstrated effective qualitative RPSA analysis in certain locations, figure 8.14. The major strength of the coating is the application process that allows for the coating to be applied around holes and bolt heads. With sheet photoelastic coatings delays for data collection and potential inaccuracies are introduced as features need to be carefully manufactured without introducing heat induced birefringence and distortion through sheet stretching [11, 12]. Whilst all liquid photoelastic coatings overcome these procedures WF-Red1 was cured in 1 minute and the removal was straightforward. WF-Red1 requires no mixing and the viscosity allows for easy brushing onto structures. Additionally, WF-Red1 was removed quickly and did not require specialised tools such as grinders to remove two-part epoxies that has often been performed at Airbus during RPSA.

However, challenges have presented themselves in these investigations resulting in the need for further work. Confidence surrounding quantitative analysis emerged from differences in calculated K values from chapter 7, GLARE samples and the aluminium dogbones used at Airbus. K is a constant ashown by reintroducing equation 2.25

$$\begin{aligned} (\epsilon_1 - \epsilon_2) &= N\left[\frac{\lambda}{2Cd}\right]\left[\frac{1+\nu_c}{E_c}\right] \\ where \quad K &= \left[\frac{1+\nu_c}{E_c}\right] \end{aligned} \tag{2.25}$$

Nevertheless, consistency of K values was shown between many coatings in chapter 7 and GLARE coating methods followed the same curing procedures. Aluminium dogbones had changes to curing method however the 1 minute cure period was deemed excessive but was used to ensure complete cure. Therefore, changes in coating properties is unlikely to be the cause. Considering methods of calculating K the strain gauges could be problematic. Inexperience in application methods for the large majority of samples would have an effect especially if the gauges were not bonded sufficiently or orientated incorrectly. Moreover, if loading directions were not along the longitudinal face then principal strain calculations would not be valid. Yet, the consistency of K values between

samples goes against these observations. It is more likely that strain gauge application and loading inaccuracies are inflicting uncertainties in the results for all samples. The changes in the value of K occurs when the sample material changes. The effects of material changes on K are not widely discussed especially as manufacturers provide only a single K value. Furthermore, considering the theory changes to sample properties do not appear to have an effect on K. However, Cloud [55] mentions that material problems are often not accounted for and that manufacturers K values are used with potential accuracy loss. Cloud then states that material calibration is important in all photoelastic investigations. The data in this chapter agree with Cloud's claims. Another issue presented in RPSA is the large uncertainty associated with the principal strain difference calculated by Deltavision. The accuracy associated with pixel values exists at a minimum of $\sim$ 0.7 nm. Due to the thickness of WF-Red1 the magnitude of measured retardation is greatly effected by the value of the software's accuracy. Considering the effects of specular reflections and brush marks the standard deviation then increases to upwards of 3 nm. If considering RPSA performed on the test wing structure retardation values reached between 10 - 15 nm (depending on location) where a 3 nm standard deviations equates to a 20 — 30 % uncertainty. Therefore, lower retardation values are effected even more by the standard deviation. As a result, users should consider different approaches to generating uncertainties. The efficiency of applying these UV curable coating provides the scope for repeat measurements in difficult locations. Finally, lighting conditions are having an effect on the captured photoelastic response. GLARE samples and the second aluminium dogbone demonstrated unexpected responses with magnitudes much higher than expected. Stray reflections are thought to be the main cause. Further work is required to quantify these issues but a user should consider the working environment and use screens to shield from unwanted light sources.

Chapter 9

Mechanoluminescence

Mechanoluminescence (ML) is a phenomenon where spontaneous emission of light is observed when a material undergoes a mechanical action. ML is of interest within this research, as it can be used to visualise stress distributions as the intensity of emitted light is linked to the intensity of a component's stress field [67]. An important aim of this research was to use ML in conjunction with photoelasticity to provide greater insight to the data extracted by RPSA. Initial observations performed by engineers at Airbus speculated that the ML light production gave a similar pattern to that produced by Thermoelastic Stress Analysis (TSA). Combination of these techniques would, in theory, allow for the determination of the individual principal stresses as can be done with combined PE and TSA [136]. However, in the review of published work, chapter 2, the light distribution images from ML resembles Von Mises stress [67, 74, 79, 80, 86] which has a close relation to stress fields captured by photoelastic stress analysis. Nevertheless, the combination of the techniques can provide insight through additional validation and the detection of failure within the coating and/or material as described in this chapter.

This chapter will first investigate the initial capture of ML light through the combination of an ML material with the UV curable formulation WF31. The aim will be to determine the compatibility of the materials and its ability to form a solid coating through UV curing methods. Simple loading applications will be used throughout the investigation in order to attempt to capture the ML light distributions in darkroom conditions. Once ML performance has been determined, simultaneous PE and ML capture will be investigated. The limitations of ML and its appropriateness as a technique will be discussed.

9.1 Capturing mechanoluminescence - initial observations

This section will aim to record ML by combining an ML material with the UV curable formulation WF31. The techniques used in this section followed advice from the National Physical Laboratory (NPL) who was in direct contact with Sakai Chemical Industry Co., LTD [137], the manufacturer of the ML coating material used in this research.

9.1.1 Methodology

Elastic loading is the focus of this research and as a result the selection of an ML material must produce light during an elastic load. Within the review by Feng *et al* [84], a list of compounds and the type of loading to trigger light are presented. Strontium aluminates doped with rare earth metals demonstrate ML under elastic loading and have been investigated in a variety of different research [70–77] and have been shown to produce greater ML light intensities than other commonly used materials such as copper doped zinc sulphides. In this research, a supply of powdered $SrAl_2O_4$:Eu (SAOE) was provided by Airbus. This material is a product from Sakai Chemical Industry Co., LTD. [137] with an estimated particle size distribution of 2 - 10 μm [138].

To produce an ML formulation, the SAOE powder was mixed with WF31, to act as a carrier, at a ratio of 3:7 (ML material:Resin formulation) as recommended by the National Physical Laboratory (NPL). NPL is performing separate ML investigations providing opportunities for knowledge exchange. The combined formulation was mixed for several hours by a magnetic stirrer at 50^{o}C to reduce the viscosity, aiding the mixing process. The resultant formulation had a thick green colour and possessed a detectable increase in viscosity due to the relatively large percentage of ML material within the formulation. The combined formulation appeared to mix successfully as the powder remained suspended in the carrier resin and did not settle at the bottom of the container. The formulations will be referred to as WF-SAOE henceforth.

The samples used in this investigation were coupons of aluminium (30 x 150 x 3) mm that had a 3 mm diameter hole drilled into the centre to act as a stress riser. Due to the viscosity of WF-SAOE, the usual spreading procedure using a K-bar was not suitable. When spread with the K-bar significant track marks were left in the cast formulation, contributing to large areas of varying coating thickness, and the effects of reticulation were strong. The K-bar was replaced with a micrometer adjustable

applicator by RK printcoat instruments [117] which used an adjustable blade to control the thickness of the coating. The applicator's blade can be moved up or down perpendicular to a sample through the use of two micrometers at each end of the blade. A user needs to balance these micrometers to ensure uniform thickness across the sample. This setup procedure slows down the application of a coating as several minutes were required for each sample before coating spreading. This process was made more efficient by first cleaning the metal surface of the sample and placing on a flat surface such as a glass plate. A piece of foam tape was applied at one end of the coupon to prevent sliding of the sample during application. A glass cover slide, thickness 85 — 115 μm, was placed in the desired coating area of the sample. The blade was carefully brought down until it touched the glass cover slide and the user could not easily remove the slide. It was important to do this gradually and carefully as overtightening would twist the applicator as the blade pushed down and the final thickness would be lower than expected. The glass slide was removed and the blade was brought down a further 10 μm to target a 50 μm thick coating. In practise, the blade applicator was unable to produce consistently thick samples and often coatings would exist in wide thickness ranges 10 — 150 μm. The sample and the blade was cleaned with the solvent acetone and 0.3 mL of WF-SAOE was applied above the desired coating area. The applicator was dragged across the sample spreading the formulation achieving a smooth finish. An image of the application setup is shown in figure 9.1.

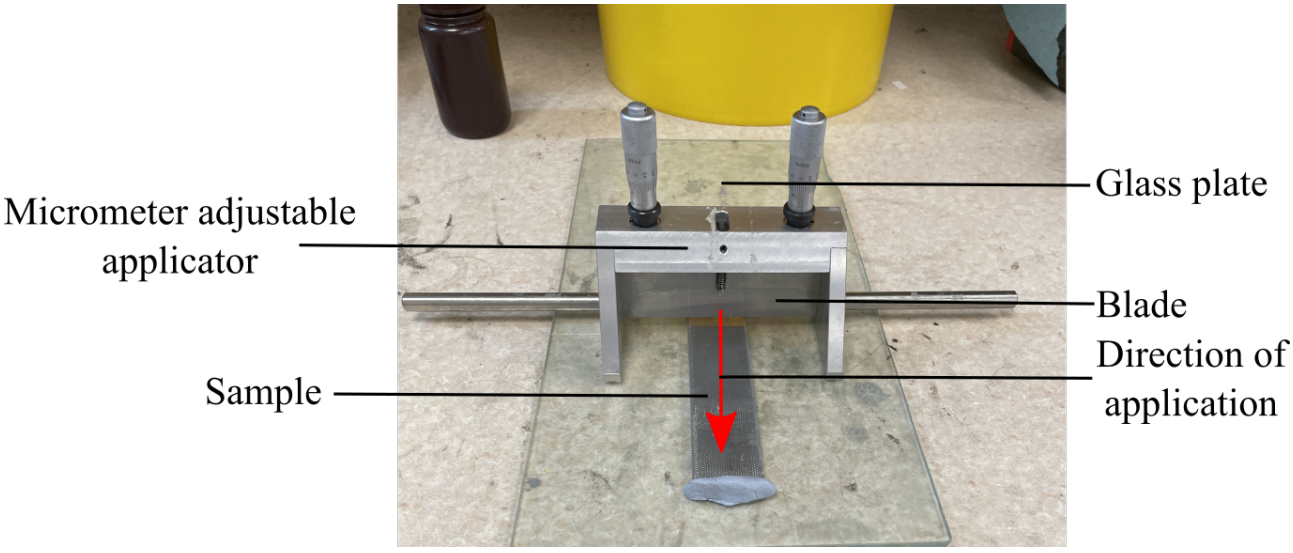


Figure 9.1: The micrometer adjustable blade applicator was used to spread the ML coating across a sample. Two micrometers adjust the position of a blade with respect to the sample. Once a sufficient thickness was setup the blade pushes the coating across the sample. The applicator was placed on a smooth glass plate to increase the uniformity of the coating's thickness.

The coated coupon was then placed under a mercury bulb for 20 s to cure into a hard-to-the-touch coating. Real-time ATR-FTIR confirmed that the curing time did not need to be increased for this formulation. The appearance of cured WF-SAOE is shown in figure 9.2. The data for the time to reach maximum cure conversion for WF-SAOE is presented in appendix E.

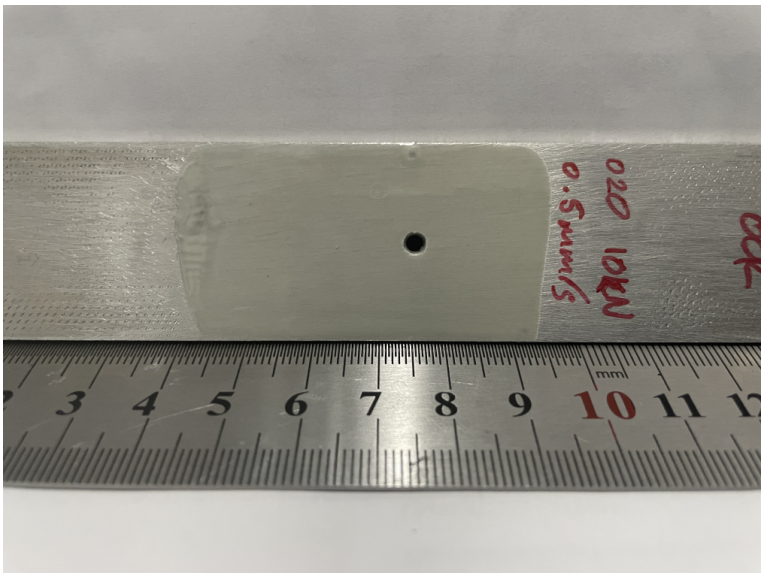


Figure 9.2: Example of cured WF-SAOE on an aluminium coupon with a circular stress riser. The coating was spread onto the sample with the hole using a micrometer adjustable blade and cured for 20 s using UVC light.

ML requires dynamic visualisation through the use of a camera [71, 74], photomultiplier [67, 139] and/or spectrometer [76, 140]. The former was selected to provide full-field imaging, a quality that the latter techniques are unable to provide. However, a relative reduction in signal will be observed due to a loss in sensitivity. A 5 MP monochrome CMOS camera from Thorlabs [141] was used alongside the capture and analysis software ThorCam. Initial ML capture used a 16 mm lens in order to get close to the sample and to keep the entire mounted sample in the field of view. Samples were mounted into a 25 kN Tinius Olsen tensile tester that was located in a darkroom. A single circular polarised light source, used alongside the GFP1600, was a suitable excitation source for the ML material within the coating. This light source was mounted next to the camera and illuminated the entire coated region of the coating. Discussions with the National Physical Laboratory stated that current best practises for these materials were to excite for 1 minute and leave for 2 minutes before applying load. This information came from a preliminary standard currently under review. The 2 minutes wait after excitation was to account for the decay in the photoluminescence (PL) that

was observed after excitation. After 2 minutes the coating produced PL at a constant intensity that did not saturate the camera. WF-SAOE produced visible PL directly after excitation in dark ambient light conditions but quickly diminished as the PL decayed. Consequentially, ML investigations had to be performed in a dark room that omitted as much ambient light as possible. Within the software used to control the camera, the exposure time, frame rate (fps) and gain could be controlled in order to capture the light. A 250 ms exposure time, which limited the frame rate to 4 fps, and a gain of 40 dB was able to capture light after the 2 minute wait time. These camera settings also provided enough signal whilst capturing a suitable amount of data across the application of load. The camera was set to record and the tensile tester applied a load at a position rates of 2.5 mm min^{-1} to a maximum load of $\sim$24 kN. The image processing programme ImageJ [1] was then used to analyse and measure the intensity of ML at a point on the sample. ImageJ was used to first translate each frame to keep the position of the hole constant. This process was automated by using the 'register virtual stack slices' plugin [142] that performed just a translation within the image. Default settings for this plugin were utilised and the resultant translation checked between images. A point 1 mm away from the hole along the lateral axis of the sample was selected and a simple macro was applied to automatically extract the grey value at each frame.

[1] https://imagej.nih.gov/ij/

9.1.2 Results and analysis

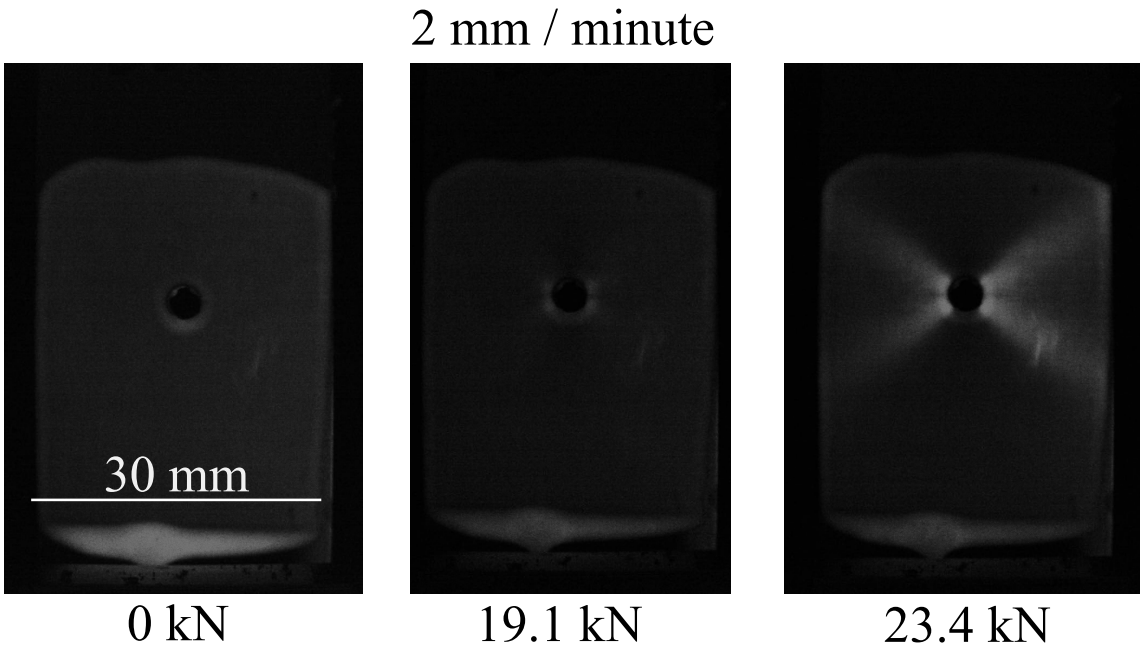


Figure 9.3: Mechanoluminescence observed in WF-SAOE applied to an aluminium coupon with a circular stress riser drilled in the middle of the sample. Across three applied loads a change in ML was observed. ML only appeared when approaching and breaching the plastic limit of the coupon.

Figure 9.3 demonstrates the production and development of ML within the sample as the load increases. Between 0 — ∼19 kN there appeared to be minimal detectable production of ML across the sample. Beyond 19 kN the production of ML greatly increased becoming intense towards the upper limit of the applied load.

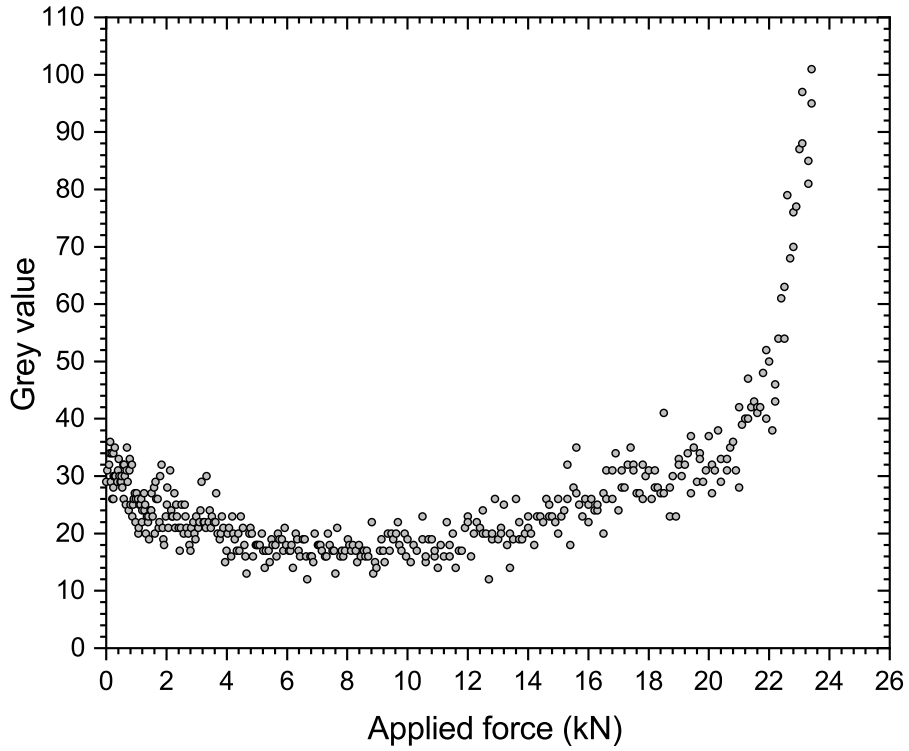


Figure 9.4: The change in grey value when the applied load increased at 2.5 mm min^{-1}. The grey value was recorded 1 mm away from the hole. Minimal detection of ML was observed until around 12 kN, the ML suddenly increased at loads greater than 19 kN.

Figure 9.4 provides several observations. Firstly, the detectable ML occurred at an applied force of $\sim$12 kN where the grey value increased at a certain rate before drastically increasing at $\sim$ 22 kN. Secondly, the initial PL was still decreasing before the production of ML. Finally, there existed poor signal-to-noise ratio as observed from the large spread of data.

Figures 9.3 and 9.4 demonstrated that ML was observed in the formulation WF-SAOE using the current setup. However, the production of light around the stress riser in the elastic region was minimal with the majority occurring when the sample went into its plastic region. Whilst the upper load limit would yield an elastic response in the main bulk of the sample, close to the stress riser the maximum stress experienced was calculated to be 786 MPa which was beyond the yield strength of aluminium at 276 MPa. The resultant plastico-ML (PML) response was not the focus of this research therefore the investigation needed to change in order to produce and capture just EML.

9.2 Capturing mechanoluminescence - cyclic loading

In an article by Li *et al* [71] EML was captured in a similar aluminium sample between a load of 0 — 5 kN. However, Li *et al* subjected their samples to a much greater load rate of 5 kNs^{-1} as compared to $\sim$ 240 Ns^{-1}. This apparent strain rate dependency on EML emission is also presented in an article by Yun *et al* [76] that discusses that increases in strain rate increase the ML intensity. Other interesting discussions within Yun's article were the comparisons between just SAOE and SAOE co-doped with dysprosium (SAOED). SAOED was discussed to have greater sensitivity and performance of that of SAOE. As a result, a sample of SAOED was provided by NPL to perform comparisons between the SAOE material and determine if a change of ML phosphor leads to increased EML.

9.2.1 Methodology

Formulation and sample creation followed the same method as section 9.1 but with the introduction of SAOED as a second ML material. The SAOED phosphor is a product from Nemoto [143] (GLL-300FF) with a documented particle size distribution between 3 $\pm$ 1 μm. The powder was combined with WF31 and will be known as WF-SAOED. WF-SAOED also had a green appearance and produced PL from the raw formulation that was visible in a well lit laboratory unlike WF-SAOE. However, the SAOED powder did not mix well with the UV curable formulation with the majority of the powder separating from the resin after a few days of storage. It was important to always mix the formulation prior to application. When cast, following the procedure in section 9.1.1, the coating produced solid coatings after 20 s of UV light irradiation.

The samples were again setup in a 25 kN tensile tester positioned in a dark room. The CMOS camera was positioned in front of the sample with the circular polarised light source used for excitation. The camera settings were altered slightly by increasing the gain to 45dB and the excitation procedure was kept the same as described in section 9.1. The loading scenario was changed to apply a position of rate 1 mms^{-1} to an upper force limit of 10 kN. To observe the effects of repeated loading, a cyclic loading scenario was utilised that applied a triangle wave of 10 kN load, from 0 kN, across several iterations. The objective was to determine if a pattern could be established to assist in translating ML into strain data. The amount of cycles varied as the ML intensity was monitored and once it was visible observed, from the camera's output, that the ML production was not distinguishable from the PL the loading stopped.

For various samples, in the preliminary investigation, it was discovered that the captured ML was not sufficient in intensity to permit the translation plugin, in ImageJ, to function as intended. As a result, a new process was created with the help of Dr Stephanie Burg at the University of Sheffield. A combination of python code and a different ImageJ plugin were utilised to allow for successful image matching. The procedure first saturated each frame within the captured video (first converted into an image stack). The 'template matching' plugin [144] was then called upon that allowed a user to define a region of interest. Within this region, the user would cover any identifiable features such as the edges of the sample and the central hole. The plugin then translated each frame onto the user defined reference image and generated a dataset that provided values of the x and y pixel shifts for each frame during translation. This dataset was then used to translate the original unsaturated image stack in order to extract the true grey values. Rather than extracting the grey value at one point, a 3 x 3 pixel area was used in order to generate an average grey value. The distance from the hole was also reduced to between 0.5 — 0.6 mm to increase the captured light intensity.

Firstly, comparisons between WF-SAOE and WF-SAOED coatings were performed by comparing the outputted ML intensity. As the first loading cycle generated the highest intensity, this cycle was used to compare intensities. A sample with the best performing coating then went through cyclic loading until the ML decayed. Repeat measurements on that coating were performed re-exciting the coating prior to loading. The performance on the coating after an initial loading procedure was monitored. Finally, any damage to the sample materials themselves were monitored by performing repeat loading on the same sample however with a new coating and the intensities compared.

9.2.2 Results and analysis

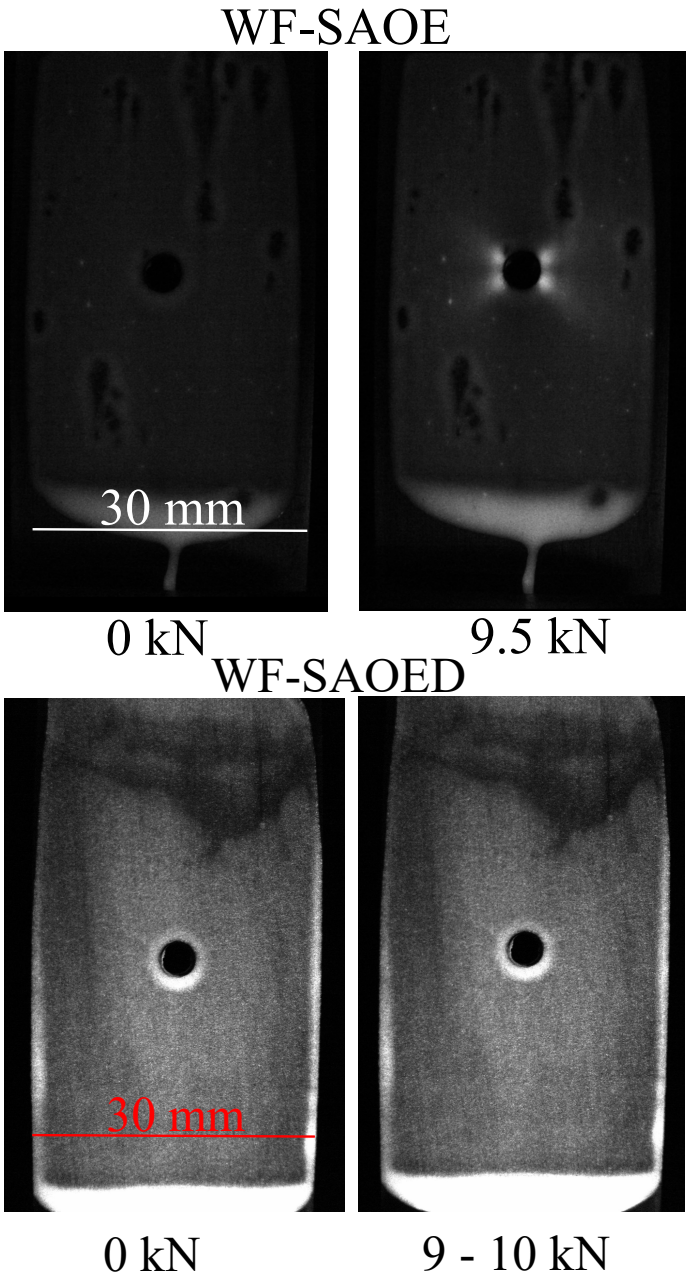


Figure 9.5: Comparison of ML produced by WF-SAOE and WF-SAOED during the first rise to the upper load limit. WF-SAOED demonstrated much greater PL but almost no ML at the maximum load. WF-SAOE demonstrated visible ML at the upper load limit.

Figure 9.5 presents an interesting comparison between the two ML materials. WF-SOAED possessed a much greater initial PL but demonstrated little to no ML when reaching the maximum load. The opposite was observed for WF-SAOE. The cause was due to the differences in particle size distribution of the two materials. It has been documented within various articles [145, 146] that

larger particle sizes demonstrate greater light production. Even within Yun's article [76], the particle size distribution of SAOE was between 1 — 20 μm compared to SOAED's which was between 2 — 60 μm. Comparisons of Nemoto's products demonstrate an increase in PL of $\sim$64 % when the particle size distribution increases from 3 $\pm$ 1 μm to 25 $\pm$ 4 μm. Consequentially, WF-SAOED was deemed not suitable for EML applications and was not used in further investigations. Due to time constraints and funding limitations procuring SAOED with a larger particle size distribution was not possible.

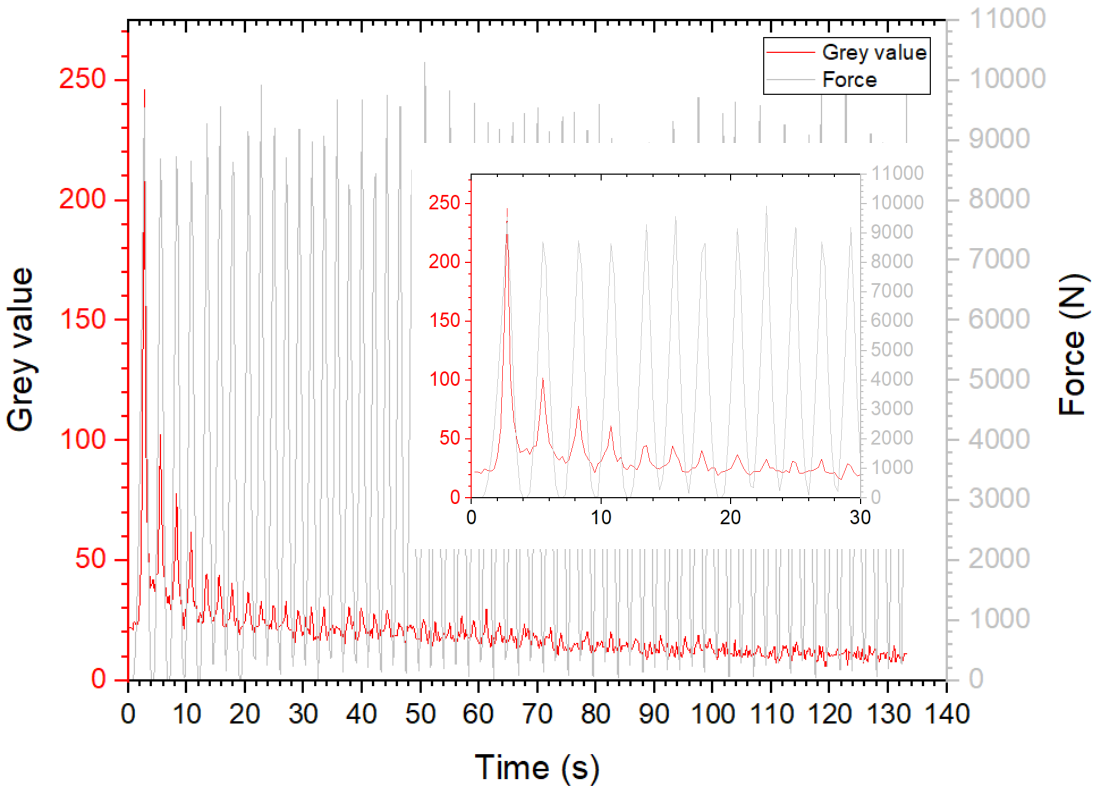


Figure 9.6: Captured ML light intensity of WF-SAOE during a cyclic loading scenario. The grey values were recorded 0.5 — 0.6 mm away from the hole. A reduction in peak ML light intensity was observed after each cycle.

Figure 9.6 presents the measured grey value across 60 loading cycles. ML was produced at lower loads when the strain rate increased demonstrating a dependency on strain rate in the production of EML. The observed response shows that a high peak intensity was achieved during the first loading cycle. The peak intensities for higher cycle orders then exponentially decayed on subsequent cycles. This finding is not surprising if considering that trapped carriers would be lost after each loading cycle resulting in decreased light production. The relatively noisy output also made data

fitting difficult. Ideally, the peak intensity values could be automatically highlighted and a potential exponential curve could be fitted onto these peak values. Whilst methods could be adopted to filter out outliers, conduct a sufficient peak detection and fit an exponential curve, the whole process can be made simpler. By recording the ML produced by a single fast rise to a maximum load the data collection time would be cut significantly resulting in much easier and faster data processing. Reducing the amount of collected data would also benefit the image processing procedure as it was slow to conduct translation on over 500 images.

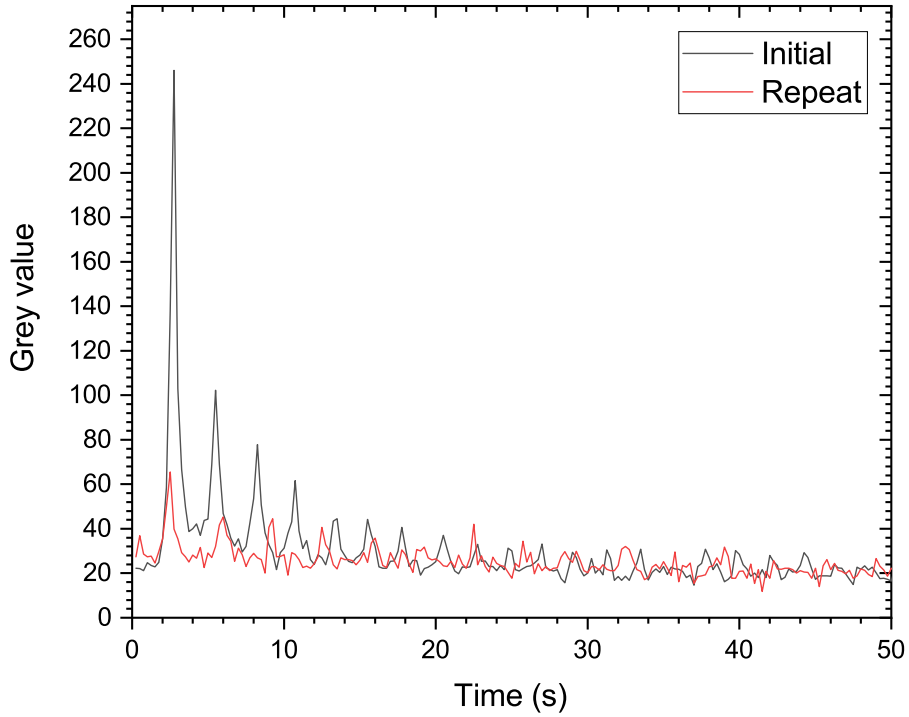


Figure 9.7: Comparison between initial captured ML and captured ML of a repeat run. The sample and coating were the same and re-excitation was performed prior to the repeat.

Figure 9.7 presents another important observation. When the same sample and coating went through a repeat loading sequence following coating re-excitation, the captured ML light distribution was not the same. The maximum peak intensities for the first several cycle orders was much lower than in the initial loading sequence. This is either a coating and/or sample effect that has reduced the intensity of ML. Suspected coating mechanisms could be a reduction in the density of detrapping carriers due to the material itself becoming debonded from the carrier resin. If debonded, then the transfer of surface strain to the coating would not affect the ML material. Scanning electron microscopy was implemented in section 9.4.1 to observe the appearance of the coating prior to and

after loading. Additionally, the sample was most likely entering plasticity due to the applied load breaching the yield strength of aluminium at the edge of the hole as shown in figure 9.8

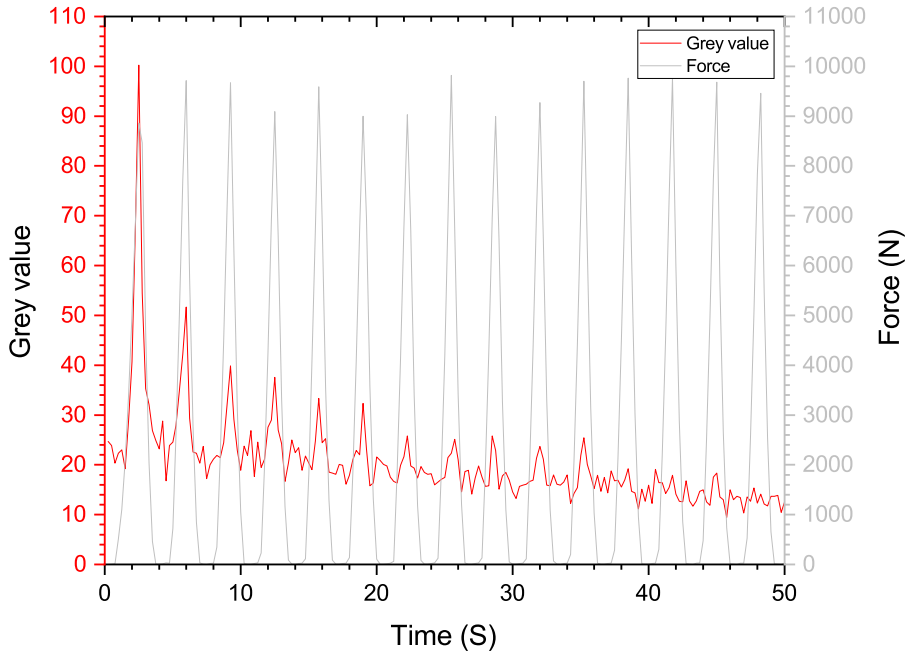


Figure 9.8: A repeat application of cyclic loading on the same sample as figures 9.6 and 9.7 but with a new coating. The maximum peak intensity is still reduced from the initial loading sequence.

Figure 9.8 demonstrates that coating effects were not the entire cause of the reduction of light intensity observed in figure 9.7. Figure 9.8 presents the ML data of the same sample coupon as figures 9.6 and 9.7 but with a new coating of WF-SAOE. The maximum peak intensity was greater than the repeat featured in figure 9.7 but less than in the initial loading sequence. This indicates that both changes within the sample and the coating after initial loading affect the intensity of ML on subsequent repeats of existing and new coatings on the same sample coupon. Further investigations explored repeat measurements on samples that are guaranteed to remain in the elastic region.

9.3 Capturing mechanoluminescence - repeatability

In order to extract stress and strain information the ML light production needs to be reproducible between samples. Quantitative analysis between ML and stress/strain has not been well documented especially in the elastic region. The aim of this section was to perform similar loading experiments demonstrating directions in which users could go in order to translate ML intensity into desired

information. Additionally, samples without stress risers will also be utilised to explore the performance of ML for different loading scenarios.

9.3.1 Methodology

Sample creation mostly followed the same procedure as outlined in section 9.1.1. To aid in the translation facility WF-SAOED's high PL was utilised to create easily identifiable features within the WF-SAOE coating. After applying and spreading WF-SAOE onto the aluminium surface, a needle was used to apply small drops of WF-SAOED away from the area of data collection, figure 9.9. These dots of a high PL formulation would provide bright identifiable features that would assist in the translation process by removing the need to saturate the images thus reducing the time for data collection by several minutes.

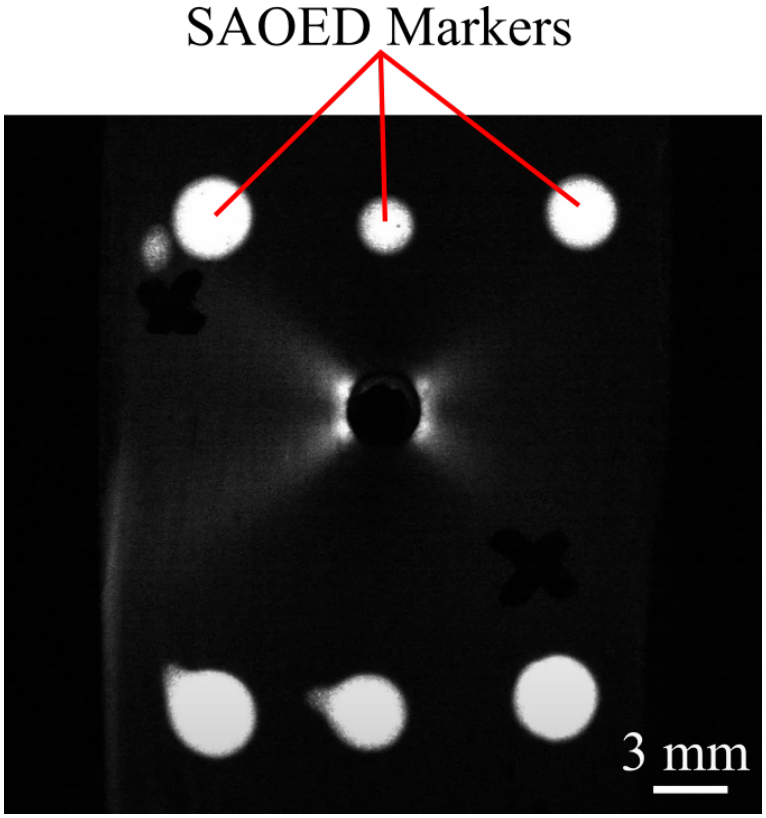


Figure 9.9: An aluminium coupon with a circular stress riser under uniaxial load. Maximum load is applied and the observed ML around the hole is observed. Several bright hot spots are shown which are thick markers of the highly photoluminescent SAOED combined with the UV curable formulation WF31 and cured.

The tensile tester now applied a faster rate of load with a displacement rate of 1 mms^{-1} to a

maximum of 10 kN. The machine then maintained the tensile load for several seconds to capture the decay in ML that was recorded by the camera. The same recording and processing procedures were utilised as described in section 9.2. Three individual samples were tested with three repeats performed each using the same coating. The effects of thickness will be reviewed and if necessary, treated similar to photoelasticity data which normalised retardation per 10 μm of coating thickness.

Additional samples were created without the stress riser to determine the performance of ML at lower applied stress. The same application and curing methods were followed. A large sample size was created to review the light intensity measurements at different displacement rate (0.25, 0.5, 1.0 & 2.0 mms^{-1}) and maximum applied loads (5, 7.5, 10, 12.5 kN). WF-SAOE's adaptability to these changes will be reviewed. Additionally, several repeats at the same loading interval were be performed to further investigate ML's repeatability. Table 9.1 outlines the tests performed with sample thickness.

Test Performed	Sample ID	Load Applied (kN)	Displacement rate (mms^{-1})	Sample Thickness ($\pm$ 4μm)
Single rise with stress riser (3 repeats per sample)	WF-SAOE_Hole_001	10	1	33
	WF-SAOE_Hole_002	10	1	73
	WF-SAOE_Hole_003	10	1	15
Single rise without stress riser (1 repeat per sample)	WF-SAOE_NoHole_001	10	1	54
	WF-SAOE_NoHole_002	10	1	46
	WF-SAOE_NoHole_003	10	1	54
	WF-SAOE_NoHole_004	10	1	40
	WF-SAOE_NoHole_005	10	1	50
Changes in load applied (1 repeat per sample)	WF-SAOE_10kN_001	10	1	149
	WF-SAOE_10kN_002	10	1	74
	WF-SAOE_10kN_003	10	1	130
	WF-SAOE_7.5kN_001	7.5	1	122
	WF-SAOE_7.5kN_002	7.5	1	116
	WF-SAOE_7.5kN_003	7.5	1	135
	WF-SAOE_5kN_001	5	1	78
	WF-SAOE_5kN_002	5	1	95
	WF-SAOE_5kN_003	5	1	96
Changes in displacement rate (1 repeat per sample)	WF-SAOE_0.25_001	10	0.25	72
	WF-SAOE_0.25_002	10	0.25	86
	WF-SAOE_0.25_003	10	0.25	94
	WF-SAOE_0.5_001	10	0.5	88
	WF-SAOE_0.5_002	10	0.5	100
	WF-SAOE_0.5_003	10	0.5	80
	WF-SAOE_1_001	10	1	149
	WF-SAOE_1_002	10	1	74
	WF-SAOE_1_003	10	1	130
	WF-SAOE_2_001	10	2	73

Table 9.1: An outline of the tests performed to investigate repeatability of the ML response and how changes to maximum load and displacement rate affect the measured ML intensity.

9.3.2 Results and analysis

9.3.2.1 Single rise with stress riser

Firstly, the three samples with the stress riser were each repeated three times following re-excitation procedures before each loading. The captured ML and decay was recorded. Normalisation of thickness was not performed and believed to be a contributor to the different measured peak intensities observed in figure 9.10 between the samples.

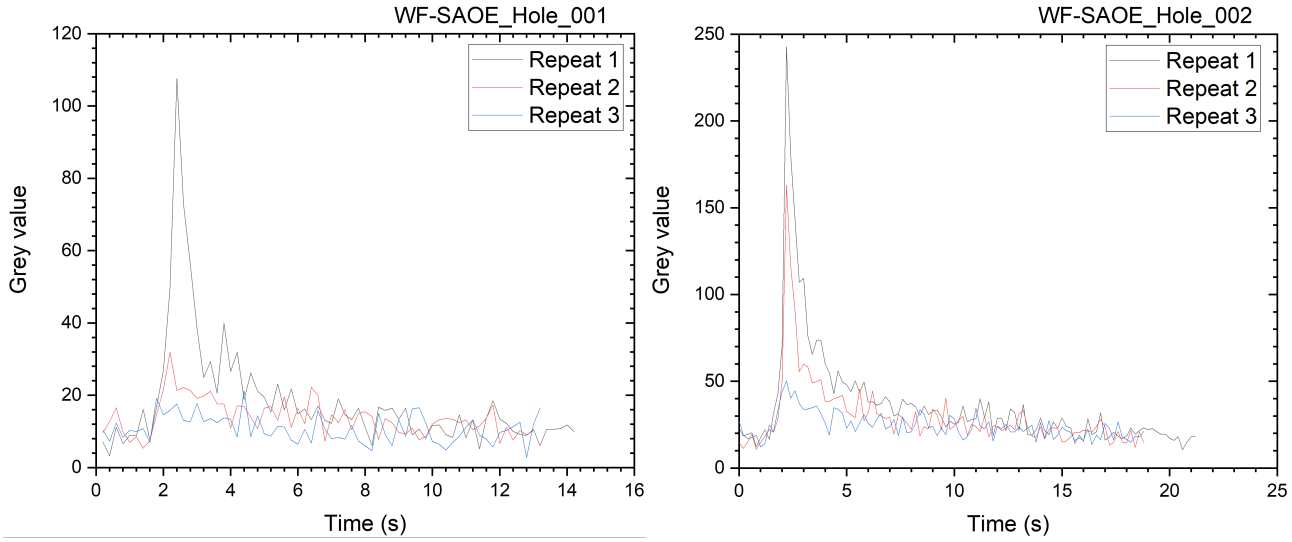


Figure 9.10: The recorded ML of WF-SAOE on two samples undergoing a tensile load of up to 10 kN at a position rate of 1 mms^{-1}. Each sample had three repeats that results in a loss of ML intensity at each repeat.

Two of the three samples produced ML of an adequate intensity as observed in figure 9.10. The third sample produced ML with a peak grey value of 30 on its first run which was not as easily discernible from the relaxed PL of the coating. This sample's dataset was omitted. As was seen in figure 9.7, subsequent measurements showed a reduction in the peak intensity. The peak intensities of all three coatings differ in value and the trend between them matches their respective thickness. WF-SAOE_Hole_002 had the greatest thickness (73 $\pm$ 4 μm) whilst WF-SAOE_Hole_003 had the lowest (15$\pm$ 4 μm) with WF-SAOE_Hole_001 in the middle (33$\pm$ 4 μm). Normalising the captured ML intensities and reviewing only the first run, the samples' grey values were brought closer to one another as shown in figure 9.11.

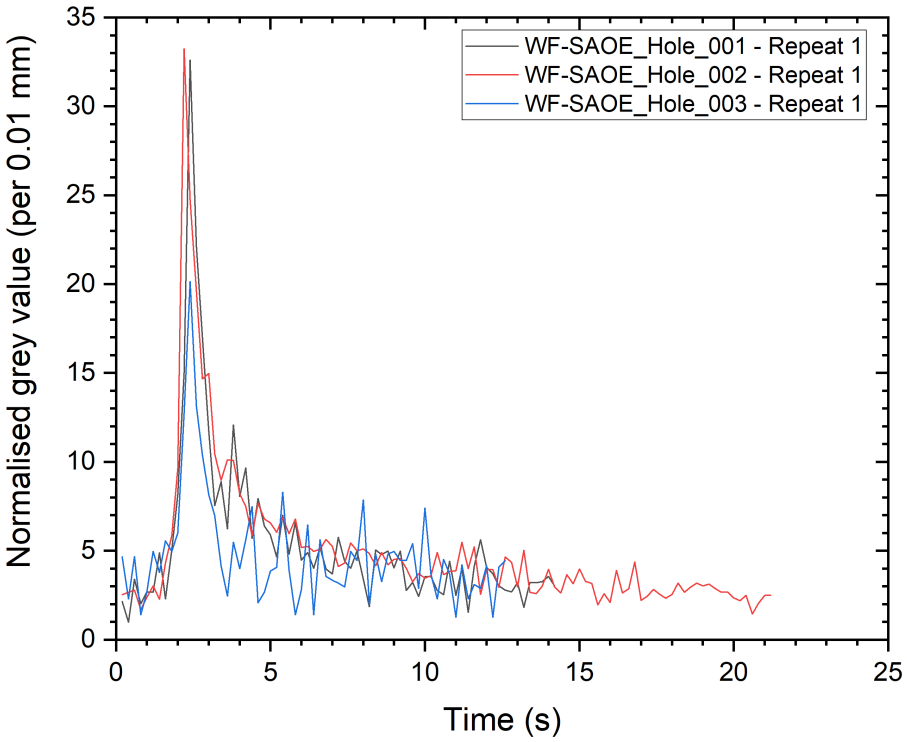


Figure 9.11: Normalised grey value vs time. The applied force ranged from 0 - 10 kN at a position rate of 1mm/s. Comparing between figure 9.10 demonstrates that coating thickness affects the intensity of ML light.

Figure 9.11 demonstrates the significance of coating thickness on the measured ML response. Similar to photoelasticity, thickness has an effect on the sensitivity of the ML response with thicker coatings possessing higher measured intensities for the same load as best illustrated in figure 9.10. Whilst WF-SAOE_Hole_003 demonstrated an observable peak there was a proposed limitation on the coating's performance as a result to coating thickness paired with the imaging device used in these investigations. Reviewing the datasets of normalised WF-SAOE_Hole_001 & 002, The max intensities are within 0.6 of each other and their exponential decay closely matched one another.

A second order exponential decay function, that contains five constants, was used to fit against the decays of samples 001 and 002. The data was manipulated to focus on the decay from the peak intensity only. The time was reset so the decay started at the peak intensity value at 0 s. Due to the large magnitude of noise in the 003 plot, analysis was not performed on this sample. The corresponding function, constant values, and coefficients of determination are presented in table 9.2.

Sample ID	$y = y_o + A_1 e^{\frac{-x}{t1}} + A_2 e^{\frac{-x}{t2}}$					R^2
	y_o	A_1	t_1	A_2	t_2	
WF-SAOE_Hole_001 — Repeat 1	2.93	22.1	0.295	7.91	2.97	0.944
WF-SAOE_Hole_002 — Repeat 1	2.93	23.2	0.485	6.94	4.27	0.979

Table 9.2: The second order exponential decay function that has been fit against two samples that demonstrated a decaying ML light distribution. The five constants within the function are outlined along with the coefficient of determination. These samples were aluminium coupons that had a uniaxial tensile load of 10 kN applied at a displacement rate of 1 mms^{-1}. A 3 mm circular hole was drilled into the sample acting as a stress riser. Data was collected 0.5 mm away from the hole.

The exponential function demonstrated a good fit onto both datasets with constants that match closely with one another. These initial findings show that a relationship can be formed between samples when normalising the light intensity to coating thickness. Whilst these connections show a potential link between strain and ML, the experimental procedure requires further investigation.

9.3.2.2 Single rise without stress riser

Figure 9.12 demonstrates qualitatively the detected increases in ML light due to different maximum loads for four separate samples. The changes in ML through the load ranges 5 — 10 kN were small however they were detectable by the camera.

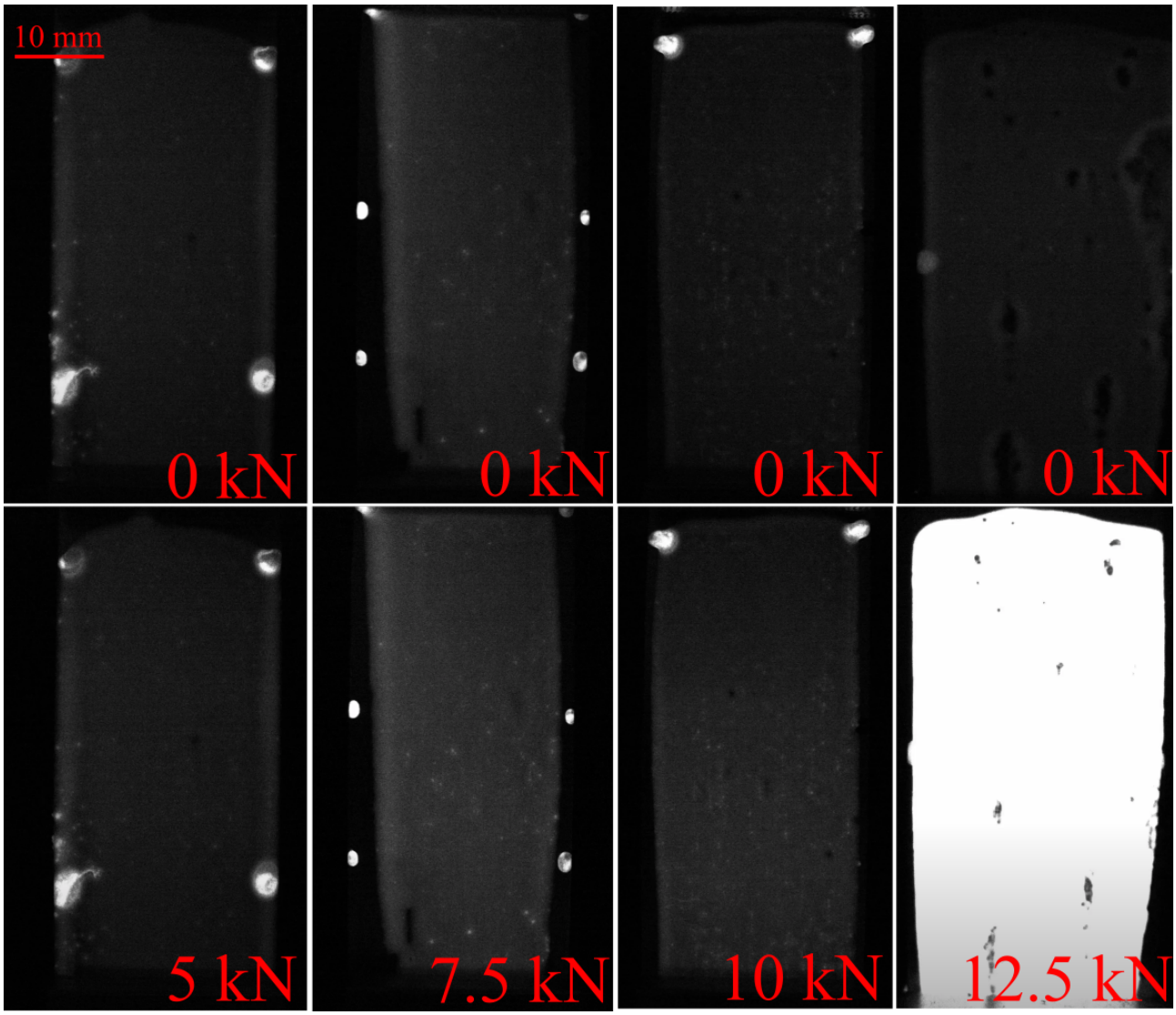


Figure 9.12: The qualitative comparisons between recorded ML light intensities at different maximum loads, at a displacement rate of 1 mms^{-1}, applied to an aluminium coupon in uniaxial tension. The increase in light intensity is minimal until the sample goes into plasticity where the measured light output saturates the detector.

It is important to understand due to thickness differences 7.5 kN produces more light than 10 kN. An interesting observation was made at 12.5 kN where the coupon went into into plasticity. The coating produced a bright flash that saturated the camera. Once the load was removed and coating inspected the coating was still adhered to the sample surface.

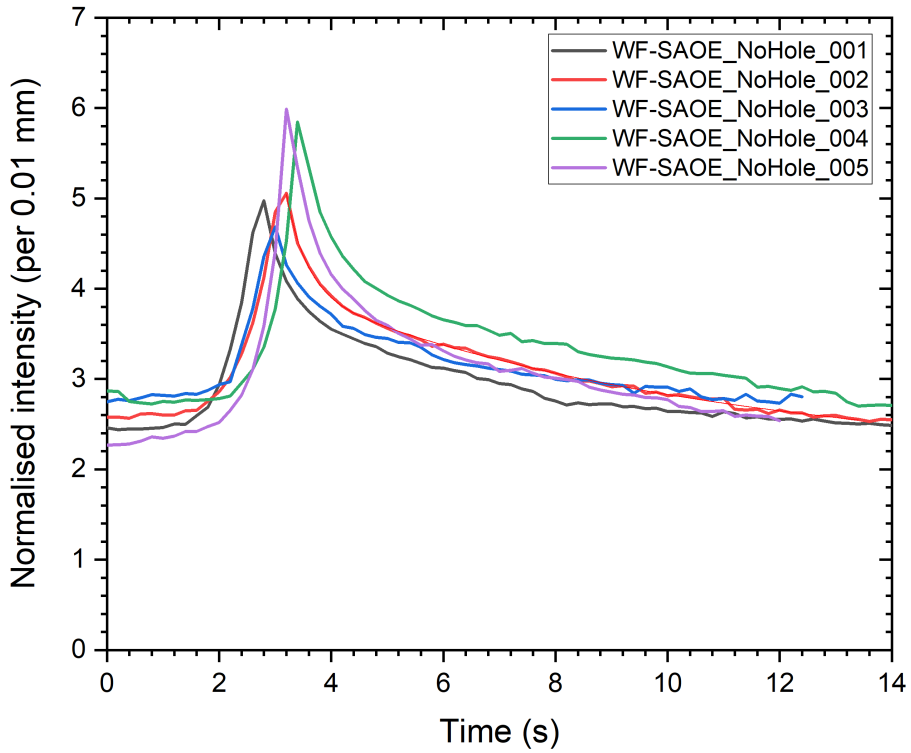


Figure 9.13: Normalised grey value against time for aluminium coupons without a stress riser. Each sample was applied with a 10 kN load at a displacement rate of 1 mms^{-1}. The peak intensities were observed however very low in signal when compared to previous applications. Exponential fits were applied to determine repeatability.

Figure 9.13 quantitatively shows the measured normalised peak intensity for five samples at a maximum load of 10 kN at a displacement rate of 1 mms^{-1}. The first observation was the comparisons between figure 9.11 with the magnitude of measured intensities being ∼five times greater. The stress at 0.5 mm away from the hole was calculated to be ∼242 MPa whereas the stress calculated for aluminium coupons in figure 9.13 was ∼111 MPa. This indicated a non-linear response between stress and measured light intensity. Another observation was the reduction in noise between figure 9.13 and 9.11. As a result, exponential fits were closer to the extracted experimental value and demonstrated in table 9.3.

Sample ID	$y = y_o + A_1 e^{\frac{-x}{t1}} + A_2 e^{\frac{-x}{t2}}$					R^2
	y_o	A_1	t_1	A_2	t_2	
WF-SAOE_NoHole_001	2.41	0.985	0.283	1.58	3.78	0.998
WF-SAOE_NoHole_002	2.27	1.00	0.327	1.78	5.85	0.998
WF-SAOE_NoHole_003	2.66	0.715	0.343	1.30	3.79	0.995
WF-SAOE_NoHole_004	2.02	1.70	0.518	2.16	9.77	0.998
WF-SAOE_NoHole_005	1.84	2.09	0.528	2.07	8.21	0.998

Table 9.3: The second order exponential decay function that has been fit against two samples that demonstrated a decaying ML light distribution. The five constants within the function are outlined along with the coefficient of determination. These samples were aluminium coupons that had an uniaxial tensile load of 10 kN applied at a displacement rate of 1 mms^{-1}.

The coefficients of the second order exponential equation demonstrate similarities but with WF-SAOE_NoHole_0
& 005 contributing diffidence to the results. The similarities reinforce discussions made in regard to data collected in table 9.2 where repeatability is achievable, yet difficulties are present. There exists a limitation in the accuracy of extracted data from ML as highlighted by differences between captured decays between samples. Unlike in figure 9.11 where WF-SAOE_NoHole_003 had an unexpected low thickness contributing to poor signal extraction, WF-SAOE_NoHole_001 — 005 in figure 9.13 all posses similar thicknesses between 0.4 — 0.54 μm. As a result, it was challenging to establish an obvious major contributor to the differences in measured light intensity.

9.3.2.3 Changes in load applied

Further issues are observed when reviewing the ML captured at different loads, figure 9.14.

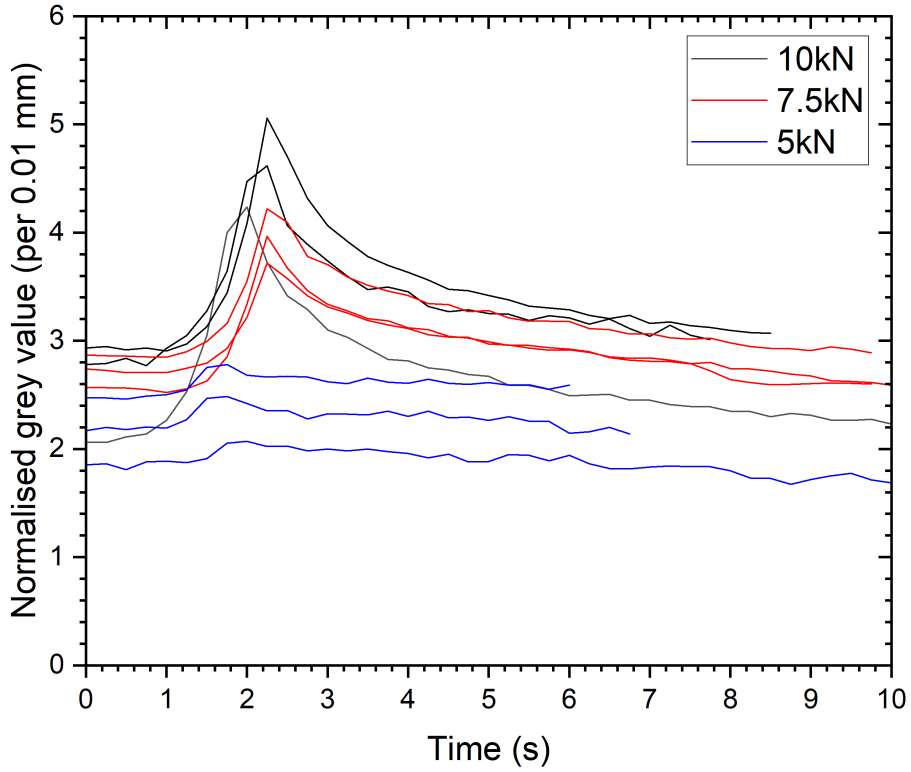


Figure 9.14: Intensity of ML for aluminium coupons at different maximum loads. A limitation in the applied load can be observed with low peak ML from 5 kN samples. An overlap between 7.5 — 10 kN is also observed further demonstrating difficulties that lie with the technique.

Figure 9.14 demonstrates the effect of differing maximum loads on the measured ML response. All coatings possessed thicknesses between 75 — 150 μm. Firstly, samples loaded to a maximum of 5 kN produced minimal ML resulting in a lack of signal that almost gets hidden by the initial PL. Furthermore, there was significant spread between peak values for 5 kN samples. As a result, there exists limitations on the minimum load applied in which reliable ML data can be extracted. Other problematic observations include slight overlaps between the 7.5 — 10 kN samples which further limits ML as a technique. The challenge would be how to resolve the calculated stress if the resolution on the applied load is poor.

9.3.2.4 Changes in displacement rate

However, figure 9.15 provides data that would allow users scope to adopt different methods for ML capture to try to improve sensitivity.

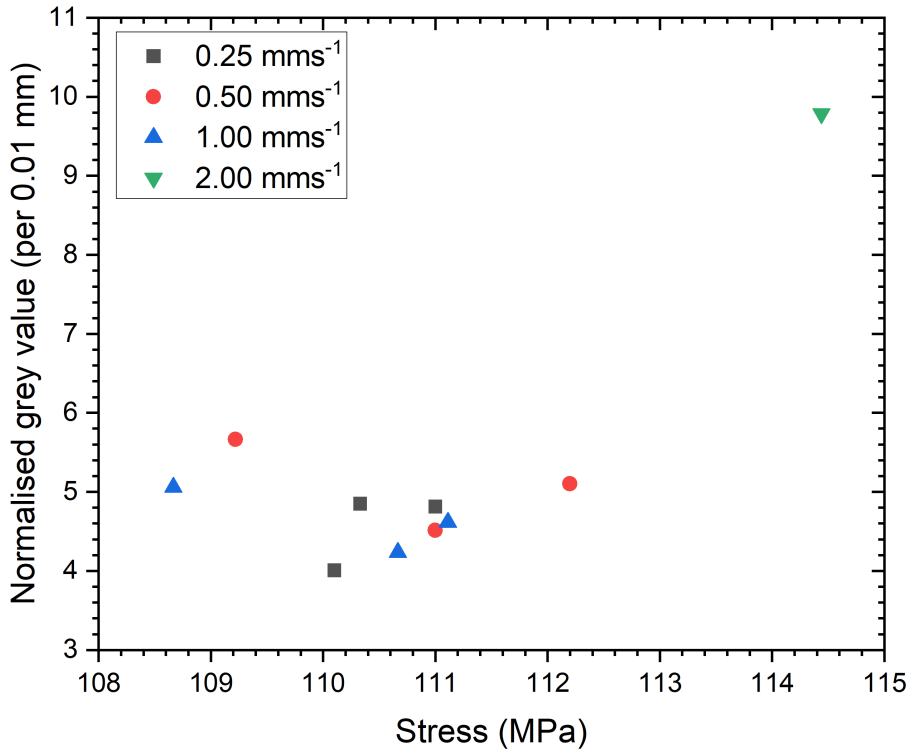


Figure 9.15: Peak intensity of ML for aluminium coupons at different calculated applied stress for various displacement rates. Rates between 0.25 — 1 mms^{-1} demonstrated no change in the captured ML intensity which allows for flexibility on the displacement rate. However, higher displacement rates, 2 mms^{-1}, produced higher captured intensity but with it being harder to capture all information.

Displacement rates between 0.25 — 1 mms^{-1} possessed no changes in the peak intensities between samples. As a result, a user would be able to use slower shutter speeds to in order to increase exposure but there is a limit as shown in figure 9.4. Conversely, figure 9.15 demonstrated that higher displacement rates, 2 mms^{-1}, produce increased ML intensities. One sample was plotted due to the difficulties in capturing the light with the equipment and setup used. Furthermore, samples could not be reused making repeat measurements time-consuming and difficult to manage with large sample sets. The problem with the 'one-shot' attribute of the coating further places limitations on the technique in its form in this investigation. It is important to try and understand the mechanisms of the material within the UV curable formulation to understand why these observations were occurring.

9.4 Mechanoluminescence mechanisms

An observation made in this investigation is the inability to replicate captured intensities within the same sample and coating. This is a major concern as it produces inefficiencies as a user would have to perform the experiment then strip and reapply the coating for additional measurements. Moreover, it places additional pressure on the user to record the desired data each test or else waste valuable application time. This section reviews the cause of this negative attribute by visualising the structure of the coating before and after the application of load. Additionally, a concept to try to measure the coating thickness will be explored.

9.4.1 Coating structures before and after load

It was proposed that the main contributor to the 'one-shot' attribute of the coating was structural changes within the coating. The ML material requires strain in order to release the trapped carriers within the oxygen vacancies. Therefore, there is a factor that is preventing the transfer of strain from the sample surface to the coating to the ML material. After the application of load, the coating remained bonded onto the metal surface, there were no apparent effects of delamination between the coating and the metal surface. However, it was thought that there could be debonding between the ML material and the carrier matrix — the UV curable formulation. Jongchansitto *et al* [85] perfomed similar experiments using SEM to capture debonding within ML epoxy dogbones (gauge length 110 mm x [9.9 x 2.15 mm]). Performing on an ML coating before and after coating has not before been investigated.

9.4.1.1 Methodology

The process to determine if debonding occurred was to use scanning electron microscopy (SEM) to produce high resolution images of the cross section of the coating before and after the application of load. SEM uses an accelerated electron beam to probe a sample and extract valuable information. The accelerated electrons (applied bias of 100 — 25 kV) are focused onto the sample which in turn generates secondary electrons which are detected. Secondary electrons occur due to interactions between the directed electron beam and electrons on the surface sample. Variations of the sample surface cause differences in the amount of secondary electrons detected. The electron beam is scanned across the sample surface to create an image. SEM imaging requires a conductive surface

therefore the coatings need to be pretreated prior to imaging. Coatings before and after load were extracted in similar ways. New coatings were cast onto aluminium coupons using techniques described in section 9.1.1. After 20 s the coating was carefully peeled away from the metal surface using a sharp blade. Loaded coatings were taken from the samples used in earlier investigations. Samples from section 9.3.2.2 were used for this investigation. The coatings were carefully peeled away using a sharp blade. The cross sections of the coatings was the area of interest for SEM imaging resulting in the appropriate preparation for the coatings. If using a blade to cleave the coating there is risk of damage to the cross section that could be misinterpreted as loading effects. After discussions with an experienced SEM user the coatings were submerged in liquid nitrogen for 30 s and snapped to produce a clean cleaved surface that could be prepared for SEM imaging. The cleaved coating samples were then further roughly broken down into 5 mm squares ensuring the cleaved edge was not touched. Carbon tape was applied to a 90 ^{o} stub where the coating sample was applied onto ensuring good adhesion. The prepared stub is shown in figure 9.16.

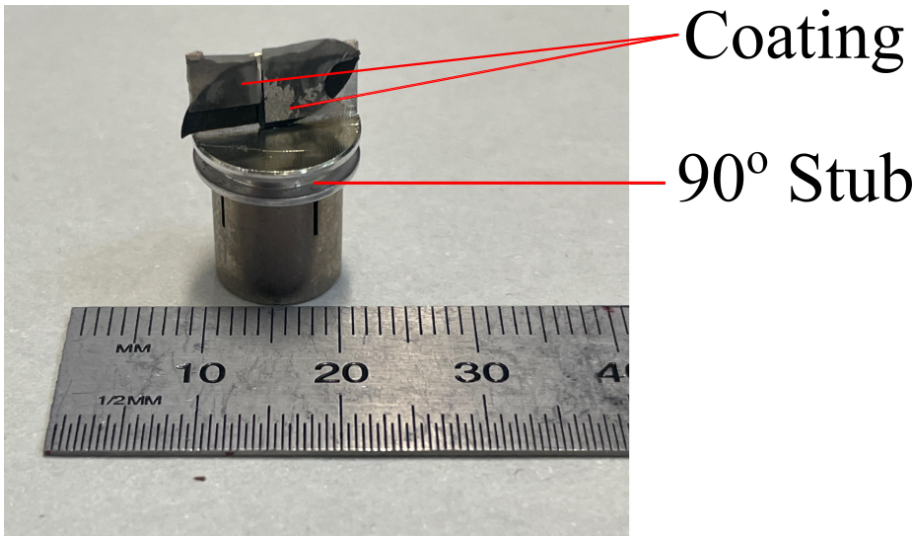


Figure 9.16: A 90 ^{o} SEM stub that has been prepared for SEM imaging. Two sections of coating (loaded and unloaded) have been placed onto a stub with the cross section orientated 90^{o} to enable imaging of that face. The coating cross sections have been coated with gold and a silver conductive paint ensures conductive contact between the stub and the coating material.

The coating protruded over the stub with the cross section the target for the directed electron beam. The cleaved edge was then deposited with a few nanometres of gold and a conductive silver paint was applied to enable contact between the conductive surfaces. The methods used followed standard operating procedures outlined by the laboratory. The SEM used was a JSM-6010LA

(JEOL) [147] that had the capability to perform backscattered electron (BE) imaging and electron backscattered diffraction spectrometry (EDS) that would allow for the validation of the location of ML materials and the surrounding formulation. Backscattered electron imaging provides contrast by measuring the quantity of electrons that backscatter from positively charged nuclei. The quantity of backscattered electrons increases with atomic number, in the context of WF-SAOE the aluminium and strontium are heavier than the carbon based formulation thus contrast between these two materials can be observed. The spectroscopy attribute of this device measures the energy of the x-rays that are emitted when electrons fill the holes left by the emission of secondary electrons. The energies of these x-rays are characteristic of the element that 'released' them thus allowing users to determine what any element is within the captured image. Images were taken at x1900 and x2000 magnifications and the appearances were qualitatively analysed. Areas of interest were also images at x10000 to highlight certain features however the sharpness of the image was very challenging to attain at these high magnifications. BE imaging also was using to demonstrate contrast whilst EDS was used to validate what was being imaged.

9.4.1.2 Results and analysis

EDS was first performed on a coating, figure 9.17, to validate the elements within the images. EDS focused on two locations: a bright spot observed throughout the image thought to be the ML material; and the dull grey region thought to be the carrier formulation.

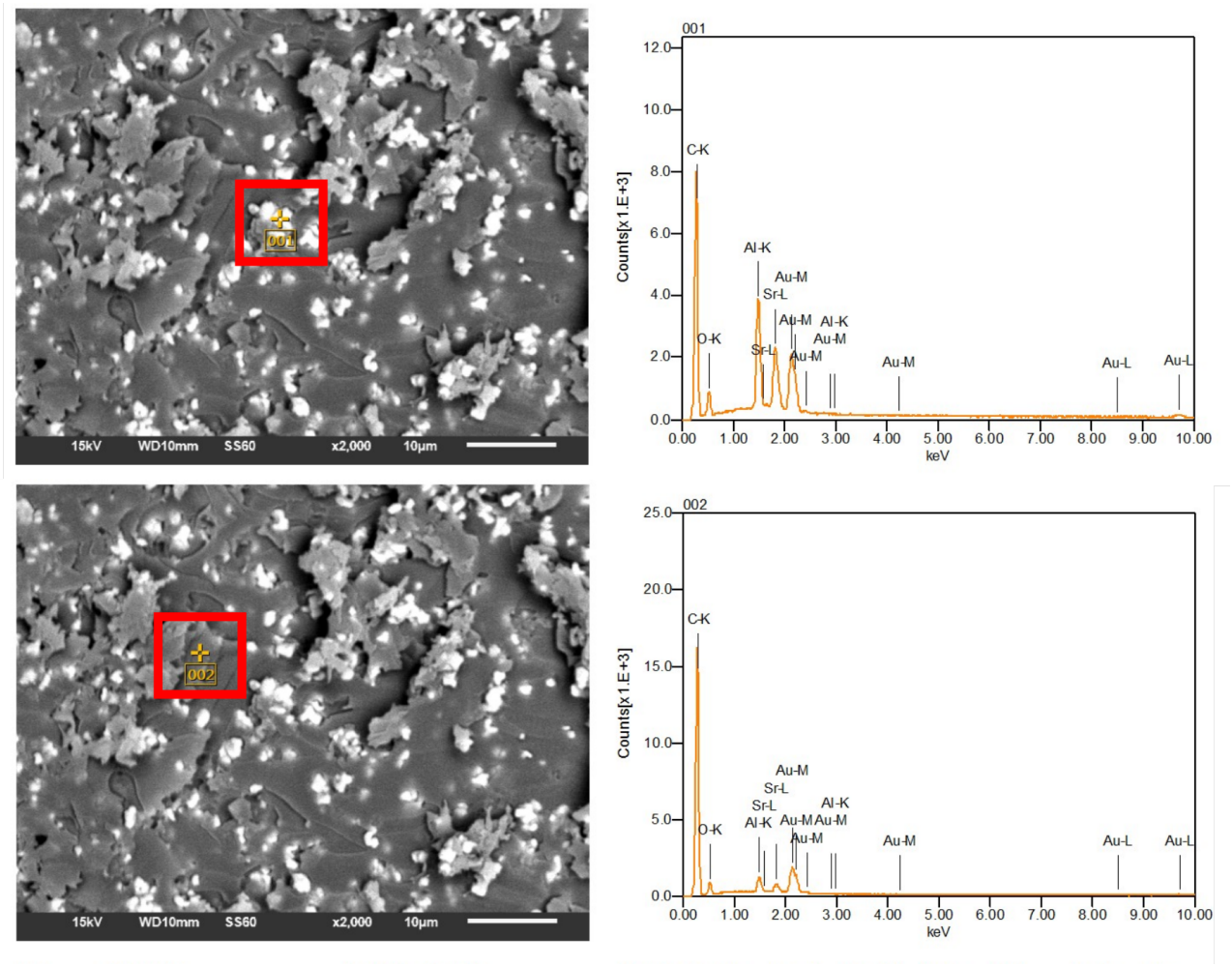


Figure 9.17: Electron backscattered diffraction spectrometry (EDS) conducted on a backscattered electron image of the coating after load. The software analysed the points in the marked regions at the bright spots thought to be the ML material and the grey surrounding medium thought to be the carrier formulation. EDS identifies these claims to be correct.

These claims were validated by the spectra outputted by the software demonstrating high quantities of aluminium (Al) and Strontium (SR) in the first image and increased amounts of carbon (C) in the second. Strontium was still observed in the second as the effect penetrates into the surface. The SEM images also show the effects of BE imaging with the high contrast between the confirmed ML material and carrier formulation. Reviewing just the captured secondary electrons the following differences are observed between the coatings, figure 9.18.

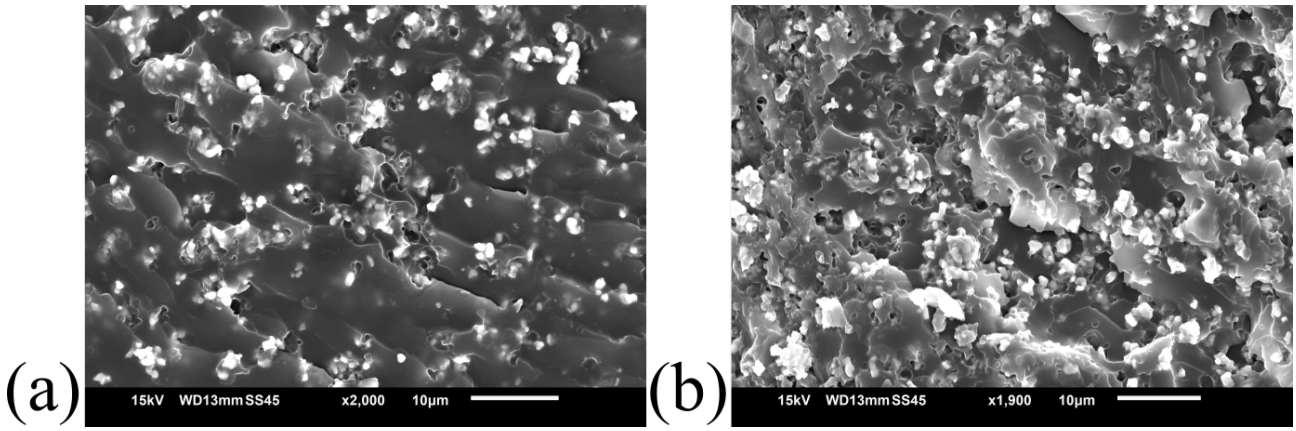


*Figure 9.18: SEM images of two coatings **(a)** before and **(b)** after the application of load at x1900 — x2000 magnification. A high density of ML material is contained within the carrier formulation. The structure of the formulation degrades from after applications of load that suggests the transfer of strain from the formulation to the ML material is disrupted.*

Figure 9.18 demonstrates the before and after loading of the coating. Before loading the images demonstrated the ML material being surrounded by the carrier formulation without disruption within the resin matrix. After load the coating has degraded with larger discontinuities between sections of the carrier formulation. Zooming into key regions of other coating these discontinuities can be observed in further detail, figure 9.19.

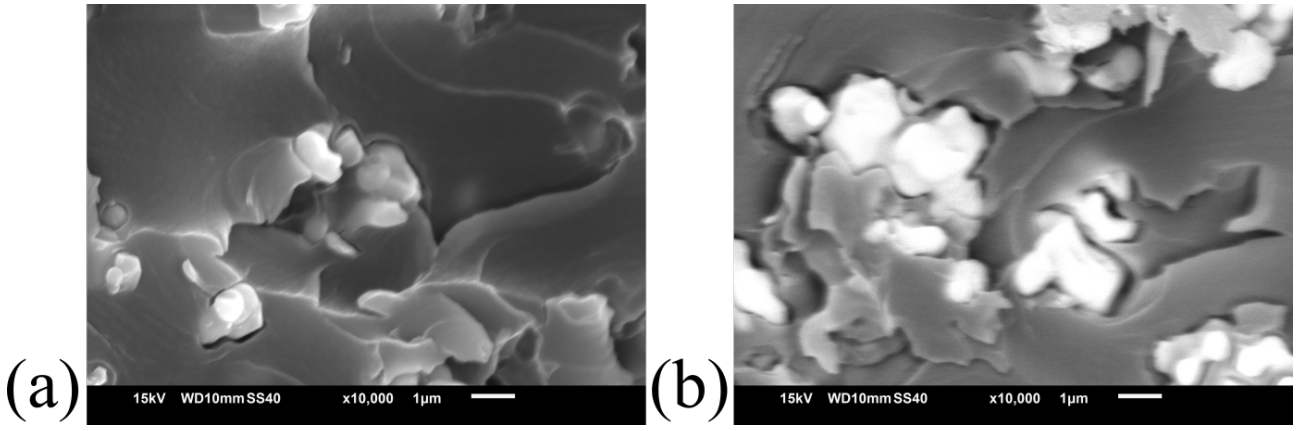


*Figure 9.19: SEM images of two coatings **(a)** before and **(b)** after the application of load at x10000 magnification. The images have focused on ML particles surrounded by the resin carrier formulation. Large voids are observed around the ML particles after load producing discontinuities that disrupt the transfer of strain.*

Figure 9.19 further highlights the increased production of discontinuities around the ML material. The production of discontinuities helps explain the reduction in ML light production in the coating for

repeat loading scenarios. The debonding prevents the continuous strain transfer from sample material to coating to ML material. Similar observations were made in [85] that contributed the differences in material stiffness to the de-bonding occurring in the combined resin and ML material. These observations highlight an incompatibility between the ML material and the UV curable formulation with the formulation breaking down after the application of the load.

9.4.2 Thickness measurements

It has been shown that coating thickness alters the measured ML intensity with comparisons between samples requiring normalisation for coating thickness. Being able to correct for thickness would allow for increased ease-of-use just as demonstrated by the tinted photoelastic coating in chapters 6 and 8. Additionally, new methods of thickness corrections will be needed for the use of WF-SAOE within PE experiments due to the appearance of the coating and the methods used to simultaneous capture ML and PE which will be described in section 9.5.

9.4.2.1 Methodology

The concept reuses the sample choice in chapter 6 using a wedge, figure 6.3, that provided a gradient of thicknesses. Three wedges of WF-SAOE were created using the procedure as described in section 6.2. Instead of calculating the ratio of different wavelengths of reflected light, the photoluminescence of the coating directly after excitation was recorded and analysed. The objective will be to image the change in intensity due to thickness changes of the coating using observations made in section 9.3. The investigation was performed in a darkroom eliminating all sources of ambient light. The wedge was positioned on a table with the Thorlabs CMOS camera directly above. The camera was fitted with a 28 mm macro lens imaging the entire wedge. A white light source was positioned above the wedge and excited the coating for 1 minute. It was crucial to determine camera settings that captured no saturation of the PL of the coating. Additionally, images need to be taken at the same time period as the PL intensity quickly diminishes. An exposure time of 350 ms with a gain of 30 dB was sufficient in keeping all samples from saturation. As soon as the white light source was switched off an image was captured and saved. ImageJ was then used to extract intensity values across the thickness gradient of the wedge. The repeatability of the method will be analysed to determine the usability of this method to allow for thickness corrections that would enable fast

full-field quantifiable analysis from ML. Three samples in total were made and analysed.

9.4.2.2 Results and analysis

An image was first taken of the wedge highlighting the PL immediately after excitation using the CMOS camera, figure 9.20

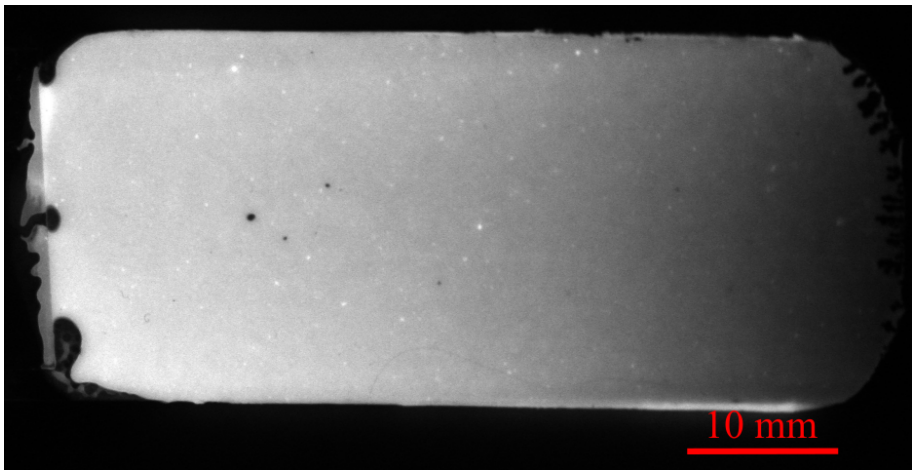


Figure 9.20: The photoluminescence captured from a wedge of WF-SAOE immediately after excitation with a white light source. The thickest part of the wedge occurs where the light intensity is at its greatest.

The captured PL demonstrated the change of light intensity as a result of differing thickness. These observations were consistent between each sample and were not included. Plotting the change in intensity against calculated thickness of the wedge the following three curves were observed, figure 9.21.

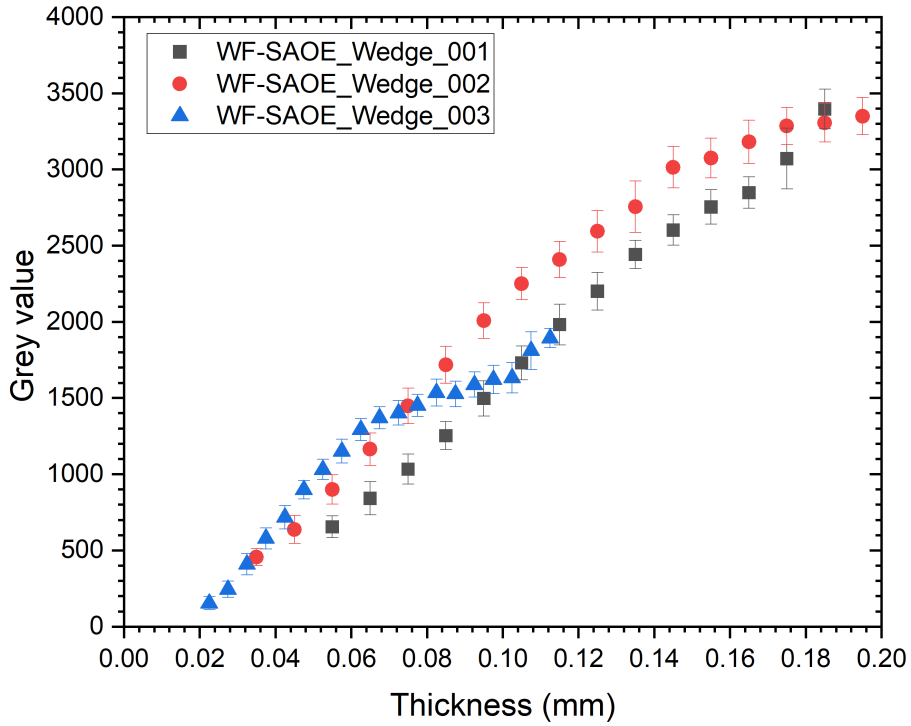


Figure 9.21: Grey value (intensity) against the thickness of the wedge for three different samples. Each plot shows differences which indicates difficulties in capturing thickness.

The data for all three wedges have been processed with data binning procedures to prevent overfitting. The binning process generated the uncertainty in each data point. The three plots are unique in shape indicating differences in the captured photoluminescence. Each plot fitted strongly to a cubic polynomial equation

Sample ID	$y = Ax^3 + Bx^2 + Cx + D$				R^2
	A	B	C	D	
WF-SAOE_Wedge_001	-3.12 $\times 10^5$	9.00 $\times 10^4$	1.36 $\times 10^4$	-332	0.997
WF-SAOE_Wedge_002	-5.64 $\times 10^5$	1.10 $\times 10^5$	1.86 $\times 10^4$	-328	0.999
WF-SAOE_Wedge_003	1.37 $\times 10^6$	-4.40 $\times 10^5$	5.72 $\times 10^4$	-972	0.993

Table 9.4: Cubic polynomial equation that has been fitted onto the three plots shown in figure 9.21. The coefficients A — D are presented with the R-square value which demonstrates the confidence of fit.

Both figure 9.21 and table 9.4 present issues with the concept of using PL for thickness measurements. The three plots along with the coefficients of the cubic polynomial fits show significant differences in the captured PL. As a result it would be difficult to translate captured PL into thickness to the same resolution as demonstrated in chapter 6 as PL is not consistent between samples. A proposed

cause was the distribution of ML particles throughout the samples both in size and density within the sample. Larger ML particles produce high intensities of PL as quoted by manufacturers of these materials and in literature [145, 146]. Additionally, large collections of these particles would produce higher intensities of PL. SEM imaging, figure 9.18 and 9.19, demonstrated both differences in size and how the distribution of particles changed throughout the sample. It is proposed that these effects give rise to differing PL qualities that would be challenging to control. As such it has been determined that thickness measurements with PL would give rise to large inaccuracies in the resultant thickness calculations.

9.5 Simultaneous photoelasticity and mechanoluminescence

The final investigation in this chapter is to combine photoelasticity with mechanoluminescence as a proof of concept. ML can be used to validate the photoelastic response qualitatively in its current form. This will be attempted by using a simple dual camera setup and manipulation of different wavelengths of light to extract photoelastic information and ML simultaneously. As ML is a dynamic process the GFP2500 poleidoscope was used to capture dynamic photoelasticity. Additionally, the GFP1600 will be used to capture images of greater resolution when necessary. WF-SAOE will also go through strain-optic coefficient calibration to determine the photoelastic sensitivity of the coating.

9.5.1 Methodology

WF-SAOE was applied onto aluminium coupons with a circular stress riser using the same procedure outlined in section 9.1.1. The objective was to produce a well defined strain field that could be easily observed by both techniques. The investigation made use of a 25 kN Tinius Olsen tensile tester located in a darkroom. The maximum applied load was 10 kN with a 0.5 mms^{-1} displacement rate. To capture both techniques simultaneously a dual camera setup was utilised with one capturing just ML and the other either a GFP2500 or GFP1600 capturing just PE. The ability to separate each signal made use of wavelength manipulation. ML requires light in the blue wavelengths for excitation whilst producing PL and ML in the green wavelength (525 nm peak intensity wavelength). Therefore light in the red wavelength ($>$630 nm) will not have an effect on the excitation of the ML material and on the ML response. PE can be conducted monochromatically however it would remove the ability for thickness corrections using the technique of analysing both blue and red light.

The Thorlabs CMOS camera was fitted with a shortpass filter [148] with a cut off wavelength of 600 nm preventing red light through to the detector. Two circular polarised light sources and the GFPs were then mounted with longpass filters [149] with a cut on wavelength of 630 nm to let only red light through. Changes to the polarisation of the light sources due to the filters would be accounted for through the post processing facilities within the software that analysed PE data. The two cameras were positioned either side of one another viewing the hole. A mixture of lenses were used to capture the hole at various magnifications. The two red polarised light sources were positioned either side of the dual camera arrangement as shown in figure 9.22.

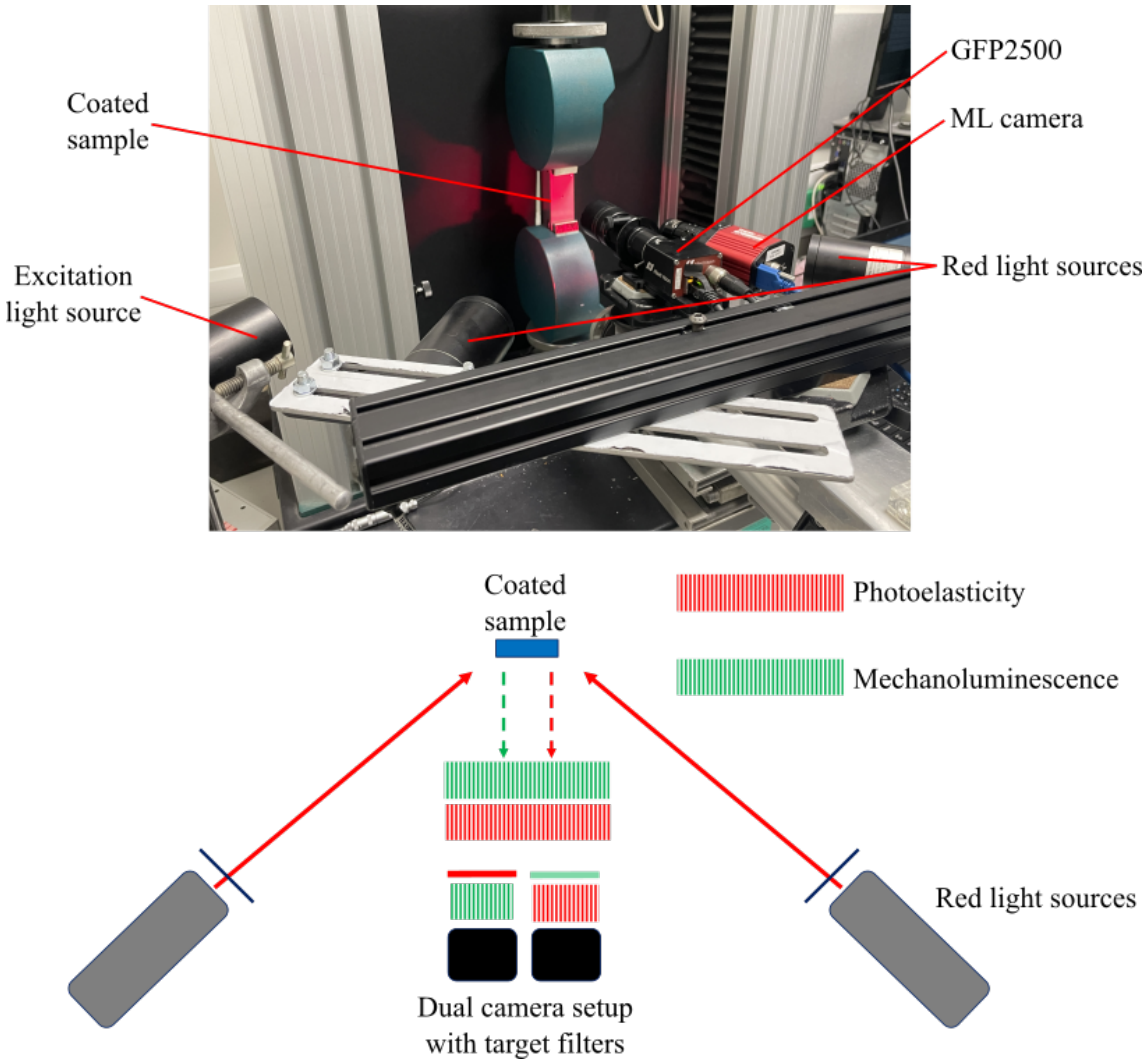


Figure 9.22: The dual camera setup for simultaneous PE and ML investigations. Target filters are attached to the cameras to allow PE to be conducted monochromatically in the red wavelengths whilst not interfering with the excitation and ML production.

The GFP2500 was setup following the outlined procedure using the GFP2500c software. The

software was used for a camera setup with individual frames able to be analysed through Deltavision. The procedure for camera setup has a user align the desired regions of interest with four close to identical images that have passed through the kaleidoscopic lens as shown in figure 9.23.

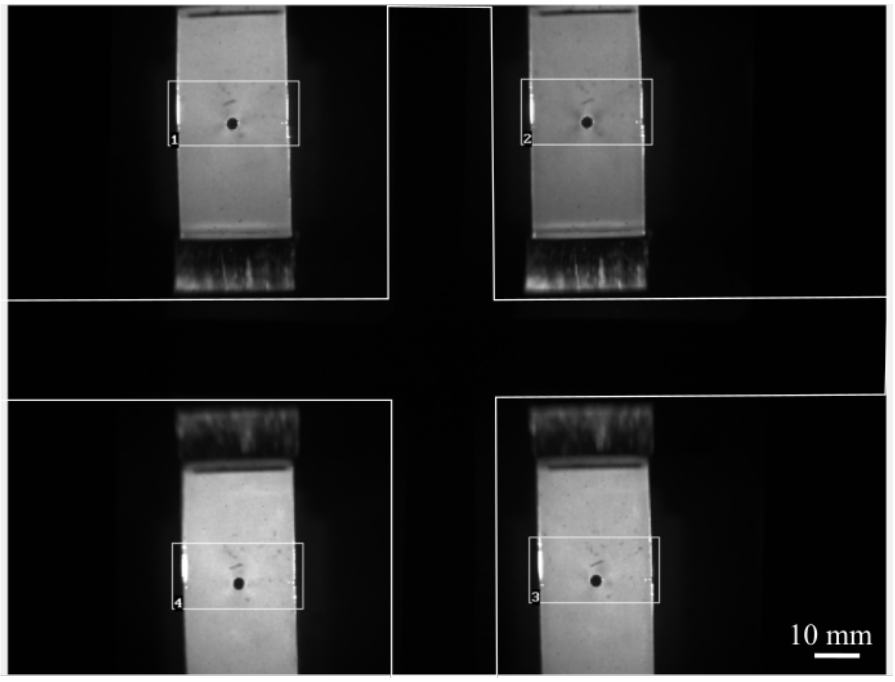


Figure 9.23: The region of interest manipulator within the GFP2500. Four images are shown that have passed through a kaleidoscopic lens. The adhesive grid of the lens has been highlighted and the region of interest are the white boxes focusing around the hole. The lens changes the field of view between the top and bottom images.

Each image in figure 9.23 has passed through different arrangements of analysing optics. The user superimposed these images over one another and the exposure was then altered to achieve a suitable light level utilising the in built camera oscilloscope in the software. The GFP2500 was set to a frame rate of 4 fps matching the framerate of the ML camera that also had a 40 dB gain parameter to increase the sensitivity of captured light. The capture procedure first excited the material with a white light source for one minute. The PL of the material was left to relax for 2 minutes with the PE apparatus primed and ready. Red light sources illuminated the sample and the software was ready to capture images. Both cameras were set to record and the loading was triggered at a frame count of 10. The data was extracted and reviewed qualitatively. Stills from the GFP2500 recording were analysed in Deltavision. The GFP1600 was also used to provide higher resolution at the max load allowing for clearer comparisons of each technique.

WF-SAOE calibration procedures follow closely to those described in chapter 7. However, the choice of sample materials have been changed. Five steel dogbones ([150 x 30 x 3] mm with a [60 x 20 x 3] mm gauge length) and six aluminium coupons (150 x 30 x 3) mm were chosen to determine the effects of material selection on the value of K. The sample choices were to enable mounting on a Tinius Olsen tensile tester, located in a darkroom to avoid any effects of ambient light. Furthermore, the width of the samples were the same as the grips of the tester. The assumption was that the grips would enable close to complete uniaxial tension as the sample could not be placed between the grips at an angle. Samples were applied with silver paint using a number 3 K-bar to spread the paint across the sample. The micrometer adjustable blade was used to spread the coating across the samples. A glass cover slide was used as a spacer and placed ontop of the sample surface. The blade was brought down to rest lightly on the cover slide. The cover slide was removed and no further changes were made to the height of the blade. Acetone was used to clean the surface and a syringe applied approximately 0.3 mL of WF-SAOE onto the surface and spread. The samples were cured for 20 s under UV light. Rosette strain gauges were applied using the same materials and techniques outlined in chapter 7. A P3 strain indicator and recorder outputted the strain values for the 0 and 90 ^{o} orientated gauges. Both samples went through stepwise loading in $\sim$ 1 kN intervals up to 8 kN for steel dogbones and 10 kN for the aluminium coupons. Linear analysis on the extracted data was performed to extract K values as described in chapter 7.

9.5.2 Results and analysis

9.5.2.1 Simultaneous capture

The concept of simultaneous capture was successful using the outlined procedure. Two dynamic events were captured with ML intensity recorded and PE data analysed. The following observations were made at maximum load for two separate samples, figure 9.24.

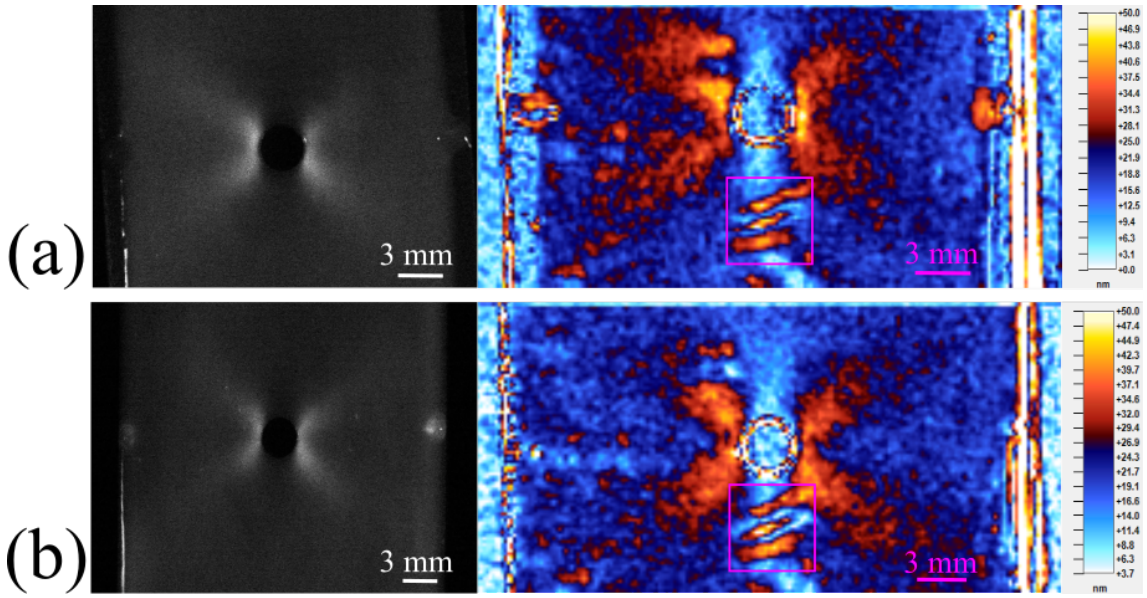


Figure 9.24: Images demonstrating the simultaneous capture of ML and PE on aluminium coupons ***(a)*** *&* ***(b)*** *with a stress riser. The coupons were in uniaxial tension with a maximum load of 10 kN applied. The area highlighted in the PE images was an artefact of the camera captured in all images.*

Due to there being no method of triggering the cameras to record at the same time, reviewing images at the maximum load allowed for direct comparison as the state was easily known in each image. A few observations were made in regard to the PE analysis. Firstly, an artefact was observed on all GFP2500 images, this has been highlighted by the purple square shown in figure 9.24. This was a camera setup issue with either a scratch or particle on the optical media. As the GFP2500 was in use for other research, a break down of the apparatus was not possible. Additionally, the resolution of the images was poor due to the selection of the region of image that effectively crops the sensor. As a result, the lens choice paired with the GFP2500 was not the most suitable. It was decided to keep lens choice the same between cameras and focus closer to the hole. For these comparisons the GFP1600 was used for added clarity and due to its ease-of-use however the concept of simultaneous capture has been achieved.

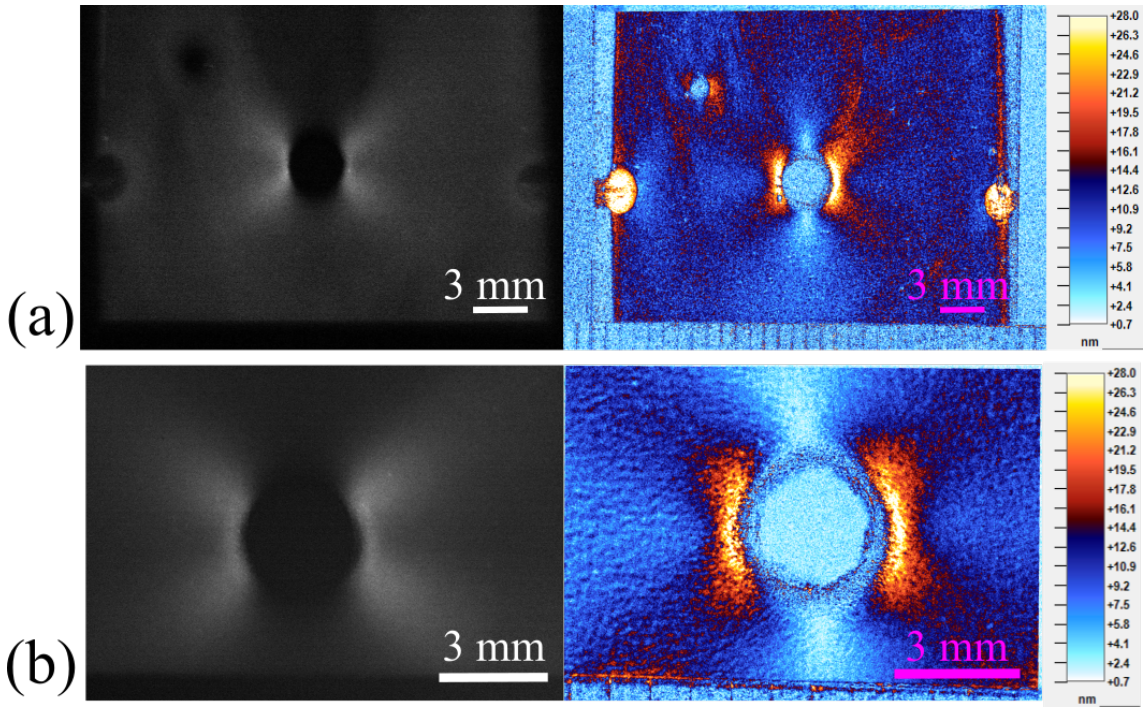


Figure 9.25: Images demonstrating the capture of ML and PE on aluminium coupons ***(a)*** *&* ***(b)*** *with a stress riser. The coupons were in uniaxial tension with a maximum load of 10 kN applied. The images were taken with different lenses to provide different magnifications around the hole.* ***(a)*** *A lens of variable focal length between 15 - 70 mm was used.* ***(b))*** *A 28 mm macro lens was used to image closer to the hole. Photoelastic images were taken using the GFP1600.*

Figure 9.25 presents the higher magnification images with the GFP1600 capturing PE analysis. The images demonstrated similarities between the two techniques as expected from the review of literature. However, PE images provide more detail especially around the hole for the highest magnification image. A small ring around the hole was observed that possessed no PE response. After inspection of the original sample that area contained no photoelasic coating which can be explained by the curing process and the meniscus formed around the hole. These details were unable to be captured from the ML response. In order for direct comparisons, the images were superimposed over one another and processed in different ways. Figure 9.26(a) compares both techniques side by side with the ML intensity image brightened for added clarity. Figure 9.26(b) superimposes the PE image over the ML with pseudo colours applied. The PE data is in cyan and transparent with brightened ML data underneath in magenta.

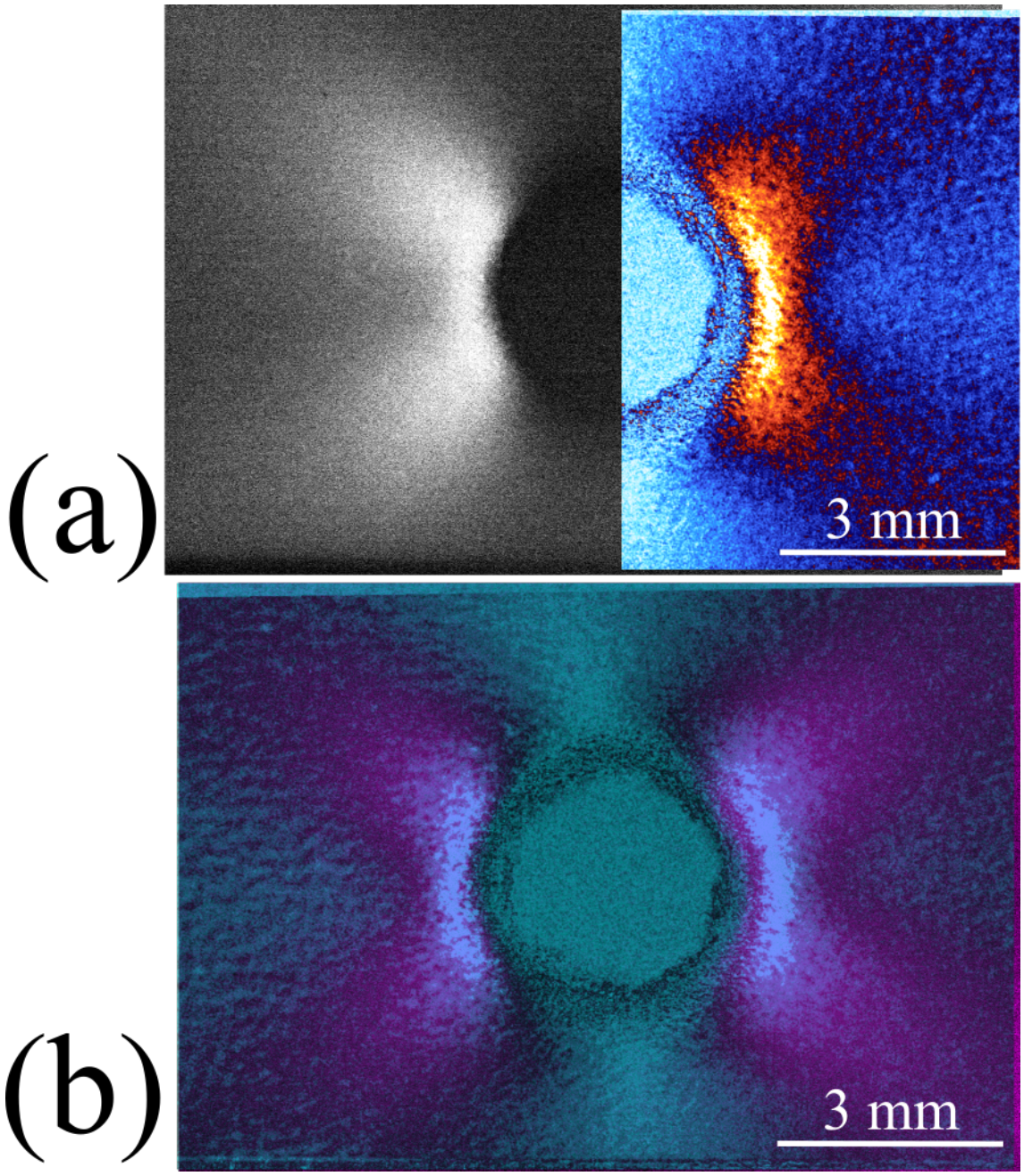


Figure 9.26: Superimposed images of the ML response (magenta) and the PE response (cyan). The PE response image was transparent allowing for any differences in between the responses to be observed.

Images were superimposed manually however the differences between the responses were minimal. Beyond qualitative comparisons no further comparisons can be made quantitatively due to the difficulties of extracting ML light. However, WF-SAOE photoelastic performance can be reviewed by the determination of its strain-optic coefficient.

9.5.2.2 WF-SAOE photoelastic calibration

The results in section 9.5.2.1 demonstrated WF-SAOE possessing a PE response that was compatible with the sensitivity of the GFP1600 and GFP2500 through the detectable photoelastic response shown in figures 9.24 and 9.25. Performing strain-optic coefficient calibrations of WF-SAOE on steel and aluminium, the following data was calculated and shown in figure 9.27.

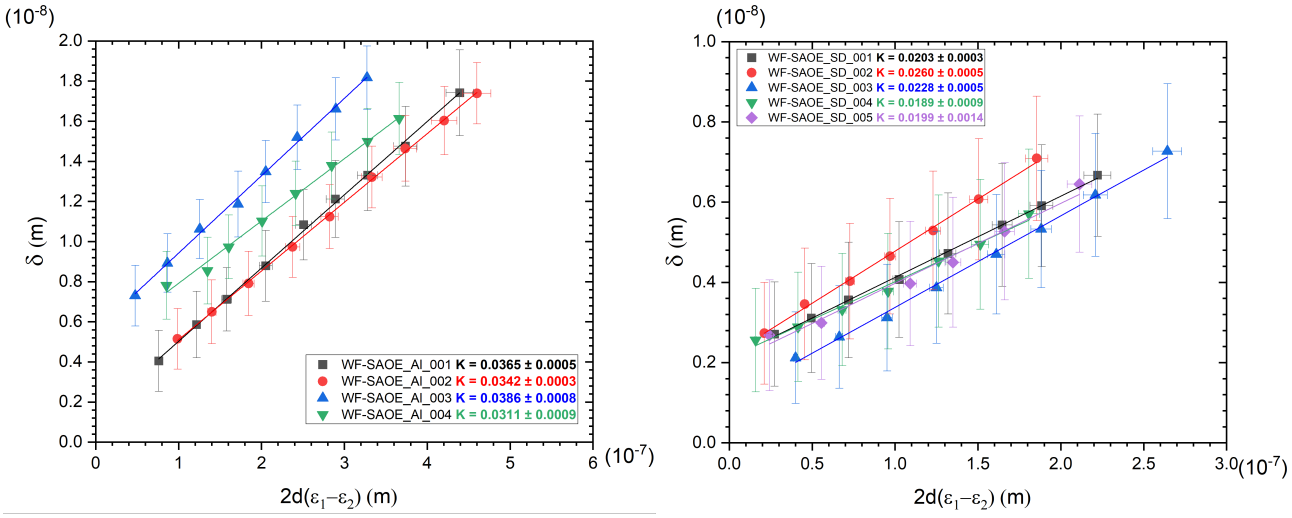


Figure 9.27: Strain-optic coefficient calculations for aluminium coupons (WF-SAOE_Al_x) and steel dogbones (WF-SAOE_SD_x) that show different values of K between the sample materials.

The same observations can be made in figure 9.27 to those made in chapter 8 where the values for K change dependent on the sample material selected for calibration. The aluminium coupon (WF-SAOE_Al_x) calibration calculated K to be higher (0.0351 $\pm$ 0.032) than those performed on the steel dogbones (WF-SAOE_SD_x) (0.0216 $\pm$ 0.0029) . Whilst statistical analysis, through two sample t-tests, came to the conclusion that the values for K were not significantly different, the change of K of more than 0.01 has a large effect on the resultant strain data. However the steel dogbone was not the most suitable sample material choice due to the stiffness of the material yielding only a measured principal strain difference between 600 — 1000 $\mu\epsilon$ resulting in maximum retardation between 5.71 — 8.62 nm. This PE response was less than half the magnitude of the data captured using the aluminium samples. Reduction in the dynamic range of data had negative impact on the measured K as demonstrated in chapter 3.3. Nevertheless, these findings support the comments made by Cloud [55] that material calibration is important and required to avoid accuracy loss. The measured values for K provided further evidence in the reduction of PE sensitivity due

changes in reflectivity in this case caused by the introduction of the ML material.

9.6 Discussion and conclusions

Extensive experimental investigations have been performed and discussed in this chapter in regard to mechanoluminescence and its performance in elastic loading scenarios. The objectives were to combine an ML material with the developed UV curable photoelastic coating in order to produce a dual-technique strain measurement coating. However, whilst the concept was proven to be possible a number of critical issues exist with ML that limits its usability.

The production of ML requires the process to be captured dynamically within a light controlled environment. The experiments conducted in this chapter were uniaxial tension tests on aluminium coupons with and without a stress riser. Initial investigations demonstrated limitations on the production of ML with displacement rate. A displacement rate of 1 mmmin^{-1} produced no ML within the sample's elastic limits. Only when the sample breached the elastic limit around a circular stress riser did the coating start to produce observable ML. Reviewing the procedures made in published research a similar loading scenario was observed in research conducted by Li *et al* [71] that managed to capture ML at upper loads of 5 kN. However, the differences were the displacement rate with Li applying 5 kNs^{-1} and this research applying 240 Ns^{-1}. Feng *et al* [84] demonstrates that ML intensity is proportional to the rate of strain and as a result further investigations increased the displacement rate to 1 mms^{-1}. This enabled ML to be captured much earlier with the apparatus used in these investigations, comparisons between figure 9.4 and 9.6. However, figure 9.15 demonstrated no changes in the captured peak intensities for displacement rates between 0.25 — 1 mms^{-1} indicating resolution limitations of the imaging setup. However, increases to 2 mms^{-1} demonstrated a large increase in the captured intensity. An article by Chen *et al* [87] recently managed to capture ML production at a displacement rate of 0.005 mms^{-1} and determine a non-linear relationship between ML intensity and loading rate. Continuing with ML light production, the comparisons between materials with different particle size has not been a discussion point in previously published literature. SAOED is thought to be more intense within elastic conditions than SAOE [76]. However, whilst an increase in PL was observed, figure 9.5, no ML was captured for the same loading cycles. Therefore, a user must consider the particle size when conducting ML procedures as well as the loading scenario to be performed.

It was established that the ML material in a powdered form, with particle size distribution of 2 — 10 μm, was able to be mixed within the UV curable formulation WF31 and produce solid coatings. The effects of reticulation were minimised by using a blade applicator and not K-bars. The K-bar's ridges triggered significant reticulation which provides difficulties in its application. Whilst the coating was solid and able to produce ML light during loading applications, the ability to replicate ML intensities using the same coating following re-excitation was not possible, figure 9.10. Subsequent loading on the same coating produced significantly less light, resulting in the coating becoming a 'one-shot' technique. A user would need to remove and reapply the coating in order to capture further datasets on the same location resulting in time loss. SEM imaging, figures 9.17 — 9.19, captured the degradation of the ML material and carrier resin after loading that indicated a disturbance in the strain transfer to the ML particles. These findings back up similar observations and comments made by Jongchansitto *et al* [85]. The compatibility between the materials has been shown to possess a major issue that would need further coating optimisation in order for the breakdown to not occur. However, there would be a risk to decrease the photoelastic sensitivity of the coating dependent on the conditions required to prevent the loss in strain transfer such as increase adhesion.

The repeatability of ML light production has been demonstrated, figures 9.11 and 9.13, when normalising per coating thickness. The thickness dependency on the ML intensity has been demonstrated recently by Chen *et al* [87] however they determined that there exists an upper thickness limit where ML intensity decreases. This investigation compared the fits of a second order exponential decay equation that mathematically described the decay of ML after reaching a maximum load. Whilst similarities were observed there existed a major issue with the resolution of the captured responses. Figure 9.14 demonstrated overlap between maximum loads of 7.5 — 10 kN. These overlap would contribute significant inaccuracies if a user was to translate ML intensity into stress or strain information. Furthermore 9.14 demonstrated a load limitation on the production of ML light with a load of 5 kN producing a minimal rise in intensity. The thickness dependency on the ML intensity provides further concerns. Photoelasticity requires accurate thickness measurements for quantifiable data, the same has been highlighted for ML materials. WF-Red1 is able to utilise facilities within the GFP1600 processing software in order to correct for thickness differences during application. The facility is able to translate differences in the ratio of two wavelengths of light (blue:red) to thickness. It was proposed in section 9.4.2 that the PL of WF-SAOE after excitation would be able to provide a method of thickness measurement by observing changes in the intensity

of PL due to thickness, figure 9.20. Whilst thickness gradients were observed in the wedge samples used for the calibration, further inconsistencies between samples demonstrated difficulties. Figure 9.21 confirmed that PL was not repeatable and that determining thickness through this method would not be possible. Additionally, due to the green tint of WF-SAOE procedures used in chapter 6 would prove challenging. The software utilising differences between red and blue wavelengths. If changes could be made to the software to target different wavelengths, then perhaps this method could be adopted and performed in the excitation stage of ML procedure.

Novel simultaneous capture of ML and PE was proven to be achievable with minimal difficulties using a dual camera setup filtering out the green ML from red light used to perform PE monochromatically. Qualitative comparisons demonstrated similarities between the responses from samples in uniaxial tension with a circular hole acting as a stress riser, figures 9.24 - 9.26. From these investigations a user can validate PE from the ML response, however the information is limited due to ML limitations. In elastic conditions the production of ML light was weak with unpredictable peak intensities making accurate and precise calculations of the state of strain/stress challenging to achieve. Furthermore, details were lost in ML that were easily identified by PE, figure 9.25.

A user conducting ML experiments needs to consider various parameters: how can ambient light be controlled in the testing location? Is the strain rate high enough to trigger a response that is detectable using the imaging apparatus? Are the ML particle sizes consistent between samples? Is the carrier material able to prevent debonding from the ML particle allowing for repeat measurements? How is thickness being controlled and/or measured? All these limitations question the applicability of ML as a validation tool to be used alongside PE. However, ML does produce interesting and insightful observations. For example, within figure 9.12 as the coupon entered plasticity a sudden production of intense ML light was observed. The production of this light is observable in ambient light conditions. A user could adopt these materials as methods of determining failure. Additionally, throughout this investigation the production of ML has been intense close to stress risers. These singularities within samples provide locations where ML light production was the most intense in elastic conditions. If these singularities are known prior to the loading application or if detection of failure is the objective then more sensitive apparatus could be utilised that only focuses on certain areas similar to a strain gauge. For example, spectrometers could be applied with a fibre measuring the production of light at a location within ambient conditions.

These investigations have provided and supported many findings in regard to the practical uses of ML. Furthermore the novelty of combining ML with PE to form a dual technique coating capable of simultaneous data collection as also been outlined for the first time. Key conclusions from these investigations include:

- Full field ML light production was measured from thin UV curable coatings at thicknesses between 15 - 149 μm. Full field measurements at these thicknesses are not discussed widely in previously published literature.
- Particle size distribution of the ML material is an important parameter to consider when measuring ML light. Larger particles produce increased ML. A number of previously published research do not highlight these findings their investigations.
- Repeatability between samples has been demonstrated however not without challenges. Low signals produce variations which make it hard to resolve between applied loads.
- Displacement rates between 0.25 - 1 mms^{-1} have no measured affect on the resultant peak intensity allowing for control over camera settings. However, at 2 mms^{-1} the peak intensity suddenly increased.
- The ML coating produced, WF-SAOE, was 'one-shot' requiring re-coating for subsequent repeats. The strain transfer between the carrier resin formulation and the ML degraded after load due to reduction in structural integrity. This finding has not before been demonstrated within coatings before and after load.
- Variations in measured PL provide challenges to thickness measurements via PL.
- Simultaneous capture of ML and PE has been demonstrated for the first time with qualitative similarities explored.

Chapter 10

Discussion

10.1 Summary

This research aimed to develop a new reflection photoelastic coating with the objective of improving application and data collection efficiency, whilst also providing more insightful data.

Current commercially available coatings are in the form of polycarbonate sheets and contourable plastics [7] that require skilled engineers and take up to several weeks to apply onto large structures. Their instructions are "subjective" with methods becoming "apparent with practice" [11, 12] which, alongside other significant drawbacks, dissuades users from applying these techniques. Furthermore, the effects of mishandling, contact issues between the coating and adhesive, and sample reinforcement all contribute to inaccuracies with photoelastic data [45]. Spreadable two-part epoxies have also been used [8] however their availability and published PE specifications are not widely available. Additionally, they still suffer from long application times, due to the curing process, bubbling in the mixing procedure and because of their viscosity the process of application is slow and not easy to work with. There have been developments in the application of sprayable photoelastic coatings [10] however the application remains slow due to curing processes and their applications are limited.

This research utilises high performing UV curable resins and photoinitators to allow for easy application, rapid curing whilst maintaining a high sensitivity to strain and the ability to allow for thickness corrections at applied coating thickness of ~ 50 μm. The coating development was used alongside a GFP1600 grey-field polariscope [150] with the acquisition and processing software Deltavision, that allowed for automatic collection and analysis of full field data. The data could also be subjected to

post processing facilities such as residual retardation subtraction and thickness correction. A variety of formulation optimisation experiments and investigations into the best operating procedures were conducted and discussed.

Finally, the photoelastic coating was combined with a mechanoluminescence (ML) material to provide a novel dual-technique full field coating for strain measurements. The coating was combined with a rare-earth ion doped alkaline aluminate and silicate, $SrAl_2O_4$:Eu, that has been shown to provide high intensities of ML during elastic loading conditions [70–80]. The aim of this investigation was to provide simultaneous capture of ML and PE data to enable side-by-side validation of the captured data.

10.2 Research aims

The research was given criteria that outlined desired qualities for the coating. The criteria were as follows:

1. Birefringent to enable photoelastic measurements, with a constant or at least a definable strain optic coefficient.
2. Luminescent when energised by strain with definable strain characteristics.
3. Ideally sprayable, with a constant or known thickness, for ease of application.
4. As thin as practically possible whilst keeping reinforcing effects to a minimum.
5. Fast curing.
6. Easy to remove, leaving no evidence on the final component or structure.
7. Meet current and known future health and safety requirements.
8. For use within confined spaces without need for specialist protective equipment.

This research has met the large majority of the controllable criteria. Criteria that were out of scope were criteria 7 and 8 as they were constrained by measures outlined by the organisation the investigations were conducted in. However, health and safety constraints were minimal with the formulation requiring adequate ventilation, no respirators or masks were required when handling. Spraying would require the implementation of certain safety measures that need to be discussed

further with Arkema and the industries where spray coating would take place. The coating poses no health risk once cured. The coating was birefringent with strain-optic coefficients able to be measured and repeated within the same sample materials. Mechanoluminescent materials were added producing a dual technique coating that enabled simultaneous capture of both techniques. The coating was targeted at a thickness of 50 μm producing **one of the thinnest photoelastic material documented** whilst still producing a measurable response. The UV curable coating achieved **maximum cure conversion in 20 s being the fastest applicable photoelastic coating.** Finally, the coating was shown to be **easily removable** that left no signs of damage on the applied coating. However, criterion 3 was not fulfilled completely.

Including a tint into the coating enabled thickness measurements and corrections that satisfied the ease-of-use criterion. However, the objective to achieve a sprayable coating was not achieved due to the lack of facilities within the University, and with scope of procuring equipment not possible. The formulation WF31's viscosity was measured using cone and plate rheometry through a temperature range between 5 — 60 ^{o}C as shown in figure 10.1.

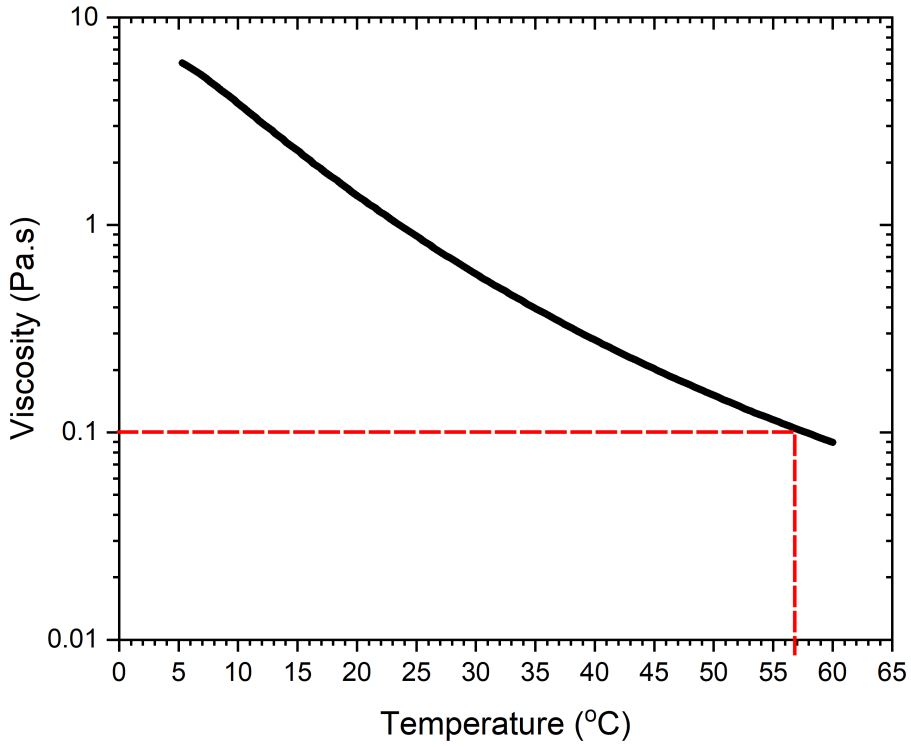


Figure 10.1: The viscosity of WF31 measured using cone and plate rheometry at a temperature range between 5 — 60 ^{o}C. Through heating the sample beyond room temperature the viscosity decreases allowing for potential spray coating operations.

Figure 10.1 demonstrates a reduction in viscosity as the temperature of the formulation increases. The American Coating Association recommends a viscosity of approximately 0.1 Pas (100 cP) [108] for adequate spray coating which is achieved just below 60 ^{o}C. Further experiments that introduced a solvent as a diluent demonstrated that the addition of 10 % of solvent reduced viscosity by $\sim$85 %. Further work is required to establish conclusions and suitability with these coatings and is discussed further in chapter 12.

10.3 Development of a UV curable photoelastic coating

Chapters 3.2 — 4 provided an understanding of the mechanisms of the UV curable coatings that enabled coating optimisation, initial photoelastic performance investigations and outlined the curing procedures. A large sample set of UV curable formulations, $>$30, were investigated for their photoelastic performance as well as various physical and chemical properties. Six resins were selected by recommendation of the manufacturer and were combined in multiple ways. The main significant conclusion was that the photoelastic sensitivity was greatly affected by the amount of the resin S160.

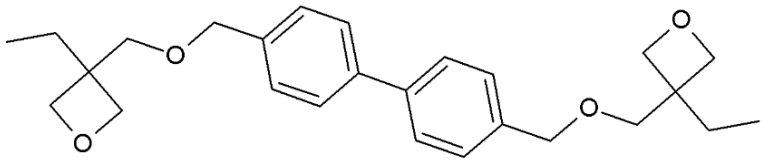


Figure 10.2: Chemical Structure of the oxetane resin UviCure S160

Figure 10.2 highlights S160, having a double aromatic ring structure, that increased coating stiffness and refractive index. This in turn provided sufficient photoelastic sensitivity that this research employed. Double aromatic ring structures are found in polycarbonates which are one of the most sensitive photoelastic coating materials. PhotoStress' PS-1 utilises polycarbonate and states a strain-optic coefficient (K) of 0.15. The research used PS-1E as a comparison due to its availability and wide use in research and industry. Through investigations used to optimise the UV curable formulation, supporting resins were added that reduced viscosity and assisted removability whilst maintaining sufficient adhesion during elastic deformations of metal surfaces. This research used the optimised formulation WF31 (also known as DOE9) that possessed a strain-optic coefficient K of 0.0982 $\pm$ 0.0018, a medium-high sensitivity coating, comparable to existing coating materials.

The associated value for K for WF31 further supported an objective to target a thickness of $\sim$ 50 μm that would aid application efficiency whilst removing the negative effects of reinforcement. This targetted thickness is approximately **five times thinner than the current range of photoelastic coatings** and has several benefits.

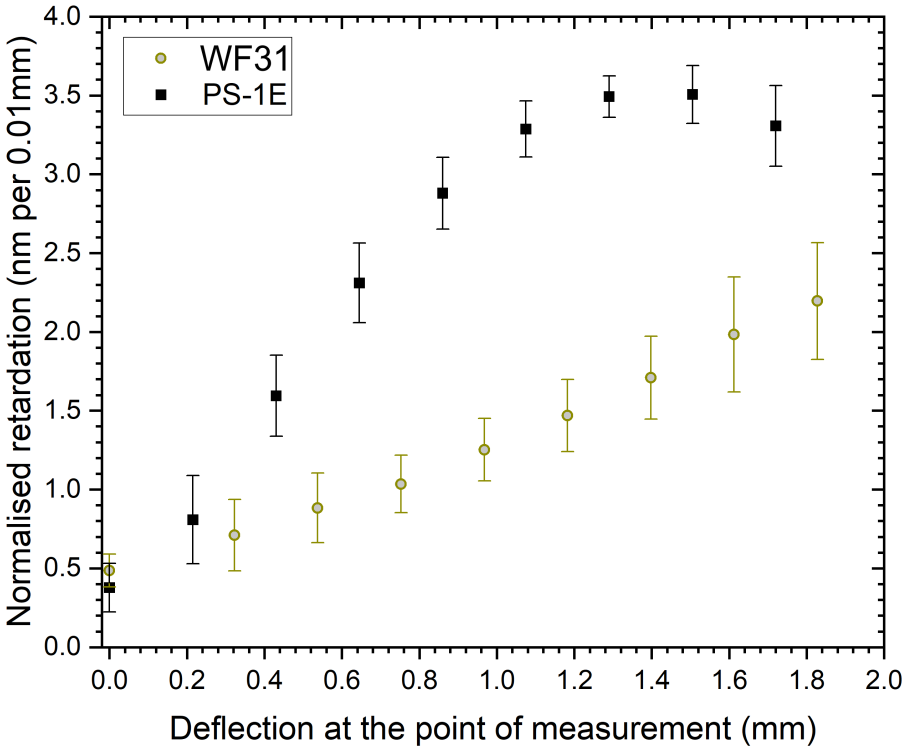


Figure 10.3: Comparisons of normalised retardation between WF31 and PS-1E. The data has not been post-processed. Aluminium beams coated with either WF31 or PS-1E were subjected to cantilever loading and at various deflections photoelastic data was captured.

Figure 10.3 compares WF31 (DOE9) with PS-1E in a cantilever loading experiment with a GFP1600 capturing the PE data. The GFP1600 has a high resolution of 0.5 nm with an upper limit of 0.5 fringe orders. The shape of PS-1E's photoelastic response appeared to demonstrate a reduction in the captured retardation beyond a deflection of 1 mm however this analysis was due to PS-1E breaching the upper limit of the polariscope device. WF31 remained linear throughout. This example demonstrates the versatility of WF31 as it removes the need to determine the most suitable sensitivity of a photoelastic coating for a given loading application. Furthermore, phase unwrapping procedures, that would be used to correct PS-1E in figure 10.3, are no longer required (similar to the technique developed by Hubner *et al* [10]). Another benefit allowed for the use of rapid curing through UV light irradiation. **Unique to all other photoelastic coatings was WF31's capability to achieve**

a maximum cure conversion after 20 s of continuous light irradiation. This arguably has the potential to update reflection photoelasticity into a rapid full field strain measurement technique. It vastly improves the efficiency compared to the PhotoStress contourable plastic method, that can take upwards of weeks to apply bespoke shaped coatings onto to complex structures, and the application of two-part epoxy coatings. The UV curable coating outlined by Hubner *et al* additionally takes several hours to fully cure with the coating applied in many thin layers. A predicted time period of two — three days was associated with Hubner's coating for application and data collection. Taking into account the application of a non-optimised reflection paint, further discussions made in section 12.2, **WF31 has the capability to be applied, data measured and processed, and coating removed between $\sim$12 — 24 hours** (dependent on sample size, location and application techniques).

This research focused on one further vital coating development investigation in regard to the control of the applied thickness. PhotoStress sheets are precast or formed into uniformly thick coatings that satisfy a requirement to accurately know the thickness of the photoelastic coating to enable calculations of stress and/or strain. However, liquid formulations applied directly to a sample surface do not possess this attribute which results in application difficulties through needing to control thickness application. The approach utilised in this research adopted techniques used by Stress Photonics in their Tintcoat product that enables the correction of thickness based on ratio of certain wavelengths of light that pass through the coating material. Applying this technique to calibrate thicknesses between 30 — 150 μm has not been attempted before. Introducing a red tint, a red resin dye [130], to the coating allowed for a relationship to be formed between captured red and blue wavelengths of light by the GFP1600 that were analysed through the software. By developing a relationship between thickness and the ratio of blue and red light the software was able to accurately correct for thickness differences. As a result, a user can apply the tinted coating, known as WF-Red1, onto the desired surface without the need to try to achieve thickness uniformity. The coating developed by Hubner [10, 62, 63] also adopted thickness corrections through the use of luminescent qualities within an undercoat material however requires a light controlled environment which limits its use. WF-Red1 can be applied directly using simple methods following a procedure outlined throughout this research.

10.4 Using a UV curable coating for reflection photoelastic strain analysis

The procedure for using a UV curable formulation as a photoelastic coating is outlined in figure 10.4.

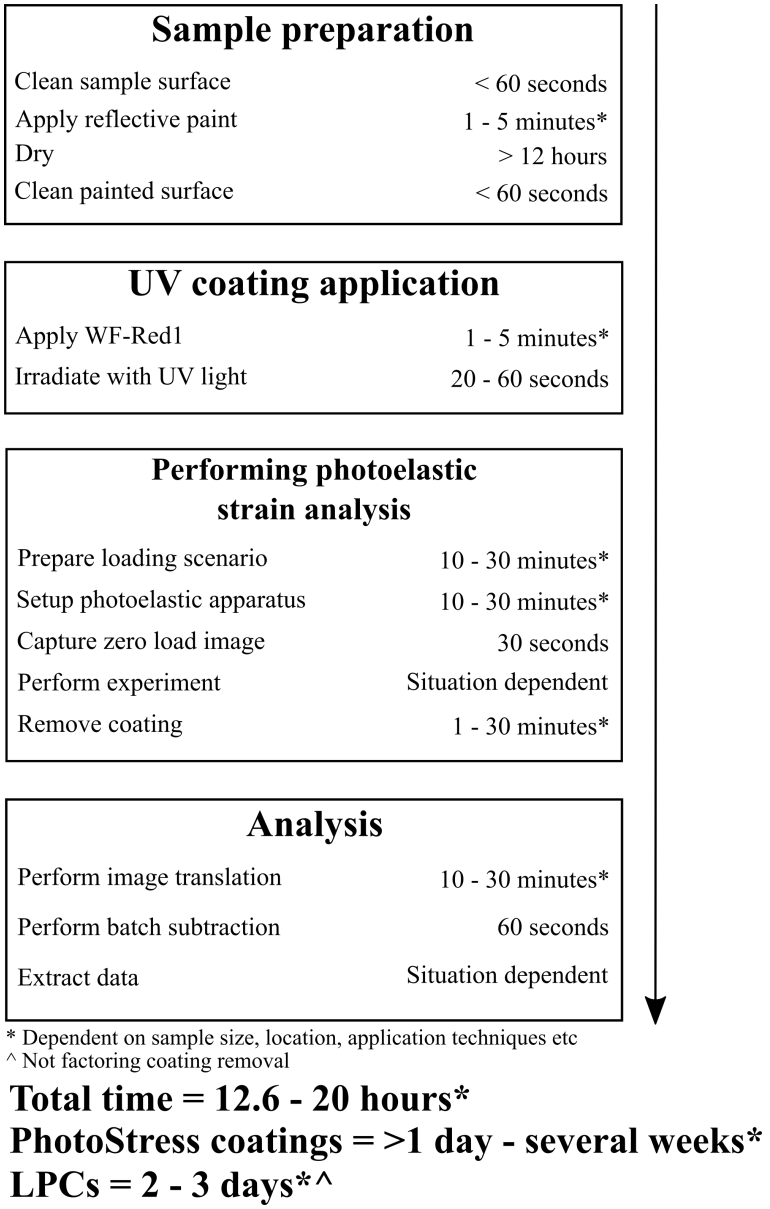


Figure 10.4: The outlined procedure a user should follow to use a UV curable formulation as a reflection photoelastic coating for strain analysis. Timescales are associated to each task.

Figure 10.4 provides a flow chart for the application of WF-Red1 for RPSA alongside timescales for each task. The timescales were based on user experiences within research laboratories and industrial

settings. The development of the procedure is based on the experimental investigations that have been outlined in this thesis. This section will discuss each step discussing major processes where appropriate.

10.4.1 Sample preparation

The procedure of most importance within sample preparation is the choice of a reflective backing. It is common practice to utilise a reflective backing that is diffusive and minimises specular reflections [10, 55,131]. However the effects of the reflective backing on the photoelastic response has previously not been explored in detail in published literature. Chapter 5.2 highlighted differences in the magnitude of the photoelastic response as a result of the choice of reflective backing as shown in figure 10.5.

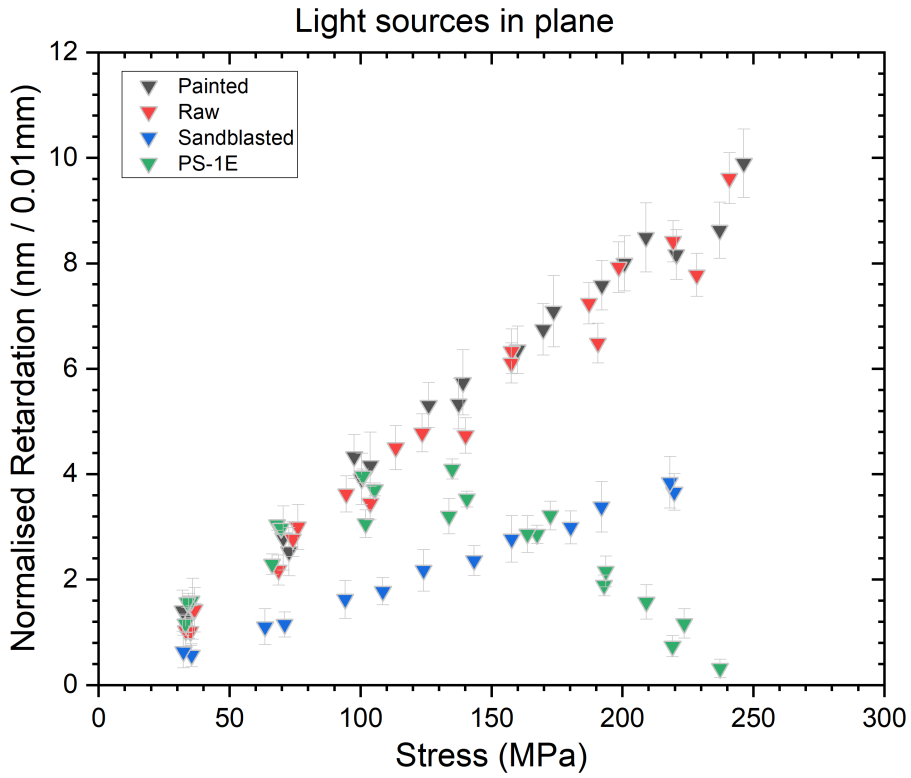


Figure 10.5: Comparisons of all four surface finishes when the light sources were in plane. A difference in response magnitude was observed.

Figure 10.5 demonstrated a limit to the diffusive effect of a reflective backing. The sensitivity of WF31 was reduced when the aluminium samples were sandblasted compared to bare and painted aluminium samples. Figure 10.6 quantifies the diffuse reflection from a light source at a fixed detector position.

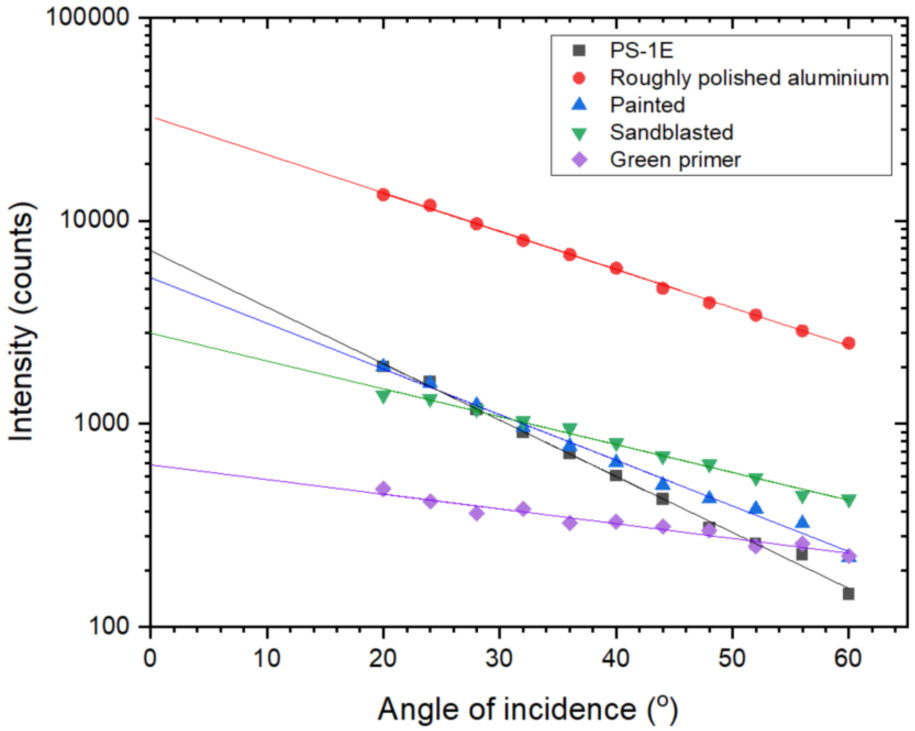


Figure 10.6: The intensity of the reflected light from various surface finishes at a fixed detector position.

A user must choose a reflective backing that possesses a suitable intensity at shallow angles of incidence. Polished samples, PS-1E and Hammerite smooth silver paint all had extrapolated initial intensities of greater than $\sim$ 6000 counts. A user could calibrate their choice of reflective backing using a similar method described in section 5.2.3.

Whilst the choice of paint in this investigation yielded the maximum photoelastic sensitivity of WF31 and WF-Red1, the paint had one major drawback. The drying time of the paint was upwards of 12 hours that degraded the overall efficiency. The paint chosen, Hammerite smooth silver [127], remained intact during the curing process of the UV curable material and it was widely available whilst being cost effective. Additionally, the specularity of the paint also induced inaccuracies by degrading the signal-to-noise ratio. Specular reflections in the form of high densities of hot spot pixels introduced noise that disturbed the photoelastic response. As a result, the extracted data from the software possessed inaccuracies that reduced the confidence of outputted strain values. Attempts to optimise the reflective backing were out the scope of this research fitting into future work and will be discussed in further detail in chapter 12.

10.4.2 UV coating application

Following the application of the reflective backing the UV curable coating is applied on top. The application procedure is not limited to a certain technique however the important factor to consider is the quality of the final finish and the initial state of the reflective surface. The former describes the appearance and qualities the coating may have due to certain application procedures. For example, a brush was used in industrial application to coat a large area in a difficult to reach location. Brush size, user inexperience and coating properties all contributed to a poor coating finish that featured large variations in thickness due to brush marks. Section 8.2 demonstrated difficulties correcting thickness for poorly applied coatings using the software's built in facilities. The initial state of the reflective surface also has a consequence on the cast coating. The effects of reticulation were triggered by unclean surfaces that contained particles of dust, paint and other contaminants. Poor pretreatment of the reflective surface would render the coating unusable as many holes would form. The addition of additives to reduce coating surface tension could be added to try to combat reticulation. This is another investigation for further work and will be discussed in section 12.1.

The UV curable coating in all its forms (WF31, WF-Red1 and WF-SAOE) was measured, using real-time ATR-FTIR, to achieve maximum cure conversion at a minimum of $\sim$20 s. **This attribute is the coating's greatest strength allowing for fast application and data collection.** A quality of the UV curable materials is its physical appearance and feel prior to this target time. It was noticed that curing for as little as two seconds would produce hard-to-the-touch coatings that were inferred as being fully cured. The research in chapter 4 demonstrated that differences in the cure conversion has an effect on the outcome of the photoelastic response. As a result achieving maximum cure conversion was recommended to improve the precision of the collection data. Real-time ATR-FTIR investigations demonstrated that the maximum epoxy conversion to be between 21 — 32 % and the oxetane conversion to be between 30 - 37 %. These results indicated that the majority of the formulation has not formed into the polymer matrix. A higher cure conversion would increase coating stiffness that would resultant in a more sensitive photoelastic material [55]. This could be achieved by removing the monofunctional group within the formulation, S140, however the viscosity would increase reducing the ease-of-use. This analysis indicated factors that WF31 is not fully optimised as not all the important conclusions have been considered in the optimisation. The outcomes from the Design of Experiments conducted in chapter 3.3 were less

than ideal but this was performed without considering the effects of cure conversion which has since been shown to be an important factor with these coating materials. Further work is recommended and outlined in chapter 12.

10.4.3 Performing photoelastic strain analysis

This work has demonstrated in detail that a user must consider the position of the light sources, how to correct for any ellipticity within the initial polarisation state of the polarised light sources and the environment the investigation is being performed in. Quarter-wave plates are wavelength dependent and using white light sources does not satisfy that requirement. As a result, inaccuracies are introduced through wavelength mismatch less than 9.75 nm (red light at wavelength 650 nm) [126] that describe the measured ellipticity. Optical setups for reflection photoelasticity investigations prevent normal incidence which introduce inaccuracies in the relation between birefringence and strain [3]. However, keeping the angle of oblique to a maximum of 4^o has negligible effect on the optical pattern interpretation. The configuration of the GFP1600 and light source/s in this research followed the advice of experienced photoelasticians who ignored the recommendation of the 4^o angle of oblique in favour of normal incidence of the camera. The configuration focused on the GFP being positioned at a normal to the coated area with the light source placed in a location that satisfies the user and is able to illuminate the coating area appropriately (suitable exposure captured and measured using the GFP1600 alongside the acquisition and processing software). Furthermore, positioning the light sources at this low angle of incidence caused too much direct reflection back into the GFP thus a wider light placement was used to easily control the light input. Using multiple light sources positioned at opposite sides to the camera demonstrated improvements in signal-to-noise ratio compared to light illuminated from a single direction, as shown in figure 10.7.

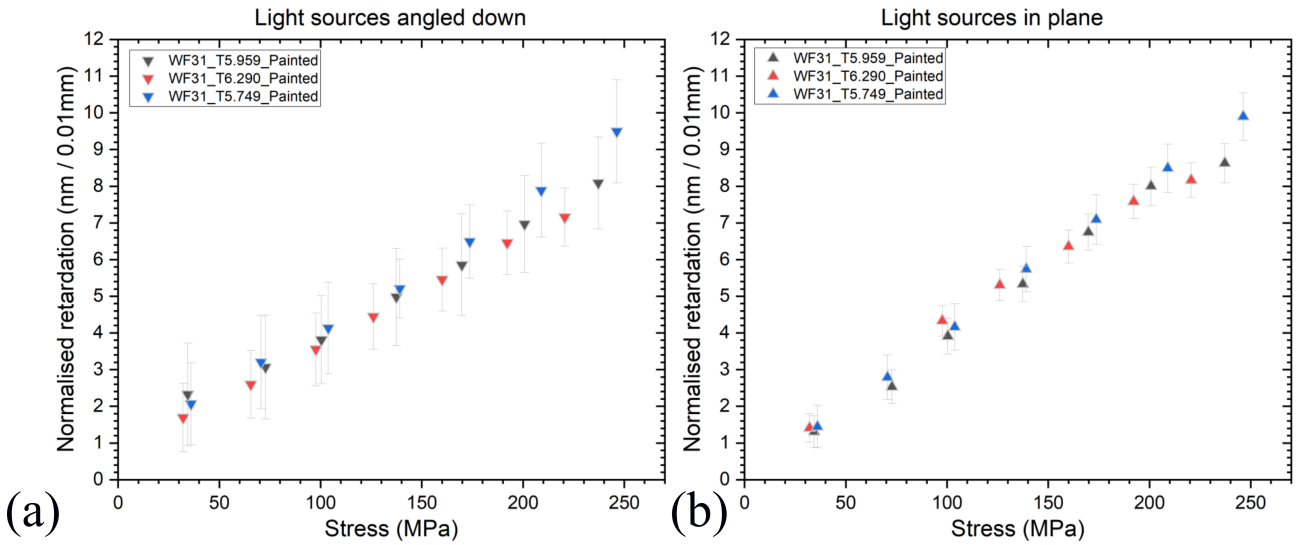


Figure 10.7: Normalised retardation against stress for aluminium samples coated with the UV curable formulation. The aluminium samples were initially coated with a silver paint. The data points represent the average retardation values and the error bars represent the corresponding standard deviations. This data was extracted from an area drawn within the images taken by the GFP1600.

This comprehensive analysis has not been widely discussed in published literature and is essential in demonstrating to users the effects of certain configuration changes that may often be overlooked. There are several other findings in this research that further support the decisions made for the configuration. Firstly, figure 10.6 quantifies the reflective qualities of the reflective backings for various angles of incidence (can also be described as the angle of oblique as the detector was fixed) of the light source. The light sources used emitted over a large diffuse area that would satisfy light entering the GFP at these low angles. Additionally, the GFP analysis software was able to accurately measure the coating thickness through the relationships of the light passing through the material. This provided evidence of accurate capture of the photoelastic response. However, it must be noted that light source angles were not recorded and monitored and these claims to support the used configurations could be argued against. The angle of obliques that were contributing to the majority of the photoelastic signal were not measured. A wide range of these angles that breach the 4^o restriction would contribute to inaccuracies in the measured photoelastic response. As a result, future work should consider these configuration effects and outline methods to minimise any inaccuracies caused by wide angles of oblique. The second light source factor to consider is the initial state of the polarisation if using circular polarised light for RPSA investigations. Devices such as the GFP1600 are incredibly sensitive, 0.5 nm resolution, and slight deviations from a circular polarised

light source will be captured and inferred as coating effects. Being able to account for any ellipticity must be applied within the post processing. Capturing a zero load image that includes the ellipticity inaccuracies as well as other initial states of the coating, discussed in section 10.4.4, must always be performed to allow for accurate analysis. The final consideration is the environment in which the investigation is being performed in. Industrial investigations conducted in chapter 8 did not factor conditions of ambient light and the effects of stray reflections. Quantifying the dominant factor has not yet been performed but evidence suggested that the surrounding area must be considered and any highly reflective surfaces and background features that produce light must be monitored. The use of opaque screens behind the sample being analysed and additional screening should be applied appropriately. This finding was backed up anecdotally by experienced photoelasticians, even though the documented advice is limited.

Upon completion of a RPSA investigation many situations require that the coating is removed without damaging the sample. The UV curable material benefits by being relatively easy to remove by using a sharp blade to get between the sample and coating. The user is then able to easily lever the coating off taking care not to scratch the surface with the blade. Coating removal is not widely discussed in the literature and the use of an easy to remove photoelastic coating would be a beneficial attribute that assists with the overall efficiency of the technique. Discussions with photoelasticians describe the process of removing PhotoStress products to be laboursome and difficult often requiring hammers, chisels and power tools to work away the coating and adhesive. Therefore this novel UV coating is a **vast improvement** in this respect

10.4.4 Analysis

As the coating was used alongside the GFP1600 and the analysis software, a number of crucial post-processing procedures must be able to be performed by the choice of apparatus that the user decides to implement. The most important post-processing procedure was the subtraction of parasitic birefringence that was contributed by several factors. This post-processing will be referred to as subtraction. Light source polarisation ellipticity has been discussed, in section 10.4.3, and is corrected using subtraction. The materials used to create the UV curable formulations boast low shrinkage however the sensitivity of devices such as the GFP1600 detected this shrinkage as residual birefringence, which if left uncorrected, distorts the true photoelastic response. Subtraction

is required for the accurate use of these materials as a photoelastic coating. It is important as the sensitivity of the device easily detects changes due to residual strains that have larger impact on thin coatings rather than thicker coatings where these effects are relatively minimal.

Translation of the measured retardation into principal strain difference requires the coating's strain-optic coefficient (K) and thickness. K values for WF31 and WF-Red1 were calculated to be 0.0982 $\pm$ 0.0018 and 0.080 $\pm$ 0.003 when applied onto 6082 - T6 aluminium samples and calibrated using the tensile methods as described by Cloud [131]. These values represent medium-high sensitivity coatings. Whilst materials such as PhotoStress PS-1 (0.15), PS-2 (0.13), epoxy-anhydride (0.12) and the luminescent photoelastic coating (0.1) developed by Hubner [10,62,63] posses higher values, it has been shown that the sensitivity is more than sufficient when using devices similar in sensitivity to the GFP1600. Critical analysis made in this research were the calculated changes to K when the coating was applied onto different material types. Published K values are always provided as a constant do not provide an associated variance. However, Cloud [55] states that material problems are often not accounted for and that manufacturers K values are used with potential accuracy loss. Cloud then outlines that material calibration is important in all photoelastic investigations. This coincides with the calibration experiments conducted for WF-Red1 on various materials (alumninium alloys, GLARE and carbon fibre composites) that calculated a variety of values of K ranging between 0.069 — 0.097. Experiments conducted on aluminium samples, chapter 7, provided consistent calculations of K between a number of repeats that provides confidence in the values for K for the materials that the coatings were applied onto. **As a result, a user is recommended to perform calibration for the material of the sample or structure on which RPSA will be performed**. Additionally, the coating material itself could be subjected to differences when approaching its shelf life. It therefore is recommended to frequently perform calibration to monitor any changes during storage and when using different batches. The thickness of coating material is corrected within the software and uses the relationship between red and blue light. As the ratio of blue and red light changes due to coating thickness, a fourth degree polynomial equation was used to map the changes to thickness. As a result, thickness across the captured image was measured and corrected for within the RPSA investigations. This facility finalises the ease-of-use aspect of the coating allowing for RPSA measurements. Without this facility, RPSA through the use of UV curable materials would be very challenging.

10.5 Overall performance of the photoelastic material

Photoelasticity is a very powerful and insightful technique allowing for the visualisation of strain in a material. Its qualitative nature allows for useful applications onto assemblies where mathematical modelling is complex [3]. Quantitatively, RPSA has been quoted to achieve 5 — 20 % accuracy in practical applications [55]. At this current point the exact accuracy of WF-Red1 depends on many factors such as the choice of reflective backing and resolution of the imaging device with further work needed to provide definitive accuracy of the coating. However, applications onto carbon fibre composites demonstrated an accuracy of $\sim$ 10 %, figure 10.8.

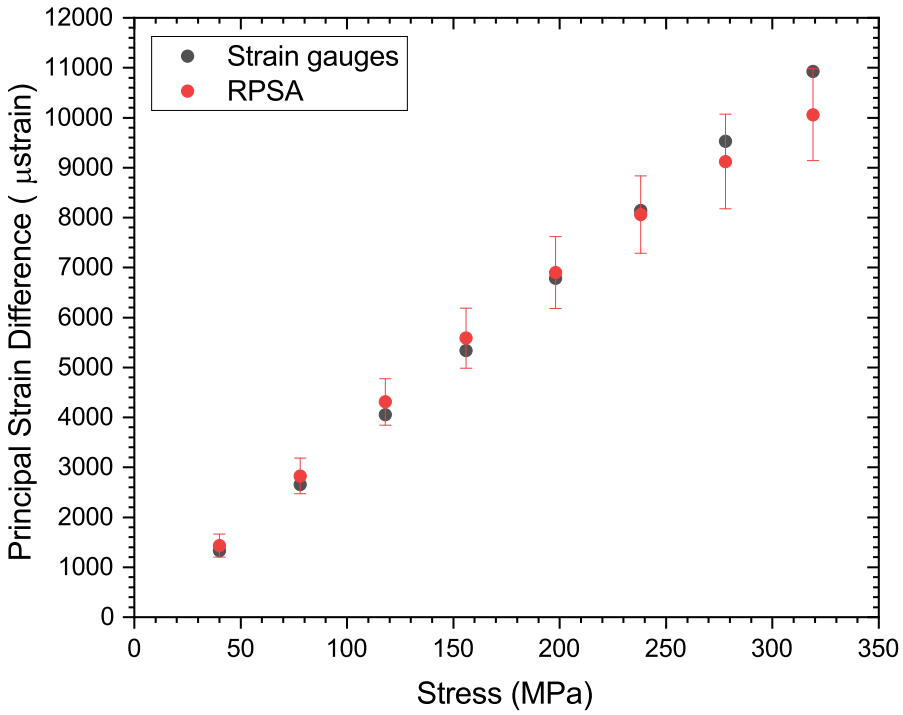


Figure 10.8: Comparisons of principal strain difference calculated using RPSA and measured directly using strain gauges. RPSA data was calculated using a strain-optic coefficient of 0.083.

However, the applications on the test wing structure at strain values below and around 500 $\mu\epsilon$ were observed to have attached uncertainties of upwards of 50 %. Nonetheless, the calculated uncertainties were directly taken from the standard deviation of the average of the pixels contained in the analysed area. Poor camera resolution (1.3 MP) and signal-to-noise degradation (paint effects) have contributed negatively to the outputted uncertainties. Repeat measurements would be a more appropriate way to perform error analysis as well conducting future work to improve the signal-to-noise ratio. For example Hubner [10] performed repeat measurements and extracted a

repeatability of 4 %.

10.6 A dual photoelastic and mechanoluminescent coating

The ability to conduct two techniques simultaneously would provide users with additional information thus producing a more insightful strain measurement technique. **It was shown for the first time that a novel dual photoelastic and mechanoluminescent coating and optical arrangement can be used to visualise and capture signals from both techniques simultaneously.** This is a novel concept that currently provides information that qualitatively validates the photoelastic response. However, mechanoluminescence (ML) in elastic conditions featured many challenges that limits its applications and provides concerns with its use and capability to add insight to RPSA.

The major limitation was the sensitivity of the ML signal. Sensitivity is dictated by several factors such as thickness, particle size, strain rate and detection methods. All have been discussed in detail in section 9.6. **In summary, this research focused on coatings between 40 — 150 μm that have not been explored previously in elastico-ML applications.** A number of articles utilise ML coatings with thickness close to 1 mm [74, 79] with some success, attempts to quantify strain however not without difficulties. Azad *et al* [79] managed to quantify effective strain from ML and compare to FEA models. However, many errors were highlighted that had similar outcomes within this research. Examples of similar observations contributing inaccuracies include: ambient light conditions and camera noise; concentration and dispersions of ML materials differing between samples; thickness changes altering ML concentrations (however the thickness dependency on ML signal is not directly mentioned); disconnects between sample and ML materials. Additionally, this research confirmed further inaccuracy contributors, as the ML intensity was thickness dependent as discussed recently by Chen *et al* [87]. Normalisation was required in order to compare between samples. Finally particle size has been shown to have an effect on the resultant intensity of emitted ML [145, 146]. Analysis in this research further demonstrated this by investigating ML capture using two different materials of differing particle size distributions. All these factors combined provide challenging experimental conditions that are hard to control and not applicable in the majority of industrial applications. The addition of an ML material also reduced the photoelastic sensitivity with values of K calculated to be between 0.0216 — 0.0351 dependent on the material it was applied to. Furthermore the uncertainty associated with these K values was greater than 10 %, this translates

to a major degradation of the PE coating's signal-to-noise ratio.

Ultimately the dual technique coating in this current form is not an improvement to current photoelastic methods. The difficulties of capture, the inconsistency in quantifiable data, and the reduction in photoelastic sensitivity do not justify the additional information gathered. Also, if considering applications within Airbus and similar industries then large scale assemblies do not provide the correct conditions in order to extract ML light.

Chapter 11

Conclusions

11.1 Photoelastic coatings

A UV curable formulation with rapid curing performance was created and used for the first time as a reflection photoelastic coating that significantly improved data collection efficiency and the ease of application. The development of this coating utilised the GFP1600 grey-field polariscope and made use of post-processing facilities within the acquisition and processing software that were fundamental to its success. This coating can be applied in a wide range of applications in both research and industry and it has been demonstrated to be **applied, data collected and processed then removed in a single day**. This is an order of magnitude faster than other commercially available products

Coating optimisation finalised on a coating design that enabled maximum cure conversion to be achieved in 20 s with measurable changes of birefringence at a targetted thickness of 50 μm. Such fast application gives rise to a new category of photoelastic coatings, for rapid application, whilst the thickness is up to **five times thinner than current commonly used materials** [8, 10–12]. The sensitivity of the coating is **comparable to existing materials** with values of strain-optic coefficient (K) ranging from 0.069 — 0.0982 and represents a medium-high sensitivity photoelastic coating. The variance of K was dependent on the addition of a coloured tint for thickness measurements and changes due to material type differences. Comparisons between clear coatings and tinted coatings are demonstrated in figure 11.1a and b respectively where the confidence in the accuracy is illustrated.

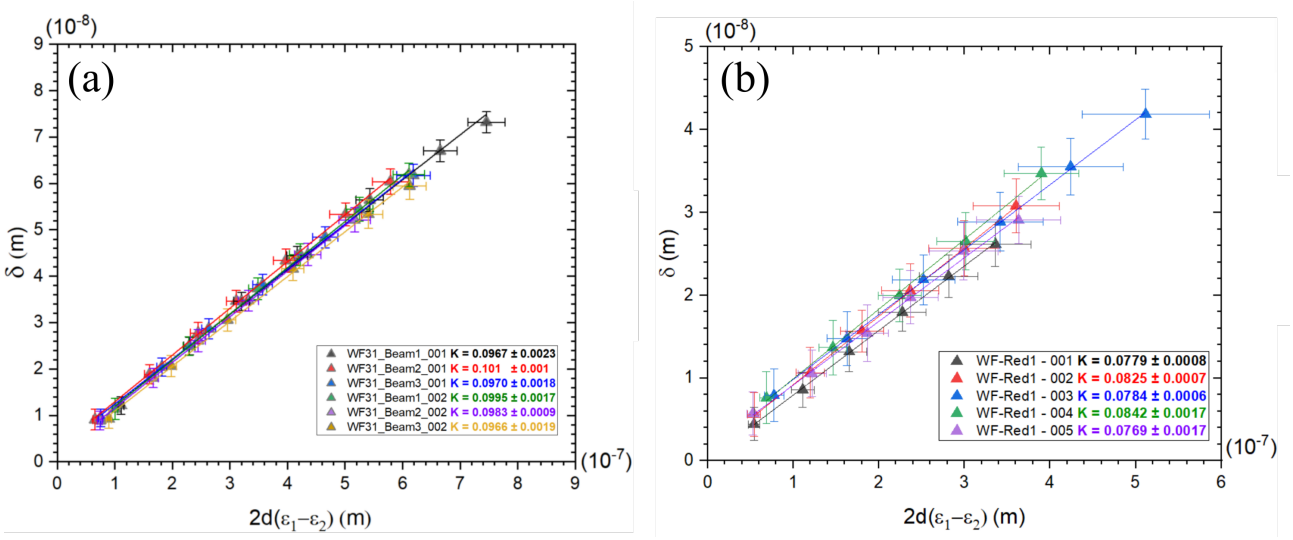


Figure 11.1: Comparisons between the determination of strain-optic coefficient (K) of WF31, ***(a)****, and WF-Red1,* ***(b)****, from experiments. The calculated values of K for each dataset are highlighted in the legend*

A procedure to use these materials has been outlined in this research with various important considerations required for successful use. This research outlined that UV curable materials can exhibit changes to the photoelastic response dependent on the cure conversion, figure 11.2. A user must achieve consistency to prevent introducing inaccuracies. Real time monitoring of cure conversion enabled the research to determine that a **20 s minimum cure time was required in order to achieve maximum cure conversion**.

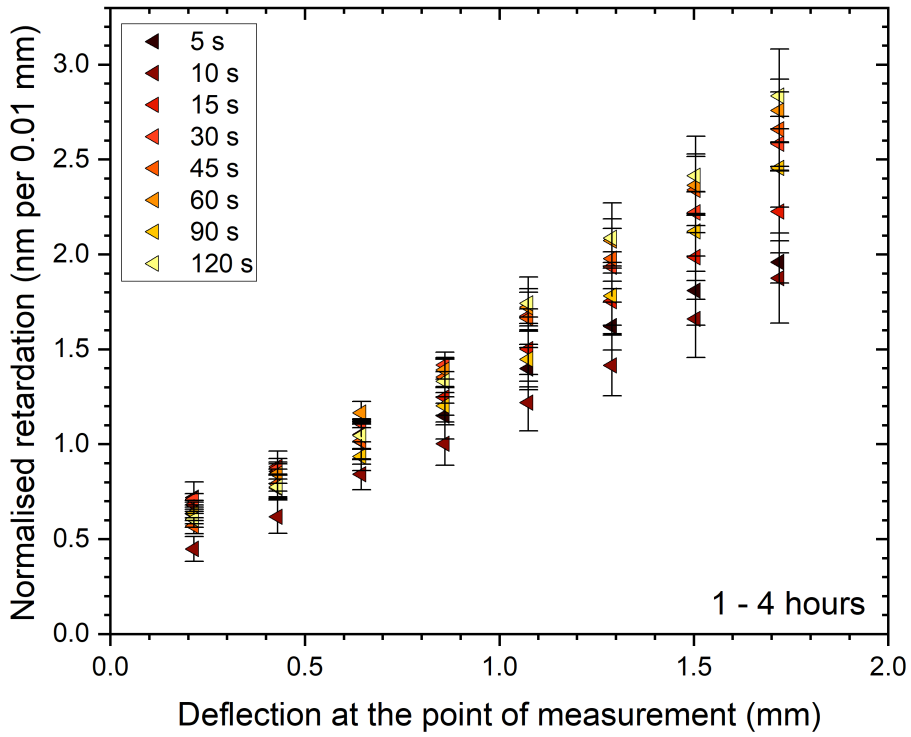


Figure 11.2: The captured difference in photoelastic response as a result of differences in curing time. Measurements were taken on coated beams in cantilever deflections with post processing performed to remove the effects of residual birefringence and light source errors.

It was demonstrated that a user must consider the placement of any light sources and choose an appropriate reflective backing. Signal-to-noise ratio was improved by illuminating in plane surrounding the coated area rather than focusing on one particular angle, figure 11.3.

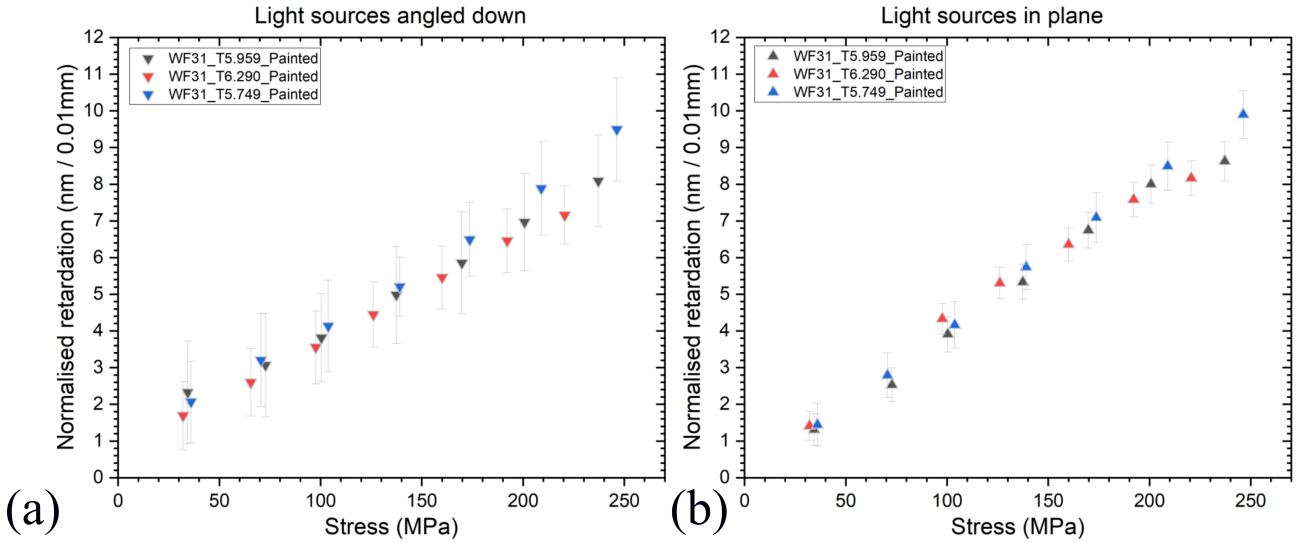


Figure 11.3: Normalised retardation against stress for aluminium beams coated with the UV curable formulation. The aluminium beams were initially coated with a silver paint. The data points represent the average retardation values and the error bars represent the corresponding standard deviations. This data was extracted from an area drawn within the images taken by the GFP1600.

The signal-to-noise ratio was also improved by careful introduction of a reflective backing. Bare metal surfaces suffer from noise that can be controlled by applying a diffusive reflective paint. Surface reflectivity has an effect on the photoelastic sensitivity. Figure 11.4 demonstrates differences in magnitude between sandblasted beams (SB) and when the same beams are coated with a silver paint.

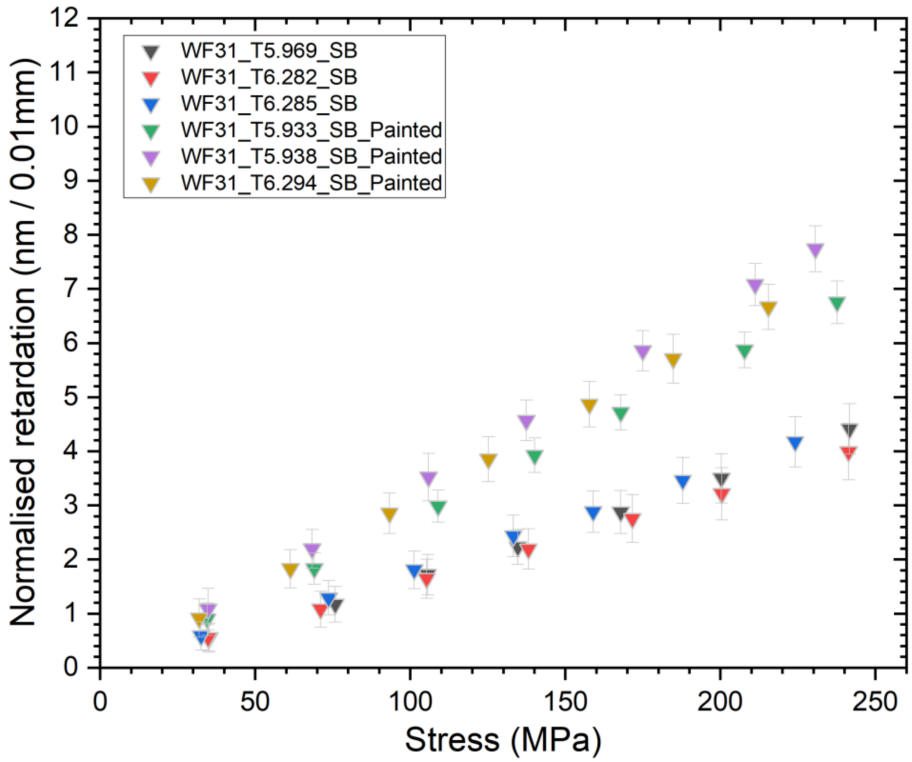


Figure 11.4: The photoelastic response of three aluminium beams that were sandblasted (SB) and then subsequently painted with a silver paint. A measured rise in magnitude was observed when using the silver paint.

It is imperative that reflection photoelasticity is conducted on a reflective surface that minimises specular reflections whilst being sufficiently reflective. The ease-of-use of the coating benefits from automatic thickness correction. Using an inbuilt facility in the GFP software, the addition of a red tint allowed for mapping thickness relationships between the ratios of captured blue and red light. A user can apply the coating in any way without regard of the final thickness removing the complexity of the application of contourable plastic sheets [12]. **Additionally, the coating can be removed easily leaving no evidence on the component**. As a result, novel work on ultra thin coatings has been performed that has not been documented before . The development of this coating satisfies, in many ways, each criterion outlined at the start of this thesis. The potential of this coating is large with applications on a variety of materials in various environments without restrictions that limits its usability. Reflection photoelasticity struggles to maintain relevancy within research and industry however the work conducted, in this thesis provides a new and accessible means of structural health monitoring.

The criteria outlined at the start of the research has been reintroduced with current standard/s and

research fulfilments summarized in table 11.1.

Criterion	Current state-of-the-art	Research fulfilments
Birefringent to enable photoelastic measurements.	strain-optic coefficient K = 0.008 - 0.015	K = 0.069 - 0.983
Luminescent when energised by strain.	Minimal practical research utilising ML in thin (30 – 150 µm) coatings	Novel simultaneous capture of PE and ML data using thin coatings
Ideally sprayable, with a constant or known thickness, for ease of application	Difficult and long applications with minimal thickness corrections for direct application coatings	Evidence demonstrates spray capabilities. Accurate thickness correction allowing for increased ease-of-use. This was performed on thin coatings for the first time.
As thin as practically possible whilst keeping reinforcing effects to a minimum.	Coating thickness = 0.25 – 3.2 mm. Requires wide range of materials dependent on requirements.	Target thickness of 50 µm. Application onto a variety of different surfaces and use case scenarios.
Fast curing	Upwards of 24 hours to cure. Can take weeks to apply and extract data.	20 s to cure. Application, data collection and analysis, removal less than one day.
Easy to remove, leaving no evidence on the final component or structure.	Hammers, chisels and power tools often required.	Easily removable by levering the coating.

Table 11.1: The criteria provided at the start of the research with current state of the art and research fulfilments summarised.

11.2 Mechanoluminescence

Mechanoluminescence is a relatively new technique that has not been established fully as a strain measurement approach. **Its unique characteristics provide a novel concept, such that the production of ML light could be detected alongside photoelasticity to generate increased insight than is possible with photoelasticity alone.** Whilst this concept was experimentally demonstrated, figure 11.5, the challenges and limitations surrounding this method make it difficult to discern its relevance within research and industry.

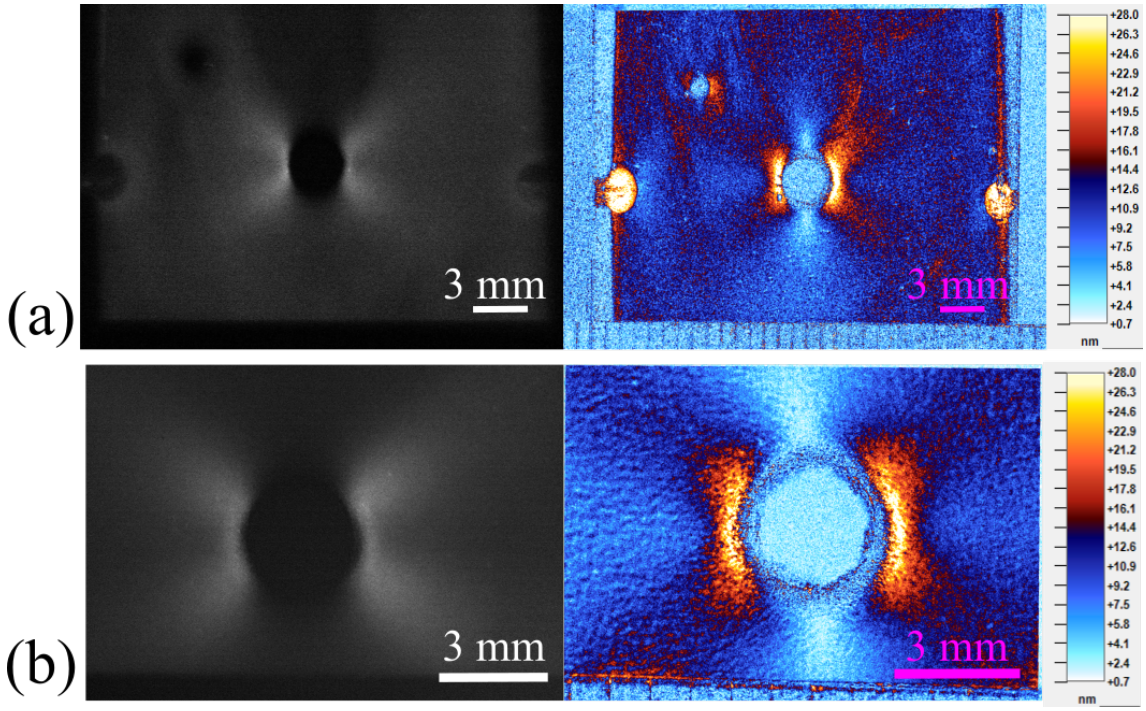


Figure 11.5: Images demonstrating the capture of ML and PE on an aluminium coupon with a stress riser. The coupons were in uniaxial tension with a maximum load of 10 kN applied. The images were taken with a series of lenses to provide different magnifications around the hole.

The combination of ML materials with UV curable materials is a new concept. This provides potential for the ML materials to be applied rapidly in thin coatings. It now has applications of being rapidly applied and cured improving efficiency compared to two-part adhesives. Moreover the thicknesses used, 40 — 150 μm, were still able to generate and produce detectable ML using basic camera setups. The dependence on the coating thickness, particle size distribution and strain rate on the outputted intensity of ML were all investigated supporting surrounding literature. But the inconsistencies in repeat measurements, variable photoluminescence and the single use

aspect provided new information that limits its overall performance. As a result, comparisons with photoelastic measurements could only be performed qualitatively with the final verdict being that similarities exist however detail is lost in both techniques. A lack of light signal increased noise whilst the photoelastic sensitivity was reduced due to a significant decrease in the coating's strain-optic coefficient. These failings are the major limitations that question the usability of this dual technique coating.

However, a novel technique/apparatus has been designed and implemented which allows for the first time PE and ML data to be measured simultaneously. This and the thin UV coating provides a platform on which further research can be performed.

Chapter 12

Future development

The development of rapidly curing photoelastic materials has not been conducted before. Throughout this research the understanding of the coating's strengths and limitations became more apparent, therefore further improvements have been highlighted to reinforce the coating's impact. Additionally, certain investigations that cover the experimental procedure that need to be developed further to provide increased ease-of-use that enables additional confidence in the measured data.

12.1 Coating optimisation and application

The research alighted on WF31 as the basis of all subsequent coatings used in this research, WF-Red1 and WF-SAOE. However, the optimisation of this coating only factored the sensitivity and the shape of the photoelastic response as well as the misdirection in trying to overcome the effects of residual stresses in the coating through optimisation. Post processing subtraction was determined to be a vital facility, in order to correct for light source polarisation misalignment that also corrected for initial residual strains. Optimisation experiments also did not employ best practises in sample preparation, best curing practises and light source placement, these were investigated after the finalisation of the formulation. Furthermore, the desired qualities of the coating were not established completely. Recommendations on how to approach re-optimisation are outlined as follows.

Optimisation requires that desirable properties are outlined with target goals. Design of experiments provides rational design, however it should be performed with knowledge of the technique. Sensitivity is still a parameter of utmost importance that should be measured using procedures outlined in this research. Calculating the K values for each coating on the same sample material will allow

for direct comparisons with values of high confidence as demonstrated in chapter 7. **Sensitivity** was shown to be reduced by the addition of a coloured tint vital for thickness corrections. The appropriate amount of tint was not investigated in depth and should be systematically explored to determine a balance between being able to accurately measure thickness whilst maintaining high sensitivity. Post-processing facilities remove the need to minimise residual birefringence effects and can therefore be ignored in future optimisation. Future optimisation requires consideration of its application. **Surface wetting additives that aim to reduce reticulation effects** would allow for increased ease of use however the effects on the photoelastic response are unknown and would need to be factored in. Most importantly consideration of the techniques used for application should be considered.

An objective of this research was to enable spray coating for fast applications. This was not achieved due to the lack of facilities within the University and the scope of procuring equipment not being possible due to pandemic financial constraints. It has been discussed that spraying resins is possible with the correct apparatus however spraying benefits from materials possessing lower viscosity. The American Coating Association recommends a viscosity of approximately 0.1 Pas [108] which is achievable for WF31 through heating to temperatures close to 60 ^{o}C. Lechler [109] spray technology documented spray capabilities of coatings up to 2 Pas however with issues. It was determined that a target viscosity for a coating should be between 0.1 — 0.5 Pas (100 - 500 cP) in order to enable spray coating. Heating the formulation to a minimum of $\sim$ 32 ^{o}C would satisfy the minimum requirement. Additionally, the introduction of solvent to dilute the formulation is also possible with a 10 % introduction of a solvent causing an 85 % reduction in viscosity. These data show the possibility of spray coating applications however there is potential to introduce further components to the formulation that may have an effect on the photoelastic performance. Additionally, introducing a solvent would affect the storage of the formulation. For future research, a direction for a sprayable coating needs to be determined. Dependent on available apparatus, the preferred method would be to introduce heat to remove any changes in the photoelastic sensitivity. However, if introducing diluents, then a balance between viscosity and photoelasticity will need to be investigated to optimise the coating. Finally, if the coating could be applied as an aerosol the ease of use of the coating would be increased significantly with a user not needing to invest in a specialised spray coating apparatus. However, the additional health and safety risks would need to be reviewed to determine the safe application of a sprayable UV curable resin blend. Dependent on the environment spray application

would be performed in, certain measures (such as implementation of specialist equipment) could in fact reduce the ease of use of the coating.

12.2 Reflective backings

Currently, the majority contributor to the amount of time required to conduct RPSA in this research is the drying time associated with the silver paint. The paint chosen, Hammerite smooth silver, enabled the UV curable formulation to be applied and it withstood the effects of shrinkage that stripped away acrylic paints. This paint was not optimised for this research and as a result future work should work on finding or designing alternatives. The objective for future development of reflective backings should focus on efficiency of application and cure whilst maintaining suitable diffusive properties whilst minimising specular reflections. UV curable materials posses rapid curing capabilities that can be manipulated to produce an efficient reflective backing. The PhotoStress product range use reflective backings and adhesives that have desirable finishes with minimal specular reflections. These backings are made with fine metallic particles [47,55] that can be added to a fast curing UV curable formulation. Additionally, metallic inks could be utilised and combined with these materials to also generate fast curing reflective backings. It is recommended to use low viscosity UV curable materials to allow for easy application such as spray coating or the production of an aerosol. The reflective properties should be measured similar to investigations in chapter 5.2 using PS-1E as a reference material.

12.3 Quantifying environmental effects and setup

Transitioning into industrial applications in chapter 8.2 provided evidence that changes within the environment can have an effect on the measured photoelastic response. Perspex screens, reflective surrounding structures and disturbances in background light were all suspected contributors to unusual changes in the photoelastic response. The uncertainty on the major contributors provides concern that the proposed developed procedure is not established completely. Systematic testing of environment effects should be focused upon in future work focusing on the outlined potential contributors.

The setup of the photoelastic apparatus should also be reviewed. Light sources were positioned to

satisfy the light conditions entering the GFP1600. Close to direct reflection produced too much light with the GFP1600 unable to account for the amount of light being captured. As a result, the lights were placed at wide angles of oblique following advice from photoelasticians at Airbus and in external consultancies. However, it has been documented that wide angles of oblique produce inaccuracies [3]. This research did not monitor the angles of light or document any changes. It is recommended that systematic testing of light source angles should be monitored using reference materials. Additionally, light sources could be manufactured to enable the desired low angle of oblique ($<4^o$) whilst possessing intensity controls. Lighting conditions are a vital issue to overcome in techniques such as Digital Imaging Correlation (DIC). By taking the same approach in RPE any inaccuracies will be reduced. A ring of LED lights are often used to provide high performing lighting conditions whilst enabling a camera to be situated in between. It is not known if light rings have been used for RPE previously.

12.4 Mechanoluminescence

The challenges presented with mechanoluminescent materials and the involvement with photoelasticity question the demand for continued work. In elastic conditions the intensity of ML was minimal whilst reducing the general PE sensivity. However, there is scope for improvement and potential for other applications. A small sample size of two ML material were selected in this research due to difficulties in procuring new materials. There are possibilities of using a variety of materials with larger particle sizes to increase sensitivity. Furthermore, the coating should be optimised to balance ML sensitivity with PE. If considering different applications, a few recommendations are highlighted. Additional imaging techniques such as spectrometers and photomultipliers could be adopted to monitor locations similar to strain gauges. Utilising these devices would enable sensitive detection of any production of ML whilst still being able to perform PE for full field imaging. Analysis can be performed on the same surface that would benefit materials such as composites with differing orientations of lay-ups between surfaces. Additionally, ML was shown to produce intense productions of light during failure and this property could be manipulated further. For example this property could be used for failure detection and included in a potential reflective backing to prevent reduction of a PE coating's sensitivity. As long as the reflective qualities are appropriate, using imaging techniques such as spectrometers could be set up to detect any failures within the coatings and/or

the sample.

Bibliography

[1] E. Hearn. *Mechanics of Materials 2: An introduction to the Mechanics of Elastic and Plastic Deformation of Solids and Structural Materials*, volume 3. Butterworth-Heinemann, 1997.

[2] K. Ramesh. *Photoelasticity*, pages 701–742. Springer US, Boston, MA, 2008.

[3] K. Ramesh. *Digital Photoelasticity: Advanced Techniques and Applications*. Springer Berlin Heidelberg, 2000.

[4] G. Calvert, J. Lesniak, and M. Honlet. Applications of modern automated photoelasticity to industrial problems. *Insight*, 44(4):224–227, 2002.

[5] B. Neethi Simon and K. Ramesh. A Simple Method to Plot Photoelastic Fringes and Phasemaps from Finite Element Results. *Journal of Aerospace Sciences and Technologies*, 62(3), 2010.

[6] M. Geramizadeh, H. Katoozian, R. Amid, and M. Kadkhodazadeh. Comparison of finite element results with photoelastic stress analysis around dental implants with different threads. *Dental and medical problems*, 55(1):17–22, 2018.

[7] Vishay Precision Group: Micro Measurements. PhotoStress Coating Materials and Adhesives. Retrieved from `http://www.vishaypg.com/docs/11222/pscoat.pdf`, 2015.

[8] B. E. Foust, J. R. Lesniak, and R. E. Rowlands. Stress analysis of a pinned wood joint by grey-field photoelasticity. *Composites Part B: Engineering*, 61:291–299, 2014.

[9] J. Hubner, J. Nicolosi, L. Chen, P. Ifju, and W. El-Ratal. Oblique incidence response of photoelastic coatings. *Experimental Techniques*, 29(3):52–56, 2005.

[10] J. P. Hubner, P. G. Ifju, K. S. Schanze, Y. Liu, L. Chen, and W. El-Ratal. Luminescent photoelastic coatings. *Experimental Mechanics*, 44(4):416–424, 2004.

[11] Vishay Precision Group: Micro Measurements. Instructions for Casting and Contouring PhotoStress Sheets: Application note B-221. Retrieved from `http://www.vishaypg.com/docs/11221/ib-221.pdf`, 2015.

[12] Vishay Precision Group: Micro Measurements. Instructions for Bonding Flat and Contoured PhotoStress Sheets: Application Note B-223. Retrieved from `http://www.vishaypg.com/docs/11223/ib-223ib.pdf`, 2015.

[13] Airbus. A320ceo. `https://aircraft.airbus.com/en/aircraft/a320-the-most-successful-aircraft-family-ever/a320ceo` Date Accessed 03/04/2023.

[14] J. Lesniak and M. Zickel. Applications of automated grey-field polariscope. In *Proceedings of the 1998 SEM Spring Conference on Experimental Mechanics*, pages 298–301, Houston, Texas, 1998.

[15] H. D. Young, R. A. Freedman, F. W. Sears, and M. W. Zemansky. *Sears and Zemansky's university physics : with modern physics technology update*. Pearson Education, Harlow, Essex, thirteenth edition, 2014.

[16] E. Hecht. *Optics*. Pearson, 5th edition, 2017.

[17] M. Bass, E. W. V. Stryland, D. R. Williams, and W. L. Wolfe. *Handbook of Optics Volume II Devices, Measurements, and Properties*. McGraw-Hill Professional, 2nd edition, 1995.

[18] J. Pavlin, N. Vaupotič, and M. Čepič. Direction dependence of the extraordinary refraction index in uniaxial nematic liquid crystals. *Eur. J. Phys.*, 34(2):331–344, jan 2013.

[19] E. Wolf and M. Born. *Principle of Optics*. Pergamon Press, 5th edition, 1975.

[20] A. Praveen, Z. Weijun, and R. Raghunath. Photoelastic birefringence of copolymers with non-planar structure. *Polymer (Guildf).*, 164:217–222, 2019.

[21] D. Harrington and S. Sueoka. Polarization modeling and predictions for DKIST part 3: focal ratio and thermal dependencies of spectral polarization fringes and optic retardance. *J. Astron. Telesc. Instruments, Syst.*, 4(1), 2018.

[22] F. El-Diasty, M. A. Soliman, A. F. T. Elgendy, and A. Ashour. Birefringence dispersion in uniaxial material irradiated by gamma rays: cellulose triacetate films. *J. Opt. A Pure Appl. Opt.*, 9(3):247–252, feb 2007.

[23] G. Cloud. Optical methods in experimental mechanics - Part 29: Photoelasticity I - Birefringence and relative retardation. *Exp. Tech.*, 31(6):27–29, 2007.

[24] P. Theocaris and E. Gdoutos. *Two-Dimensional Photoelasticity*, page 113. Springer Berlin Heidelberg, Berlin, Heidelberg, 1979.

[25] G. H. Ryder. *Strength of materials*. The Macmillan Press Ltd, 3rd edition, 1969.

[26] T. H. G. Megson. *Structural and stress analysis*. Elsevier Butterworth-Heinemann, 2nd edition, 2005.

[27] G. Cloud. Optical Methods in Experimental Mechanics - Part 30: Photoelasticity II - Birefringence in Materials. *Exp. Tech.*, 32(1):13–16, 2008.

[28] Tadashi Inoue. Strain-Induced Birefringence of Amorphous Polymers and Molecular Design of Optical Polymers. *ACS Applied Polymer Materials*, 3(5):2264–2273, 2021.

[29] T. Freegarde. *Introduction to the Physics of Waves*. Cambridge University Press, 2012.

[30] P. Hariharan. *Basics of interferometry*. Elsevier Academic Press, 2nd edition, 2006.

[31] K. Ramesh. Photoelasticity. In *Springer Handbook Experimental Solid Mechanics*, pages 701 – 742. Springer, 2008.

[32] M. Ramji and K. Ramesh. Whole field evaluation of stress components in digital photoelasticity - Issues, implementation and application. *Opt. Lasers Eng.*, 46(3):257–271, 2008.

[33] E. A. Patterson. Digital Photoelasticity: Principles, Practice and Potential. *Strain*, 38(1):27–39, 2002.

[34] K. Ramesh and S. Sasikumar. Digital photoelasticity: Recent developments and diverse applications. *Optics and Lasers in Engineering*, 135, 2020.

[35] F. W. Hecker and B. Morche. Computer-Aided Measurement of Relative Retardations in Plane Photoelasticity. In H Wieringa, editor, *Exp. Stress Anal.*, pages 535–542, Dordrecht, 1986. Springer Netherlands.

[36] E. A. Patterson and Z. F. Wang. Towards full field automated photoelastic analysis of complex components. *Strain*, 27(2):49–53, 1991.

[37] A. Asundi, L. Tong, and C. Boay. Phase-shifting method with a normal polariscope. *Appl. Opt.*, 38(28):5931–5935, oct 1999.

[38] Z. F. Wang and E. A. Patterson. Use of phase-stepping with demodulation and fuzzy sets for birefringence measurement. *Opt. Lasers Eng.*, 22(2):91–104, 1995.

[39] W. Ji and E. Patterson. Simulation of errors in automated photoelasticity. *Exp. Mech.*, 38(2):132–139, 1998.

[40] M. Ramji and K. Ramesh. Stress separation in digital photoelasticity part a-photoelastic data unwrapping and smoothing. *Journal of Aerospace Sciences and Technologies*, pages 5–15, 2008.

[41] G. M. Brown and J. L. Sullivan. The computer-aided holophotoelastic method. *Experimental Mechanics*, 30(2):135–144, 1990.

[42] A. Ajovalasit, S. Barone, and G. Petrucci. A method for reducing the influence of quarter-wave plate errors in phase stepping photoelasticity. *J. Strain Anal. Eng. Des.*, 33(3):207–216, 1998.

[43] G. Cloud. Optical Methods in Experimental Mechanics Part 38: Photoelasticity X—Transfer of Stress Data From Model to Prototype. *Exp. Tech.*, 33(5), 2008.

[44] K. Ramesh. Basics of photoelasticity and photoplasticity. In *Developments in Photoelasticity*, 2053-2563, pages 1–41. IOP Publishing, 2021.

[45] Vishay Precision Group: Micro Measurements. Corrections to Photoelastic Coating Fringe-Order Measurements: Technical Note TN-706-1. Retrieved from `https://docs.micro-measurements.com/?id=2536`, 2015.

[46] E. A. Patterson and Z. F. Wang. Simultaneous observation of phase-stepped images for automated photoelasticity. *J. Strain Anal. Eng. Des.*, 33(1):1–15, 1998.

[47] J. Lesniak, S. J. Zhang, and E. A. Patterson. Design and evaluation of the poleidoscope: A novel digital polariscope. *Exp. Mech.*, 44(2):128–135, 2004.

[48] J. W. Hobbs, R. J. Greene, and E. A. Patterson. A novel instrument for transient photoelasticity. *Experimental Mechanics*, 43(4):403–409, 2003.

[49] J. Lesniak, M. Zickel, and C. W. D. Johnson. An Innovative Polariscope for Photoelastic Stress Analysis. In *Proc. 1997 SEM Spring Conf. Exp. Mech.*, pages 219 – 224, 1997.

[50] Stress Photonics Inc. GFP1400 Operator's Manual, 2014.

[51] M. Mesnager. Sur la Determination Optique des Tensions Interieures dans les Solides a Trois Dimensions (French) [On the Optical Determination of Interior Tensions in Three Dimensional Solids]. *Comptes Rendus*, (190):1249, 1930.

[52] Engineering ToolBox. Young's Modulus - Tensile and Yield Strength for common Materials. https://www.engineeringtoolbox.com/young-modulus-d_417.html Date Accessed 30/12/2019, 2003.

[53] F. Zandman, S. Redner, and J. W. Dally. *Photoelastic coatings*. Society for Experimental Stress Analysis. SESA monograph ; no. 3. Iowa State University Press, Ames, 1977.

[54] S. Paipetis. *Photoelasticity in engineering practice - Conventional Three-Dimensional Photoelasticity: A Review of Principles and Materials*. Elsevier Applied Science, London, 1985.

[55] G. Cloud. Optical Methods in Experimental Mechanics - Part 42: Photoelasticity XIV - Reflection Photoelasticity. *Experimental Techniques*, 34(4):15 – 19, 2010.

[56] ITW Performance Polymers. Devcon 2 Ton®Epoxy Technical Data Sheet. Retrieved from `https://itwperformancepolymers.com/wp-content/uploads/umb/1008/2-ton-epoxy_041318.pdf`, 2018.

[57] D. Lam and M. W. Ellens. Method for detecting stress and strain. Retrieved from `https://patents.google.com/patent/US6650405B2/en`, 2001.

[58] F. Zandman. Stress Analysis of a Guided Missile Tail Section with the Photoelastic Technique. In *SESA*, volume 17, pages 135 – 150, 1960.

[59] B. Kenny and J. W. Hugill. Comparison of Fringe Multiplication and Tardy Compensation Methods for a Frozen Stress Investigation. *Strain*, 3(1):3–7, 1967.

[60] G. H. Staab and T. G. Richard. An experimental investigation of cog-root strains in V-belts using birefringent coatings. *Exp. Mech.*, 22(12):476–480, dec 1982.

[61] B. E. Foust, J. R. Lesniak, and R. E. Rowlands. Determining Individual Stresses Throughout a Pinned Aluminum Joint by Reflective Photoelasticity. *Experimental Mechanics*, 51(9):1441–1452, 2011.

[62] J. Hubner, L. Chen, Y. Liu, K. Schanze, P. Ifju, J. Nicolosi, and W. El-Ratal. Characterization of a new luminescent photoelastic coating. *Experimental Mechanics*, 45(2):137–143, 2005.

[63] J. Hubner, S. Jiang, Y. Liu, K. Schanze, P. Ifju, D. A. Jenkins, and W. El-Ratal. Method and apparatus for measuring strain using a luminescent photoelastic coating . Retrieved from `https://patents.google.com/patent/US20040066503A1/en`, 2004.

[64] F. Bacon. *Of the advancement of learning*. J. M. Dent & sons, 1915.

[65] B. P. Chandra. Mechanoluminescence. In D. R. Vij, editor, *Luminescence of Solids*, pages 361–389. Springer US, Boston, MA, 1998.

[66] N. C. Eddingsaas and K. S. Suslick. Light from sonication of crystal slurries. *Nature*, 444(7116):163, 2006.

[67] A. Feng, S. Michels, A. Lamberti, and P. F. Smet. Mechanoluminescent Materials: A New Way to Analyze Stress by Light. *Proceedings*, 2(8):492, 2018.

[68] D. O. Olawale, T. Dickens, W. G. Sullivan, O. I. Okoli, J. O. Sobanjo, and B. Wang. Progress in triboluminescence-based smart optical sensor system. *J. Lumin.*, 131(7):1407 – 1418, 2011.

[69] B. P. Chandra, R. N. Baghel, and V. K. Chandra. Mechanoluminescence glow curve of ZnS:Mn. *Chalcogenide Lett.*, 7(1):1–9, 2010.

[70] B P Chandra, V K Chandra, and Piyush Jha. Microscopic theory of elastico-mechanoluminescent smart materials. *Appl. Phys. Lett.*, 104(3), 2014.

[71] C. Li, C. Xu, L. Zhang, H. Yamada, and Y. Imai. Dynamic visualization of stress distribution on metal by mechanoluminescence images. *J. Vis.*, 11(4):329–335, 2008.

[72] V K Chandra and B P Chandra. Dynamics of the mechanoluminescence induced by elastic deformation of persistent luminescent crystals. *Journal of Luminescence*, 132(3):858–869, 2012.

[73] H. Zhang, H. Yamada, N. Terasaki, and C. Xu. Ultraviolet mechanoluminescence from $SrAl_2O_4$:Ce and $SrAl_2O_4$:Ce,Ho. *Applied Physics Letters*, 91(8), aug 2007.

[74] W. Wang, T. Matsubara, Y. Takao, Y. Imai, and C. Xu. Visualization of Stress Distribution Using Smart Mechanoluminescence Sensor. *Mater. Sci. Forum*, 614:169–174, 2009.

[75] S. Timilsina, K. H. Lee, I. Y. Jang, and J. S. Kim. Mechanoluminescent determination of the mode I stress intensity factor in SrAl2O4:Eu2+,Dy3+. *Acta Materialia*, 61(19):7197–7206, 2013.

[76] G. J. Yun, M. R. Rahimi, A. H. Gandomi, G. Lim, and J. Choi. Stress sensing performance using mechanoluminescence of $SrAl_2O_4$:Eu (SAOE) and $SrAl_2O_4$:Eu, Dy (SAOED) under mechanical loadings. *Smart Materials and Structures*, 22(5):055006, 2013.

[77] V. K. Chandra and B. P. Chandra. Suitable materials for elastico mechanoluminescence-based stress sensors. *Optical Materials*, 34(1):194–200, 2011.

[78] A.F. Banishev and A.A. Banishev. Deformation Stimulated Luminescence of a Composite Produced on the Basis of Polymethylmethacrylate Transparent in the Visible Region and Finely Dispersed Powder of $SrAl_2O_4$:(Eu^{2+}, Dy^{3+}) Phosphor. *Inorg. Mater. Appl. Res.*, 10:647 – 651, 2019.

[79] A. I. Azad, M. R. Rahimi, and G. J. Yun. Quantitative full-field strain measurements by SAOED (SrAl2O4:Eu2+,Dy3+) mechanoluminescent materials. *Smart Materials and Structures*, 25(9):95032, 2016.

[80] K. Kanamaru and H. Utsunomiya. In-situ observation of nonuniform deformation during tensile test of aluminum alloy sheet by means of screen-printed mechanoluminescence film. *Scripta Materialia*, 209:114388, 2022.

[81] C. N. Xu, T. Watanabe, M. Akiyama, and X. G. Zheng. Preparation and characteristics of highly triboluminescent ZnS film. *Mater. Res. Bull.*, 34(10):1491–1500, 1999.

[82] C. N. Xu, T. Watanabe, M. Akiyama, and X. G. Zheng. Artificial skin to sense mechanical stress by visible light emission. *Appl. Phys. Lett.*, 74(9):1236–1238, 1999.

[83] D. Olawale, O. Okoli, R. Fontenot, and W. Hollerman. *Triboluminescence: Theory, synthesis, and application*. Springer International Publishing, 2016.

[84] A. Feng and P. F. Smet. A Review of Mechanoluminescence in Inorganic Solids: Compounds, Mechanisms, Models and Applications. *Materials (Basel, Switzerland)*, 11(4), mar 2018.

[85] P. Jongchansitto, D. Boyer, I. Preechawuttipong, and X. Balandraud. Using Mechanoluminescent Materials to Visualize Interparticle Contact Intensity in Granular Media. *Experimental Mechanics*, 60(1):51–64, 2020.

[86] N. Terasaki, Y. Fujio, S. Horiuchi, H. Akiyama, and M. Itabashi. Mechanoluminescent study for optimization of joint design on cross tension test. *The Journal of Adhesion*, 98(6):637–646, 2022.

[87] B. Chen, D. Peng, P. Lu, Z. Sheng, K. Yan, and Y. Fu. Modeling and validation of mechanoluminescent strain sensing mechanism at quasi-static loading rates. *Materials & Design*, 226:111588, 2023.

[88] Arkema. UviCure S105. Technical Data Sheet. Retrieved from `https://emea.sartomer.arkema.com/en/product-finders/product/f/sartomer_LambsonCationics/p/uvicure-s105/`, 2019.

[89] M. Boyle, C. Martin, and J. Neuner. Epoxy Resins. In *Composites*, volume 21. ASM International, 2001.

[90] K. B. Tator. Epoxy Resins and Curatives. In *Protective Organic Coatings*, volume 5B. ASM International, 2015.

[91] J. Crivello. Investigations of the reactivity of "kick-started" oxetanes in photoinitiated cationic polymerization. *J. Polym. Sci. Part A Polym. Chem.*, 53(4):586–593, 2015.

[92] Arkema. UviCure S140. Technical Data Sheet. Retrieved from `https://emea.sartomer.arkema.com/en/product-finders/product/f/sartomer_LambsonCationics/p/uvicure-s140/`, 2019.

[93] J. Crivello. The discovery and development of onium salt cationic photoinitiators. *J. Polym. Sci. Part A Polym. Chem.*, 37(23):4241 – 4254, 1999.

[94] Arkema. SpeedCure 992. Technical Data Sheet. Retrieved from `https://emea.sartomer.arkema.com/en/product-finders/product/f/sartomer_Lambson/p/speedcure-992/`, 2019.

[95] Y. Yagci, S. Jockusch, and N. J. Turro. Photoinitiated Polymerization: Advances, Challenges, and Opportunities. *Macromolecules*, 43(15):6245–6260, 2010.

[96] M. Sangermano, I. Roppolo, and A. Chiappone. New Horizons in Cationic Photopolymerization. *Polymers (Basel).*, 10(2):136, jan 2018.

[97] Arkema. UviCure S128. Technical Data Sheet. Retrieved from `https://americas.sartomer.arkema.com/en/product-finders/product/f/sartomer_LambsonCationics/p/uvicure-s128/`, 2019.

[98] Arkema. UviCure S160. Technical Data Sheet. Retrieved from https://americas.sartomer.arkema.com/en/product-finders/product/f/sartomer_LambsonCationics/p/uvicure-s160/, 2019.

[99] Arkema. UviCure S150. Technical Data Sheet. Retrieved from https://emea.sartomer.arkema.com/en/product-finders/product/f/sartomer_LambsonCationics/p/uvicure-s150/, 2019.

[100] Arkema. UviCure S130. Technical Data Sheet. Retrieved from https://emea.sartomer.arkema.com/en/product-finders/product/f/sartomer_LambsonCationics/p/uvicure-s130/, 2019.

[101] Arkema. SpeedCure 976. Technical Data Sheet. Retrieved from https://emea.sartomer.arkema.com/en/product-finders/product/f/sartomer_Lambson/p/speedcure-976/, 2019.

[102] Arkema. UviCure and SpeedCure. https://emea.sartomer.arkema.com/en/ Accessed 05/04/2023.

[103] Q-Lab Corporation. Specification Bulletin LP-0862-A: Q-panel - Steel and Iron Phosphated Panels, 2018.

[104] RK PrintCoat Instruments Ltd. K Hand Coater. Retrieved from https://www.rkprint.com/wp-content/uploads/2018/02/New-K-HAND-COATER.pdf, Accessed 20/06/2023.

[105] Dymax. UVC - 5 Manual and Technical Data. Retrieved from https://dymax.com/images/pdf/manuals/man088eu_uvc-5_conveyor_user_guide.pdf, 2015.

[106] Jenton Group. Flexible Solutions for Modular UV Curing. Retrieved from http://www.jentonconverting.co.uk/index_html_files/Jenton_UV_Brochure_31012011.pdf, (n.d).

[107] D. Lam and M. W. Ellens. Photoelastic coating for structural monitoring. Retrieved from https://patents.google.com/patent/US8432537B2/en, 2013.

[108] American coatings association. Optimum Viscosity for Paint Application. Retrieved from https://www.paint.org/coatingstech-magazine/articles/optimum-viscosity-paint-application/#:~:text=There%20is%20a%20rule%20of,%2C%20brushing%2C%20or%20roll%20coating., Accessed 17/04/2023.

[109] Lechler GmbH. Atomization methods. Retrieved from https://www.lechler.com/de-en/technology/basics-nozzle-technology/atomization-methods., Accessed 17/04/2023.

[110] C Yuangyai and H B Nembhard. Design of Experiments: A Key to Innovation in Nanotechnology. In *Emerging Nanotechnologies for Manufacturing*, Micro and Nano Technologies, pages 207–234. William Andrew Publishing, Boston, 2010.

[111] R. Kent. Design quality management. In *Quality Management in Plastics Processing*, pages 227–262. Elsevier, 2016.

[112] Minitab. Design of experiment statisical software. Retrieved from https://www.minitab.com/en-us/, Accessed on 10/02/2020.

[113] Vishay Precision Group: Micro Measurements. Calibration of Photostress Coatings: Tech Note TN-701-1. Retrieved from http://www.vishaypg.com/docs/11211/11211_te.pdf, 2011.

[114] SPOTS Project. Good Practice Guide to Reflection Photoelasticity. *Calibration and Assessment of Optical Strain Measurements*, 2005.

[115] Omega. 3 element 0/45/90 planar, compact rosette strain gauges. Retrieved from https://www.omega.com/en-us/force-strain-measurement/strain-gauges/rosette-strain-gauges/p/SGD-3-ELEMENT45.

[116] National Instruments. NI-9235 C Series Strain/Bridge Input Module. Retrieved from https://www.ni.com/en-gb/support/model.ni-9235.html.

[117] RK PrintCoat Instruments Ltd. K Control Coater. Retrieved from https://www.rkprint.com/products/k-control-coater/.

[118] R. Schaefer. Mechanical Properties of Rubber. In *Harris' Shock and Vibration Handbook*, chapter 33. 2002.

[119] A. N. Gent and R. P. Campion. *Engineering with Rubber: How to Design Rubber Components*. Engineering with Rubber: How to Design Rubber Components. Hanser, 2001.

[120] X. Fernández-Francos, S. Kazarian, X. Ramis, and A. Serra. Simultaneous Monitoring of Curing Shrinkage and Degree of Cure of Thermosets by Attenuated Total Reflection Fourier Transform Infrared (ATR FT-IR) Spectroscopy. *Applied spectroscopy*, 67:1427–1436, 2013.

[121] Arkema. Arkema's Photoinitiator Centre of Excellence. https://sartomer.arkema.com/en/innovations/collaborative-partnerships/photoinitiator-center-of-excellence/ Accessed 18/05/2023.

[122] ThermoFisher Scientific. Nicolet™ iS50 FTIR Spectrometer. Retrieved from https://www.thermofisher.com/order/catalog/product/912A0760, Accessed 22/10/2021.

[123] Specac. Golden Gate Diamond ATR Datasheet. Retrieved from https://www.specac.com/en/documents/data-sheets/golden-gate-datasheet, Accessed 22/10/2021.

[124] Excelitas. OmniCure S2000 Spot UV Curing System.

[125] Lambson. SpeedCure 976. Retrieved from https://www.lambson.com/_documents/tds/speedcure_976.pdf, 2020.

[126] W. Ji. Error analysis and system improvements in phase-stepping methods for photoelasticity. 1998.

[127] Hammerite - AkzoNobel. Direct to Rust Metal Paint Aerosol Smooth Finish. Retrieved from https://www.hammerite.co.uk/product/direct-to-rust-metal-paint-aerosol-smooth-finish/, Accessed 30/05/2023.

[128] Matweb. Aluminium 6082-T6 datasheet. Retrieved from http://www.matweb.com/search/datasheet_print.aspx?matguid=fad29be6e64d4e95a241690f1f6e1eb7.

[129] Ocean Insight. High resolution spectrometers. Retrieved from https://www.oceaninsight.com/products/spectrometers/high-resolution/, Accessed 31/05/2023.

[130] Resin8. Transparent Red Tint. https://www.resin8.co.uk/collections/transparent-tint/products/transparent-tint-red?variant=41105454071988, Accessed on 09/16/2022.

[131] Gary Cloud. *Photoelasticity methods and applications*, pages 101–144. Cambridge University Press, 1995.

[132] Vishay Precision Group: Micro Measurements. General purpose strain gages - Rectangular Rosette. Retrieved from http://www.vishaypg.com/docs/11077/060wr.pdf, 2015.

[133] Micro-measurementsl. P3 Strain Indicator and Recorder. Retrieved from https://micro-measurements.com/pca/detail/p3-strain-indicator-and-recorder, Accessed 13/06/2023.

[134] Vishay Precision Group: Micro Measurements. Two-element 90 deg tee rosette for general-purpose use. Retrieved from https://micro-measurements.com/pca/detail/125uta, Accessed 30/06/2023.

[135] Jochum Beetsma. Coating film defects. Retrieved from https://www.ulprospector.com/knowledge/451/pc-coating-film-defects/, Accessed 20/06/2023.

[136] R. J. Greene and E. A. Patterson. An Integrated Approach to the Separation of Principal Surface Stresses Using Combined Thermo-Photo-Elasticity. *Experimental Mechanics*, 46(1):19–29, 2006.

[137] Edmund Optics. BARIUM AND STRONTIUM PRODUCTS. Retrieved from https://www.sakai-chem.co.jp/en/products_services_barium_strontium.php, Accessed 30/06/2023.

[138] N. Terasaki, C. Xu, Y. Imai, and H. Yamada. Photocell System Driven by Mechanoluminescence. *Japanese Journal of Applied Physics*, 46(4B):2385–2388, apr 2007.

[139] H. Zhang, N. Terasaki, H. Yamada, and C. Xu. Mechanoluminescence of europium-doped $SrAMgSi_2O_7$ (A = Ca, Sr, Ba). *Jpn. J. Appl. Phys.*, 48(4 PART 2):04C109–1 – 04C109–4, apr 2009.

[140] Y. Jia, M. Yei, and W. Jia. Stress-induced mechanoluminescence in SrAl2O4:Eu2+,Dy3+. *Opt. Mater. (Amst).*, 28(8):974–979, 2006.

[141] Inc Thorlabs. CS505MU CMOS Camera. Retrieved from https://www.thorlabs.com/thorproduct.cfm?partnumber=CS505MU, Accessed on 11/10/2022.

[142] ImageJ. Register virtual stack slices - Image Jplugin. Retrieved from https://imagej.net/plugins/register-virtual-stack-slices, Accessed on 11/10/2022.

[143] Nemoto & co., Ltd. Phosphorescent pigments. Retrieved from https://www.nemoto.co.jp/en/luminouspigment/, Accessed 23/06/2023.

[144] I. Arganda-Carreras, C. O. S. Sorzano, R Marabini, J. M. Carazo, C. Ortiz-de Solorzano, and J. Kybic. Consistent and Elastic Registration of Histological Sections Using Vector-Spline Regularization. In Reinhard R Beichel and Milan Sonka, editors, *Computer Vision Approaches to Medical Image Analysis*, pages 85–95, Berlin, Heidelberg, 2006. Springer Berlin Heidelberg.

[145] W. Wang, W. Widiyastuti, T. Ogi, I. W. Lenggoro, and K. Okuyama. Correlations between Crystallite/Particle Size and Photoluminescence Properties of Submicrometer Phosphors. *Chemistry of Materials*, 19(7):1723–1730, 2007.

[146] Y. Kim and S. Kang. Effect of particle size on photoluminescence emission intensity in ZnO. *Acta Materialia*, 59(8):3024–3031, 2011.

[147] JEOL Ltd. Phosphorescent pigments. Retrieved from `https://www.jeol.com/products/scientific/sem/JSM-6010LA.php`, Accessed 26/06/2023.

[148] Thorlabs, Inc. Hard-Coated Edgepass Filters. Retrieved from `https://www.thorlabs.com/newgrouppage9.cfm?objectgroup_id=6082&pn=FESH0600`, Accessed 26/06/2023.

[149] Edmund Optics. SCHOTT RG-630, 50mm Dia., 3mm Thick, Colored Glass Longpass Filter. Retrieved from `https://www.edmundoptics.co.uk/p/rg-630-50mm-dia-longpass-filter/20628/`, Accessed 26/06/2023.

[150] Stress Photonics Inc. `https://glassphotonics.com/all-products/grey-field-polariscopes/`, Accessed on 08/04/2020.

[151] AMETEK Brookfield. Dial Reading Viscometer. Retrieved from `https://www.brookfieldengineering.com/products/viscometers/laboratory-viscometers/dial-reading-viscometer`, Accessed 17/04/2023.

[152] C. Kallendorf, D. Cyterski, A. Spinks, and D. Dreifus. D3359 - 87: Measuring Adhesion by Tape Test. In *Radiation Curing Test Methods*, pages 339 – 343. RadTech International, Cincinnati, 1988.

[153] Tinius Olsen. Model 5ST: Electromechanical Testing Machine. Retrieved from `https://www.tiniusolsen.com/product/model-5st/`, Accessed on 18/04/2023.

[154] TA Instruments. DSC 25. `https://www.tainstruments.com/dsc-25/`, Accessed on 06/01/2019.

[155] P. Gill, T. T. Moghadam, and B. Ranjbar. Differential scanning calorimetry techniques: applications in biology and nanoscience. *Journal of biomolecular techniques : JBT*, 21(4):167–193, 2010.

[156] ThermoFisher Scientific. Nicolet™ iS™ 10 FTIR Spectrometer. Retrieved from `https://www.thermofisher.com/order/catalog/product/IQLAADGAAGFAHDMAPC`, Accessed 22/10/2021.

[157] ASTM International. D523 - 14 Standard Test Method For Specular Gloss, 2018.

Appendix A

Coating development

This appendix outlines the methodology, results and analysis for various properties in the formulation screening, section 3.2. The properties described in this appendix includes viscosity, solvent resistance, adhesion, flexibility and glass transition temperature. Whilst these properties are of importance they do not directly influence the optimisation of the formulation with photoelasticity being the major influence.

A.1 Viscosity

A.1.1 Methodology

Viscosity testing made use of a Brookfield LVT Dial Reading Viscometer using the 31 labelled low viscosity spindle [151]. The spindle was submerged in 9 mL of the liquid formulation that was inserted into an aluminium cylinder placed into a holder that was temperature controlled via a water loop. After the formulation adjusted to the set temperature, 25 ^{o}C, the test began. The spindle rotated within the formulation, at a set user defined RPM, and the analogue dial on the viscometer outputted a reading. The viscosity was then calculated by multiplying the dial reading with a factor which is dependent on the selected spindle and RPM. An error was calculated from the spread of data collected after five repeat measurements.

A.1.2 Results and analysis

Table A.1 provides numerical viscosity data alongside each formulation design.

Formulation Reference	S105 (%)	S128 (%)	S160 (%)	S150 (%)	S140 (%)	S130 (%)	992 (%)	Viscosity (cP)	Group Reference
WF1			98				2	2075	**a**
WF2				98			2	162.5	
WF3		98		98			2	612.5	
WF4	98						2	212.5	
WF5	88					10	2	137.5	**b**
WF6	68					30	2	68.75	
WF7	48					50	2	43.75	
WF8	88				10		2	137.5	**c**
WF9	68				30		2	62.5	
WF10	48				50		2	37.5	
WF11	88		10				2	262.5	**d**
WF12	68		30				2	400	
WF13	48		50				2	637.5	
WF14	28		70				2	1025	
WF15	8		90				2	1875	
WF16			88		10		2	812.5	**e**
WF17			68		30		2	206.25	
WF18			48		50		2	62.5	
WF19			88		5	5	2	937.5	**f**
WF20			68		15	15	2	212.5	
WF21			48		25	25	2	75	
WF22	48		40		10		2	275	**g**
WF23	28		60		10		2	450	
WF24	8		80		10		2	650	
WF25	48		40			10	2	275	**h**
WF26	28		60			10	2	450	
WF27	8		80			10	2	725	

Table A.1: The table of formulations created for the placement. There are six resins, S105, S128, S150, S160, S130 & S140, and one photoinitiator, 992 [88, 92, 94, 97–100]. Different combinations of resin with 2% photoinitiator make up the 27 formulations. The table is spilt into eight groups, within each group the formulations are related with each other.

Figure A.1 highlights the large difference in viscosity between S160 and the other individual resins and the effects of introducing different amounts of diluent resins.

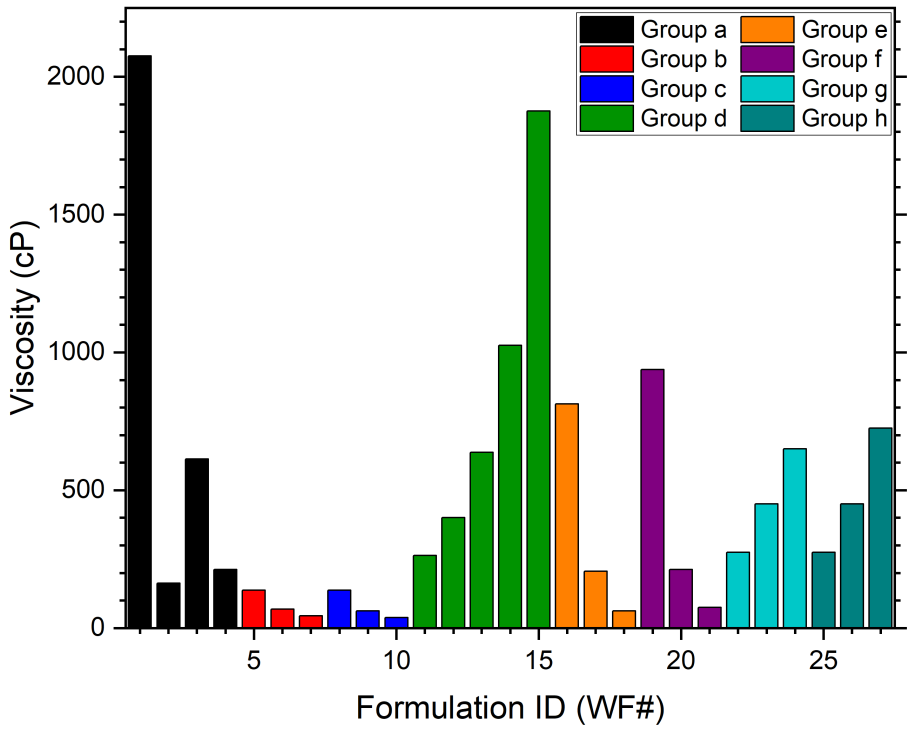


Figure A.1: A bar chart demonstrating the viscosity changes between all groups. S160 is the most viscous individual resin with S105, S140 and S130 acting as diluents.

A.2 Solvent resistance

A.2.1 Methodology

The procedure was recommended by Arkema and consisted of rubbing a butanone-soaked cotton bud back and forth until visible signs of damage was observed, figure A.2.

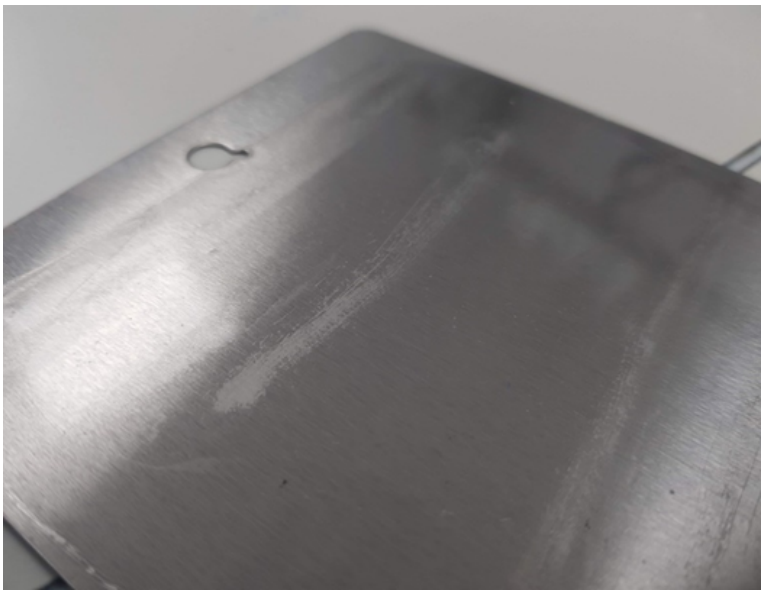


Figure A.2: Example of the visible streak observed on sample WF4 during the solvent resistance test. At this point the number of cycles, back and forth motion, of solvent soaked cotton bud was recorded.

The back and forth motion was counted as one cycle. The cotton bud was saturated in solvent and applied parallel to the sample to prevent inflicting a downwards force into the sample. As it was not possible to measured the force applied, each formulation was tested five times and the cotton bud was reapplied with solvent every 50 cycles. If a formulation resisted 300 cycles it was then labelled as robust and chemically resistant.

A.2.2 Results and analysis

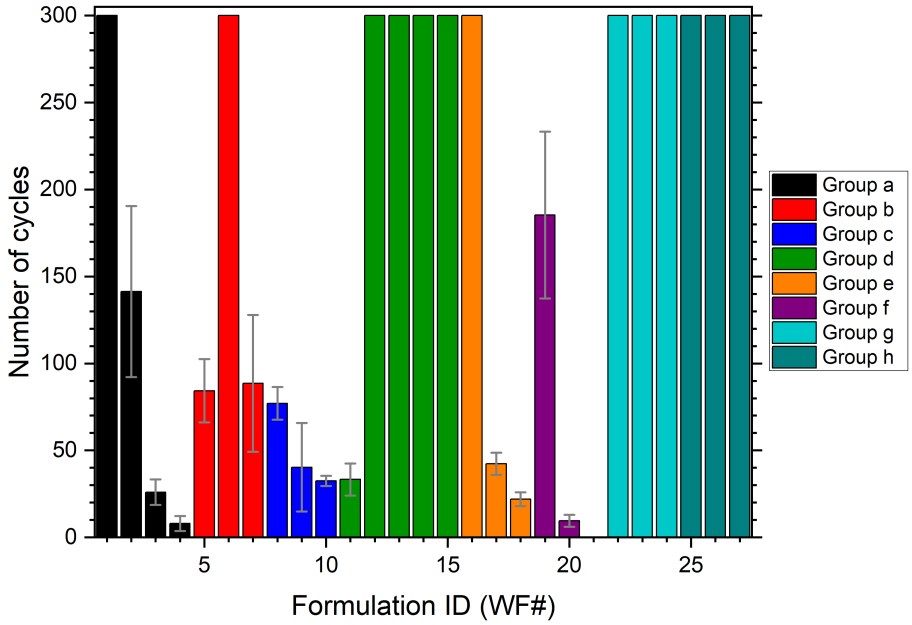


Figure A.3: A bar chart demonstrating the solvent resistance of the 27 formulations. 13 formulations were shown to be chemically resistant.

Figure A.3 demonstrates the solvent resistance of each formulation with 13 of the 27 formulations indicated as being chemically resistant. These chemically resistant formulations consistently achieved 300 cycles without showing any signs of damage. Error bars represent the spread of data between the five repeats. Large error bars are observed in several datasets and can be contributed to human error as test methodology was not consistent between samples. It was noticed that it was often difficult to stay along the same path as the user dragged the cotton bud across the surface. Additionally, completely avoiding applying force into the coating was challenging and was not monitored during the testing. However, figure A.3 provides a good indication of the potential of formulations' solvent resistance.

A.3 Adhesion

A.3.1 Methodology

The adhesion test was conducted using the procedure described by the American Society for Testing and Materials international's 'D3359: Standard Test Methods for Measuring Adhesion by Tape

Test [152].' The test required a 5 x 5 grid (2 mm spacing), figure A.4, to be marked into the coating by a sharp knife with sufficient pressure in order to reach the steel substrate.

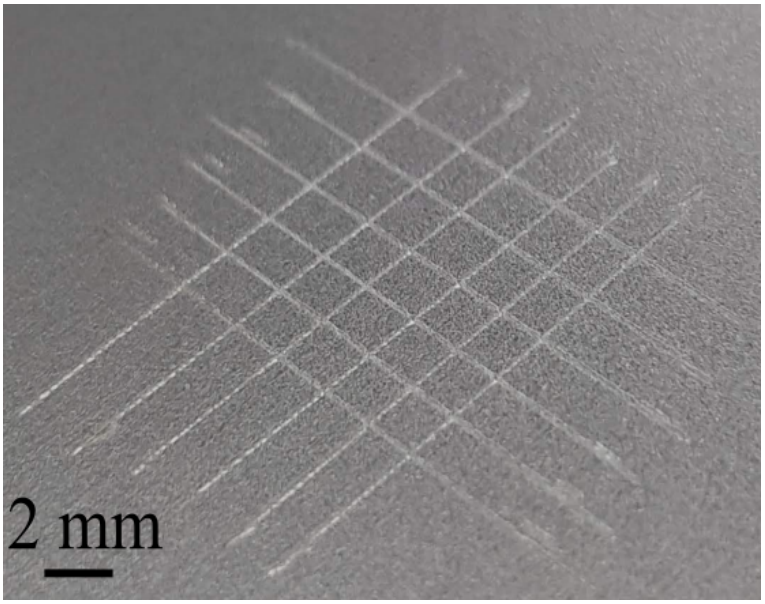


Figure A.4: 5 x 5 grid marked into a cured formulation coated onto a steel Q-panel. The spacing between the lines were 2 mm.

Using standard ISO 2409 adhesive tape, the grid was covered, smoothed over and left for 90 seconds. The tape was then removed peeling back on itself and the remaining residue was compared to the classification images provided in the standard. One of the following adhesion classifications were supplied to each formulation:

- **5**: No coating removal.
- **4**: Less than 5 % affected.
- **3**: Between 5 % and 15 % affected.
- **2**: Between 15 % and 35 % affected.
- **1**: Between 35 % and 65 % affected.
- **0**: Greater than 65 % affected.

The classifications were allocated approximately by eye to provide a basic understanding of the formulations' adhesion. The test was repeated three times per sample.

A.3.2 Results and analysis

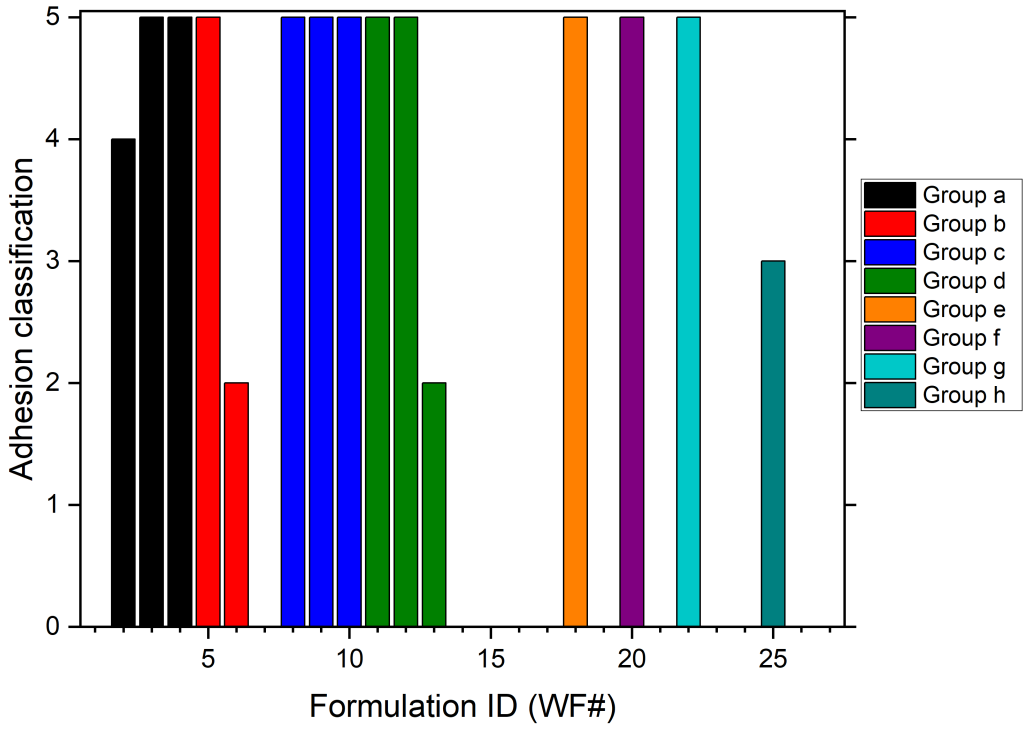


Figure A.5: A bar chart demonstrating the adhesion of the 27 formulations. A large proportion of the formulations either possess great or poor adhesion.

The majority of formulations was either classified as 0 or 5 with S160 possessing poor adhesion qualities and S105, S140 and S130 all possessing and improving adhesion qualities. Each formulation consistently provided the same classification between measurements. For all the formulations classified as 0, 100 % of the coating was removed. As a result, it was trivial to allocate these formulations the 0 classification with human error being not a concern in this particular experiment. As S160 majority formulations have the greatest photoelastic performance, the optimised formulation will most likely have poor adhesion. This is a beneficial quality as procedures could be developed for manual removal of the coating. However, further investigations are required to understand if poor adhesion equates to undesirable responses to sample deformation as discussed next.

A.4 Flexibility

A.4.1 Methodology

To measure flexibility a Tinius-Olsen 5 kN tester [153] was implemented along with a four-point and three-point bend rig, figure A.6.

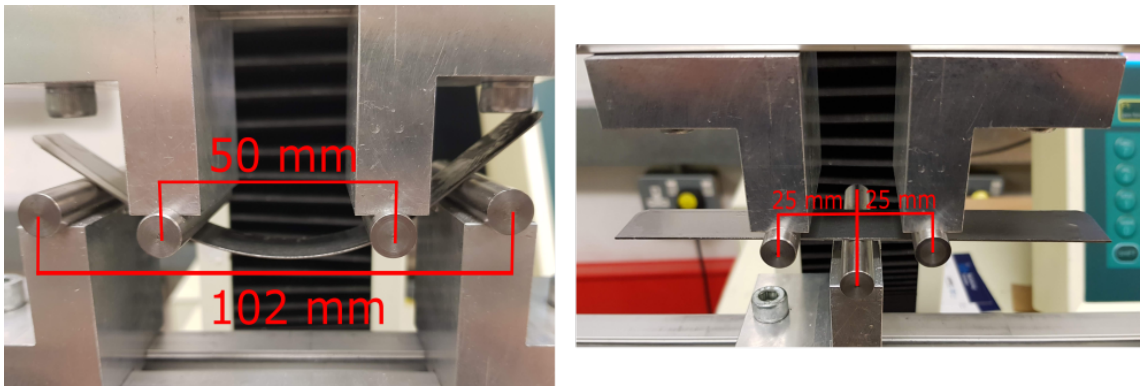


Figure A.6: Four-point and three-point bend test rigs used to measure the flexibility of the 27 formulations. The separation of the contact points is highlighted

The two setups provided a wider range of the radius of curvature inflicted by the test. Therefore, if a coating resists failure during the four-point bend it can then be tested using the three-point bend. For this test a steel strip with the coating on one side was bent steadily until failure was observed on the coating. For these investigations the coating was positioned so that it would experience a tensile force during the testing. By recording the position and force, a bending stress at failure could be measured to determine the ranking of flexibility of each coating compared with one another. Five repeat measurements were made and data recorded with an error.

A.4.2 Results and analysis

Each formulation did not fail when conducting two repeats per sample on both four-point bend and three-point bend test setups. There was no alternative setup available that could be attached to the tensile machine. As a result, the strips were manually bent around an 8 mm rod simulating a three-point bend test setup. Using this approach resulted in no measurement of bending stress however a determination of the coatings' flexibility was measured by roughly calculating the radius of curvature of the strip when it exhibited failure. The strip was slowly bent around the rod with

ease and at the moment of failure the strip maintained its shape. The radius of curvature was then measured by tracing the bend of the strip onto paper and manually intersecting the tangent points. Table A.2 presents this data with relevant sections highlighted.

Formulation Reference	Flexibility (mm)	Error (mm)
WF1	7.55	0.4
WF2	N/A	N/A
WF3	N/A	N/A
WF4	N/A	N/A
WF5	N/A	N/A
WF6	9.16	6.1
WF7	6.52	0.8
WF8	N/A	N/A
WF9	N/A	N/A
WF10	N/A	N/A
WF11	N/A	N/A
WF12	N/A	N/A
WF13	N/A	N/A
WF14	4.90	0.7
WF15	6.40	1.4
WF16	4.00	N/A
WF17	N/A	N/A
WF18	N/A	N/A
WF19	N/A	N/A
WF20	N/A	N/A
WF21	N/A	N/A
WF22	N/A	N/A
WF23	5.62	1.3
WF24	4.09	0.2
WF25	N/A	N/A
WF26	N/A	N/A
WF27	N/A	N/A

Table A.2: This table demonstrates the flexibility data for all 27 formulations. The term N/A describes that the coating demonstrated no failure.

Table A.2 demonstrates that the majority of coatings did not break during the investigation. Many coatings could withstand when the sample was bent back close to completely upon itself. The error associated to the flexibility of coatings that failed was calculated from the standard deviation of the repeat runs. By looking at the error of the least flexible coating, WF6, consistency in repeat measurements was not precise leading to a high error value. The three coatings, WF16, WF24 & WF27, had no error because only one area of failure was observed. Coatings WF6, W16, W23, W24, W26 & W27 only showed failure towards the ends of the steel strip, no failure observed in the bulk of the sample.

A.5 Glass transition temperature

A.5.1 Methodology

To capture the T_g transitions of each formulation a Differential Scanning Calorimeter (DSC) was used. The investigation utilised a DSC 25 from TA instruments [154] along their Tzero pans and lids. The procedure used required approximately 2 mg of formulation which was scraped from the cured coating of a sample. The amount was weighed using a balance that had a resolution of 1x10^{-4} mg. The mass was recorded and used during the DSC process to provide a normalised heat flow reading. Before DSC investigations were conducted a thermogravimetric analysis (TGA) test was performed to prevent considerable mass loss. The TGA demonstrated a mass loss at temperatures above 120 ^{o}C, this enabled determination of the upper temperature constraint of the DSC procedure around 180 ^{o}C based on experienced users' advice. The procedure was as follows:

1. An equilibrate to -50 ^{o}C
2. An isothermal for 2 minutes
3. A ramp in temperature at 20 ^{o}C·min^{-1} to 180 ^{o}C
4. Isothermal for 1 minute
5. Ramp in temperature at 20 ^{o}C·min^{-1} to -50 ^{o}C
6. Isothermal 2 minutes
7. Ramp in temperature at 10 ^{o}C·min^{-1} to 180 ^{o}C
8. Isothermal for 1 minute
9. Ramp in temperature at 10 ^{o}C·min^{-1} to -50 ^{o}C

Two heat cycles per sample were chosen to reset the thermal history of the sample. This was important as not performing this two cycle process would result in the distortion of the T_g transitions by melting processes that result in endothermic peaks that superimpose over the transition event preventing calculation of T_g. The dual cycle process is demonstrated in figure A.7.

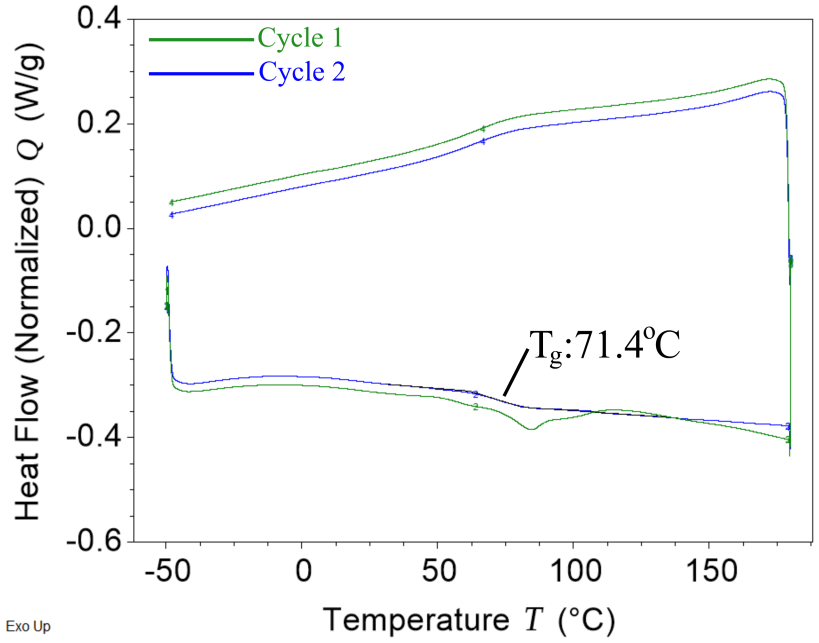


Figure A.7: Differential scanning calorimetry of WF1 performed to measure the formulation's glass transition temperature. The DSC procedure used two cycles to reset the thermal history, both cycles are presented. Within cycle 1, the location of the T_g transition is unclear as a melting peak has superimposed over the transition event.

Cycle 2 features a step like decrease in the heat flow that is the common representation of T_g transition. Within cycle 1 this pattern was initially observed however superimposing with a melting peak prevents calculation of the transition as shown figure A.7. Testing all 27 formulations took over 24 hours of testing which prevented multiple tests to be run.

A.5.2 Results and analysis

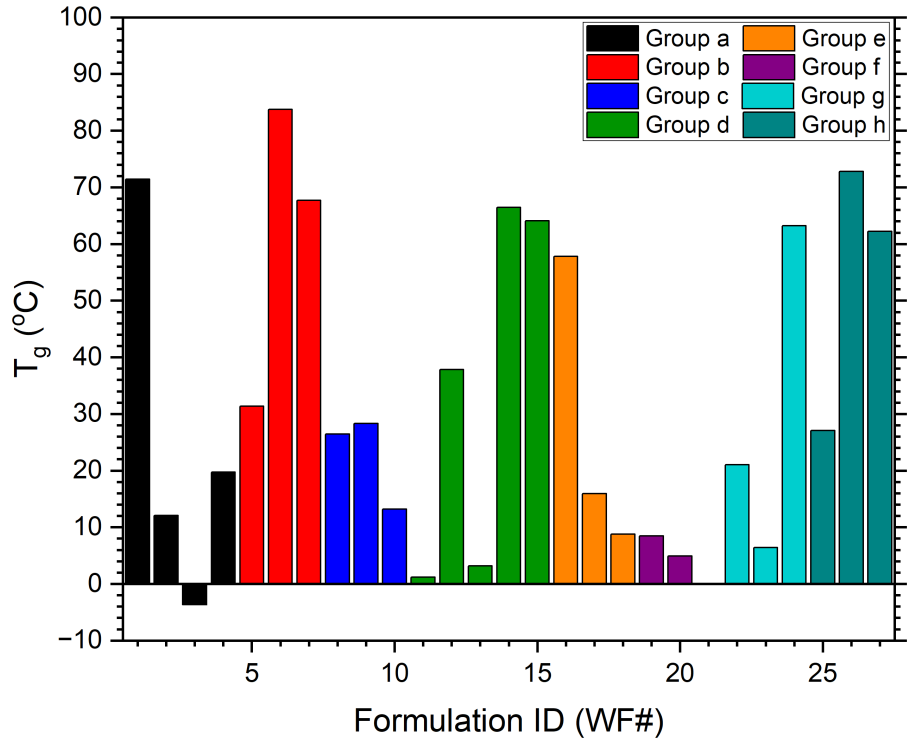


Figure A.8: A bar chart demonstrating the glass transition temperature of the 27 formulations.

Figure A.8 demonstrates the T_g of all formulations having only a single repeat. Running 26 formulations with the outlined procedure took 26 hours in total. The T_g of all resins varied from -4 — 84 ^oC. However, the confidence of these results is unclear as Arkema UK flagged concern over these values being lower than once thought. As a result, no conclusions can be made from this dataset and T_g should be investigated in future experiments, chapter 4.

Appendix B

Maximising cure conversion

This appendix contains methodology, results and analysis from DSC and ATR-FTIR experiments that were conducted to measure the cure conversion of the formulation at various curing times, chapter 4. These investigations lead to the use of real-time ATR-FTIR to successfully measure the time required to achieve maximum conversion.

B.0.1 Theory

B.0.1.1 Differential scanning calorimetry

Differential scanning calorimetry (DSC) is a tool that provides qualitative and quantitative information regarding physical and chemical changes in a material. DSC measures the temperatures and heat flows associated with the transitions of a material such as melting, glass transition and cure reactions. DSC will measure these properties as a function of temperature and time all within a controlled environment [155]. The DSC apparatus used in this research is a type of heat-flux DSC. In heat-flux DSC instruments, the sample material is placed and encapsulated into a small pan and placed in a chamber, the furnace, on a thermoelectric disk. Alongside the sample there an empty pan, known as the reference, that is placed on its own separate thermoelectric disk. The temperature within the furnace can be raised or lowered at a constant rate and the differential heat flow is measured through thermocouples. Due to the heat capacity of the sample, there exists a temperature difference between the sample and reference which leads to heat flow being determined via equation B.1

$$\frac{dQ}{dt} = \frac{\Delta T}{R} \tag{B.1}$$

where $\frac{dQ}{dt}$ is the heat flow, ΔT the difference in temperature between sample and reference and R the resistance of the thermoelectric disk. This equation can be equated to equation B.2 which possesses information regarding the transition events of a material

$$\frac{dQ}{dt} = Cp\left(\frac{dT}{dt}\right) + f(T,t) \tag{B.2}$$

where Cp is the sample specific heat capacity, $\frac{dT}{dt}$ is heating rate and $f(T,t)$ is the kinetic response at a specific temperature and time. This equation is used in the data processing to express various transition events. For cure reactions, which are of importance in this chapter, the kinetic function, $f(T,t)$, is used. Cure reactions are exothermic events as heat is generated during the reaction. DSC data will be in the form of a graph of normalised heat flow, W/g, against temperature. For a given temperature, an uncured or partially cured material may be triggered into a cure reaction, the heat emitted will be measured by the DSC and a peak will be observed on the data output. By comparing the enthalpy, the integrated area under the curve, of the partially cured sample to the uncured sample the conversion percentage, $\%C$, can be calculated from the following equation.

$$C\% = \left(1 - \left(\frac{H_p}{H_p - H_u}\right)\right) \times 100 \tag{B.3}$$

H_p is the partially cured enthalpy and H_u is the uncured formulation enthalpy. The area under the exothermic peak will decrease the closer the sample is to maximum cure conversion. If a sample placed in a DSC is fully cured, no exothermic peak will be observed.

B.0.2 Methodology

B.0.2.1 Differential scanning calorimetry

In order to determine the maximum cure conversion of WF31, samples had to be made effectively considering the DSC's run time. The DSC used in this investigation was TA Instruments' DSC 25 [154] which took upwards of an hour and a half to complete a single run of a single sample. Samples were created by spreading a small amount of formulation onto a clean silicone pad, which enabled easy extraction of the cured material, and were then placed under a mercury bulb for various time intervals. The time intervals of interest were: 5 s, 15 s, 30 s and 45 s. These exposure times were selected based on findings from chapter 4.2. Once 'cured', the coatings were left for two wait periods. One wait period was between 3 — 4 hours and would simulate how industries may use the coatings in their experiments. This wait time was selected after discussions with Airbus on the logistics on how they perform photoelastic analysis. The second wait period was 24 hours and was selected to determine if any further cure occurred once the photopolymerisation process was triggered. If further cure did occur then any repeat photoelastic measurements made in the curing time would possess inaccuracies. It was important to suspend the sample in its corresponding cure state before DSC analysis as it would ensure each sample had the same wait period. After a sample's designated wait time, samples were placed into a freezer awaiting DSC analysis.

The DSC apparatus was first programmed with the following heating cycle:

1. Equilibrate both the sample and reference to a start temperature of 20 ^{o}C
2. A heat ramp at a rate of 10 ^{o}C min^{-1} to 250 ^{o}C
3. Equilibrate both the sample and reference at 250 ^oC for 1 minute.
4. A heat ramp at a rate of 10 ^{o}C min^{-1} to 20 ^{o}C
5. Equilibrate both the sample and reference at 20 ^oC for 1 minute.
6. A heat ramp at a rate of 10 ^{o}C min^{-1} to 250 ^{o}C

The heat cycle follows a heat-cool-heat pattern to provide cure reaction information on the first heat sequence and glass transition (T_g) information on the second heat sequence. By running two heat sequences within the cycle, the thermal history of the coating was removed making the T_g easier to locate. To prepare DSC samples, pans were filled with as much coating material as possible then sealed. An exception was made for the uncured, liquid formulation as too much material could rupture the pan as it heats to high temperatures. Only one drop of liquid formulation was placed in a pan, approximately 20 — 40 mg. The pans were then weighed using a scale, with a resolution of $\pm$0.0001 mg, and recorded. An empty pan was weighed and the value subtracted from the filled pans to obtain the sample material mass, approximately 5 — 10 mg of solid material. Measuring the mass was crucial in order to normalise the heat flow for direct comparisons between samples. DSC samples were made in one session and when complete, were placed straight into a freezer awaiting DSC analysis. Samples were loaded into the furnace manually to reduce the time they spent at room temperature. The heat cycle was performed and data extracted for each sample.

B.0.2.2 ATR-FTIR

Similar to DSC, creating samples required consideration of data collection times. However, ATR-FTIR is a non-destructive technique meaning one set of samples were made to cover both wait times described in section B.0.2.1. Samples were made by depositing the UV formulation WF31, using a number 6 K-bar, onto steel Q-panels [103]. The Q-panels provided a large and flat surface that created approximately consistently thick samples. The formulations were cured using the same curing times as described in section B.0.2.1. After a wait time of 3 — 4 hours, a section of the hard coating was peeled from the panel using a sharp razor blade and placed on the ATR crystal.

The spectrometer used was the Nicolet iS 10 from ThermoFisher Scientific [156] with a golden gate ATR attachment.

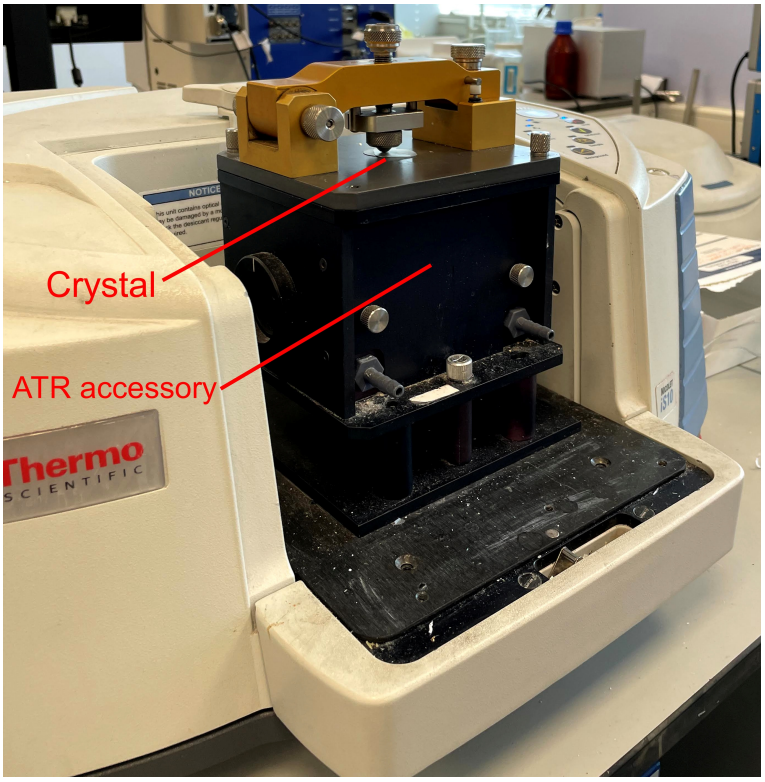


Figure B.1: FTIR spectrometer with a Golden Gate style ATR accessory attached. A section of cured WF31 is firmly pressed onto the ATR crystal ready for analysis.

Figure B.1 illustrates the Golden Gate ATR accessory mounted onto the FTIR spectrometer. A clamp secures and presses down onto the sample material providing increased contact between the sample and crystal. Before positioning and clamping a sample, a background scan was first performed taking approximately 1 minute. Performing a background scan accounts for any signal contributed by the instrument and environment to the sample being analysed. A background scan was performed before each sample. The sample was positioned and the spectrometer scanned over a range between 500 — 4000 cm^{-1} taking between 1 — 2 minutes. A single sample was repeated five times using different locations on the sample. After a 24 hour wait, the samples were analysed once more to determine if any changes in cure conversion occurred. For uncured samples, a pipette was used to apply a single drop of liquid formulation onto the crystal making sure to cover the entire area.

B.0.3 Results and analysis

B.0.3.1 Differential scanning calorimetry (DSC)

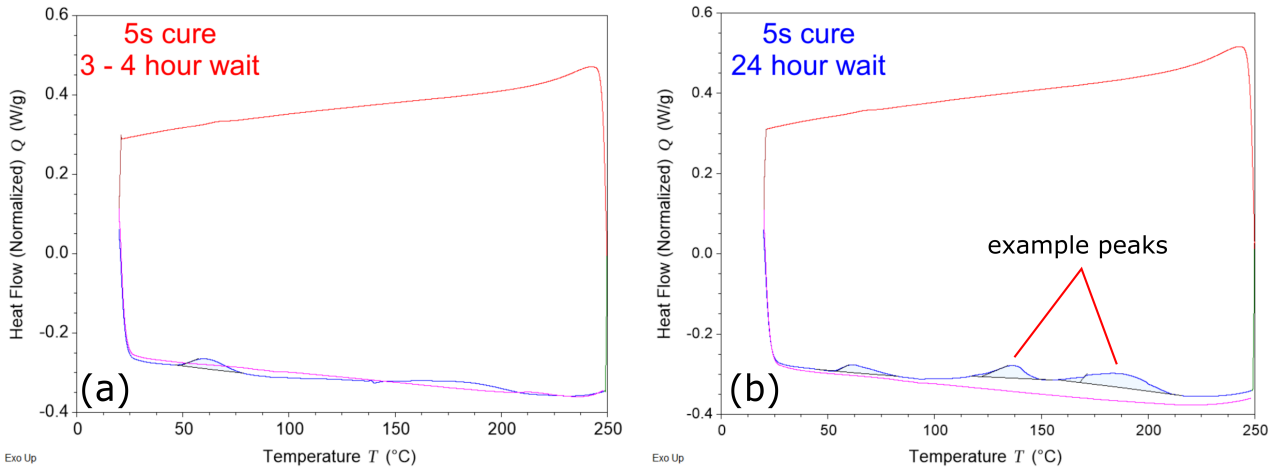


Figure B.2: Differential scanning calorimetry analysis of WF31 that was subjected to a 5s cure with two different wait periods.

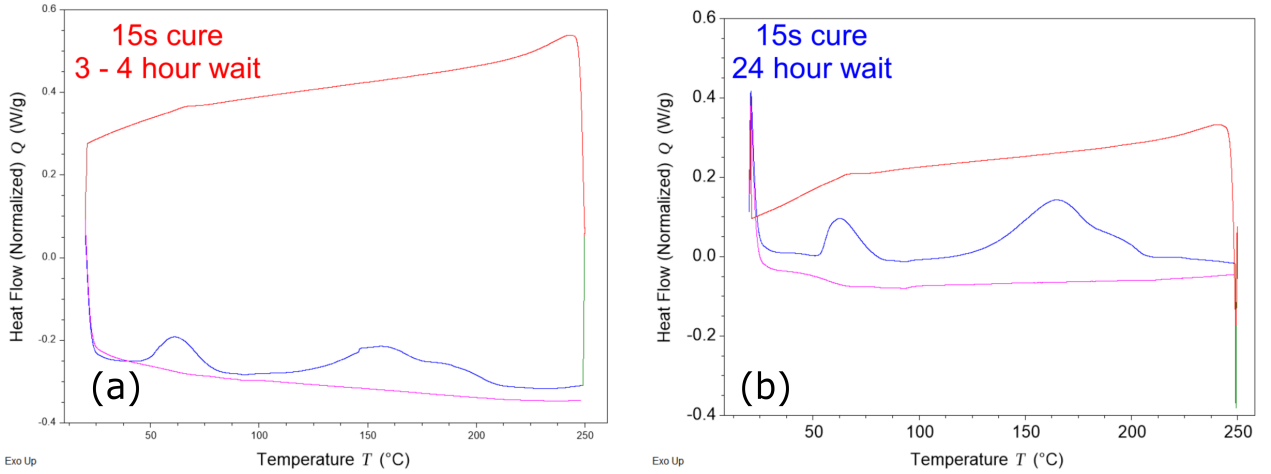


Figure B.3: Differential scanning calorimetry analysis of WF31 that was subjected to a 15s cure with two different wait periods.

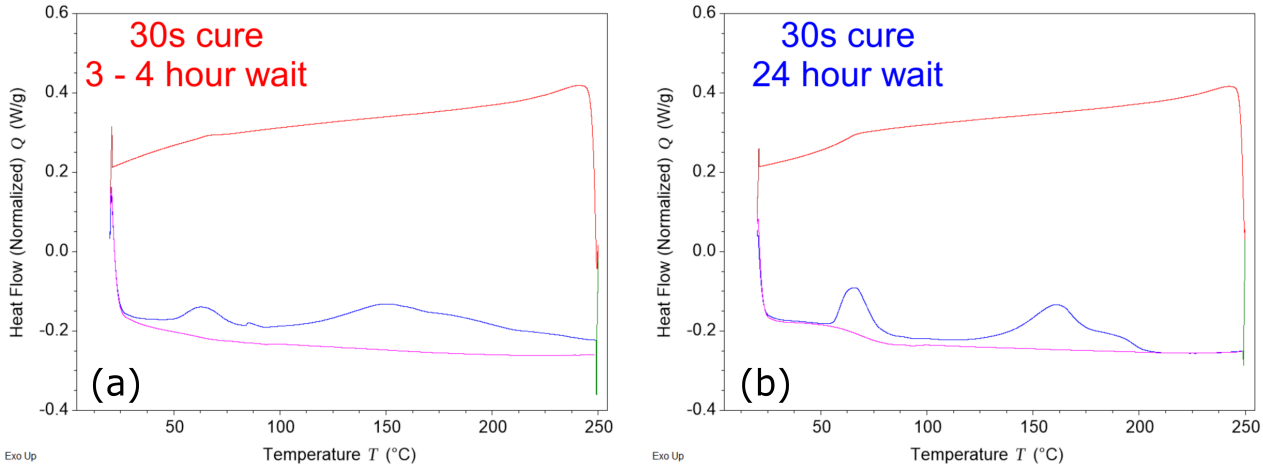


Figure B.4: Differential scanning calorimetry analysis of WF31 that was subjected to a 30s cure with two different wait periods.

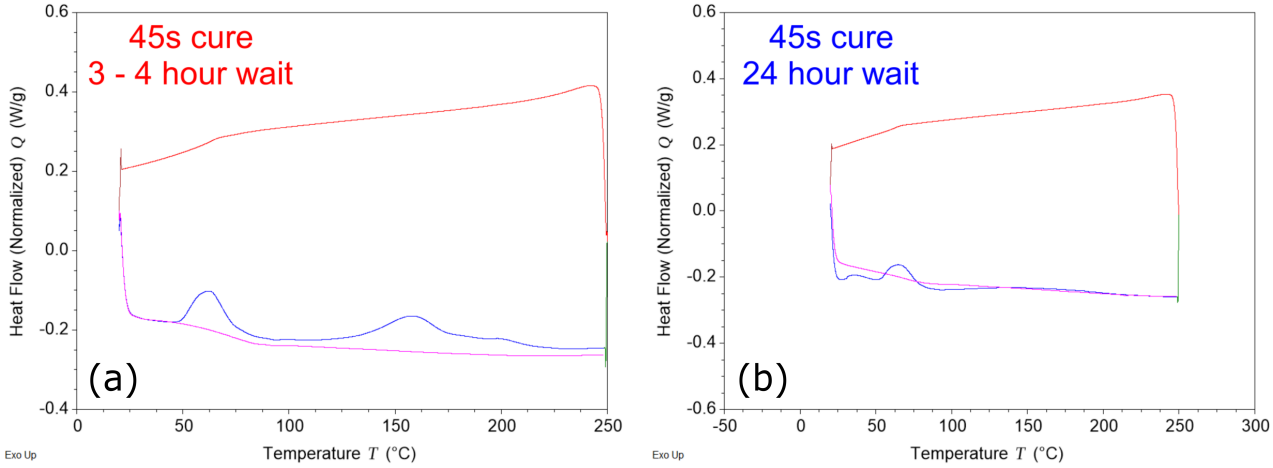


Figure B.5: Differential scanning calorimetry analysis of WF31 that was subjected to a 45s cure with two different wait periods.

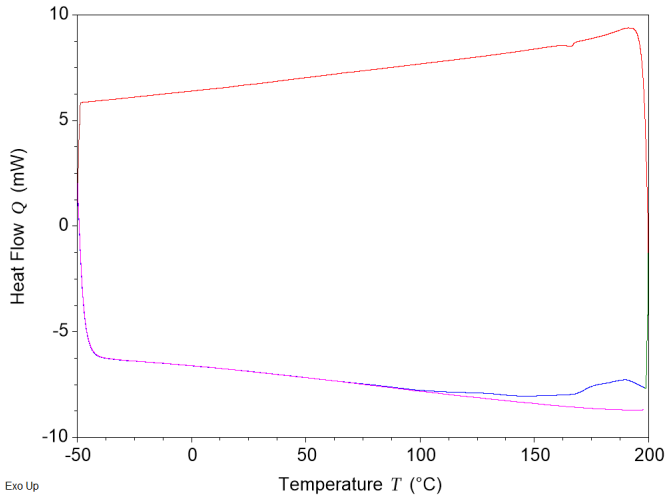


Figure B.6: Differential scanning calorimetry analysis of uncured WF31.

Within figures B.2 — B.5 several peaks are observed that resemble cure reactions. These peaks consistently appear at $\sim 60^{o}$C and between ~ 150 — 200^{o}C within all graphs apart from 45s cure with a 24 hour wait. At the higher temperature range, multiple cure reactions can be observed but due to their proximity, their peaks have merged together. Therefore, calculating enthalpy for these reactions was not possible as the true area under the peak has been distorted. Enthalpy measurements, for the peak at ~ 60 ^{o}C, appeared to fluctuate randomly between cure and wait times. For example at a 5 s cure with a 3 — 4 hour wait, the enthalpy was much smaller than at a 45 s cure with a 3 — 4 hours wait. This result goes against what was expected. Furthermore, figure B.6 demonstrates no cure reaction events throughout the heat cycle resulting in calculations for quantifying cure conversion impossible to achieve.

The results demonstrated that DSC was an unsuitable analysis technique to calculate the cure conversion of the UV formulation at various UV irradiation times. This issue was caused directly by the complexity of the UV formulation. The data output of the DSC reflects the thermal behaviour of the whole body of the sample and cannot differentiate between the structures that make up that sample. Prior to curing, there are several kinds of monomers, PLS chemical components and oligomers within the UV curable formulation. After curing, there will more polymers added to the matrix of the sample as not all the starting materials will be converted. Any of these could contribute to the generation of heat when the temperature of the bulk changes. This makes DSC impossible to provide precise and accurate results. Moreover, if there are any defects (micro-scale imperfection of the molecular structures, inhomogeneity resulted by the curing reactions from surface to depth, etc.) of the sample, there can be sampling problems in getting representative data.

B.0.3.2 ATR-FTIR

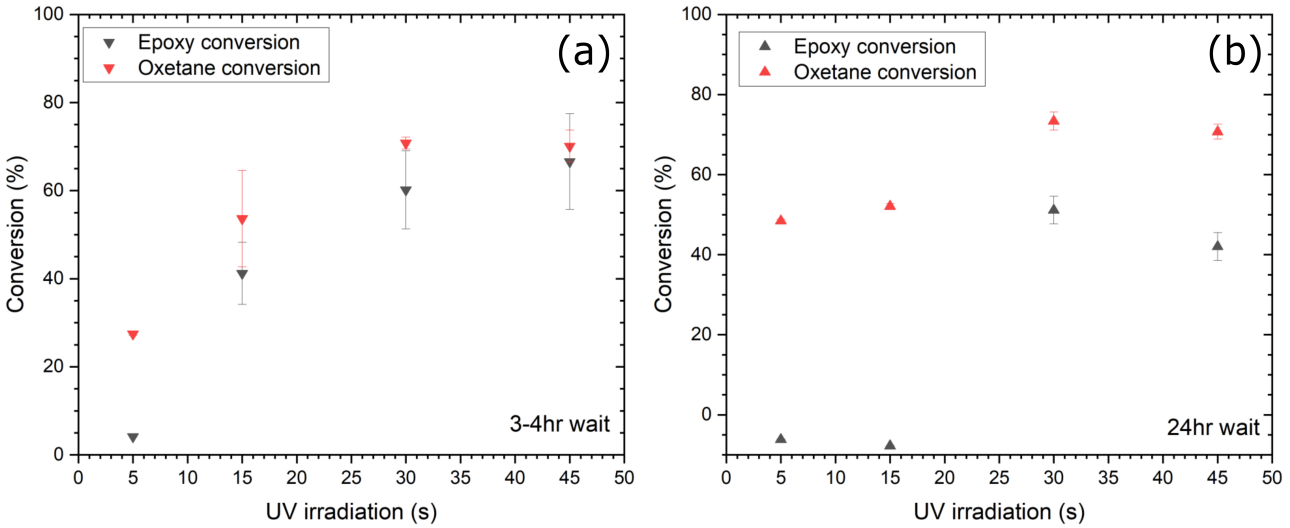


Figure B.7: Graphs of cure conversion, calculated from ATR-FTIR data, against curing time for two separate wait periods. Data points represent the mean whilst errors bars represent the standard uncertainty for the five repeat measurements.

Figure B.7 presents two graphs of mean cure conversion percentage at various UV irradiation times for two wait periods. The error bars represent the standard uncertainty for five repeat measurements. At the 3 — 4 hours wait period, figure B.7a, the cure conversion percentage steadily increased and appeared to reach a maximum at 45 s of UV light irradiation for both epoxy and oxetane conversions. The magnitude of the errors fluctuated from negligible amounts to ± 20 %. By leaving the coating for 24 hours, figure B.7b, a noticeable change in the measured cure conversion was observed when compared to the shorter wait period. A reduction in cure conversion was observed in the epoxy conversion whilst the opposite was observed within the oxetane conversion. Within the epoxy conversion, inaccuracies were observed throughout. Firstly, at 5 s and 15 s the cure conversion percentages were negative which would be impossible to achieve. Secondly, the cure conversion decreased from 30 s to 45 s. Between the two wait periods, the oxetane conversion increased considerably at 5 s and 15 s whilst at 30 s and 45 s the maximum cure conversion remained approximately the same.

ATR-FTIR spectroscopy was a more appropriate analytical technique when compared to DSC. Firstly, the time taken to prepare and extract data was a lot less. Three repeats per sample could be conducted in under 10 minutes compared to the 6 hours it would take for DSC. Secondly, the spectra produced by ATR-FTIR spectroscopy was able to provide information on the actual chemical structures that made up the UV curable formulation. The latter was used to calculate cure conversion that was shown in figure B.7. Figure B.7 presented expected results where the cure conversion would increase with UV light irradiation up to a certain time period. The time period for max conversion was $\sim$30 s and the 24 hour wait period after cure did not have any effect on the calculated value. However, there were uncertainties present in the collected data. Firstly, the calculated values for epoxy conversion percentage for 5 and 15 s of UV irradiation were below 0 % at a wait period of 24 hours. Secondly, the conversion percentage decreased from 30 to 45 s within the same 24 hour wait dataset. Thirdly, the data for the 3 — 4 hour wait period demonstrated poor precision due to

large error bars present in the majority of data points. These issues put the validity of the findings at risk. The cause of these inaccuracies are most likely attributed to the apparatus. Conditions such as the contact between the sample and the crystal and moisture within the detector could all have an effect on the measured results. These factors can be controlled and improved upon through the use of real-time ATR-FTIR spectroscopy as follows in section 4.3.2.

Appendix C

Primed samples

This investigation reviewed the photoelastic performance of a UV curable formulation, WF31, when applied to samples coated with an aerospace primer. The effectiveness of analysing data straight from primed components is an important study for this research. All aircraft components are primed with a coloured primer, usually a dull green, figure C.1.



Figure C.1: One half of a friction shim coated with an aerospace primer. This image shows the matt finish of the green paint

The photoelastic coatings, that are currently used by Airbus, all utilise a reflective backing that adheres the coating to the component. This investigation will determine if a reflective backing will be required for the UV curable formulation.

C.1 Methodology

Ten aluminium samples of dimensions (300 x 25 x 6) mm were sprayed with a green aerospace primer. The application was conducted at Airbus as the paint was chromate based and required specialised apparatus to apply safely. Gloves were always worn when handling the samples to prevent the transfer of paint onto hands and other surfaces. Due to the time it took to send and paint additional samples, care was taken throughout the experiment to not scratch or damage the primed surface. Initially, three samples were prepared for photoelastic analysis. Acetone was used to clean the curing surface of the sample. Due to the primer being epoxy based, its level of chemical resistance was able to

withstand thorough cleaning using solvents. Prior to WF31 application, a segment of heat-resistant tape was applied at one end of the desired coating area. WF31 was then applied, using a number 6 K-bar (wet film thickness of 60 μm), over the tape and spread $\sim$150 mm down the sample ensuring the middle was covered. The tape was used to assist in the removal of the cured coating for thickness measurements. It allowed a sharp razor blade easier access under the coating which would enable the cured coating to be peeled away. This process prevented scratching of the primed surface when removing the coating resulting in prolonging the uniformity of the painted surface and preventing fine particles of paint coming free from the samples. The tape was selected to be heat-resistant to withstand the heat of the Hg bulb during curing. The UV curable formulation was illuminated with UV light for 20 s before being stored in a dark place ready for photoelastic analysis. The samples were subjected to the same photoelastic analysis procedure as described in section 5.2.1. For these experiments strain gauges were applied, stacked rosette gauges [132], to plot normalised subtraction retardation against principal strain difference. The principal strain difference was calculated from a stacked rosette strain gauge adhered to the sample at the location of retardation extraction with 0^o and 90^o gauges orientated along the principal strain axes. Strain data was used in preparation for coating calibration experiments, chapter 7.

C.2 Results and analysis

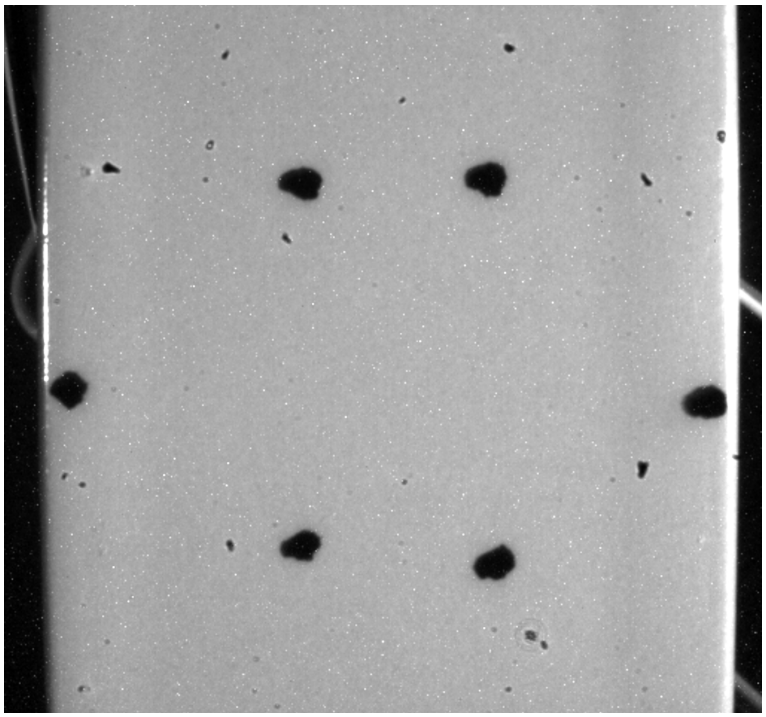


Figure C.2: The light output image of a primed aluminium sample, sprayed aerospace epoxy paint, coated with a UV curable formulation. The image demonstrates uniform shade of grey across the central region of the sample.

Figure C.2 demonstrates the light output image of a primed sample coated with WF31. A uniform shade of grey was observed through the central region of the sample, ideal for reducing the noise that would be present in the measured retardation. However, it was immediately apparent that

minimal changes in retardation (2 - 3 nm) were being measured by the GFP1600 through the entire loading scenario.

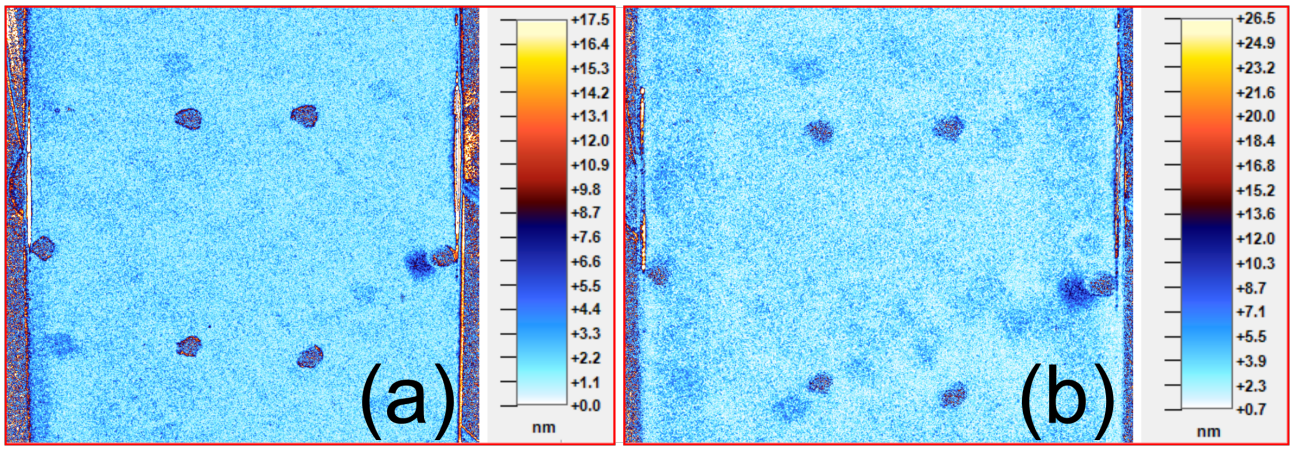


Figure C.3: Shear Max images taken by the GFP1600 observing a primed and coated aluminium sample during zero load, ***(a)****, and maximum load,* ***(b)****.*

Figure C.3 shows a similar level of retardation of an aluminium sample applied with zero load, figure C.3(a), and the same sample applied with maximum load (33 kN), figure C.3(b). As a result, it was confirmed that a reflective backing was required to extract a measurable retardation from the primed samples. The coatings from the three sample were removed and a silver paint, described in section 5.2.1, was applied to the primed surface of the sample. The same coating application procedure described in section C.1 was followed.

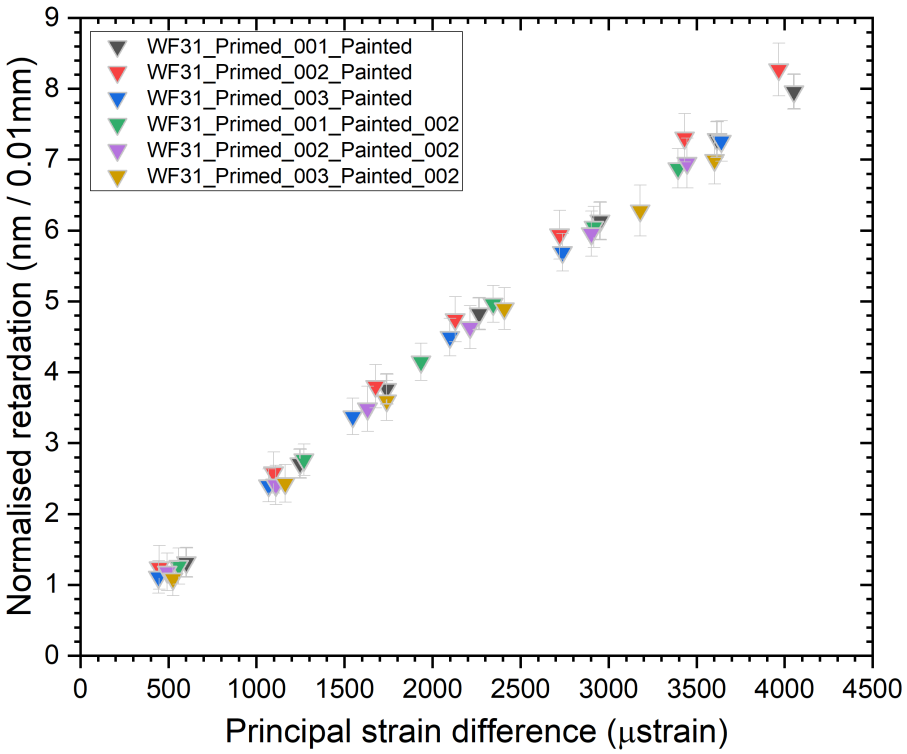


Figure C.4: The measured normalised retardation against the principal strain difference. The principal strain difference was calculated from a stacked rosette strain gauge adhered to the sample at the location of retardation extraction. Three primed samples were coated with silver paint and subjected to two loading cycles each. The coating was reapplied after each cycle.

Figure C.4 presents the measured retardation, subtracted and normalised, against the principal strain difference. The principal strain difference was calculated from the data supplied by a stacked rosette strain gauge. Six individual coatings were investigated using three primed samples to reduce the number of strain gauges being used. The six responses were all linear and possessed a high level of precision throughout.

The results, in figure C.3, demonstrate that applying the clear UV curable coating directly onto a primed aerospace component would yield no measurable photoelastic response. The direct cause of this finding requires further investigation and was performed in the following section 5.2.3. However, a relationship between this sample finish and the sandblasted finish can be made. Both finishes possessed a greater dullness than raw aluminium, the silver paint, and the silver appearance of PS-1E. Within figure 5.14, the response for the sandblasted samples had a reduced magnitude compared to the other three finishes. Many aerospace primers are quoted with a gloss level of less than 20 GU (gloss units). A measurement of gloss is performed by using a highly polished black glass as a reference [157]. This reference would possess a gloss level of 100 GU. As a result, 20 GU can be considered on the edge of low to medium gloss, therefore the primed surface's reflection capabilities are poor. By conducting a future investigation on the reflection capabilities of these surfaces finishes, a connection could be formed between surface dullness and measured retardation. This information would provide a deeper insight into best practises for reflection photoelasticity.

The responses shown in figure C.4 provide positive findings for this research. The precision of these

responses, for six individual coatings, boasts high repeatability for WF31. Furthermore, they suggest that the experimental setup was appropriate and effectively optimised.

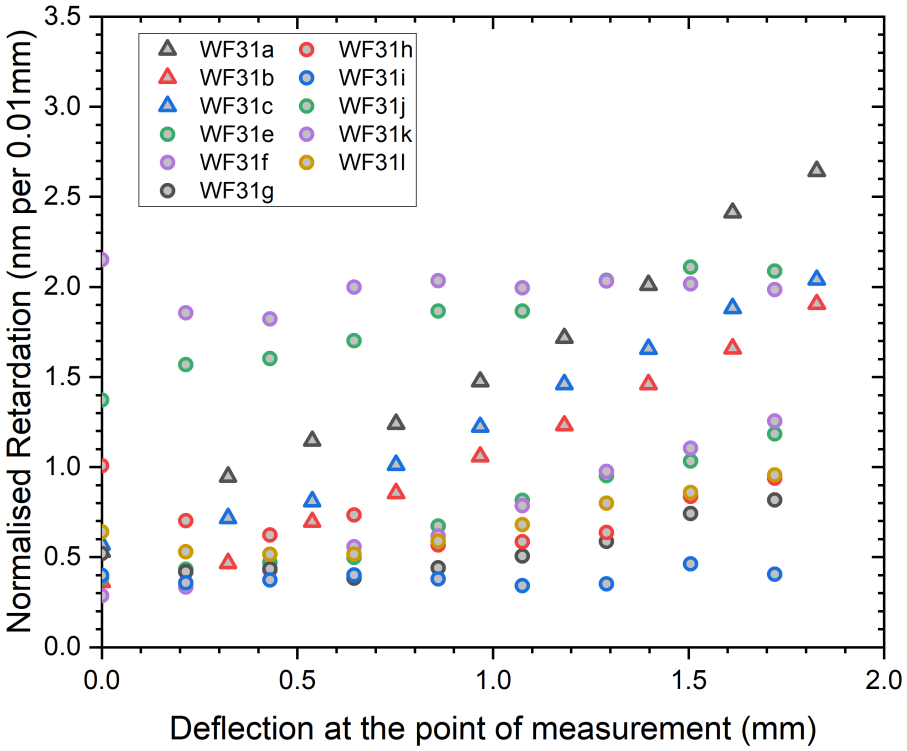


Figure C.5: Measured retardation against cantilever deflection for an aluminium sample at the point where retardation data was extracted. 11 samples were tested providing responses that lacked precision.

Comparing current responses, in figure C.5, to the previous, in figure C.4, highlights the importance of a deeper understanding of photoelastic experimental methods. Both graphs feature samples coated with the same formulation in different loading scenarios. The increase in dynamic range, optimised the coating illumination and the consistent light path from light source to GFP all contribute to the increase in precision observed in figure C.4.

Appendix D

t-test verdicts

By performing t-tests on a variety of dataset combinations, the population means can be compared and determined if they were statistically significant or insignificant. The former describes the situation were the datasets **reject** the null hypothesis, there was no difference between comparisons. The latter describes the situation were the datasets **accept** the null hypothesis, there was a difference between comparisons. The following tables demonstrate the major t-test verdicts from comparisons between groups (5 sets within each group) of samples that had different wait periods after curing.

Set Number	TestID	1 hr vs 24 hr						
	5s vs 5s	10s vs 10s	15s vs 15s	30s vs 30s	45s vs 45s	60s vs 60s	90s vs 90	120s vs 120s
Set 1	accept	accept	reject	accept	accept	reject	reject	accept
Set 2	reject	reject	accept	reject	reject	accept	accept	accept
Set 3	accept	accept	reject	reject	accept	reject	reject	accept
Set 4	accept	accept	accept	reject	accept	reject	accept	accept
Set 5	accept	accept	reject	accept	reject	accept	reject	accept
Average	accept	accept	reject	reject	accept	accept	accept	accept

Set Number	TestID	5s 1hr vs 1hr						
		5s vs 10s	5s vs 15s	5s vs 30s	5s vs 45s	5s vs 60s	5s vs 90	5s vs 120s
Set 1		accept	reject	accept	accept	accept	reject	accept
Set 2		accept	reject	reject	reject	reject	reject	reject
Set 3		accept	reject	reject	reject	reject	reject	reject
Set 4		reject	accept	reject	accept	accept	reject	accept
Set 5		reject	accept	reject	reject	reject	accept	accept
Average		reject	accept	reject	accept	accept	accept	accept

Set Number	TestID	5s 24hr vs 24hr						
		5s vs 10s	5s vs 15s	5s vs 30s	5s vs 45s	5s vs 60s	5s vs 90	5s vs 120s
Set 1		reject	accept	accept	accept	accept	reject	accept
Set 2		accept	accept	reject	reject	reject	reject	reject
Set 3		accept	reject	accept	reject	accept	accept	reject
Set 4		reject	accept	reject	reject	accept	accept	accept
Set 5		accept	reject	accept	accept	accept	accept	accept
Average		reject	accept	accept	accept	accept	accept	accept

Set Number	TestID	10s 1hr vs 1hr						
	5s vs 10s		10s vs 15s	10s vs 30s	10s vs 45s	10s vs 60s	10s vs 90	10s vs 120s
Set 1	accept		reject	accept	reject	accept	reject	accept
Set 2	accept		accept	reject	reject	reject	reject	reject
Set 3	accept		reject	reject	reject	reject	reject	reject
Set 4	reject		reject	reject	reject	reject	reject	reject
Set 5	reject		reject	reject	reject	reject	accept	accept
Average	reject		reject	reject	reject	reject	reject	reject

Set Number	TestID	10s 24hr vs 24hr						
	5s vs 10s		10s vs 15s	10s vs 30s	10s vs 45s	10s vs 60s	10s vs 90	10s vs 120s
Set 1	reject		reject	reject	reject	reject	reject	reject
Set 2	accept		accept	accept	reject	reject	reject	reject
Set 3	accept		reject	reject	reject	reject	reject	reject
Set 4	reject		reject	accept	reject	reject	reject	reject
Set 5	accept		reject	accept	accept	accept	accept	accept
Average	reject		reject	reject	reject	reject	reject	reject

Set Number	TestID	15s 1hr vs 1hr						
	5s vs 15s	10s vs 15s		15s vs 30s	15s vs 45s	15s vs 60s	15s vs 90	15s vs 120s
Set 1	reject	reject		reject	accept	accept	reject	accept
Set 2	reject	accept		reject	accept	accept	reject	accept
Set 3	reject	reject		accept	accept	reject	reject	accept
Set 4	accept	reject		accept	accept	accept	accept	accept
Set 5	accept	reject		accept	accept	accept	accept	accept
Average	accept	reject		reject	accept	accept	accept	accept

Set Number	TestID	15s 24hr vs 24hr						
	5s vs 15s	10s vs 15s		15s vs 30s	15s vs 45s	15s vs 60s	15s vs 90	15s vs 120s
Set 1	accept	reject		accept	reject	reject	reject	accept
Set 2	accept	accept		accept	reject	reject	reject	accept
Set 3	reject	reject		reject	reject	reject	reject	reject
Set 4	accept	reject		reject	reject	reject	accept	accept
Set 5	reject	reject		accept	accept	reject	accept	reject
Average	accept	reject		reject	accept	accept	accept	accept

Set Number	TestID	30s 1hr vs 1hr						
	5s vs 30s	10s vs 30s	15s vs 30s		30s vs 45s	30s vs 60s	30s vs 90	30s vs 120s
Set 1	accept	accept	reject		reject	reject	accept	accept
Set 2	reject	reject	reject		reject	reject	accept	accept
Set 3	reject	reject	accept		reject	accept	accept	accept
Set 4	reject	reject	accept		accept	accept	accept	accept
Set 5	reject	reject	accept		accept	accept	reject	reject
Average	reject	reject	reject		accept	accept	reject	accept

Set Number	TestID	30s 24hr vs 24hr						
	5s vs 30s	10s vs 30s	15s vs 30s		30s vs 45s	30s vs 60s	30s vs 90	30s vs 120s
Set 1	accept	reject	accept		reject	reject	reject	reject
Set 2	reject	accept	accept		reject	reject	reject	reject
Set 3	accept	reject	reject		reject	accept	accept	reject
Set 4	reject	accept	reject		accept	reject	reject	reject
Set 5	accept	accept	accept		accept	accept	reject	reject
Average	accept	reject	reject		reject	reject	accept	reject

Set Number	TestID	45s 1hr vs 1 hr						
	5s vs 45s	10s vs 45s	15s vs 45s	30s vs 45s		45s vs 60s	45s vs 90	45s vs 120s
Set 1	accept	reject	accept	reject		reject	reject	reject
Set 2	reject	reject	accept	reject		reject	reject	reject
Set 3	reject	reject	accept	reject		accept	reject	accept
Set 4	accept	reject	accept	accept		reject	accept	reject
Set 5	reject	reject	accept	accept		accept	reject	reject
Average	accept	reject	accept	accept		reject	accept	reject

Set Number	TestID	45s 24hr vs 24hr						
	5s vs 45s	10s vs 45s	15s vs 45s	30s vs 45s		45s vs 60s	45s vs 90	45s vs 120s
Set 1	accept	reject	reject	reject		reject	reject	accept
Set 2	reject	reject	reject	reject		reject	reject	accept
Set 3	reject	reject	reject	reject		accept	accept	accept
Set 4	reject	reject	reject	accept		reject	reject	reject
Set 5	accept	accept	accept	accept		accept	reject	reject
Average	accept	reject	accept	reject		accept	reject	accept

Set Number	TestID	60s 1hr vs 1hr						
	5s vs 60s	10s vs 60s	15s vs 60s	30s vs 60s	45s vs 60s		60s vs 90	60s vs 120s
Set 1	accept	accept	accept	reject	reject		reject	accept
Set 2	reject	reject	accept	reject	reject		reject	accept
Set 3	reject	reject	reject	accept	accept		reject	reject
Set 4	accept	reject	accept	accept	reject		accept	accept
Set 5	reject	reject	accept	accept	accept		accept	reject
Average	accept	reject	accept	accept	reject		reject	accept

Set Number	TestID	60s 24hr vs 24hr						
	5s vs 60s	10s vs 60s	15s vs 60s	30s vs 60s	45s vs 60s		60s vs 90	60s vs 120s
Set 1	accept	reject	reject	reject	reject		reject	accept
Set 2	reject	reject	reject	reject	reject		reject	accept
Set 3	accept	reject	reject	accept	accept		accept	reject
Set 4	accept	reject	reject	reject	reject		reject	accept
Set 5	accept	accept	reject	accept	accept		accept	reject
Average	accept	reject	accept	reject	accept		reject	accept

Set Number	TestID	90s 1hr vs 1hr						
	5s vs 90	10s vs 90	15s vs 90	30s vs 90	45s vs 90	60s vs 90		90s vs 120s
Set 1	reject	reject	reject	accept	reject	reject		accept
Set 2	reject	reject	reject	accept	reject	reject		accept
Set 3	reject	reject	reject	accept	reject	reject		reject
Set 4	reject	reject	accept	accept	accept	accept		accept
Set 5	accept	accept	accept	reject	reject	accept		reject
Average	accept	reject	accept	reject	accept	reject		reject

Set Number	TestID	90s 24hr vs 24hr						
	5s vs 90	10s vs 90	15s vs 90	30s vs 90	45s vs 90	10s vs 90		90s vs 120s
Set 1	reject	reject	reject	reject	reject	reject		accept
Set 2	reject	reject	reject	reject	reject	reject		accept
Set 3	accept	reject	reject	accept	accept	accept		reject
Set 4	accept	reject	accept	reject	reject	reject		reject
Set 5	accept	accept	accept	reject	reject	accept		reject
Average	accept	reject	accept	accept	reject	reject		reject

Set Number	TestID	120s 1hr vs 1hr						
	5s vs 120s	10s vs 120s	15s vs 120s	30s vs 120s	45s vs 120s	60s vs 120s	90s vs 120s	
Set b	accept	accept	accept	accept	reject	accept	accept	
Set c	reject	reject	accept	accept	reject	accept	accept	
Set d	reject	reject	accept	accept	accept	reject	reject	
Set e	accept	reject	accept	accept	reject	accept	accept	
Set f	accept	accept	accept	reject	reject	reject	reject	
Average set	accept	reject	accept	accept	reject	accept	reject	

Set Number		120s 24hrs vs 24hrs						
	5s vs 120s	10s vs 120s	15s vs 120s	30s vs 120s	45s vs 120s	60s vs 120s	90s vs 120s	
Set b	accept	reject	accept	reject	accept	accept	accept	
Set c	reject	reject	accept	reject	accept	accept	accept	
Set d	reject	reject	reject	reject	accept	reject	reject	
Set e	accept	reject	accept	reject	reject	accept	reject	
Set f	accept	accept	reject	reject	reject	reject	reject	
Average set	accept	reject	accept	reject	accept	accept	reject	

Figure D.1: The main t-test results from the effects of UV light irradiation time (curing time) on the photoelastic response. The Photoelastic response was normalised to enable independent and paired t-tests.

Appendix E

Time to achieve maximum cure conversion: WF-Red1 & WF-SAOE

The time to reach maximum cure conversion of both WF-Red1 and WF-SAOE was measured utilising real-time ATR-FTIR with the method outlined in chapter 4 section 4.3.1. Technicians at Arkema performed all the measurements with the calculations performed within the University. The calculated time to reach maximum conversion for both WF-Red1 and WF-SAOE are presented in figures E.1 and E.2 respectively.

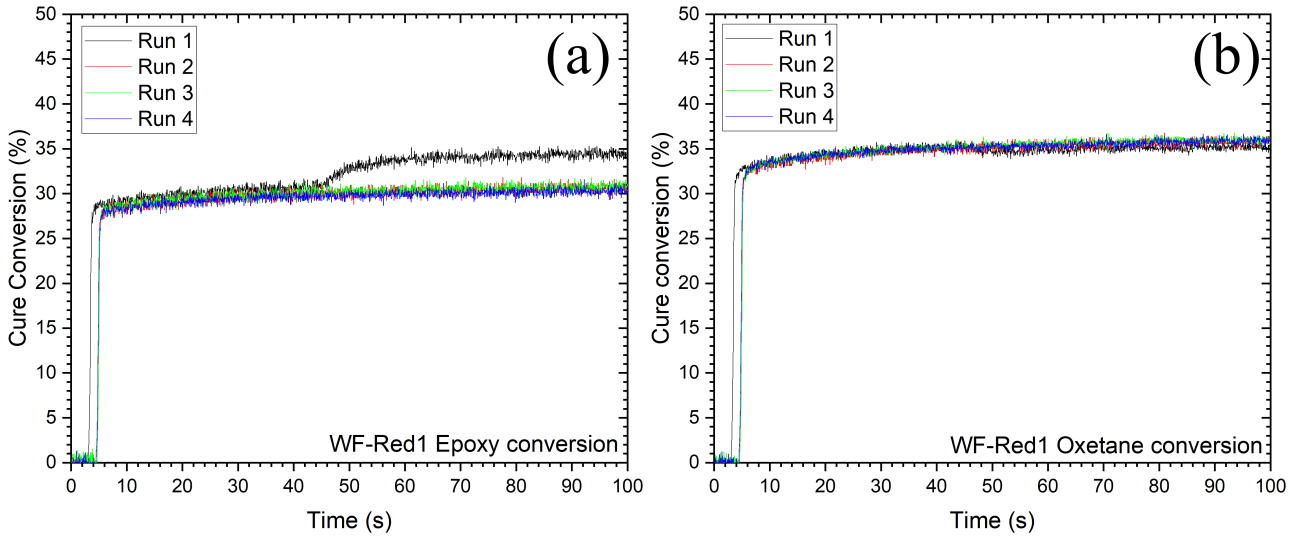


Figure E.1: Graphs of epoxy and oxetane cure conversions of WF-Red1 using real-time ATR-FTIR spectroscopy. The UV light output was reduced with an iris aperture of 100 %. The measured time to reach maximum cure conversion was the same as WF31.

The sudden increase with run 1 of figure E.1(a) was an observed outlier. The time to reach maximum cure conversion was approximately 20 s the same result as WF31.

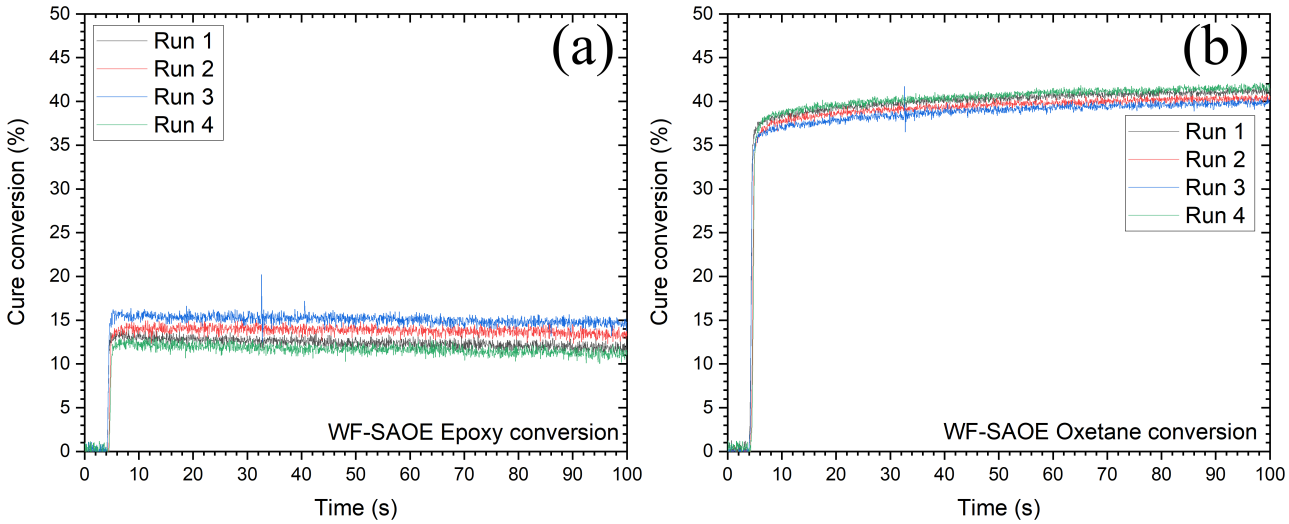


Figure E.2: Graphs of epoxy and oxetane cure conversions of WF-SAOE using real-time ATR-FTIR spectroscopy. The UV light output was reduced with an iris aperture of 100 %. The measured time to reach maximum cure conversion was the same as WF31.

A reduction in the maximum epoxy cure conversion was observed for WF-SAOE yet the oxetane measurement remained comparable to both WF31 and WF-Red1. However, the time to reach maximum cure conversion was approximately 20 s the same result as WF31.

Appendix F

GFP1600 data: Incremental loading example

Figure F.1 presents the GFP data for each applied load for the Glass Laminate Aluminum Reinforced Epoxy (GLARE) specimen analysed in section 8.1.1. To summaries, a GLARE specimen with a circular stress riser was subjected to a simple tensile test. The Deltavision software calculates the induced birefringence for each load. As a result, the shift in fractional fringe order is observed and translated into principal strain difference. Figure F.1 demonstrates the formation of interference patterns captured and analysed by the GFP1600 and software Deltavision.

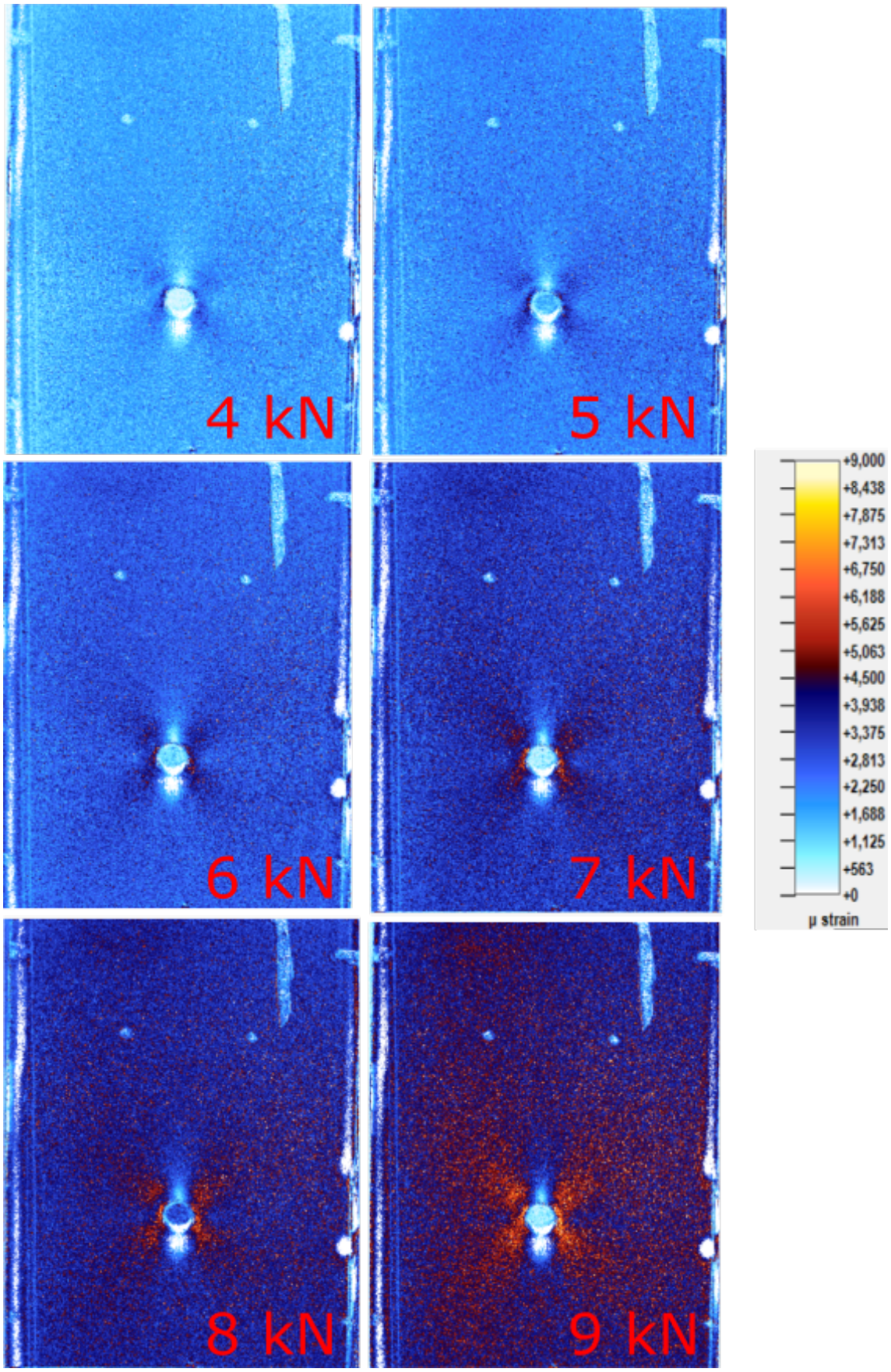


Figure F.1: GFP1600 data for each applied load of the Glass Laminate Aluminum Reinforced Epoxy (GLARE) specimen analysed in section 8.1.1.